NASA/TM–20220012155

X-59 Sonic Boom Test Results from the NASA Glenn 8- by 6-Foot Supersonic Wind Tunnel

Donald A. Durston[*]
John D. Wolter[†]
Patrick R. Shea[‡]
Courtney S. Winski[‡]
Alaa A. Elmiligui[‡]
Sarah L. Langston[‡]
Michael D. Bozeman[‡]
Melissa B. Carter[‡]
Jonathon D. Ponder[†]
James T. Heineck[*]
Christopher A. Bellido[§]

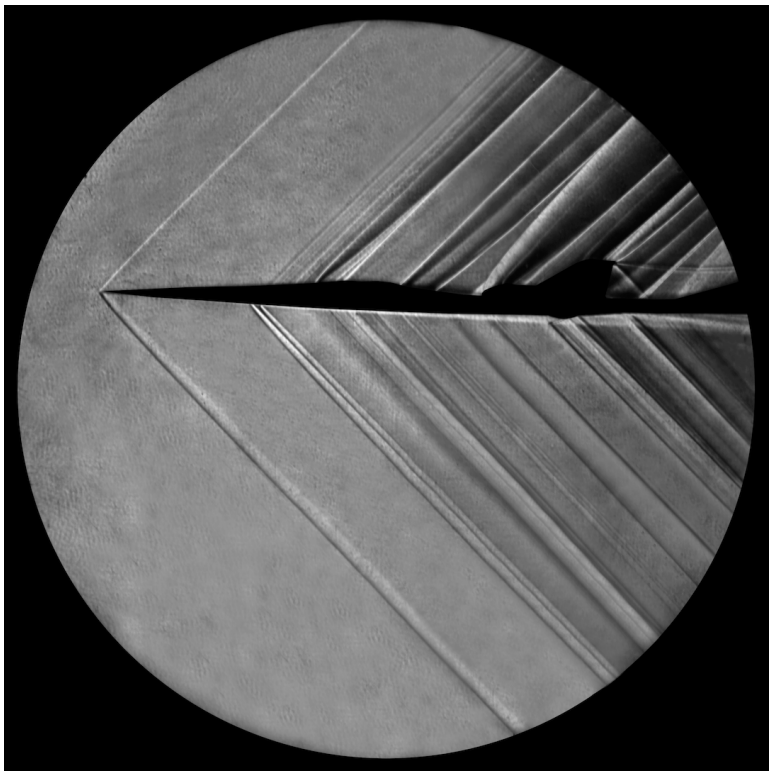

[*] *NASA Ames Research Center, Moffett Field, California*
[†] *NASA Glenn Research Center, Cleveland, Ohio*
[‡] *NASA Langley Research Center, Hampton, Virginia*
[§] *Lockheed Martin Corporation, Palmdale, California*

September 2022

NASA STI Program ... in Profile

Since its founding, NASA has been dedicated to the advancement of aeronautics and space science. The NASA scientific and technical information (STI) program plays a key part in helping NASA maintain this important role.

The NASA STI program operates under the auspices of the Agency Chief Information Officer. It collects, organizes, provides for archiving, and disseminates NASA's STI. The NASA STI program provides access to the NTRS Registered and its public interface, the NASA Technical Reports Server, thus providing one of the largest collections of aeronautical and space science STI in the world. Results are published in both non-NASA channels and by NASA in the NASA STI Report Series, which includes the following report types:

- TECHNICAL PUBLICATION. Reports of completed research or a major significant phase of research that present the results of NASA Programs and include extensive data or theoretical analysis. Includes compilations of significant scientific and technical data and information deemed to be of continuing reference value. NASA counterpart of peer-reviewed formal professional papers but has less stringent limitations on manuscript length and extent of graphic presentations.

- TECHNICAL MEMORANDUM. Scientific and technical findings that are preliminary or of specialized interest, e.g., quick release reports, working papers, and bibliographies that contain minimal annotation. Does not contain extensive analysis.

- CONTRACTOR REPORT. Scientific and technical findings by NASA-sponsored contractors and grantees.

- CONFERENCE PUBLICATION. Collected papers from scientific and technical conferences, symposia, seminars, or other meetings sponsored or co-sponsored by NASA.

- SPECIAL PUBLICATION. Scientific, technical, or historical information from NASA programs, projects, and missions, often concerned with subjects having substantial public interest.

- TECHNICAL TRANSLATION. English-language translations of foreign scientific and technical material pertinent to NASA's mission.

Specialized services also include organizing and publishing research results, distributing specialized research announcements and feeds, providing information desk and personal search support, and enabling data exchange services.

For more information about the NASA STI program, see the following:

- Access the NASA STI program home page at http://www.sti.nasa.gov

- E-mail your question to help@sti.nasa.gov

- Phone the NASA STI Information Desk at 757-864-9658

- Write to:
  NASA STI Information Desk
  Mail Stop 148
  NASA Langley Research Center
  Hampton, VA 23681-2199

NASA/TM–20220012155

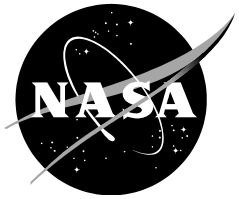

X-59 Sonic Boom Test Results from the NASA Glenn 8- by 6-Foot Supersonic Wind Tunnel

Donald A. Durston[*]
John D. Wolter[†]
Patrick R. Shea[‡]
Courtney S. Winski[‡]
Alaa A. Elmiligui[‡]
Sarah L. Langston[‡]
Michael D. Bozeman[‡]
Melissa B. Carter[‡]
Jonathon D. Ponder[†]
James T. Heineck[*]
Christopher A. Bellido[§]

[*] *NASA Ames Research Center, Moffett Field, California*
[†] *NASA Glenn Research Center, Cleveland, Ohio*
[‡] *NASA Langley Research Center, Hampton, Virginia*
[§] *Lockheed Martin Corporation, Palmdale, California*

National Aeronautics and
Space Administration

Ames Research Center
Moffett Field, California

September 2022

Acknowledgements

The X-59 sonic boom test at the NASA Glenn 8- by 6-Foot Supersonic Wind Tunnel was a successful collaboration of the Commercial Supersonics Technology (CST) project's sonic boom research teams at NASA Ames, Glenn, and Langley Research Centers, and sonic boom researchers at Lockheed Martin's Skunk Works facility in Palmdale, California. The teams would like to thank the following individuals/groups for their substantial efforts that contributed to the success of this test:

- CST project and task leaders Lori Ozoroski, Clayton Meyers, and Melissa Carter, for support and guidance
- Glenn 8x6 wind tunnel test operations crew and their management, for successful and timely tunnel operations
- CFD teams at Ames and Langley, for their pre-test predictions and guidance during model design and test planning
- The Low-Boom Flight Demonstrator project staff and the Lockheed Martin X-59 team for developing the X-59 airplane and providing the geometry
- Tri Models, Inc. for designing and fabricating the X-59 sonic boom model

This report is available in electronic form at
http://www.sti.nasa.gov/

Summary

A wind tunnel test was conducted to investigate near-field sonic boom pressure signatures from a model of the X-59 Low-Boom Flight Demonstrator aircraft. A 1.62%-scale model of the aircraft in the C612A configuration was fabricated for the wind tunnel test, which took place in the NASA Glenn 8- by 6-Foot Supersonic Wind Tunnel in September and October 2021.

The model had provisions for two different mounting options: a swept blade strut that attached at the top of model ahead of the inlet, and rear-entry sting that was made as one piece with a dummy nacelle, and which had a 2”-long cylindrical segment aft of the nozzle exit before tapering up in size. The blade strut allowed for a clean aft end of the model for evaluation of the shocks from that region, while the sting avoided the significant distortions of the flow and shocks from the blade strut along the top of the model. Both the sting and the strut had adapters that attached to a force balance. The model had alternate parts for ±0.5° deflections of the flaps, ailerons, and stabilator, and ±1° deflections of the T-tail horizontal surface.

Off-body static pressure measurements of the flow field below the model were made by use of a pressure rail which had 420 orifices along its tip. The model was positioned at various heights from the rail by vertical movement of the wind tunnel strut, and at various longitudinal stations relative to the rail by means of a linear actuator mounted between the tunnel strut and the balance. The longitudinal positioning allowed multiple pressure signatures to be obtained along different portions of the rail. These signatures were aligned by accounting for the model longitudinal movement and then averaged to take out the effects of tunnel flow distortions and the interference of the rail flow field and shocks on the model pressure signatures. The test was run at approximate Mach numbers of 1.36, 1.4, and 1.47, and the model was set at various angles of attack and roll relative to the rail.

Plots of the model signatures for all the variations of Mach number, model angles, control deflections, and height relative to the rail are provided throughout the report. Repeatability was generally very good and gave confidence in the quality of the measurements. The signatures measured at various heights from the rail provided insight into the aging of the model shocks as they propagated from 1.2 to 3 body lengths from the model. Off-track signatures up to 45° from centerline obtained by rolling the model gave indications of the shock flow fields across the width of the sonic boom carpet. The deflections of the various control surfaces allowed assessment of the boom sensitivity to the control surface movements.

Table of Contents

List of Figures

List of Tables

Nomenclature

A	=	area
AMS	=	Angle Measurement System
B/LA	=	Balance/Linear Actuator adapter
BS/B	=	Blade Strut/Balance adapter
CAD	=	Computer Aided Design
CFD	=	Computational Fluid Dynamics
CoR	=	Center of rotation
DewPt	=	dew point, °F
FAA	=	Federal Aviation Administration
Humidity	=	freestream humidity in ppm by weight
HumAvg	=	average humidity over all data samples in a run
h, h_{Nose}	=	height of model nose above pressure rail, inches
h/L, h_{Nose}/L	=	height of model nose above pressure rail normalized by model length
i	=	index of linear actuator ram positions (for uncertainty equations)
ICAO	=	International Civil Aviation Organization
j	=	index of two-second averages of data in data files (for uncertainty equations)
k	=	index for points in the X_4 vector (for uncertainty equations)
L	=	model length
LE	=	leading edge
PLdB	=	perceived level in decibels
P_{Rail}	=	static pressure at rail orifice, psf
P_∞	=	freestream tunnel static pressure, psi
q	=	dynamic pressure, psf
Re/L	=	Reynolds number per unit length
SigSet	=	Signature Set: set of runs over a range of linear actuator ram positions
SweepInc	=	X_{Ram} position increments in X sweep
SweepRng	=	range of X_{Ram} positions in X sweep
TE	=	trailing edge
TomoBOS	=	Tomographic Background-Oriented Schlieren
V	=	velocity
X	=	longitudinal coordinate, along tunnel axis or rail edge
X/L	=	longitudinal coordinate normalized by model length
X_{Orif}	=	longitudinal coordinate of rail orifice
X_{Ram}	=	extension distance of linear actuator ram, from 0” to 24”
α	=	angle of attack, degrees
ϕ	=	angle of roll, degrees
ϕ_{m2r}	=	roll angle from model to rail (aka off-track angle for sonic boom propagation)
ϕ_{Model}, ϕ_{RM}	=	roll angle of model/roll mechanism relative to wind tunnel strut
$(\Delta P/P)_C$	=	corrected pressure signature magnitude, $\Delta P/P_U$ - $\Delta P/P_R$
$(\Delta P/P)_R$	=	uncorrected pressure signature magnitude for reference run, $[(P_{Rail} - P_\infty) / P_\infty]$
$(\Delta P/P)_U$	=	uncorrected pressure signature magnitude for data run, $[(P_{Rail} - P_\infty) / P_\infty]$

1. Introduction

THE Commercial Supersonics Technology (CST) Project[1] under NASA's Advanced Air Vehicles Program[2] (AAVP) has been focused on developing technologies for enabling designs of future commercial supersonic transport aircraft. Many different technology areas are being addressed, such as designing airframes for better efficiency, improving engine integration for minimizing noise, maximizing combustion efficiency, and reducing high-altitude emissions. However, the greatest emphasis has been on understanding the contributions to sonic boom loudness and learning how to shape the airframe and integrate the engine(s) such that the boom noise is minimized. Starting in 2009, NASA funded studies by Lockheed Martin[3,4] and Boeing[5,6] to design low-boom commercial supersonic transport aircraft that would carry 50 to 75 passengers. The studies resulted in concepts that had estimated boom loudnesses with PLdB (perceived level in decibels) in the low 80s range. Small sonic boom models were made of these configurations and tested in supersonic wind tunnels at the NASA Ames and Glenn Research Centers.[7,8] The near-field pressure distributions below the models were measured in the tunnels, and computer codes were run to extrapolate these pressures from a simulated cruising altitude to ground level and calculate boom loudness. Results from the tests were compared to Computational Fluid Dynamics (CFD) predictions and served as validation test cases that have led to improvements in computational tool development for boom prediction.

In 2016, NASA received approval to start a project[9] aimed at designing and building a low-boom flight demonstrator aircraft with the primary purpose of achieving a flight-measured sonic boom loudness of 75 PLdB or less. Lockheed Martin was selected as the contractor to design and build the aircraft, designated as the X-59 by NASA, which is expected to have its first flight in late 2022. After initial flight tests and envelope expansion, the acoustics of the aircraft will be validated through measurements of the boom pressure signatures by chase aircraft and on the ground. Then the aircraft will be flown to various cities around the United States to conduct flights over populated areas and obtain reactions from the public regarding what is hoped will be more of a benign sonic "thump" than a loud sonic boom. The end goal of the project is to provide sufficient data to the Federal Aviation Administration (FAA) and International Civil Aviation Organization (ICAO) to prove that acceptably-low levels of boom loudness can be produced by an aircraft shaped for low-boom, and thus allow the FAA and ICAO to develop regulations that enable commercial supersonic overland flight for aircraft that can meet the low-boom standards.

The flight test data from the X-59 will be compared to the CFD predictions of the near-, mid-, and far-field pressure distributions, and it was desired to obtain wind tunnel test data for additional comparisons. Thus a 1.62%-scale model of the X-59 configuration C612A was designed and fabricated by Tri Models, Inc., in 2020, and was run in the Glenn Research Center 8- by 6-Foot Supersonic Wind Tunnel in the fall of 2021.[10] The purpose of this report is to present the details of this test and provide a comprehensive analysis of the data.

2. Test Objectives and Overview

The primary objective for the experiment was to acquire pressure signatures of the X-59 configuration for validation of computational models used in sonic boom prediction, and to be able to compare these signatures with the flight-test measurements. Secondary test objectives included acquisition of schlieren and tomographic background-oriented schlieren (TomoBOS) imaging to gain further insight into the flow field around the X-59 airframe and to provide validation images for CFD.

Data were measured in the test among variations in Mach number, near-field propagation distance (model height relative to a pressure rail), angles of attack and roll, and control surface deflections. The model was tested with two different mounting options: a 65°-swept blade strut that attached to the top of the model ahead of the engine inlet, and a rear sting that attached to the model at the location of the engine nacelle. The model had alternate parts for ±0.5° deflections of the flaps, ailerons, and stabilators, and ±1° deflections of the T-tail horizontal surface.

The primary data from the test were static pressures measured on a thin blade-type pressure rail that had a line of 420 orifices along its tip over a 66” length. To get better-quality data than just from single pressure signature measurements on the rail, a linear actuator was used to measure signatures at different longitudinal positions (typically 26) on the rail. These *X* sweeps of the model enabled spatial averaging of the signatures from the different positions, which greatly reduced the scatter of the data but did result in some rounding of the peaks in the signatures.

In addition to running the X-59 model, an axisymmetric calibration body, designated AS-2, was run to obtain simple pressure signatures for validation of the test techniques.

3. Glenn 8- by 6-Foot Supersonic Wind Tunnel

3.1. Facility Overview

The NASA Glenn Research Center 8- by 6-Foot Supersonic Wind Tunnel[11] (8x6) is part of a facility (Figure 3-1) which includes a 9- by 15-Foot Low-Speed Wind Tunnel (9x15) test section on the opposite leg. Tests are run in one test section or the other, but not in both sections at the same time. The facility is a continuous-flow circuit, powered by three motors of 29,000 hp each, driving a seven-stage axial flow compressor. The 8x6 test section flow speed is controlled by compressor rpm, position of the vertical flexible walls of the two-dimensional nozzle, and the setting of the exhaust valve for the balance chamber. The Mach number range for the 8x6 tunnel is 0.25 to 2.0, and the test section is 8’ tall by 6’ wide by 23.5’ long. The upstream portion of the test section, referred to as the “supersonic test section,” has solid walls and is approximately 9’ in length. The downstream portion, referred to as the “transonic test section,” has porous walls and is approximately 14.5’ in length. The porosity is comprised of perforations on all four walls consisting of 1”-diameter holes inclined forward at a 60° angle and arranged in a herringbone pattern. The porosity is generally better suited for transonic force and moment or propulsion tests since it minimizes the model shock reflections off the walls.

Previous sonic boom testing[8,12] in the 8x6 tunnel was conducted in the transonic test section, but the rail pressure measurements were adversely affected by flow interference from the perforated walls. The subject test of the X-59 model was run with the model located in the supersonic test section to alleviate this interference. This was the first research test in the history of the 8x6 tunnel which was run in the supersonic test section, so prior to the X-59 test a calibration of that portion of the test section was performed by the Glenn wind tunnel staff. [13]

The tunnel air is dried during operations by passing it over eight layers of large desiccant beds in the air dryer (just upstream of the compressor). The dryer beds are “reactivated”—removing the moisture by heating—with the compressor not running, during an off-shift each day in preparation for the next shift’s running. The maximum acceptable dew point during wind-on operations is determined for each test, and operations are typically terminated during a running shift if the dew point exceeds this level.

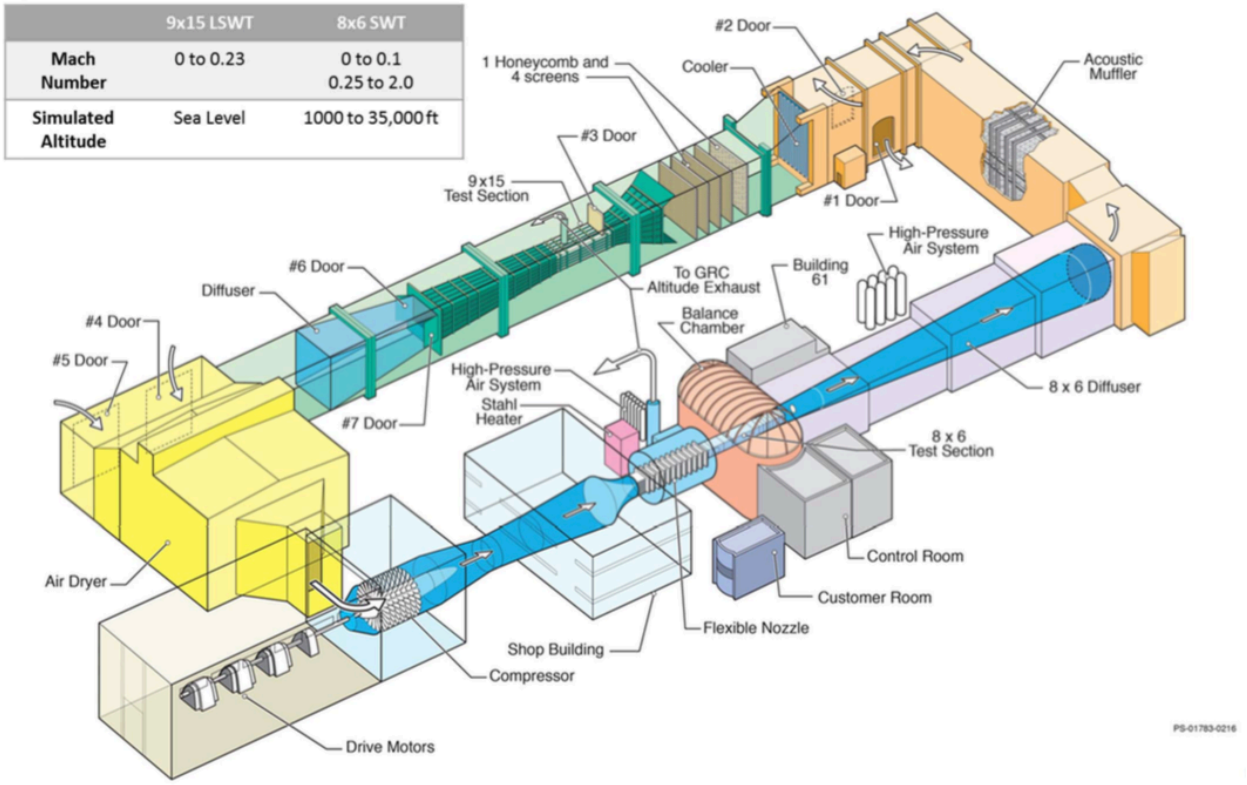

Figure 3-1 Overview of Glenn 8x6/9x15 Wind Tunnel Complex

3.2. Capabilities and Test Conditions

The 8x6/9x15 wind tunnel complex is an atmospheric facility; there are no provisions for controlling the pressure in the tunnel aside from the normal pressure variation with flow speed. In addition, there is no after-cooler or radiator section between the compressor and the 8x6 test section, so the compression of the air causes the total temperature of the air in the test section to be at or above 140° F at low supersonic Mach numbers, and higher temperatures at higher Mach numbers. The tunnel conditions which were run in the subject test are listed in Table 3-1. The Mach numbers are shown to four decimal digits as reported in the data files but will be shown in the rest of this report to two decimal digits for easier visual comparison.

Table 3-1 8x6 wind tunnel nominal operating conditions for the subject test

Mach	P_T	P_S	q	T_T	T_S	Re/ft
(Test Sctn)	(psf)	(psf)	(psf)	(°F)	(°F)	(10^6/ft)
1.3647	2625.8	867.0	1130.2	150.3	-15.2	4.846
1.3990	2675.2	841.9	1153.4	149.4	-21.9	4.921
1.4700	2746.8	781.3	1181.9	157.1	-29.0	4.902

4. Wind Tunnel Models and Support Components

Descriptions and geometry information for the two wind tunnel models and their support components are provided in this section.

4.1. AS-2 Model

The AS-2 model[6] (Figures 4-1 and 4-2) and was one of several sonic boom models designed by The Boeing Company in 2010 under contract to NASA in an experimental systems validation study for supersonic transport aircraft. The AS-2 was designed to be used as an axisymmetric calibration body in sonic boom wind tunnel testing. Its geometry consists of an ogive nose, a constant cylindrical section, a conical section to match the diameter of the support hardware behind the model, and a male taper adapter to fit within the support piece. In the case of this test, the support piece was a balance adapter that fit around the balance that was used for force measurements. The simple external shape of the AS-2 model was designed to create a simple, predictable pressure signature that could be used to give an indication of the quality of the wind tunnel flow and the measurement of the off-body pressures along the pressure rail. It has been used in previous model tests in the 8x6 tunnel and in the Unitary Plan Wind Tunnels at NASA Ames Research Center.

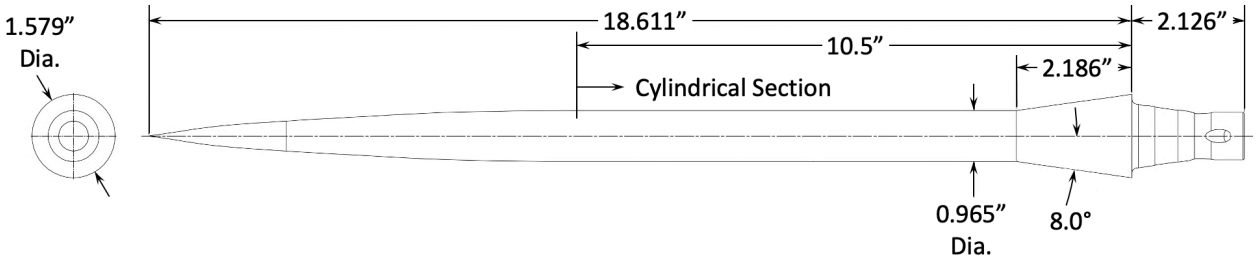

Figure 4-1 Geometry of AS-2 model

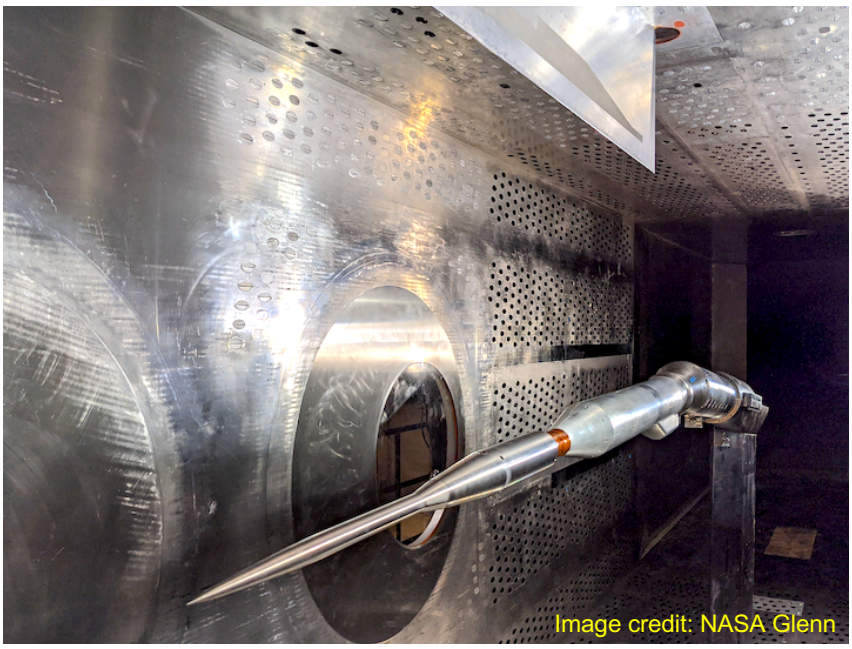

Figure 4-2 Photograph of AS-2 model installed in 8x6 wind tunnel showing rail on ceiling

4.2. X-59 Aircraft and Sonic Boom Model

The X-59 flight demonstrator aircraft[14] (Figures 4-3 and 4-4) has been designed by Lockheed Martin under contract with NASA to have a quiet sonic boom from its cruise flight condition of Mach 1.4 at 55,000 ft altitude. The boom loudness is expected to be about 75 PLdB at ground level.

Figure 4-3 X-59 flight demonstrator aircraft

Configuration C612	
MDGW	25,000 lbs
Fuel (Max)	8,700 lbs
Payload	600 lbs
Design Mach	1.4
Loudness	<75 PLdB
Engine	1xF414-GE-100
Landing Gear	F-16 Blk25 NLG F-16 Blk25 MLG

Control Surfaces	
Aileron	12.9 sq ft/+35/-25 deg
Flap	12.4 sq ft/+30/-3 deg
Stabilator	39.9 sq ft/+20/-15 deg
Rudder	8.5 sq ft/+25/-25 deg
T-tail	5.7 sq ft/+10/-0 deg

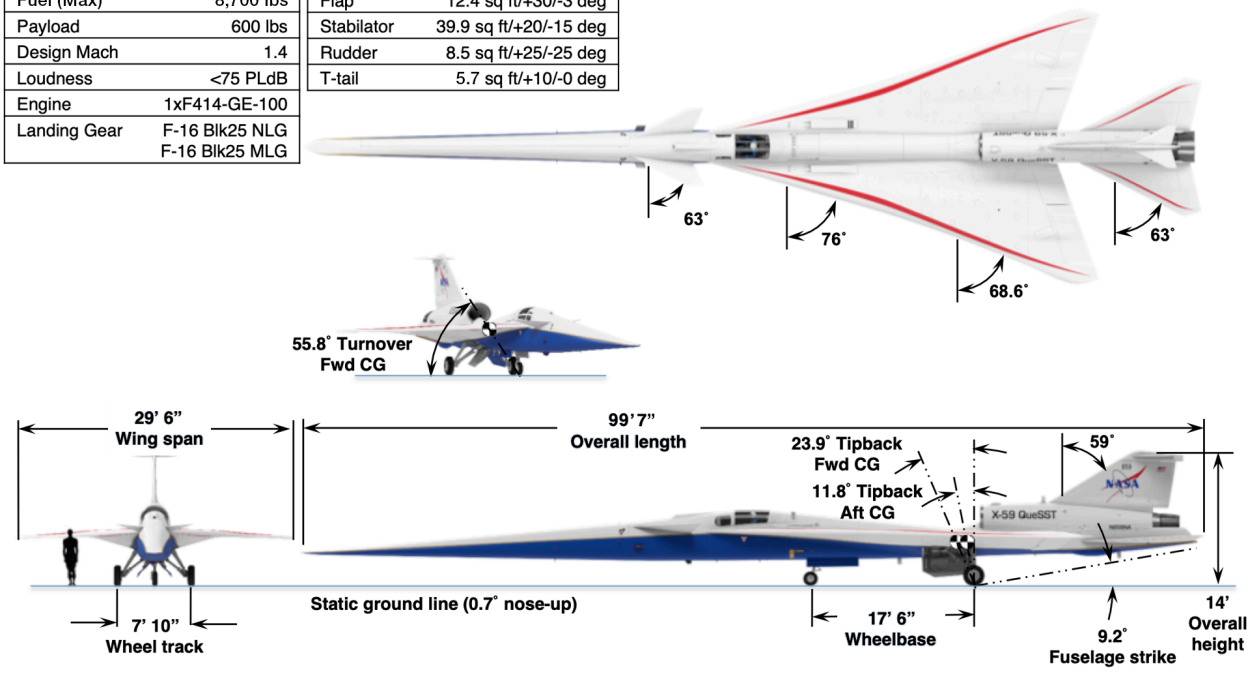

Figure 4-4 X-59 aircraft configuration overview

An 18.80-inch long, 1.6212%-scale model of the C612A version of the X-59 aircraft was designed and fabricated by Tri Models, Inc. The model features interchangeable wing aft sections with various flap and aileron deflections, a horizontal stabilator, and T-tail that can be set at various deflection angles, and two means of mounting the model to its support structure—a swept blade strut and a rear-entry sting. Views of the model and its deflectable control surfaces are provided in Figures 4-5 and 4-6. All the control deflections are positive trailing-edge down, and all deflections (including the ailerons) are symmetric left/right. This symmetry is for sonic boom tailoring; rolling moment effects on boom were not an objective of this test.

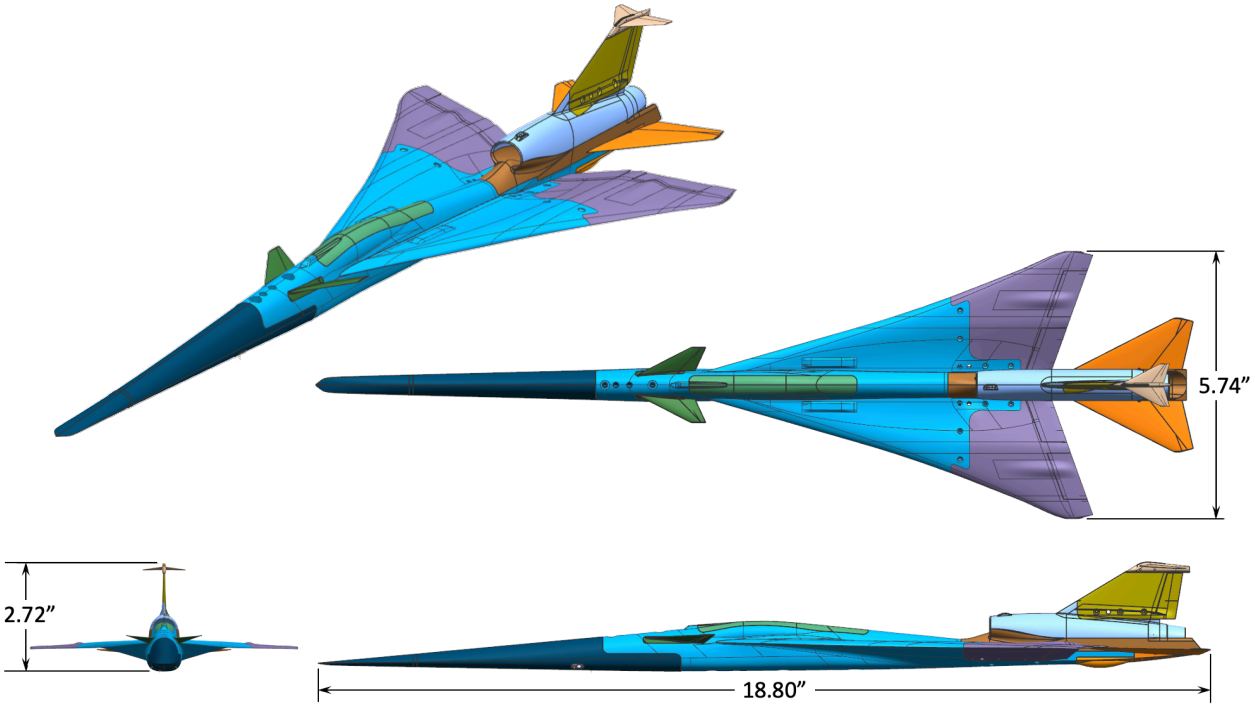

Figure 4-5 Four-view of X-59 1.62%-scale model (graphics: Tri Models)

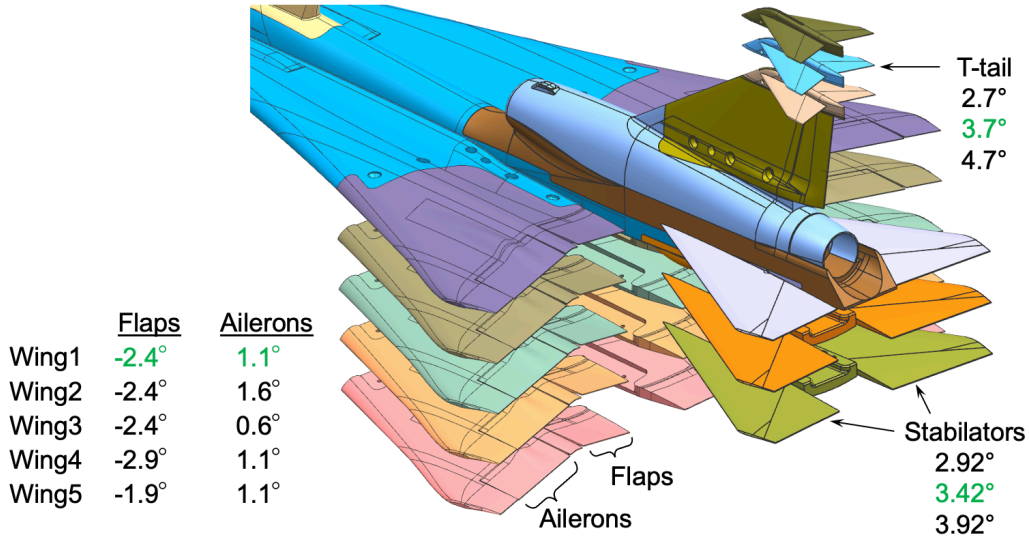

Figure 4-6 X-59 model control surface deflection options (+ TE down), baseline angles for cruise flight in green (graphics: Tri Models)

Compromises relative to the airplane geometry had to be made in the model outer mold line because of small-scale fabrication limitations, as indicated in Figure 4-7, though they were not expected to impact the pressure signatures. These included filling of the gaps along the hinge lines for the flaps and ailerons, and the removal of some of the smaller antennae, ECS and NACA inlets, wing tip lights, vortex generators, and nose air data boom. In addition, the trailing edges of the canards, wing, and tails had to be thickened to a minimum fabrication thickness of approximately 0.010”. The thinnest parts of some of the trailing edges on the full-scale airplane are 0.090” thick, which would have resulted in model-scale thicknesses of close to 0.001”!

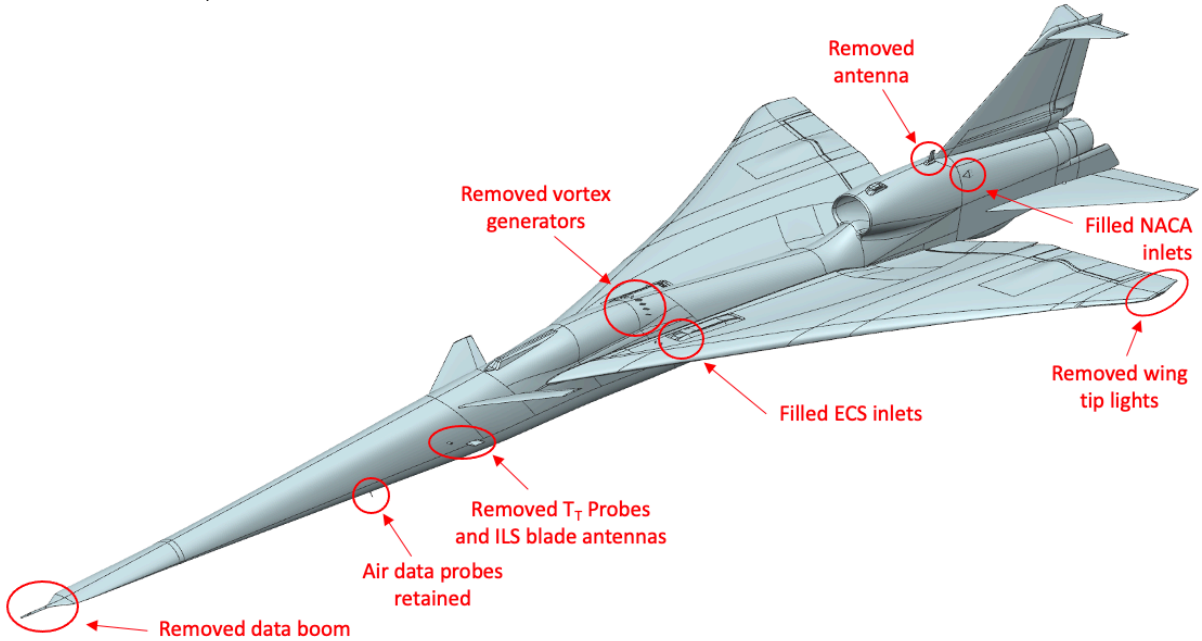

(a) Upper surface view

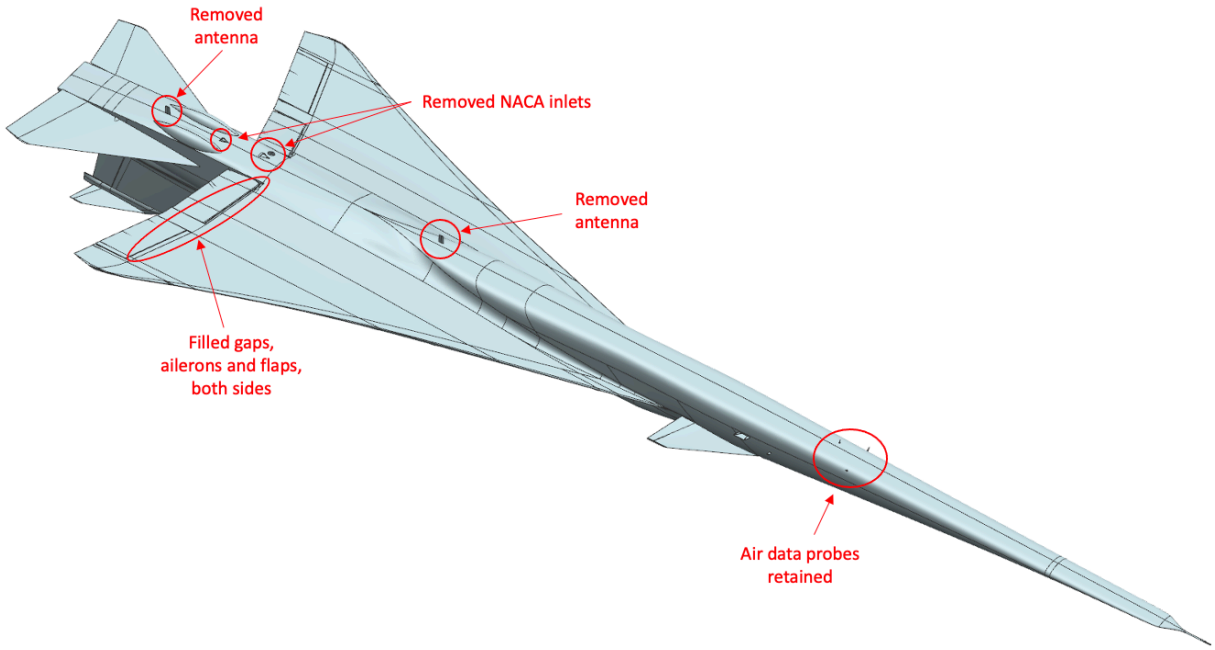

(b) Lower surface view

Figure 4-7 Model differences from airplane (graphics: Tri Models)

The geometrical parameters of the X-59 model are given in Table 4-1.

Table 4-1 X-59 Model Geometrical Parameters

Overall length (in)	18.80
Height (in)	2.724
Span, b_{ref} (in)	5.739
Theoretical* wing area, S_{ref} (sq in)	20.227
Theo.* mean aerodynamic chord, c_{ref} (in)	4.728
Theoretical* root chord (in)	6.822
Theoretical* tip chord (in)	1.495
Taper ratio (in)	0.219
Wing aspect ratio	1.79
Inboard LE sweep (deg)	76.0
Outboard LE sweep (deg)	68.6

* *Theoretical: trapezoidal wing with equivalent area*

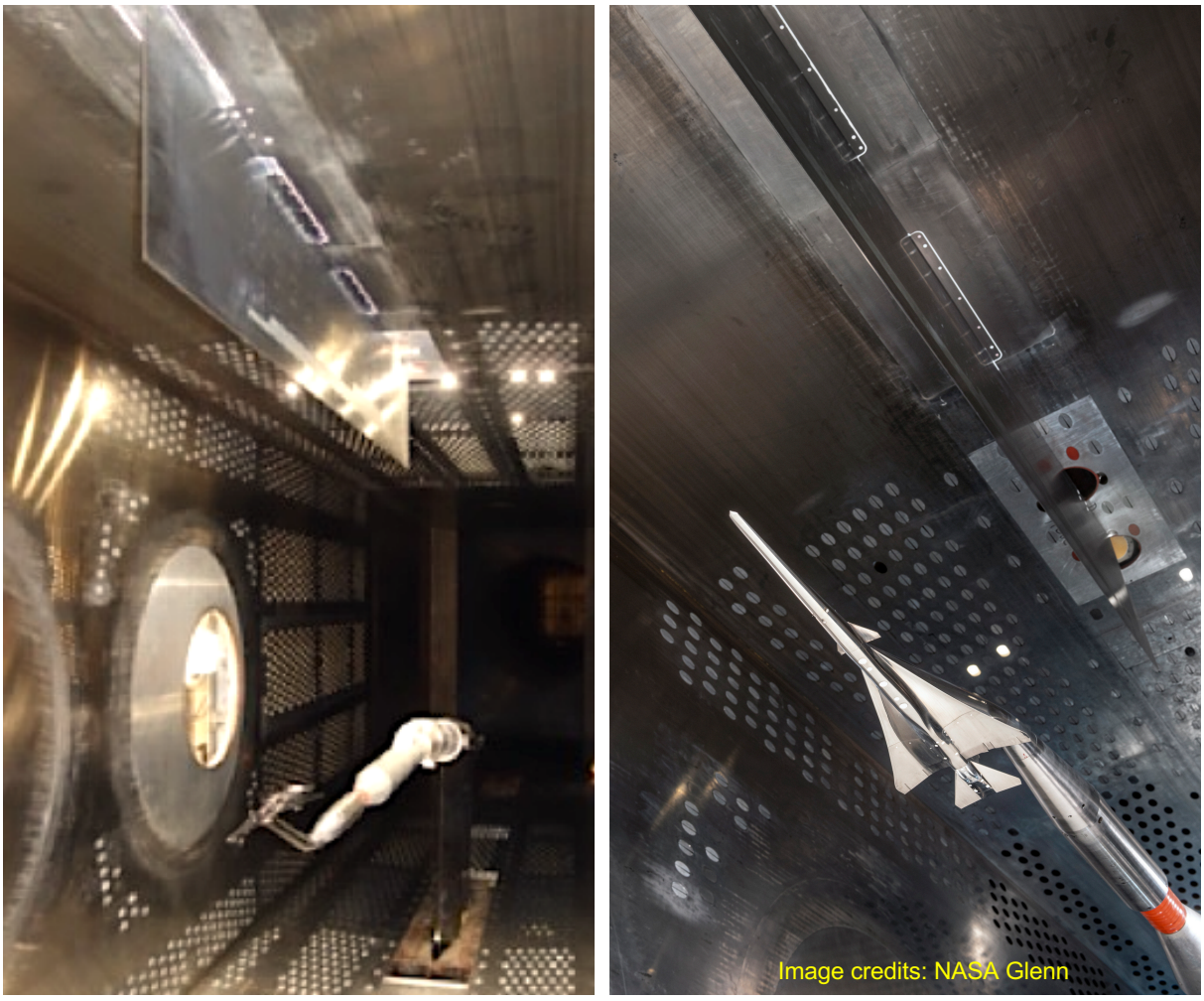

(a) View looking aft **(b) View looking forward**

Figure 4-8 Views of X-59 model mounted on blade strut in wind tunnel with pressure rail mounted in the ceiling

Photographs of the X-59 model and the pressure rail mounted in the ceiling of the Glenn 8x6 are shown in Figure 4-8 above. Close-up views of the model are shown in Figures 4-9 through 4-12 below. In Figures 4-8(a), 4-9, and 4-10, the model is inverted as in the running orientation so that the shocks from the bottom of the model would be directed to the rail. Figure 4-12 puts the scale of the model in perspective with the person in the picture.

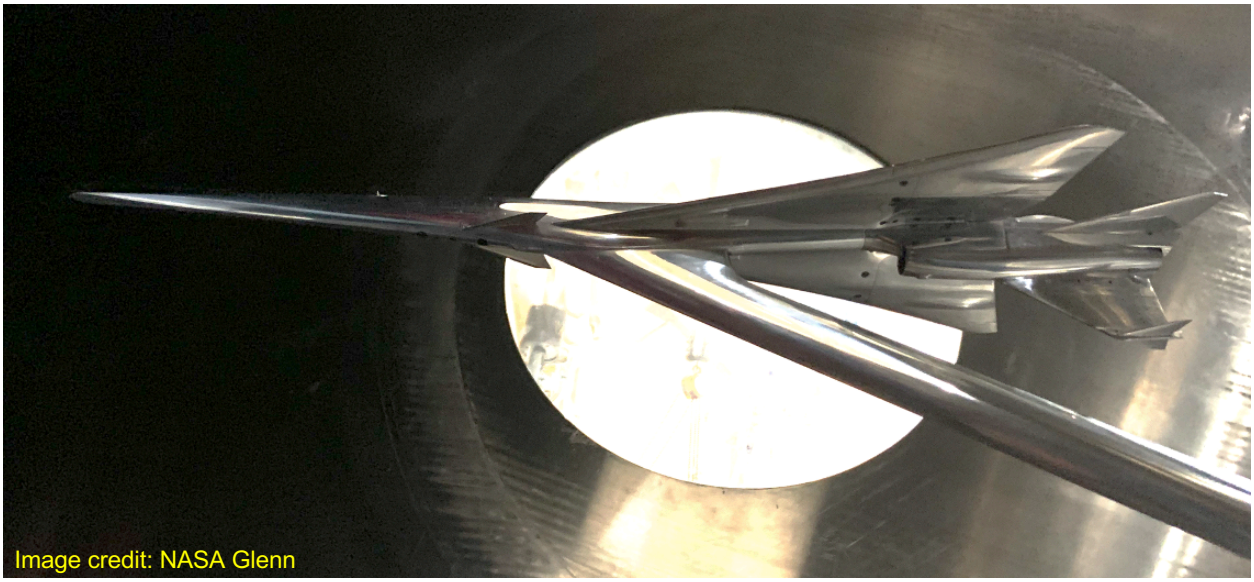

Figure 4-9 View of X-59 model mounted on blade strut in wind tunnel

Figure 4-10 View of X-59 model mounted on sting in wind tunnel

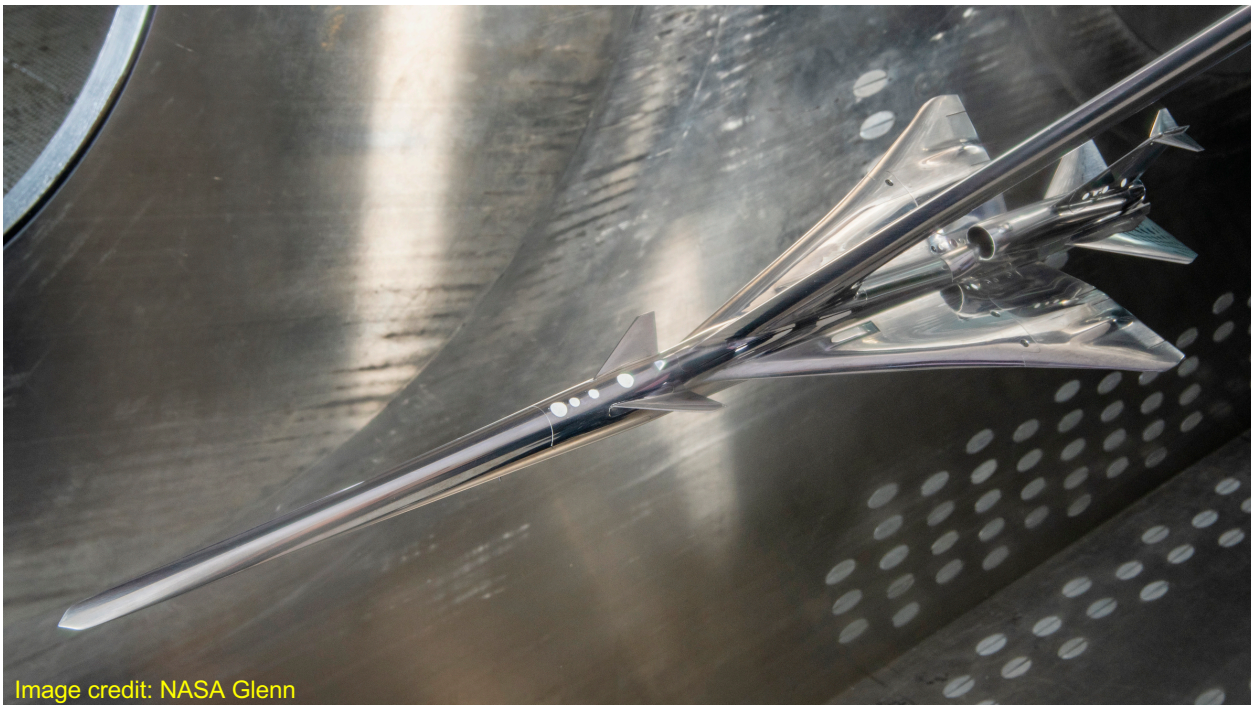

Figure 4-11 Close-up view of upper surface of X-59 model on blade strut in wind tunnel

Figure 4-12 X-59 model being inspected by first author of this report

4.3. X-59 Model Supports

CAD views of the model support hardware forward of the linear actuator are shown in Figure 4-13, with the upper view showing the model blade strut at the forward end (left) and the lower view showing the sting. The balance is in gray in the center of the views and is attached to the linear actuator by a balance / linear actuator (B/LA) adapter. The forward end of the balance is metric, measuring the forces and moments of everything attached to it. For the blade strut configuration, a blade strut / balance (BS/B) adapter holds the model strut to the balance, but for the sting configuration, the internal geometry of the rear of the sting fits directly over the front of the balance so there is no need for an intermediate adapter. A shroud (common to both configurations) is used to shield the aft portion of the balance from the wind and does not touch the balance but has a small clearance around it. Leveling plates for an Angle Measurement System[15] (AMS) are shown on both the BS/B adapter and the sting, having slightly different interface geometries since the BS/B adapter is tapered and the rear portion of the sting is not. These leveling plates and the AMS were used only for checking the level of the balance during pre-test check loads and installation in the tunnel. The plates were removed for wind-on running, while the rest of the hardware shown in the figure remained.

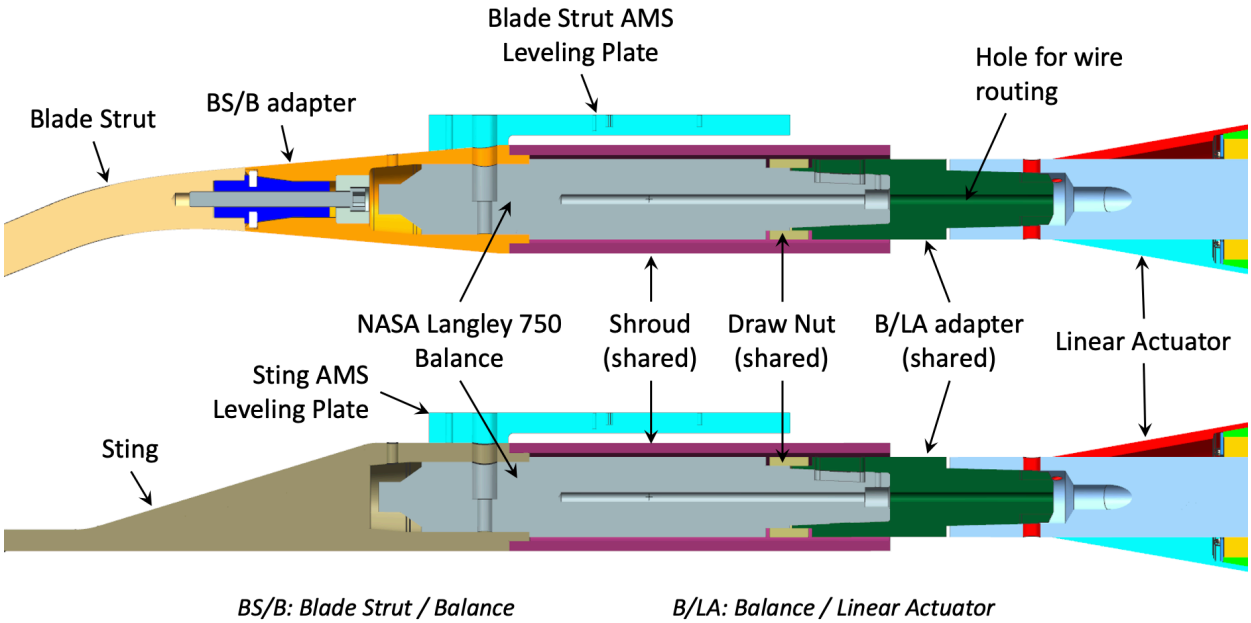

Figure 4-13 Balance and support assemblies for blade strut and sting
(graphics: Tri Models)

Assembly views of the model supported by the blade strut and sting are shown in Figure 4-14. The blade strut in subfigure (a) is shown attached to the front of the BS/B adapter and attaches to the model at the location of the canopy and a short distance aft of that. The strut has a constant chord between the transition areas for the model and BS/B adapter. This constant-chord section is swept 65° from the vertical and has a biconvex cross section. The blade strut provides a vertical offset between the centerline of the balance and the model nose of 5.52." The X-59 model has a flow-through nacelle when attached to the blade mount.

The rear of the sting in subfigure (b) replaces the BS/B adapter that is used with the strut and mounts directly over the front of the balance. The forward end of the sting extends over the rear of the model, replacing the flow-through nacelle, and it has a faired bullet in place of the inlet since no flow could pass through the nacelle with the sting in place. The vertical offset between the centerline of the balance and the model nose is much smaller with the sting (0.88") than with the blade strut.

Both the strut and the sting were designed so that they hold the model at 2.1° angle of attack (the cruise angle for the X-59 airplane flying at Mach 1.4) when the linear actuator and balance are level. This allows for the model to stay at the same vertical distance from the rail when it is moved forward in an *X* sweep, since the linear actuator is level with the rear parts of the blade strut and sting. The lengths of the strut and sting were set to place the model nose at the same axial station in the tunnel.

The blade support was developed to provide the least interference possible on the aft portion of the aircraft to allow the effects of the T-tail and stabilator deflections to be studied. It was anticipated that the presence of the blade over the model would alter the lift distribution over the wings and therefore alter the wing pressure signatures. The sting support was developed to provide the least interference possible on the forward portion of the aircraft to allow the effects of the flap and aileron deflections to be studied. It was anticipated that the engine bullet fairing and sting would alter the flow field over the empennage and therefore alter the closeout signature of the model. By combining the information from these two support systems, a more complete understanding of the entire sonic boom signature could be developed.

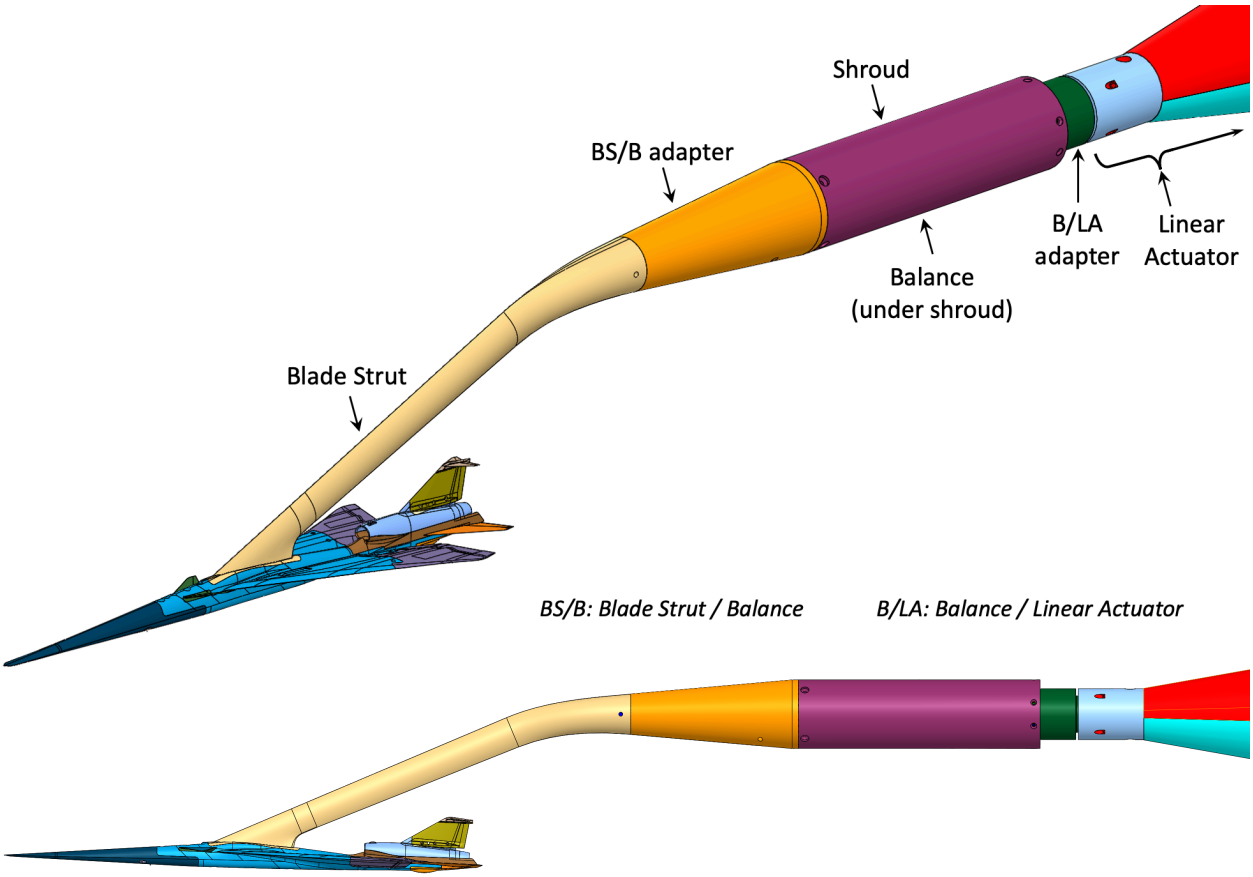

(a) Blade strut mount

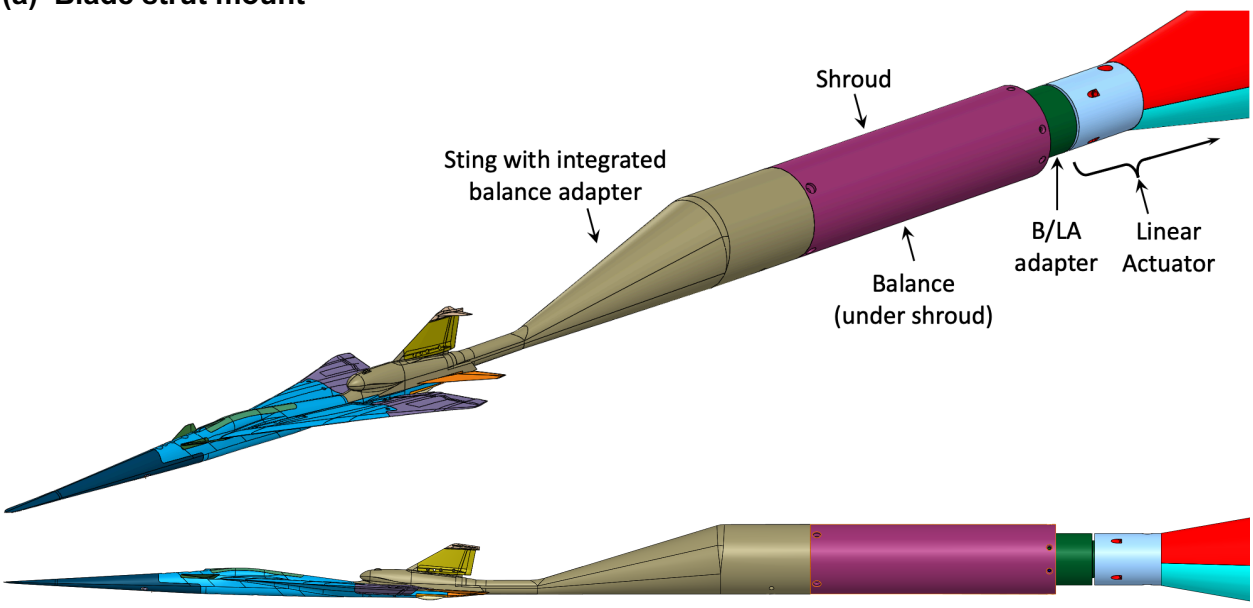

(b) Sting mount

Figure 4-14 Support options for X-59 sonic boom model (graphics: Tri Models)

4.4. Model Positioning

The position and angle of the model in the tunnel are controlled by the wind tunnel strut, a roll mechanism, and a linear actuator, as shown in Figure 4-15. The stub sting shown in the figure does not provide any movement; it is just a fixed adapter between the strut and roll mechanism. The devices upstream of the stub sting are discussed in the following sections.

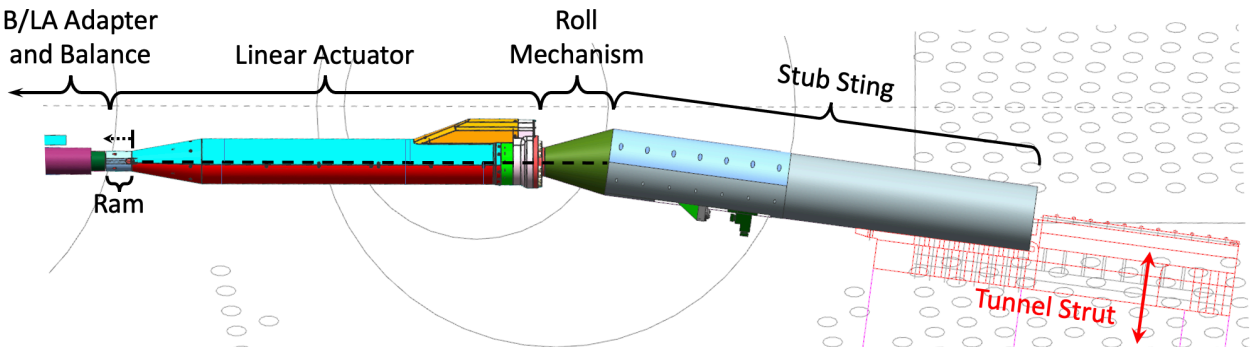

Figure 4-15 Model positioning systems

4.4.1. Wind Tunnel Layout Diagrams

Layout diagrams of the model at various heights of the nose above the rail are given in Figure 4-16. Subfigure (a) shows the model mounted on the blade strut at the three different heights run in this test. These same heights were also run for the sting-mounted configuration, which were enabled by positioning the tunnel strut higher by the difference (4.64”) between the vertical offset distances for the blade strut (5.52”) and the sting (0.88”). In most of the data plots presented in Section 6, the model height will be specified in terms of *h/L*, where *L* = 18.80”, the model body length. The model heights shown in Figure 4-16(a) of 22.6”, 37.6”, and 56.4” correspond to *h/L* values of 1.2, 2.0, and 3.0, respectively. The lowest and highest heights were near the limits of the vertical range of the tunnel strut movement. The roll mechanism is set at 0° roll in this subfigure so that the bottom of the model faces the rail.

Subfigure (b) shows the model in position for a reference run. The use of a reference run to correct the model pressure signatures will be discussed in Section 6.2. The linear actuator ram (the short segment shown in orange between the linear actuator housing and the balance adapter) is fully retracted in these views, and the roll mechanism is set at 180° roll to position the model nose shock as far aft on the rail as possible.

The pressure rail mounted on the ceiling of the test section has a 66”-long instrumented section consisting of 420 static-pressure orifices, which are denoted by the black dots along the tip between the vertical dashed lines on the rail (from tunnel station 61.9” to 127.9”). The shocks coming from the nose and rear of the model are drawn at the Mach line angle—44.4° from vertical — for Mach 1.4. No attempt was made to account for aging of the shocks nor for changes in reflections off the ceiling due to tunnel boundary layer in this layout. Rather, the shock lines were used to provide guidance for setting the model height and linear actuator extension range for each signature *X* sweep more than for trying to predict exactly where the model shocks would intersect the rail.

The Ames Small Model Roll Mechanism (SMRM) that was used in this test has a fixed 7.5° offset which made it necessary to pitch the tunnel strut by the opposite of this amount to set the model at its nominal angle of attack of 2.1° (corresponding to the balance and linear actuator being level in the tunnel, except when other model pitch angles were desired).

The wind tunnel strut raises and lowers through the tunnel floor to change the height of the model. For changing pitch angle, the strut pivots about a center of rotation that is 15” below the

floor, so for an increase in model angle of attack, the model moves forward in the tunnel slightly (~1” forward for a 1° angle increase, with model 22.6” below the rail).

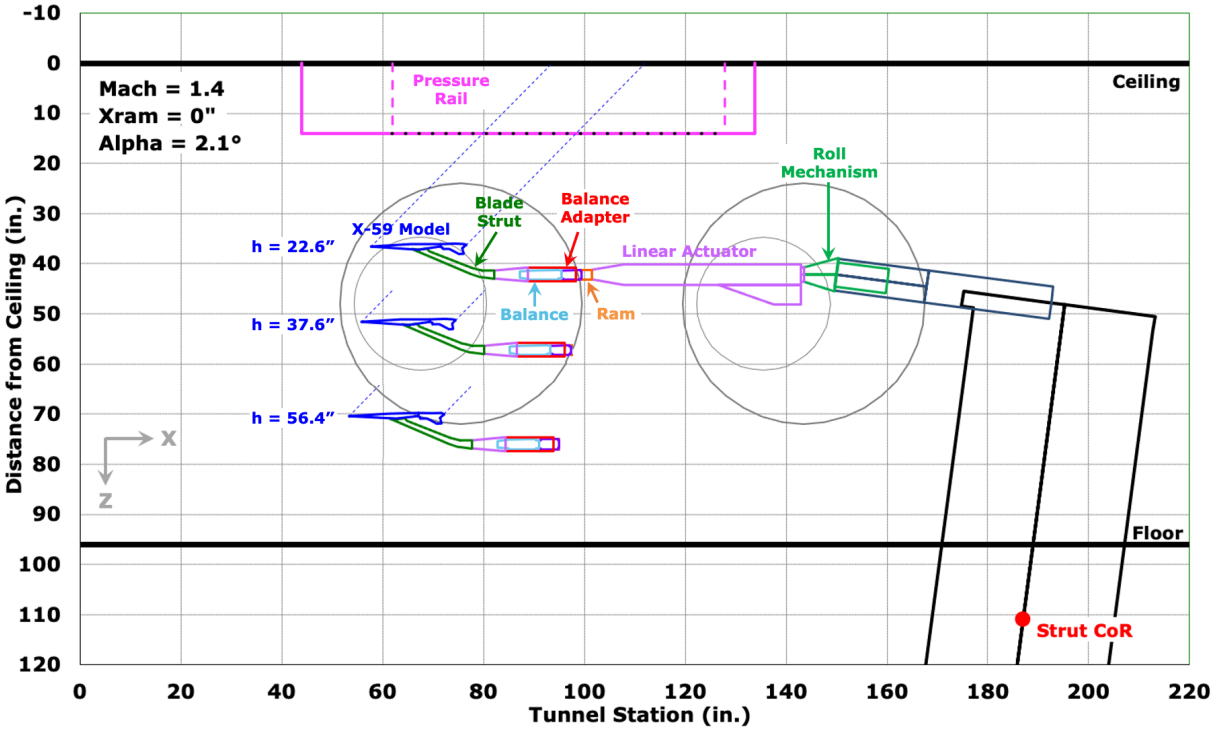

(a) X-59 model at heights for data runs, $\alpha = 2.1°$, $\phi = 0°$

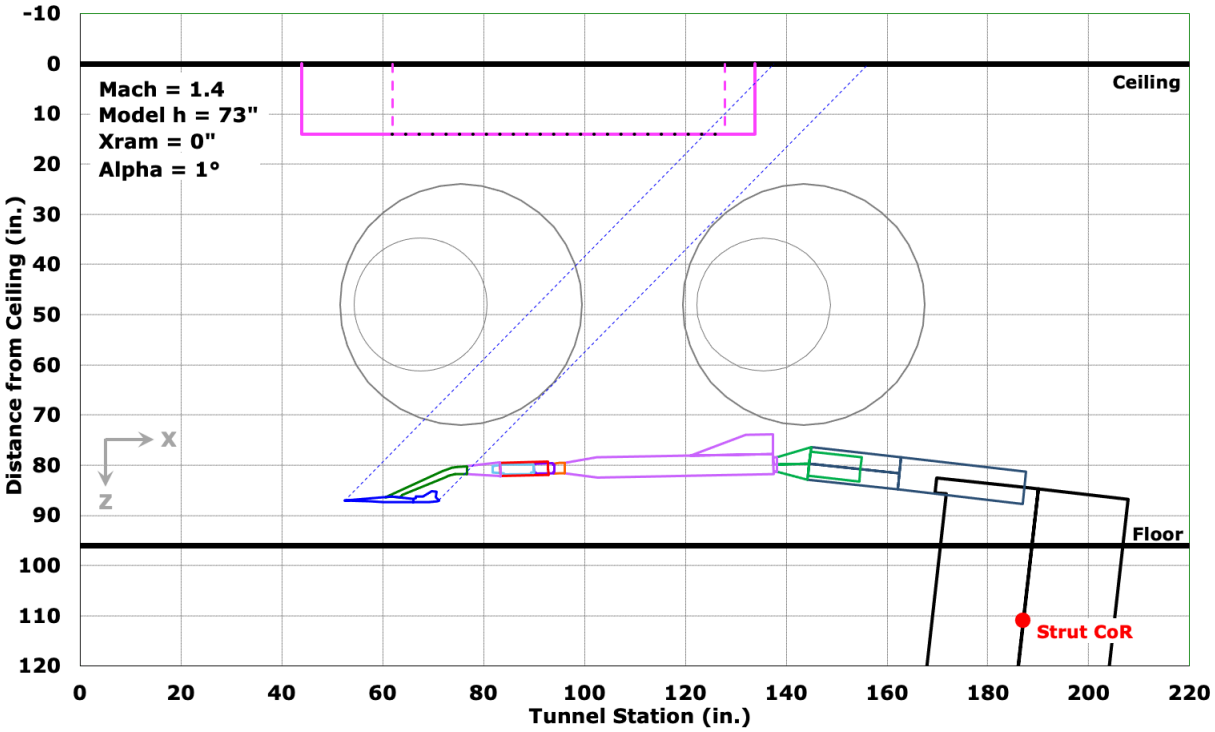

(b) X-59 model at height for reference runs, $\alpha = 1°$, $\phi = 180°$

Figure 4-16 Layout diagrams of model in tunnel

4.4.2. Roll Mechanism

The Ames SMRM provided the capability of rolling the model along the axis of the linear actuator. The model was rolled to angles ranging from 0° to 45° relative to the pressure rail to allow measurement of pressure signatures at off-track angles. The orientation of the model relative to the rail is illustrated in Figure 4-17, which shows a simplified representation of the model at the proper distance and angle for h_{Nose} = 22.56" and ϕ_{m2r} = 40°. Note that the roll angle of the roll mechanism/linear actuator combination is *not* the roll angle of the model relative to the rail because of the 5.52" blade-strut offset (or 0.88" for sting mount) of the model axis from the support system axis. The term "ϕ_{m2r}" is used in this test to indicate roll angle of the model relative to the rail, which provides the off-track angle. The nominal angles and positions for the three model heights and the lowest and highest roll angles run in this test are listed in Table 4-2, and were used to set the model position for a given h_{Nose} and ϕ_{m2r}. The equations for these parameters based on the roll mechanism angle and height are:

$$\phi_{m2r} = \phi_{RM} - \tan^{-1}\left(Y_{Nose}/Z_{Nose\_ar}\right)$$

$$h_{Nose} = \sqrt{\left(Y_{Nose}^2 + Z_{Nose\_ar}^2\right)}$$

$$Y_{Nose} = h_{Strut}\, sin(\phi_{Model})$$

$$Z_{Nose\_ar} = Z_{Nose} - Z_{Rail}$$

$$Z_{Nose} = Z_{RM} - h_{Strut}\, cos(\phi_{Model})$$

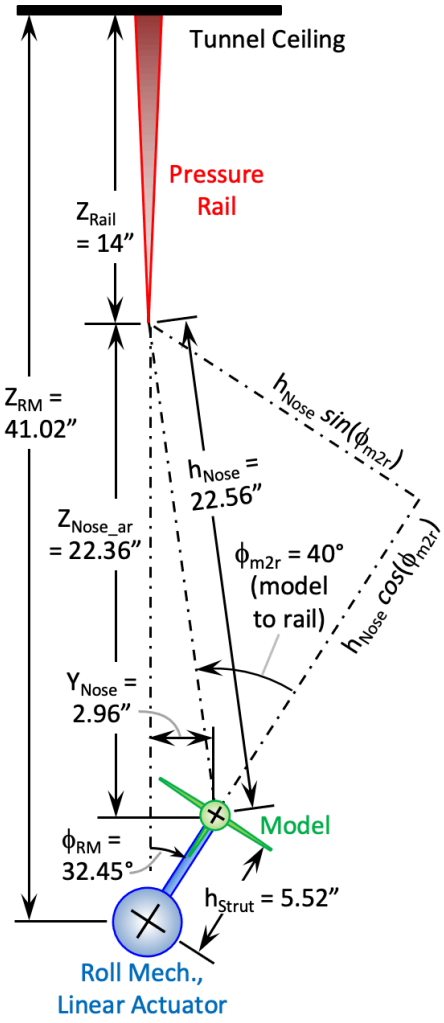

Figure 4-17 Illustration of model-to-rail roll angle

Equations for computing set points for desired model positions are:

$$\phi_{RM} = asin\left\{\frac{h_{Nose}sin(\phi_{m2r})}{\sqrt{[h_{Strut} + h_{Nose}cos(\phi_{m2r})]^2 + [h_{Nose}sin(\phi_{m2r})]^2}}\right\}$$

$$Z_{RM} = \sqrt{[h_{Strut} + h_{Nose}cos(\phi_{m2r})]^2 + [h_{Nose}sin(\phi_{m2r})]^2} + Z_{Rail}$$

Table 4-2 Model Angles and Positions Relative to Rail (for Blade Strut Mount)

h_{Nose} (in)	ϕ_{m2r}°	ϕ_{RM}°	Z_{RM} (in)	Z_{Nose_ar} (in)	Y_{Nose} (in)
22.56	0	0	42.08	22.56	0
22.56	45	36.61	40.75	22.32	3.29
37.6	0	0	57.12	37.60	0
37.6	45	39.63	55.69	37.43	3.52
56.4	0	0	75.92	56.40	0
56.4	45	41.30	74.43	56.28	3.64

Roll angles were run every 5° but only minimum and maximum are listed in this table

4.4.3. Linear Actuator

The linear actuator that has been used in sonic boom tests at Ames and Glenn since 2010 was used in this test to translate the model longitudinally over a range of up to 24” in the wind tunnel. This allowed acquisition of multiple pressure signatures at small increments in the *X* direction over a specified distance, known as an “*X* sweep,” for spatial-averaging purposes. The movement provided by the linear actuator ram also facilitated proper longitudinal positioning of the model in the tunnel so that the model signatures could fall within the instrumented length of the pressure rail over the range of model heights tested—from 22.6” to 56.4” from the rail. In this test, almost all the *X* sweeps consisted of 26 ram positions, and the total *X*-sweep distances traversed for pressure signature measurements were 4”, 8”, or 12” with nominal spacing of 0.16” (~1 rail orifice), 0.32” (~2 rail orifices), or 0.48” (~3 rail orifices), respectively. Figure 4-18 shows layout views of the model in the tunnel with the ram (in orange) retracted and fully extended.

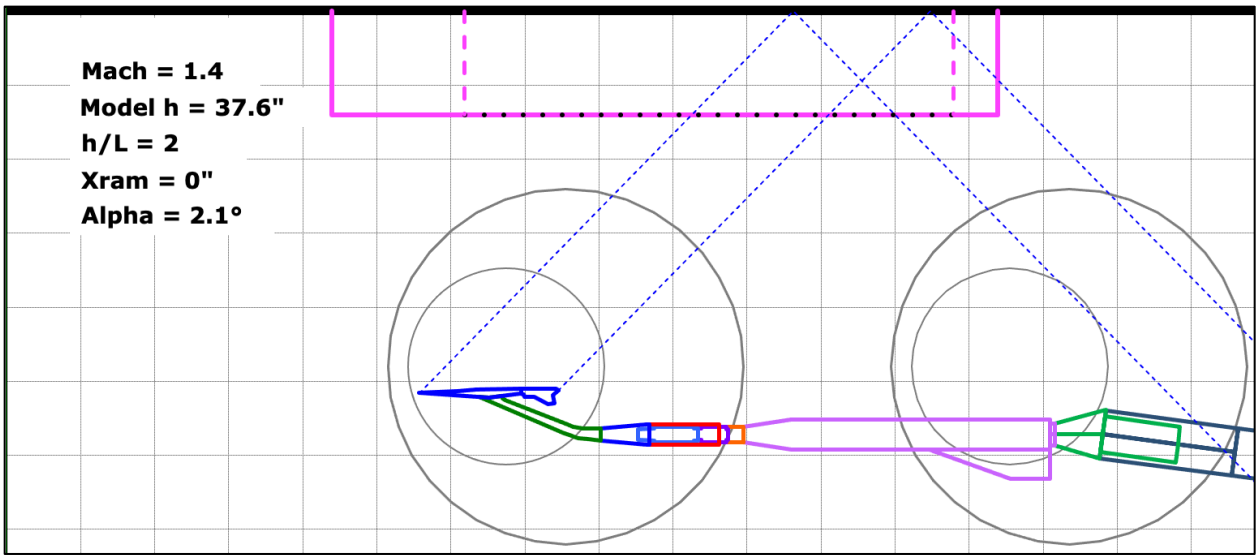

(a) Ram retracted

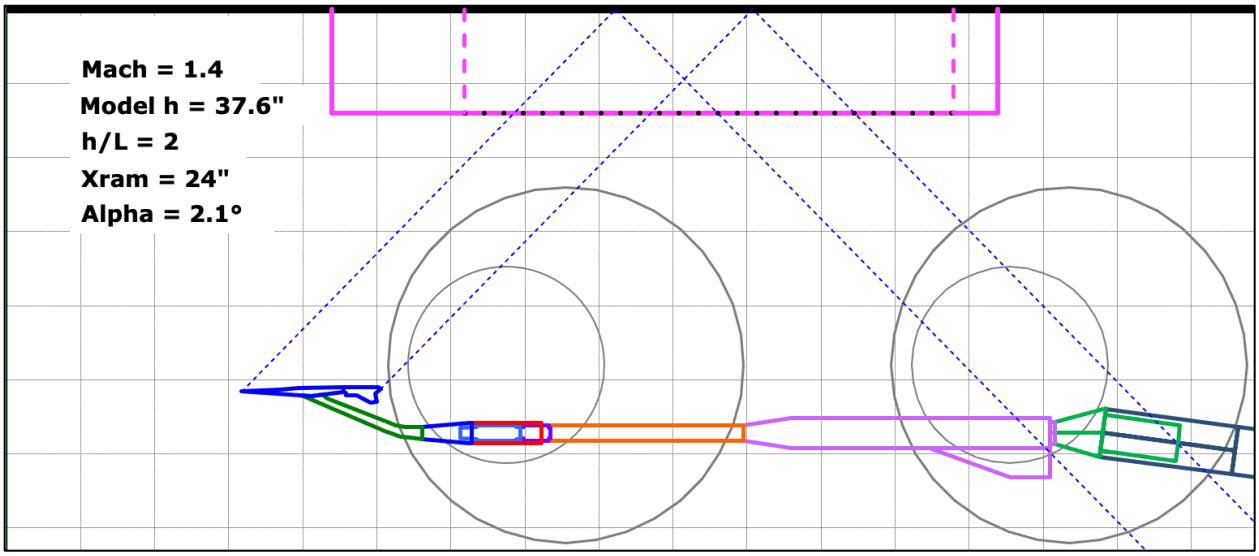

(b) Ram extended 24”

Figure 4-18 Layout diagrams showing linear actuator ram extension

5. Instrumentation, Imaging, and Test Techniques

The data collected in this test were from four different sources:

- Facility instrumentation for test-section conditions, tunnel strut height and angle, roll mechanism angle, and linear actuator ram extension
- Static pressure taps on the rail mounted on the tunnel ceiling for pressure signatures
- 6-component balance to measure forces and moments
- Schlieren images to visualize vertical cross-sections of the shock flow field

5.1. Pressure Rail and Scanners

The sonic boom pressure rail (Figure 5-1) is 14” tall, with a width of 1” at the base and tapering down to a 0.05” radius at the tip. It is 90” long with an 18”-long leading-edge section, an instrumented section 66” long, and a 6”-long trailing-edge section. The instrumented section contains 420 static pressure orifices, each of 0.015” internal diameter, spaced 0.1575” (4 mm) apart along the tip of the rail. This small radius at the tip was chosen to minimize the reflection of the incident shocks off the rail back toward the model. This gives a reflection factor (a pressure-multiplying factor) of 1, or very close to 1, where a value of 2 on a flat surface would be a full reflection of the incident shock waves.

The best pressure signatures from a model are obtained if none of the model shocks reflect off the tunnel wall at the base of the rail and pass over orifices that are within the range of the model incident shocks from the nose to the tail. If reflected shocks do pass over those orifices, then the incident pressure signature would be contaminated by the reflected signature. The rail height of 14” provides reflection-free data for the X-59 as shown in the tunnel layout in Figure 4-18(a) with a margin of about 8” at Mach 1.4 from the location of the model tail shock impingement on the rail and the reflected nose shock.

In the figure below, the purple cover plates in the middle of the rail cover the channels through which the seven bundles of (60) 0.040”-diameter stainless steel pressure tubes are routed from the orifices through the rail foot pads and out of the tunnel. Despite the various covers, channels, and lap joints shown in the images, the surfaces of the rail are smooth with no gaps or steps, and the foot pads fit flush in the tunnel ceiling.

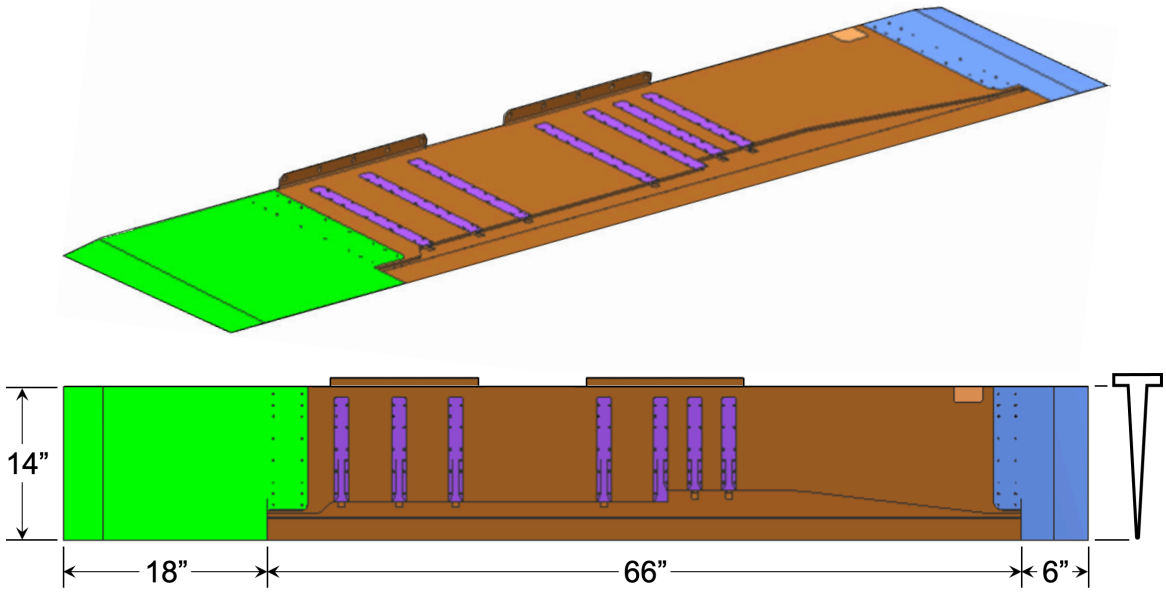

Figure 5-1 Sonic boom pressure rail (graphics: Tri Models)

Viton pressure tubing was attached to the hard tubing from the rail and routed above the tunnel ceiling to a temperature-controlled box that housed seven ESP (electronic scanner of pressure, TE Connectivity model # 64HD0511021120) modules to measure the pressures.

5.2. Balance

The balance chosen for this test was the Langley 2.0”-diameter 750 balance, shown in Figure 5-2. Though the loads for the X-59 sonic boom model were small, the balance had sufficient load capacity to handle the maximum unstart loads in the tunnel, and its size was compatible with the size of a balance adapter suitable for the blade strut and sting for the model. The balance capacities shown in the figure are in pounds and inch-pounds.

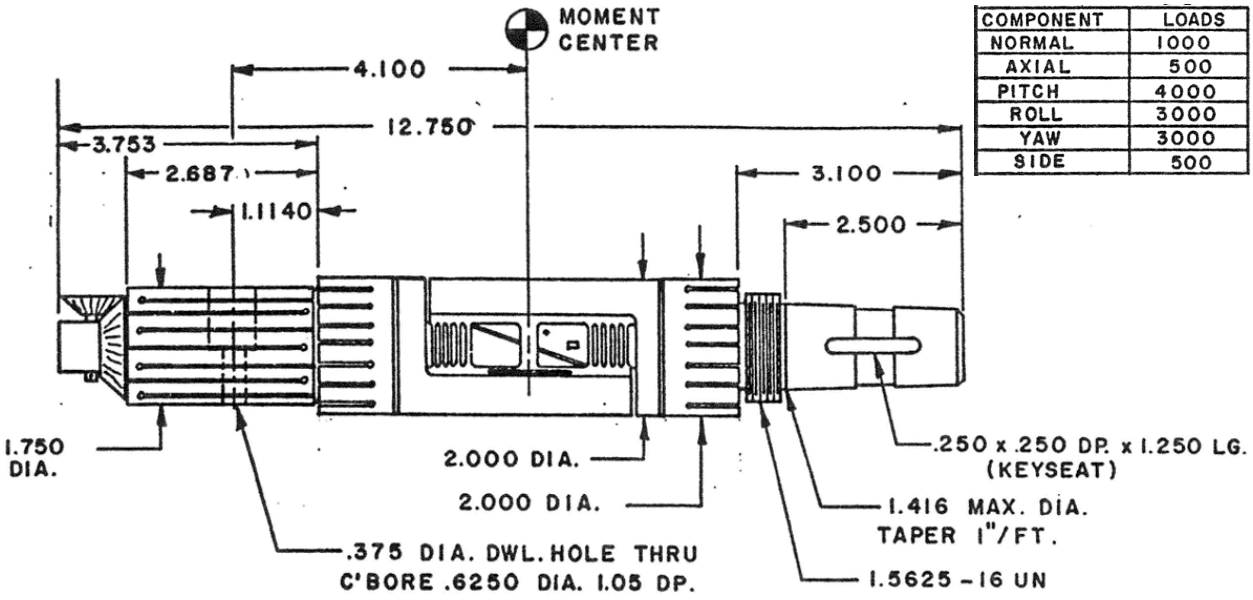

Figure 5-2 Langley 2.0”-diameter 6-component force and moment balance

The balance was used in the test primarily for the purpose of setting the correct angle of attack for the models. To set the right angle of attack, two factors had to be determined: the angularity of the tunnel flow in the vicinity of the model, and the deflection of all the model supports back to the tunnel strut under running loads. The balance was calibrated prior to the test for measured vs. applied loads, and for deflections under the maximum ranges of loads expected during the test. Flow angles were measured on both the AS-2 and X-59 models early in the test by running short pitch sweeps and comparing C_N vs. α curves for the X-59 model upright and inverted, and for the AS-2 model in just one roll orientation since it is axisymmetric. The results of the angularity checks were that no angle correction was needed at Mach 1.36 and 1.40, and only a -0.05° correction at Mach 1.47.

Early in the test the balance was found to have experienced some significant zero shifts after an hour or two of running each night. The cause was determined to be that the balance internal temperature had risen from room temperature prior to the first run of the shift up to the tunnel operating temperature as noted above in Table 3-1. The problem was mitigated by pre-heating the balance with a thermally-controlled wrap around the balance to bring the balance up to running temperature before starting the tunnel. The zero shifts were reduced to normal levels with this procedure and data quality was significantly improved.

5.3. Schlieren and TomoBOS Imaging

For the X-59 sonic boom testing in the 8x6 wind tunnel, the facility schlieren system was set up to align with the supersonic test section in which the model was installed. In this configuration, the collimating mirrors were shifted into their farthest upstream position, the receiving optics were reversed from the standard installation at the 8x6, and a pinhole light source was installed on the upstream pedestal. During initial testing with the schlieren system, a Point Grey Zebra2 4MP camera was installed to provide on-line optical diagnostics of the flow field around the model. For later testing, an Imperx Cheetah 16MP camera was utilized to provide high resolution imaging of the flow field generated by the model. These images were acquired in sets of 100 and were averaged to remove background flow.

A few of the schlieren images obtained during the test are presented below. Figure 5-3 is one of the early images taken during the test with the Point Grey camera. Figures 5-4 through 5-6 were taken with the Imperx camera later in the test, and the increased quality and resolution over the early image are apparent. These latter images were taken at model roll angles (not model-to-rail) of 0°, 45°, and 90° to show the differences in shock structure from the different views around the model. The image on the cover of this report is the one from Figure 5-4, but it has been cleaned up to remove artifacts in the image that do not represent the flow features from the model.

All the images contain shock or expansion waves that cross the model shocks and are from unknown sources away from the model. In addition, there are localized darkened areas in all the images that are likely from unknown defects in the optical path.

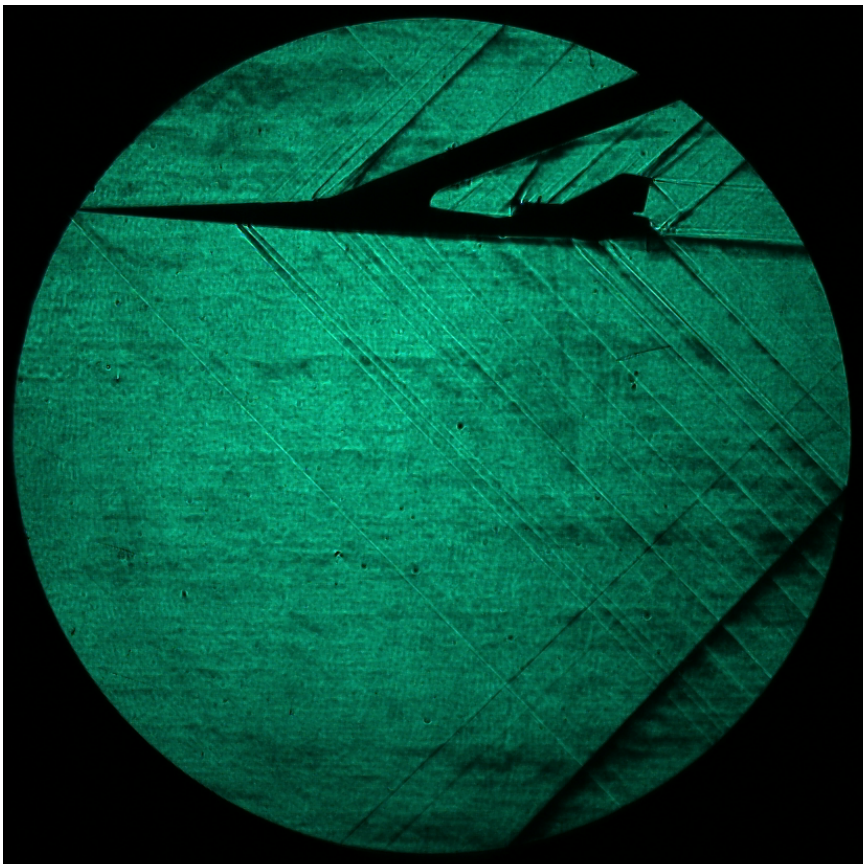

Figure 5-3 Point Grey camera schlieren image of X-59 model with blade strut Mach 1.4, α = 2.1°, ϕ_{RM} = 0°

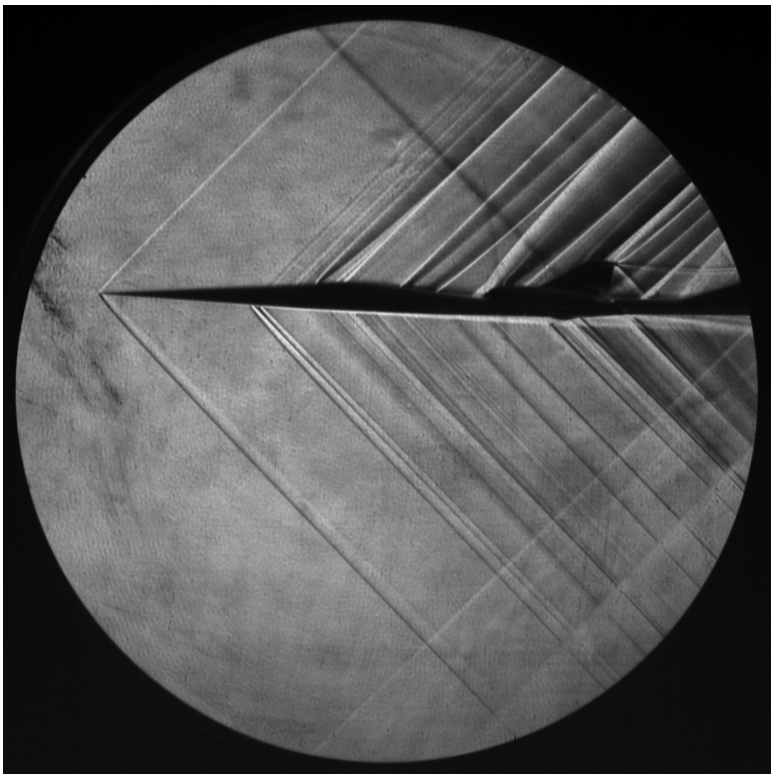

Figure 5-4 Imperx camera schlieren image of X-59 model with sting Mach 1.4, α = 2.1°, ϕ_{RM} = 0°

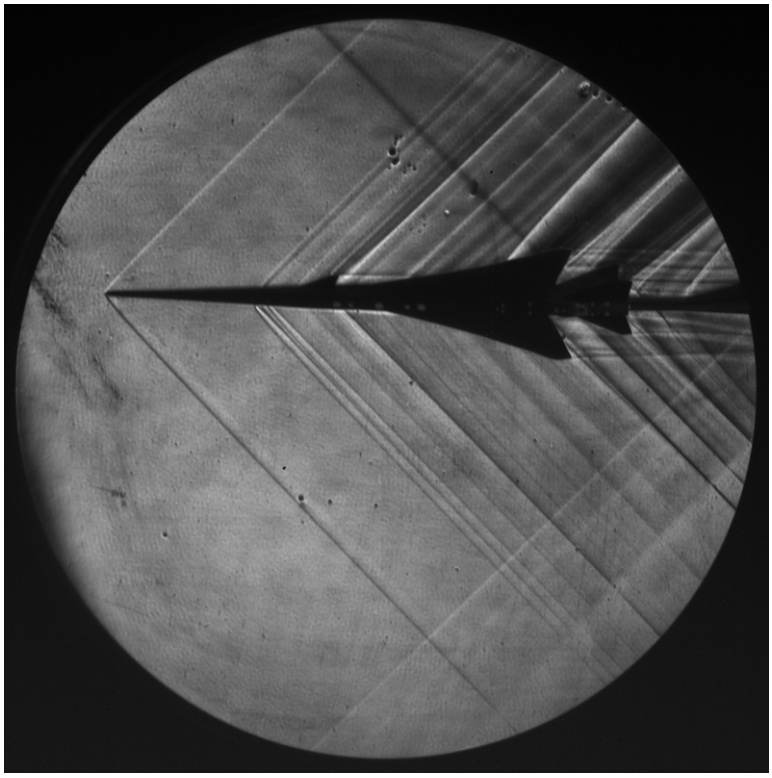

Figure 5-5 Imperx camera schlieren image of X-59 model with sting Mach 1.4, α = 2.1°, ϕ_{RM} = 45°

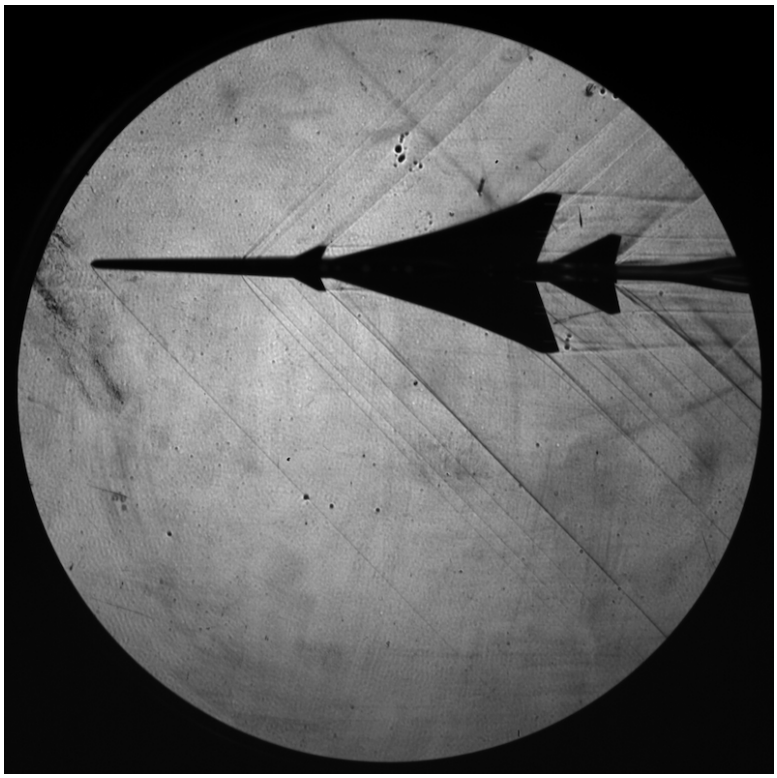

Figure 5-6 Imperx camera schlieren image of X-59 model with sting Mach 1.4, α = 2.1°, ϕ_{RM} = 90°

During a run of the sting-mounted configuration of the model, a TomoBOS (tomographic background-oriented schlieren) system was installed. The 16MP camera was repositioned outside of the north upstream schlieren window along with a 1.5kW LED excitation light source (Figure 5-7). A set of 3M 7610 retro-reflective panels printed with random dot patterns were installed in the test section over the south upstream schlieren window. Images were acquired with the model positioned every 15° of roll from -75° to +90°. The 12 resulting views were being processed at the time of this report preparation to provide a 3-D tomographic reconstruction of the flow field surrounding the model.

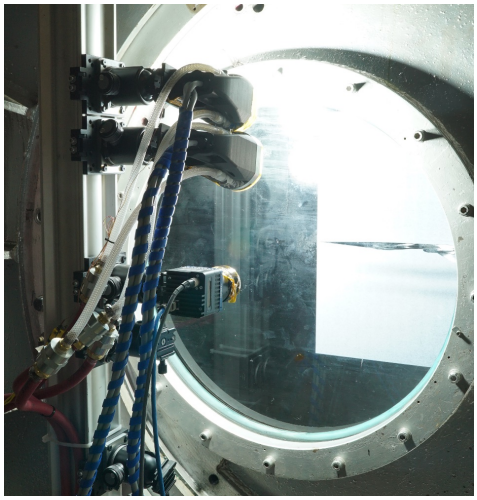

Figure 5-7 View of TomoBOS schlieren system camera and lights positioned outside of upstream test section window

5.4. Data Acquisition

Data were acquired for this test with the facility's Cobra data-acquisition system. The system sampled all the data channels at 12.5 Hz, and the following sampling durations were set for the different types of runs:

- 5 seconds for pitch runs
- 60 seconds for reference runs
- Pressure signature data runs: initially 60 seconds, then down to 30 seconds and ultimately down to 15 seconds a few days into the test after observing that the data quality did not significantly change with the shorter durations

Pitch runs for the purpose of flow angularity measurements consisted of progressive series of model angles of attack with all other model and tunnel conditions held constant. Reference and data runs referred to data taken for empty-tunnel and model pressure signatures on the rail, respectively, and consisted of data sampled over a specified duration with all tunnel and model conditions held constant. The difference between reference and data runs is that the former were acquired with the model as far aft and away from the rail as possible so that the pressure distribution on the rail would represent the variation of the tunnel flow without the influence of the model. Ideally, none of the model shocks would be on the rail for the reference runs, but in this test, the model nose shock passed over the last few inches of rail orifices in the reference runs, as shown in Figure 4-16(b). For data runs, the model was moved closer to the rail so that the shocks from the entire length of the model fell on the rail. After sampling the data for the desired duration, the model was moved forward slightly (usually 0.32", approximately equivalent to twice the orifice spacing on the rail) by the linear actuator, the run number was incremented, and data were taken for the same duration. This process continued until the desired length of the *X* sweep was completed, and the entire sweep, which typically consisted of 26 runs, was labeled as a Signature Set, or SigSet for short.

Reference runs were acquired frequently in the test so that the data runs which used them would be fairly close to them in time, thus minimizing any adverse effects of changes in the tunnel flow or ESP scanner properties. The data acquisition system was set up so that a data run would use the most recent reference run by default, but if the test customer determined that an ending reference run after a set of data runs would provide a better correction for the data runs, this was easily accommodated in post-processing.

It should be pointed out that a run as described above is termed a "reading" at Glenn Research Center, but for consistency with other NASA and industry wind tunnel terminology, the word "run" will be used throughout this report to represent such a set of data points.

Data files were provided from the Cobra system with all data parameters reported for every 12.5-Hz sample. A post-processing Python toolkit known as CoBALT (Cobra Batch Averaging and Look-up Tool) computed averages of the samples in the Cobra files for every 2, 10, 20, 30, and 60 seconds (depending on the total sampling duration), and these CoBALT files were provided to the customers as the final data files. The various averaging increments allow checking of the repeatability over the specified durations.

Review of the measured pressure signature plots in real time during the test gave insight into the data quality and whether there were any problems with the data. Bad rail pressure readings were usually obvious with consistently low or high values relative to nearby pressures, and the rail pressure parameters in the data for the bad ports were flagged with the value of 9999.

6. Results and Discussion

The test techniques, data reduction methods, uncertainty estimation, and analysis of the effects of model and test condition variations on the measured pressure signatures are presented in this section. In all the data plots that follow, the model angles of attack and roll, and all control surface deflections, are at their nominal angles unless otherwise stated in the plot titles or legends. These nominal angles are:

- angle of attack = 2.1°
- angle of roll = 0°
- flaps = -2.4°
- ailerons = 1.1°
- stabilators = 3.42°
- T-tail = 3.7°

6.1. Bad Pressure Port Identification

Real-time data plots and post-run analyses allowed visual inspection of the pressure distributions measured on the rail. Spikes in the data, caused by leaks or plugs in the pressure tubing or in the attachments to the hard lines from the rail or to the pressure modules, were usually easily recognized, especially when they were consistent over a number of runs. Many of the spikes were noted in real-time during the test, but after the test, a full set of plots of the uncorrected rail pressures versus orifice number was made to list the bad ports for every run of the test. Figure 6-1 is an example of one such set of plots, consisting of four runs of data from SigSet 10 for the X-59 model with the blade-strut mount. Note that the upper plot is over the entire 420-port range of the rail, and the three lower plots are expanded subsets of this range so that individual port numbers could be identified for the spikes, which are identified by the arrows.

The values for the pressure parameters in the data files for these bad ports were set to 9999 so that it would be obvious which ones were bad. When plotting the data, the bad ports were averaged over, using the pressures from the neighboring ports.

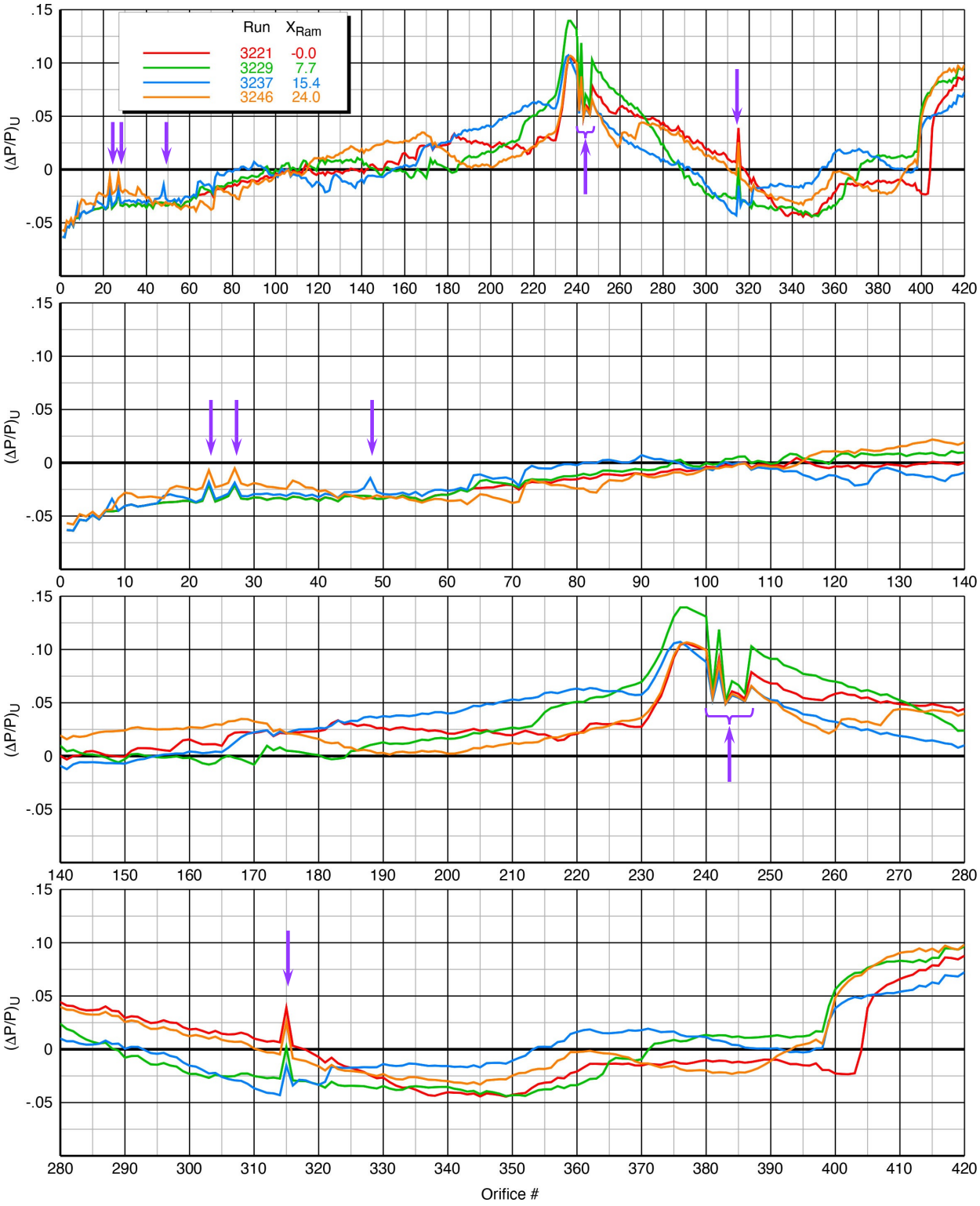

Figure 6-1 Identification of bad pressure ports (arrows) in selected runs in SigSet 10 X-59 model (blade strut), Mach 1.4, h/L = 1.2, α = 2.1°, ϕ_{m2r} = 0°

6.2. Data Corrections Using Reference Runs

A reference run is always acquired for a set of *X* sweeps for subtracting out the background tunnel signature on the rail with the model shocks either *not* on the instrumented part of the rail, or as far aft on the rail as possible. The model position for a reference run is depicted in Figure 4-16(b) with the model at a nose height of 73" relative to the rail, at an angle of attack at 1° and a roll angle of 180° with the ram retracted. Note that for this reference run position the model nose shock passes within a few inches of the rear of the instrumented part of the rail, leaving over 90% of this portion of the rail clear for the model signatures in the data runs.

Example pressure signatures for reference and data runs plotted vs. X_{Orif} are shown in Figure 6-2. The red curve is from the reference run, and the black from the data run. In the upper plot, the curves are plotted as the "uncorrected" $\Delta P/P$ pressure ratio, defined as:

$$(\Delta P/P)_R = \left(\frac{P_{Rail}-P_\infty}{P_\infty}\right)_{Reference\ Run} \quad (1)$$

$$(\Delta P/P)_U = \left(\frac{P_{Rail}-P_\infty}{P_\infty}\right)_{Data\ Run} \quad (2)$$

P_{Rail} = pressure at a given rail orifice

P_∞ = tunnel freestream static pressure

The gap between the two curves in the upper plot represents the model signature. In the lower plot, the curve which reveals the normalized model signature alone is the "corrected" $\Delta P/P$, having had the reference run signature removed, and it is defined as:

$$(\Delta P/P)_C = (\Delta P/P)_U - (\Delta P/P)_R \quad (3)$$

The uncorrected curves show a large spike in pressure just aft of the center of the signatures. This spike is not caused by anything from the tunnel itself, but rather, it is from the rail leading-edge shock reflected off the tunnel side walls and passing over the rail orifices. Since this shock affects both the reference and data runs, the subtraction of the reference run removes most of the effect of the reflected shock. However, the steep gradient of the forward part of this shock (near *X* = 98") could cause significant errors in the corrected signature from any small differences between the two runs. It is fortuitous though that the model signature (for data run 5417) ends near the region of this spike, thus allowing most of the signature to be relatively uncontaminated by errors induced by the steep gradient. In the lower plot, the rear of the model signature is where the pressure recovers to near-ambient conditions in the region of *X* = ~95" to ~99". The large pressure increase aft of this point is caused by the shocks from the upper part of the model blade strut where it makes the transition from a biconvex cross section to a round shape for mating with the balance adapter. All the shocks and expansions downstream of *X* = ~99" are from the rear part of the blade strut, the balance adapter, and linear actuator.

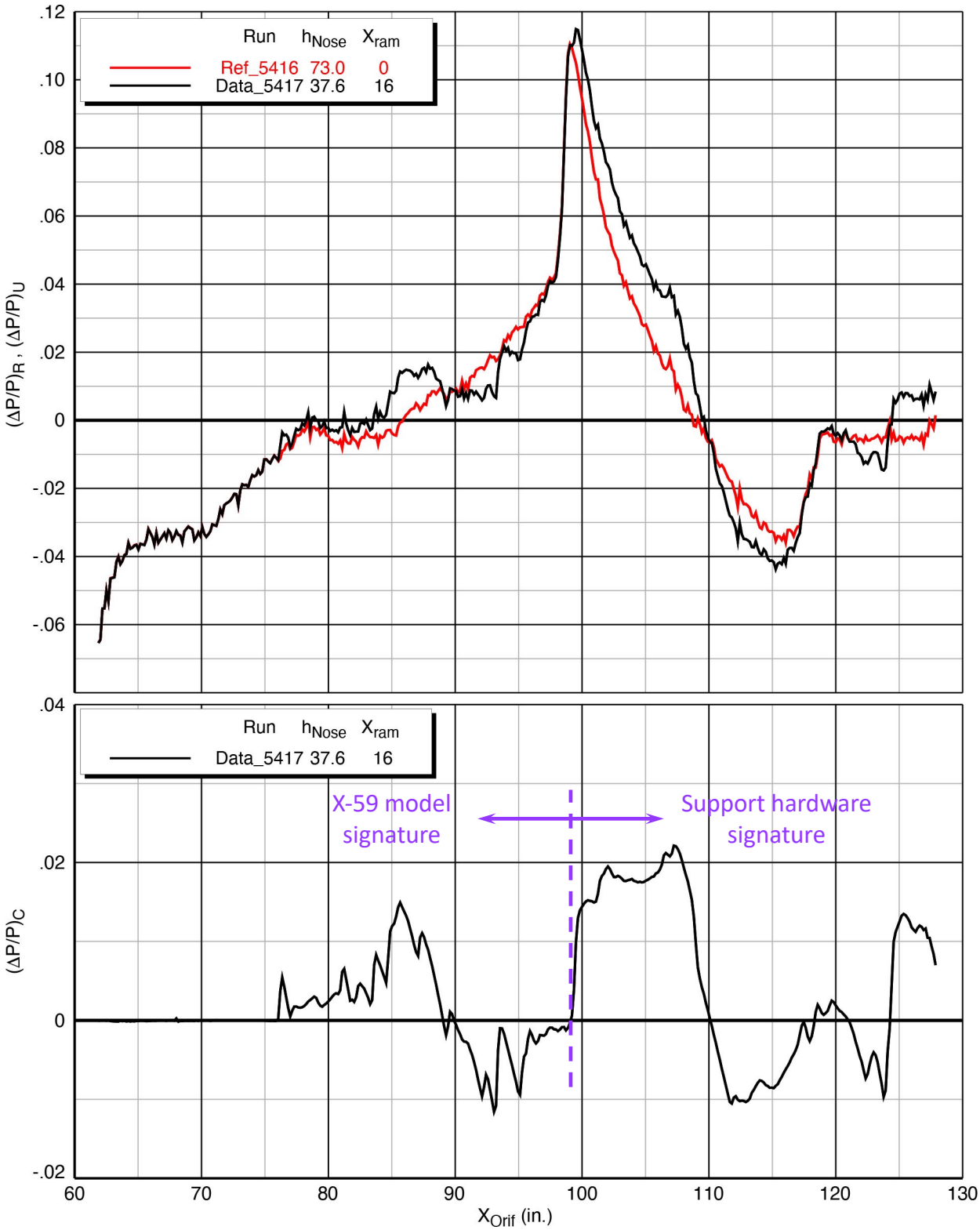

Figure 6-2 Reference- and data-run pressure signatures, with data signature corrected by subtracting reference signature
X-59 model on blade strut, Mach 1.4, α = 2.1°, ϕ_{m2r} = 0°

6.3. Pressure Signature Measurements and Spatial Averaging

The non-uniform flow field of the wind tunnel causes pressure signatures on the rail to be different for different model positions in the test section. Spatial averaging is used to produce a model pressure signature with reduced effects from the tunnel flow field spatial distortions. A set of 26 individual signatures and their spatial average from the *X* sweep corresponding to the data in Figure 6-2 are shown in Figures 6-3 and 6-4 (all but the first and last runs are removed from the legend for brevity, but the numbers for all the runs are provided in the lower plots of each figure). In the first figure, the signatures are plotted by the rail orifice locations, and the forward movement of the linear actuator ram in 25 steps of 0.32" (spacing of about 2 rail orifices) from 16" to 24" extension is reflected by the shifting of the model signatures to the left. In the second figure, the signatures are aligned by adding the X_{Ram} positions to the orifice locations for each run so that an average of all the pressures can be taken. The spatial-averaging process for the plots in this report is as follows:

- The 26 individual curves of corrected $\Delta P/P$ are interpolated at specific *X* points because the pressure taps aren't perfectly aligned after adjusting for ram position—500 points are evenly distributed over the length of the model signature plus a few inches on either end, and are used in a fit done by piece-wise linear interpolation
- At each *X* position, the average of the 26 $\Delta P/P$ values is computed
- The averages at each of the 500 *X* positions make up the average pressure signature for a given SigSet

Note that in the first figure, there is a steep rise in pressure just beyond X = 99" for the first run and the average run, and the location for this pressure rise moves forward with the ram movement. This rise occurs just beyond X = 115 for *all* the runs in the second figure because they are aligned with X_{Ram} having been added to X_{Orif}. These pressure rises are from the shock from the rear of the model blade strut where it makes a transition from the biconvex blade shape to a circular cross section for mating with the balance adapter. The model shocks can be considered terminated just prior to these pressure rises.

The upper plots in each of Figures 6-3 and 6-4 are *overlay* plots, where the signatures are plotted with their unmodified pressure values. The lower parts of the figures contain *waterfall* plots, for which the pressure values are plotted with a progressive -0.005 $\Delta P/P$ offset for each successive signature. The overlay plots give an indication of the repeatability of the signatures, while the changes from one signature to the next can be observed in the waterfall plots.

Note in the overlay plot of Figure 6-4 that the repeatability is very good from the nose shock back to $X_{Orif} + X_{Ram}$ around 100", but the repeatability is not as good in the middle part of the signature and only slightly better toward the rear of the signature until about 110" where the scatter reduces. To correlate the location of this middle region of poorer repeatability with the location of the reflected rail leading-edge shock, one must refer to Figure 6-3 which shows that this region (of the highest-pressure peaks) covers a range on the rail from approximately X_{Orif} = 77" to 88". The reflected rail shock in Figure 6-2 falls between X_{Orif} = 98" to 105", so the steep gradients in this shock region are probably not direct contributors to the poorer repeatability in the middle part of the signature.

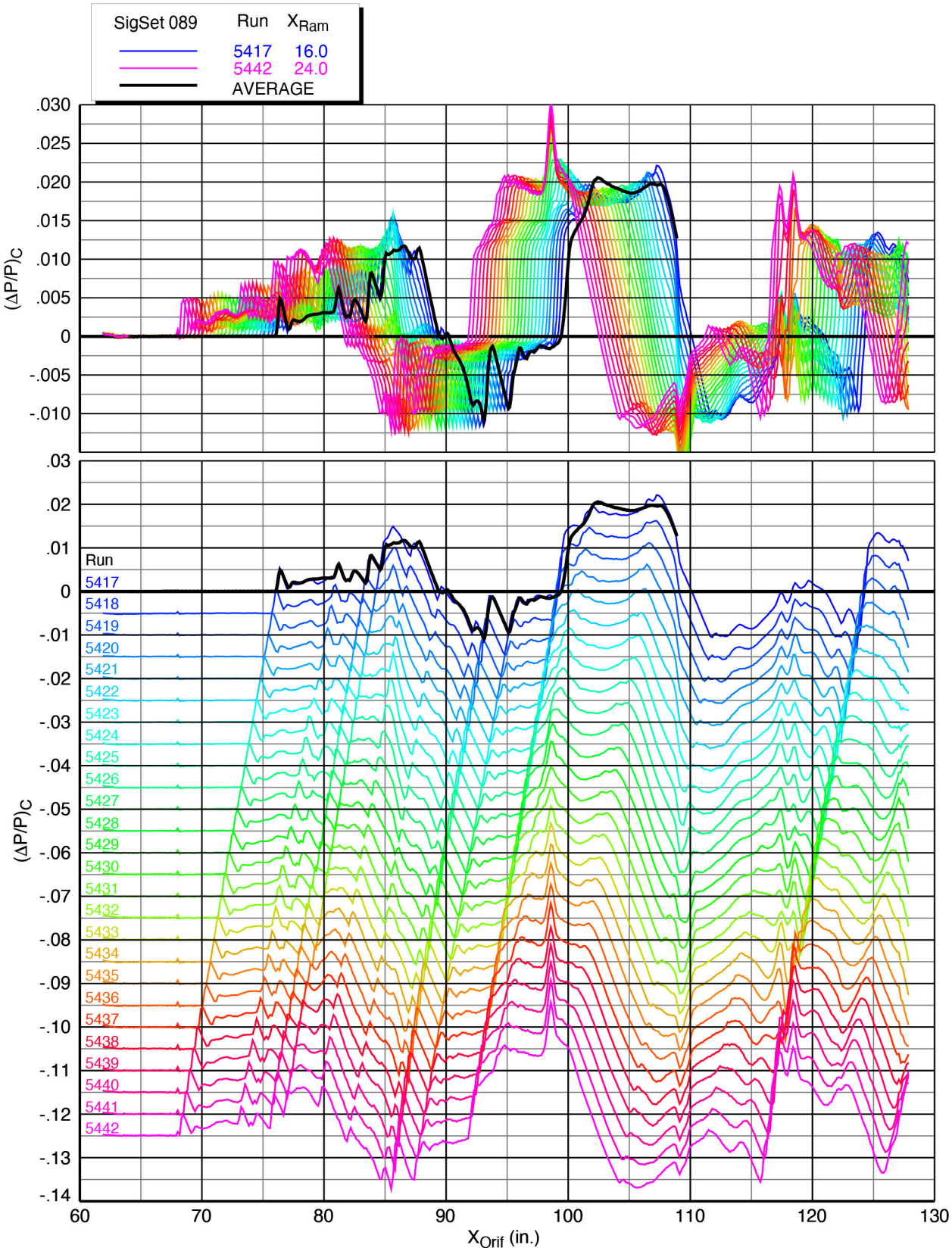

Figure 6-3 Unaligned pressure signatures for SigSet 89 in overlay and waterfall plots X-59 model (blade strut), Mach 1.4, h/L = 2, α = 2.1°, ϕ_{m2r} = 0°

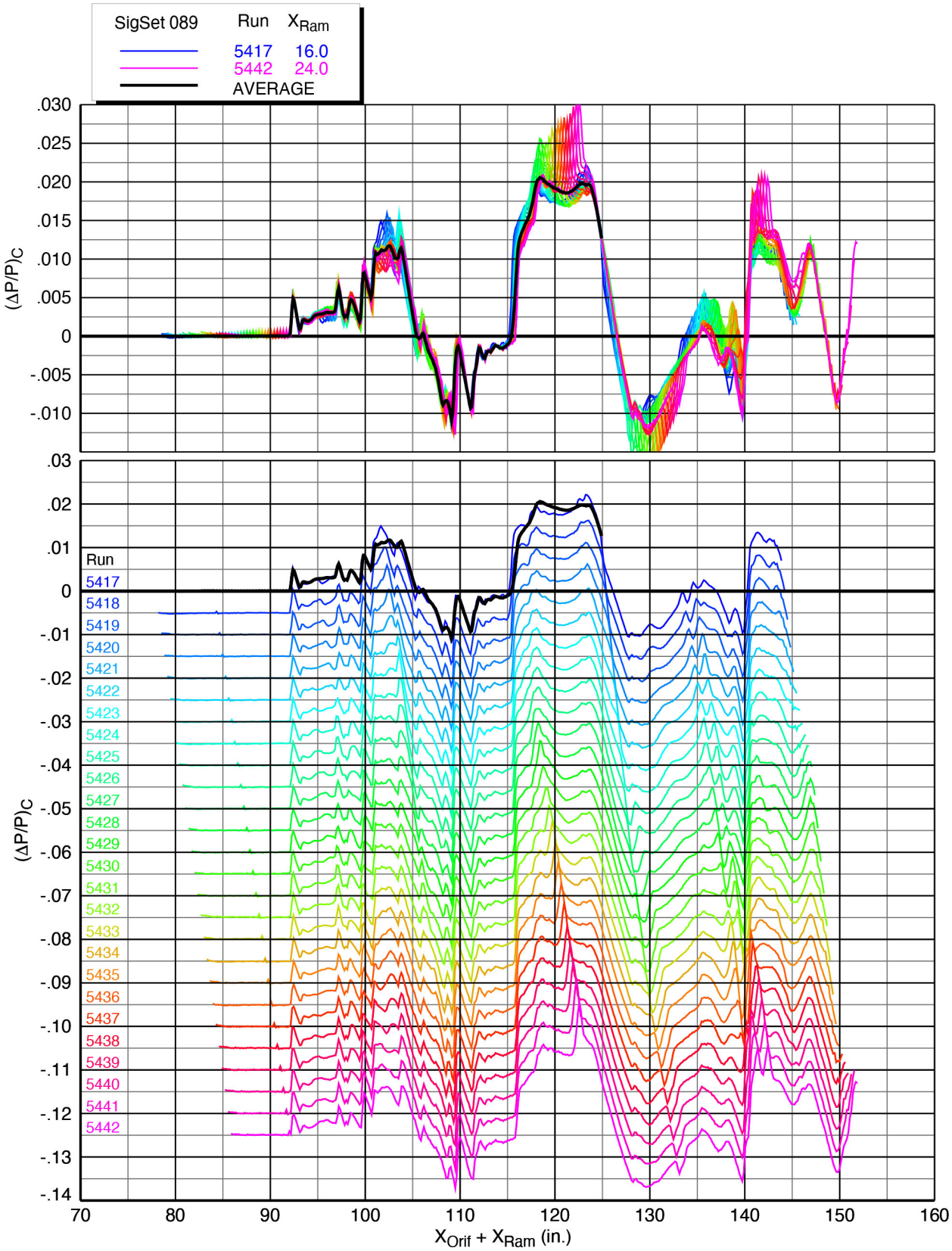

Figure 6-4 Aligned pressure signatures for SigSet 89 in overlay and waterfall plots X-59 model (blade strut), Mach 1.4, h/L = 2, α = 2.1°, ϕ_{m2r} = 0°

6.4. Signature Quality with Ram Position

The variation in the scatter of the data over the length of the aligned pressure signatures led to investigations of which parts of the pressure rail were best suited for acquiring consistent data. In this section, plots from various signature sets are presented to illustrate the differences in signature quality over different parts of the rail.

6.4.1. AS-2 Model

Early in the test, some of the signatures were measured over the full 24”-range of ram positions for the purpose of assessing the signature quality over various parts of the rail. Figure 6-5 shows the layout for the AS-2 model in SigSet 5, in which 26 pressure signatures were acquired in 0.96” ram increments from fully retracted (AS-2 model shown in blue) to fully extended (model shown in light blue). Note that shock lines from the rail (in magenta) are included in this layout to give *approximate* indications of where the rail shocks might impact the model The unaligned signatures are plotted as a function of X_{Orif} in Figure 6-6, and both this figure and the layout show that the model front and rear shocks intersected the rail at these approximate tunnel stations (X_{Orif} locations):

- X_{Ram} = 0”: 85.3” to 101.3”
- X_{Ram} = 24”: 61.3” to 77.3”

The model shocks started out roughly at the middle of the rail and moved to the forward-most portion of the rail in the *X* sweep. Note that the front shock for the ram-extended position falls almost exactly on the forward-most orifice on the rail (located at 61.9”). This can also be inferred from the lowest curve in Figure 6-6 (magenta curve for run 2979), which starts at the left end with the nearly-vertical nose shock without a horizontal line ahead of it.

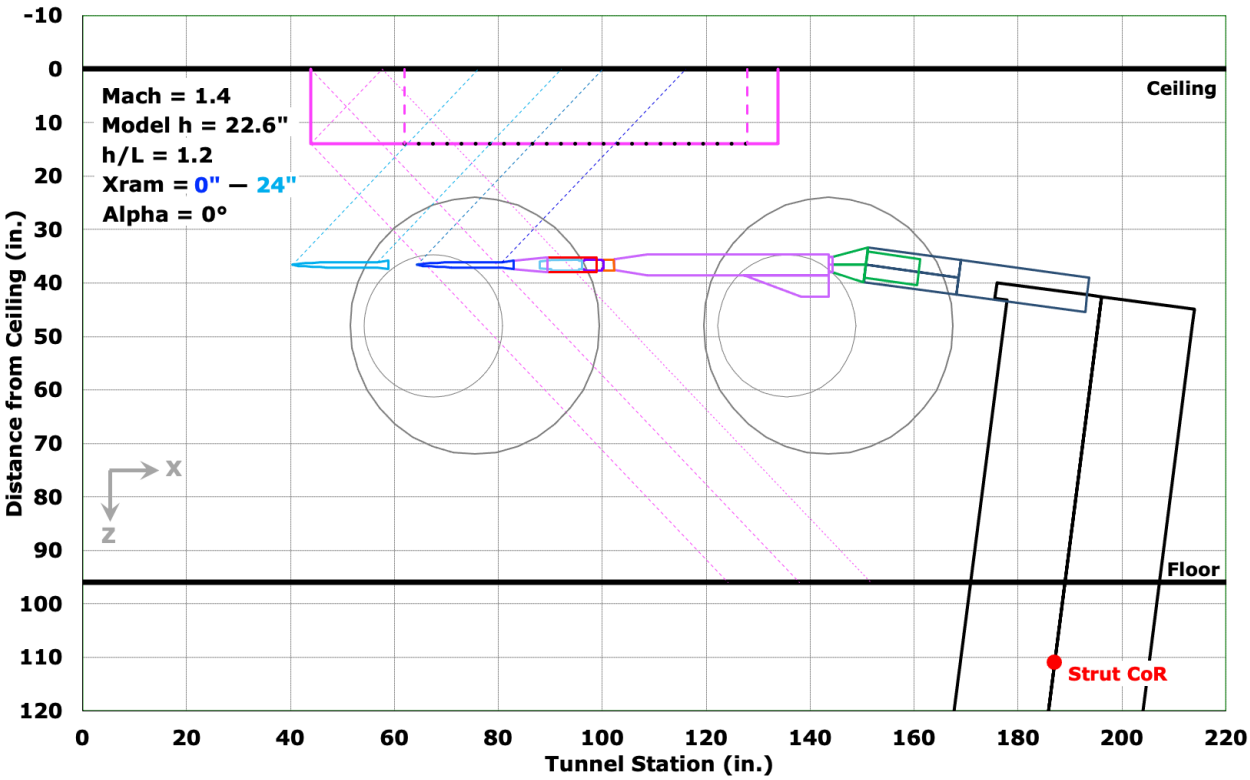

Figure 6-5 Layout diagram of AS-2 model showing full 24” ram range

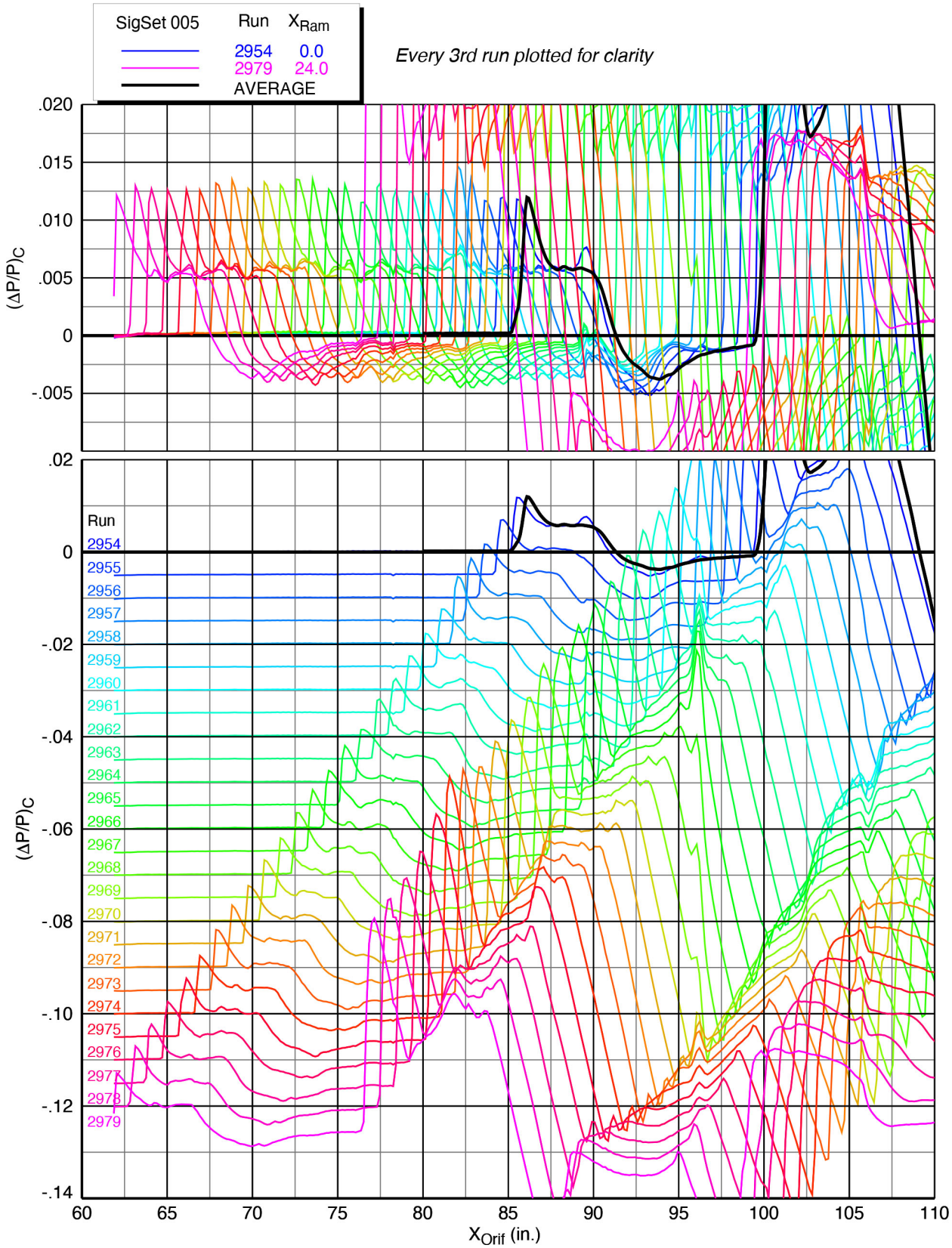

Figure 6-6 Unaligned pressure signatures for SigSet 5 in overlay and waterfall plots AS-2 model, Mach 1.36, *h/L* = 1.2, $\alpha = 0°$, $\phi_{m2r} = 0°$

An unexpected characteristic of the average curve (bold black line) in Figure 6-6 is that the pressure rise for the nose shock starts out gradually instead of abruptly as in all the individual curves. Being an average, it implies that some of the individual curves have nose shock positions that do not match those of some of the other curves. The aligned overlay plot of these signatures in Figure 6-7 illustrates this: the nose shock locations in the initial signatures for runs 2954 and up to about one-third or one-half of the following ones are significantly forward of those shock locations in the latter signatures. It is obvious in the overlay and waterfall plots that the nose shock moved aft (in terms of $X_{Orif} + X_{Ram}$) as the model was translated forward by the linear actuator ram. This means that there was some unknown mechanism in the tunnel flow that caused the nose shock position to change (and thus the shock wave angle) for some of the signatures, such as a possible static pressure gradient that would change the local Mach number.

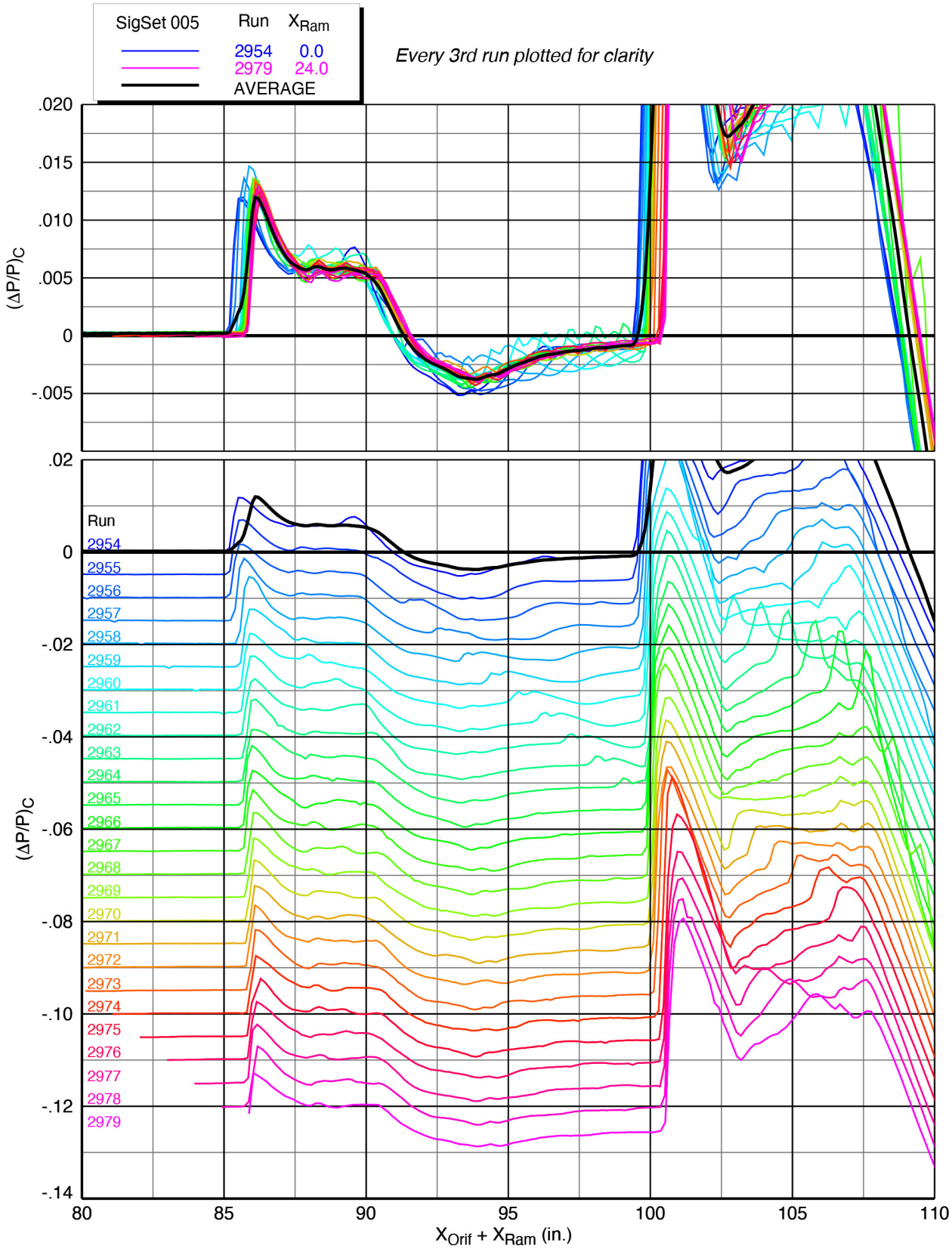

Figure 6-7 Aligned pressure signatures for SigSet 5 in overlay and waterfall plots AS-2 model, Mach 1.36, *h/L* = 1.2, $\alpha = 0°$, $\phi_{m2r} = 0°$

To help identify which of the individual signatures had the more forward nose shock positions, Figures 6-8 through 6-10 were made to break up the 24” *X* sweep into thirds with X_{Ram} ranges of roughly 0” to 8”, 8” to 16”, and 16” to 24”, respectively. Note that the SigSet designations of 5.1, 5.2, and 5.3 represent the three thirds of the set of signatures. The colors of the individual-signature curves match the colors of the curves in Figure 6-7 at the corresponding X_{Ram} positions to help the reader visually correlate the curves among the four figures. Having separated the *X* sweep into thirds makes it very obvious that there is much more scatter in the first third (Figure 6-8) than in the latter two thirds (Figures 6-9 and 6-10), and the nose shock position is more consistent in the latter figures. This is an indication that better-quality data would be obtained from the forward part of the pressure rail.

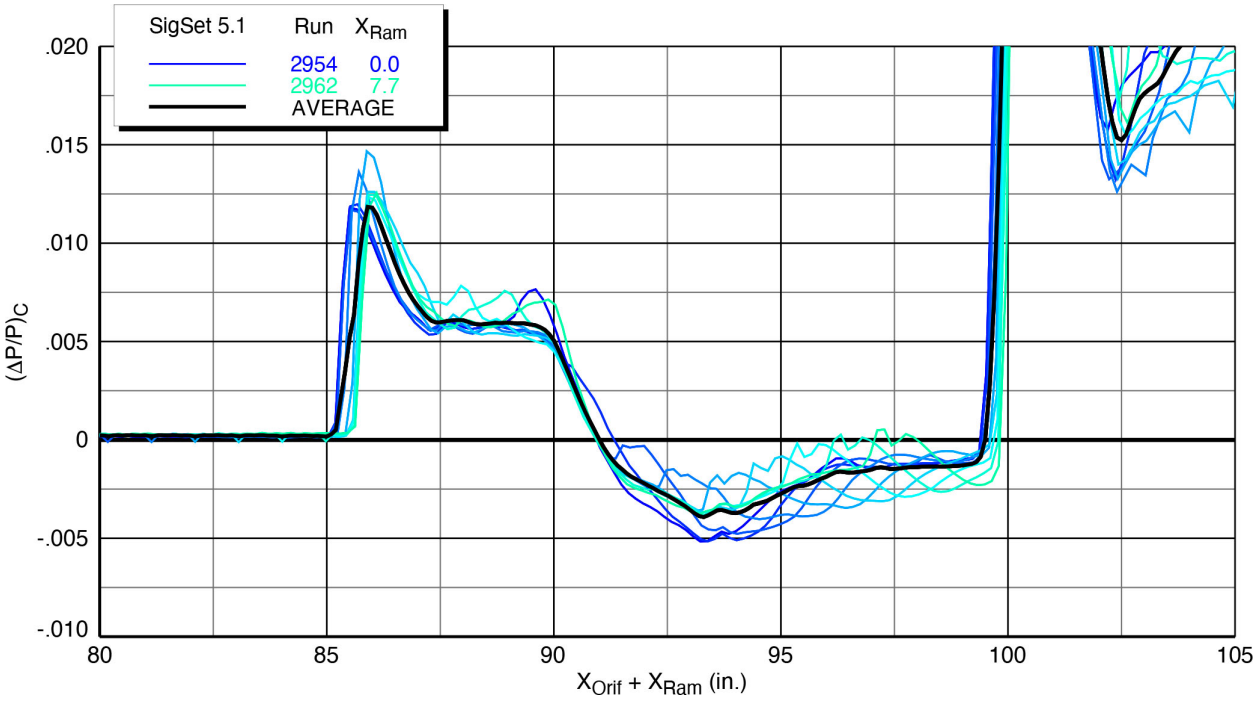

Figure 6-8 Aligned pressure signatures for first third of SigSet 5 in overlay plot AS-2 model, Mach 1.36, *h/L* = 1.2, $\alpha = 0°$, $\phi_{m2r} = 0°$

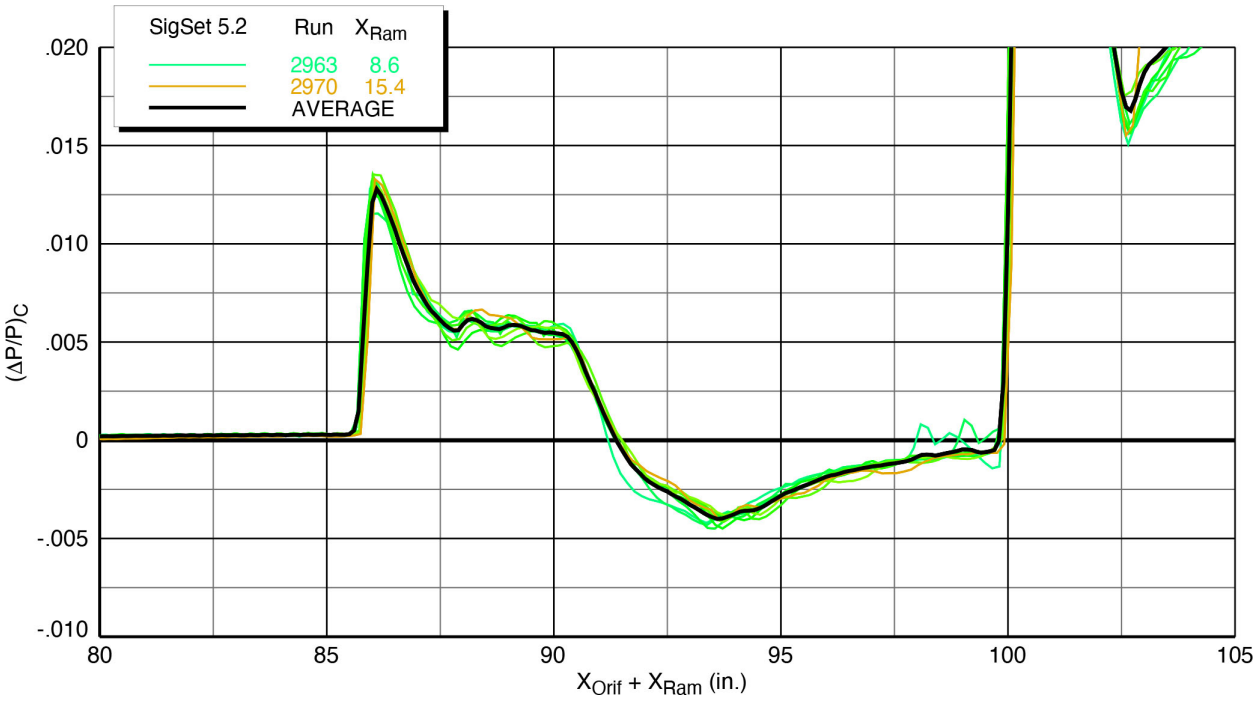

Figure 6-9 Aligned pressure signatures for middle third of SigSet 5 in overlay plot AS-2 model, Mach 1.36, *h/L* = 1.2, $\alpha = 0°$, $\phi_{m2r} = 0°$

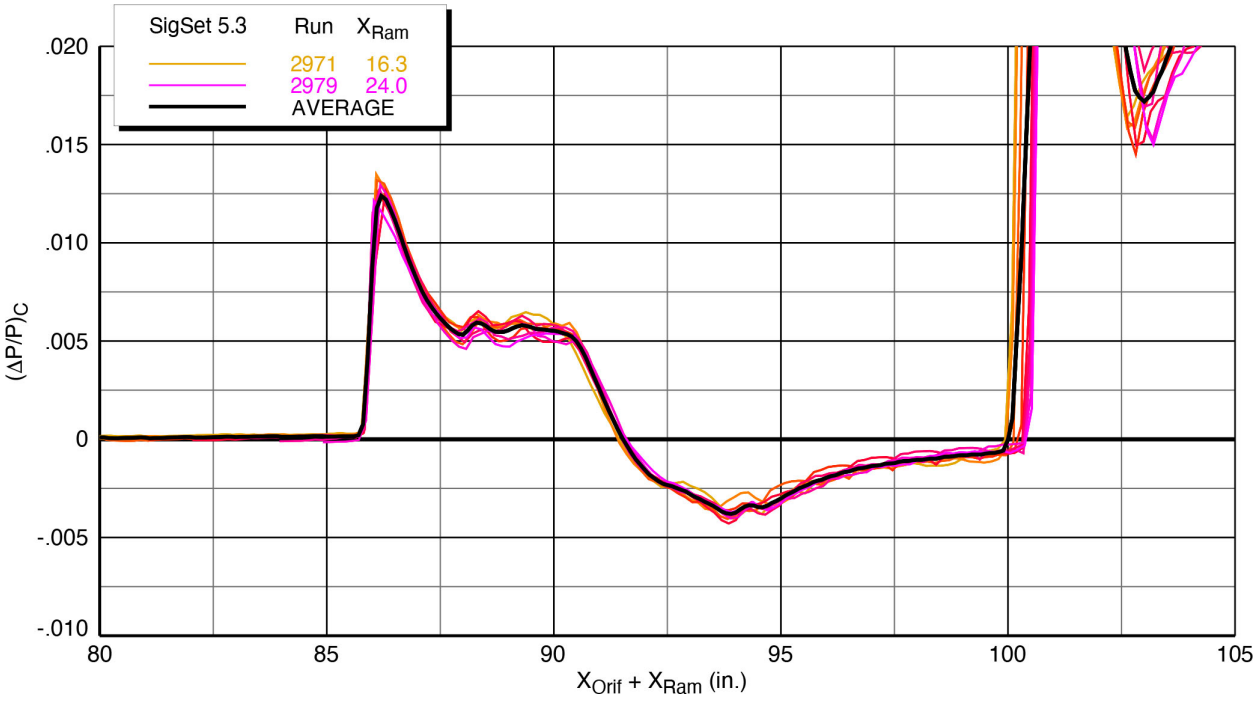

Figure 6-10 Aligned pressure signatures for last third of SigSet 5 in overlay plot AS-2 model, Mach 1.36, *h/L* = 1.2, $\alpha = 0°$, $\phi_{m2r} = 0°$

6.4.2. X-59 Model

An analysis of a set of signatures for the X-59 model similar that above for the AS-2 model over the full range of ram positions is presented here. A layout diagram for the X-59 model is shown in Figure 6-11, which is for SigSet 100, at Mach 1.4 and a model height of 1.2 body lengths below the rail. A difference in this *X* sweep, however, is that 76 signatures were acquired in 0.32” increments over the 24” ram range. This was done to get better resolution of the changes among the signatures over the different parts of the rail. In the layout diagram, similar to the one with the AS-2 model, the ram range is shown from fully retracted (X-59 model shown in blue) to fully extended (X-59 model shown in light blue). Note that shock lines from the rail (in magenta) give *approximate* indications of where the rail shocks might impact the model. In reality, the rail shocks make up a complex 3-dimensional flow field, and their 2-D depiction in this diagram is an oversimplification, yet this depiction could be useful in illustrating where the model *might* be free from the influence of the rail.

The aligned pressure signatures are plotted vs. $X_{Orif} + X_{Ram}$ in Figure 6-12, but only every third signature is shown to allow enough spacing among them in the waterfall plot so that the variations can be easily seen. The average curve in the plot was computed for all 76 signatures.

This plot as well as the layout show that the model front and rear shocks intersected the rail at these approximate tunnel stations (X_{Orif} locations):

- X_{Ram} = 0”: 79.8” to 98.3”
- X_{Ram} = 24”: 55.8” to 73.7”

The model shocks impinged on the middle part of the rail at the start of the *X* sweep and moved off the forward end of the instrumented part of the rail (first orifice located at 61.9”) by the end of the sweep. Thus, the model nose shock was not captured in the last ~6” of the sweep, as evidenced in the aligned signatures of Figure 6-12, where the nose shock disappeared from the front of the signature which starts at the offset $\Delta P/P$ value below -0.09.

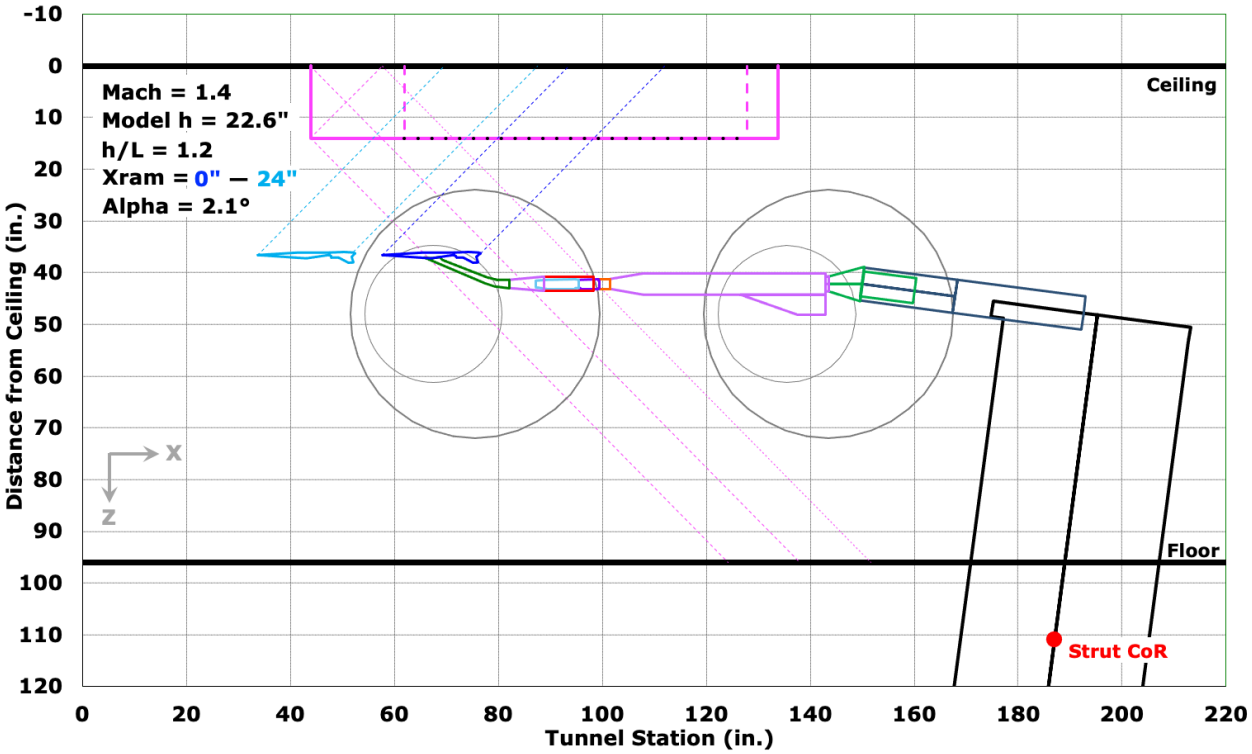

Figure 6-11 Layout diagram of X-59 model at *h/L* = 1.2 showing full 24” ram range in SigSet 100

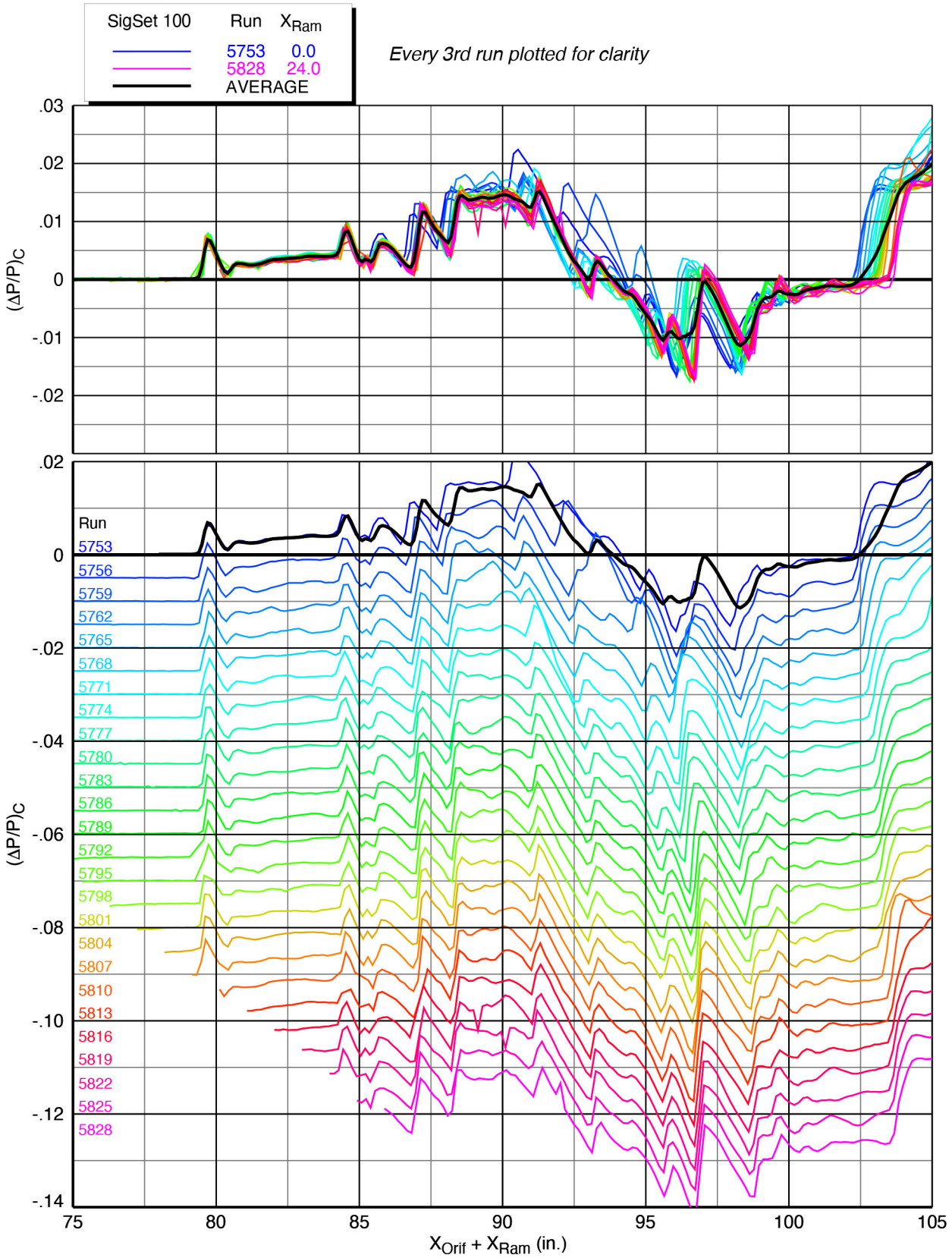

Figure 6-12 Aligned pressure signatures for SigSet 100 in overlay and waterfall plots X-59 model (blade strut), Mach 1.4, h/L = 1.2, α = 2.1°, ϕ_{m2r} = 0°

Figures 6-13 through 6-15 consist of overlay plots of each third of the 76 signatures of SigSet 100. As was the case for the AS-2 model, there is much more scatter in the first third of these signatures than in the latter two-thirds, and the last third shows the least amount of scatter overall. Again, this is an indication that better-quality data would be obtained from the forward part of the pressure rail as long as the entire model signature is captured within the range of rail orifices. A possible reason for this could be less influence of the rail shock waves on the model shocks as they propagate toward the forward part of the rail.

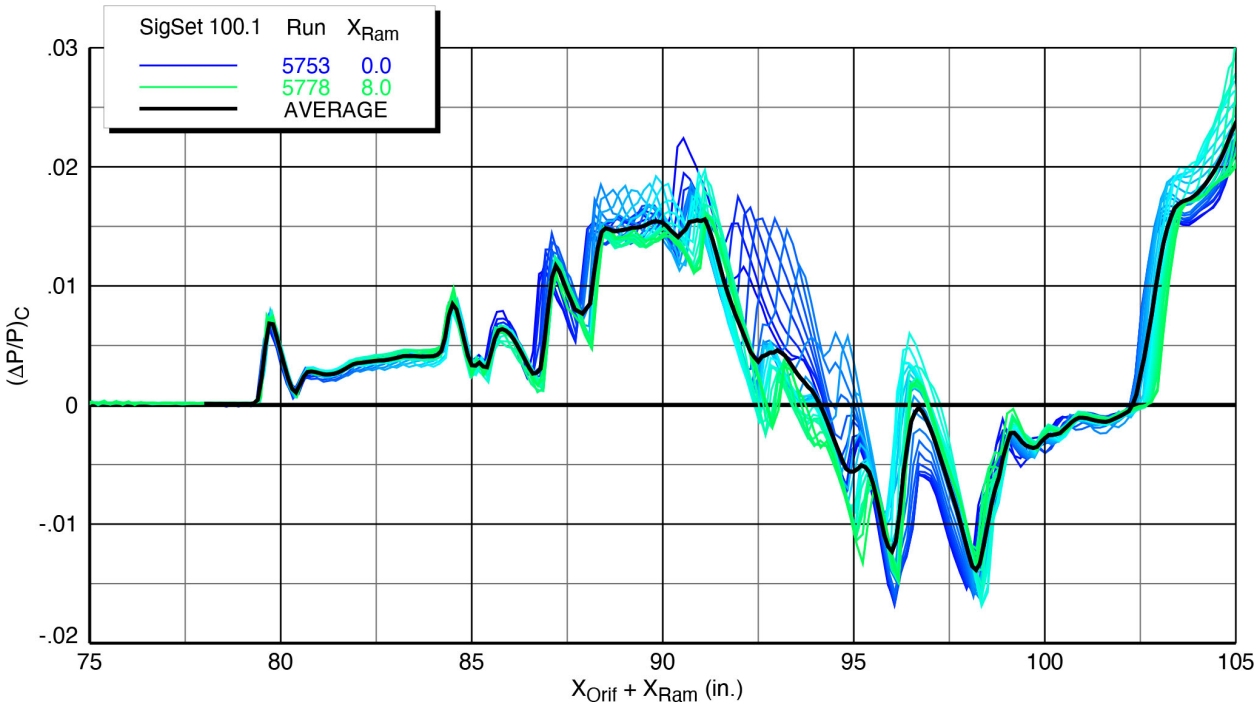

Figure 6-13 Aligned pressure signatures for first third of SigSet 100 in overlay plot X-59 model (blade strut), Mach 1.4, *h/L* = 1.2, α = 2.1°, ϕ_{m2r} = 0°

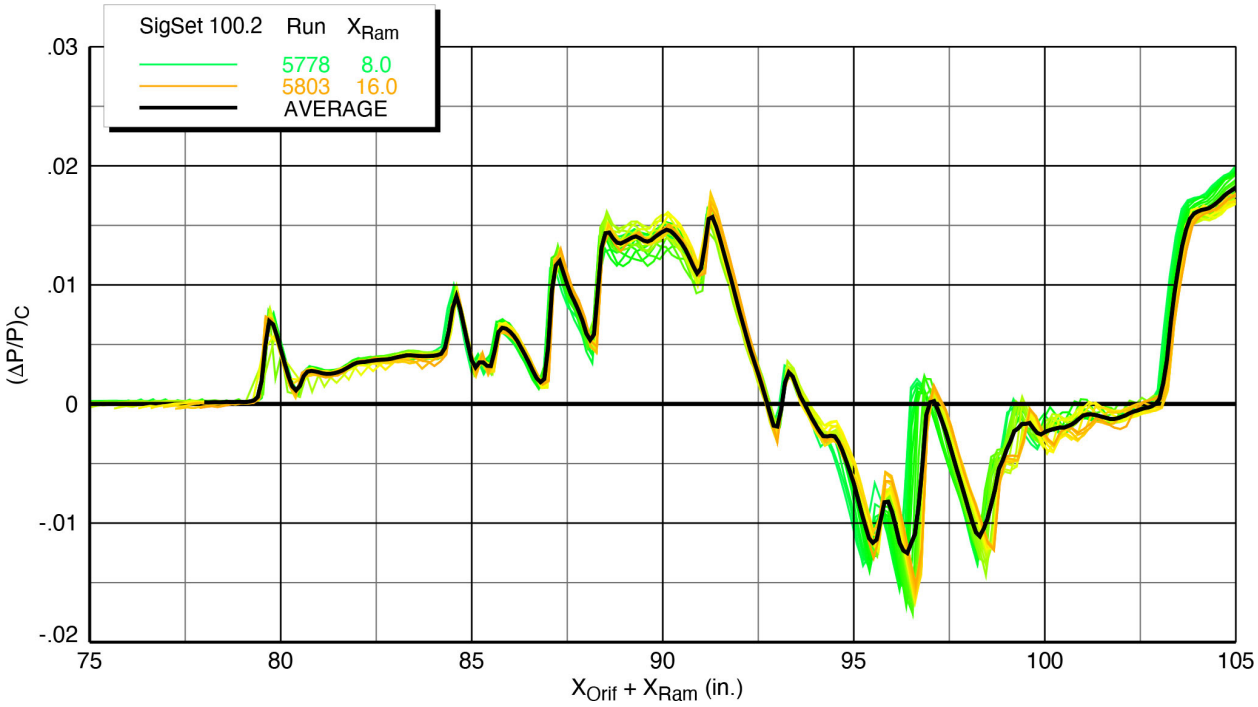

Figure 6-14 Aligned pressure signatures for middle third of SigSet 100 in overlay plot X-59 model (blade strut), Mach 1.4, h/L = 1.2, α = 2.1°, ϕ_{m2r} = 0°

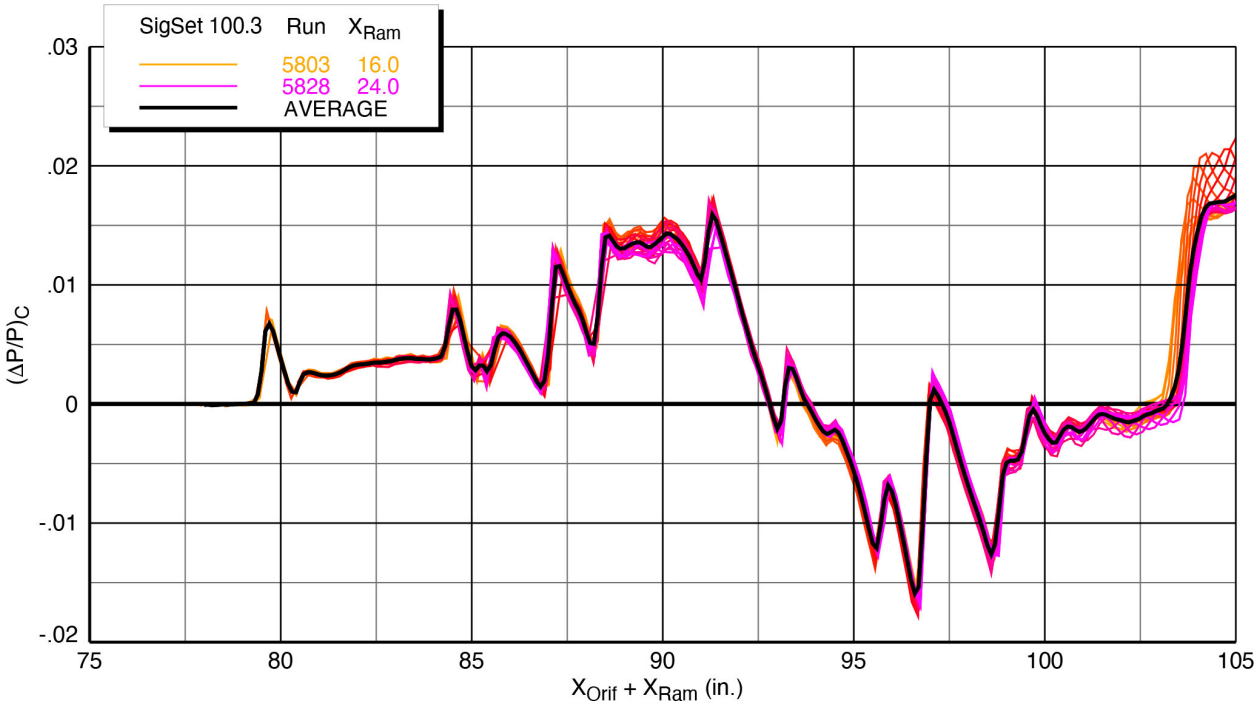

Figure 6-15 Aligned pressure signatures for last third of SigSet 100 in overlay plot X-59 model (blade strut), Mach 1.4, h/L = 1.2, α = 2.1°, ϕ_{m2r} = 0°

The averaged signatures by themselves for each third of the sweep are compared in Figure 6-16. Note the *SweepRng* parameter in the legend: this indicates the range of X_{Ram} positions over which the spatial average was computed for the signature. The range is identified as start.end of the extension length of the linear actuator ram, and the numbers are approximate as the ram positions for the runs acquired in the sweep may not have necessarily landed on the integer values of the ram extension.

The signature for the first third of the sweep (SigSet 100.1) deviates significantly from the other two signatures (SigSets 100.2 and 100.3) starting near the middle of the signature, whereas the other two agree very well except for some slight differences in shock strengths toward the rear.

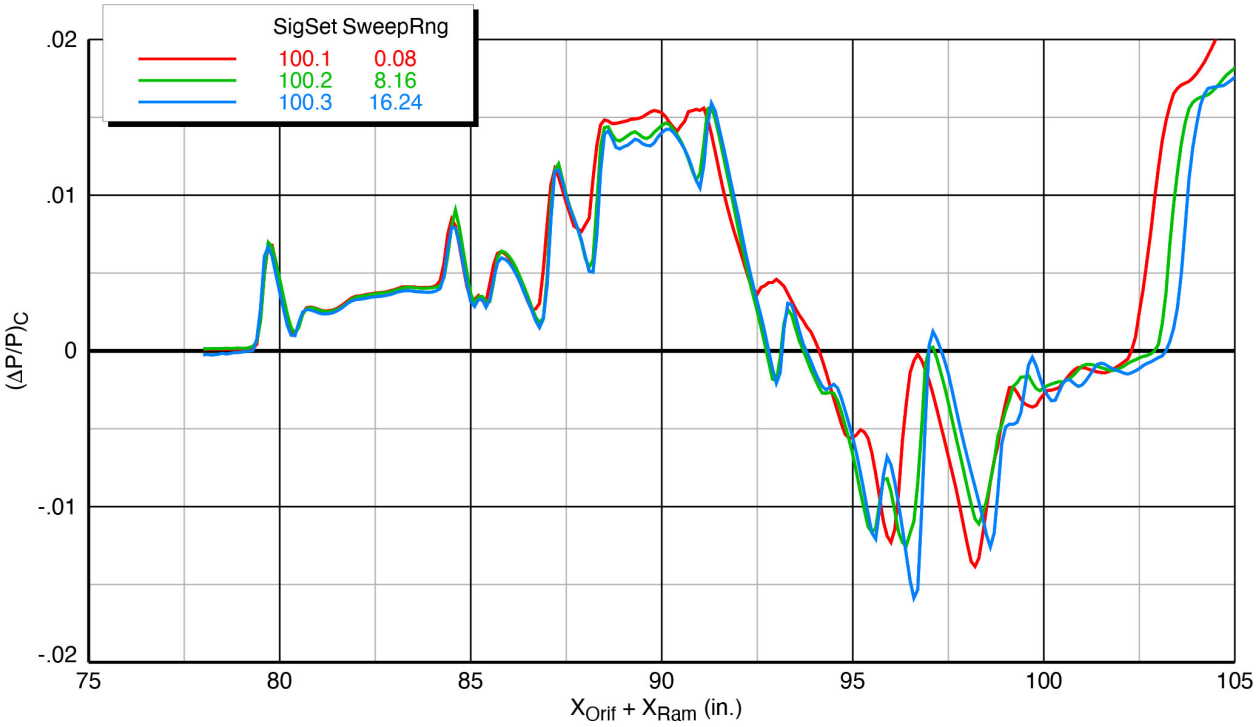

Figure 6-16 Average pressure signatures for each third of SigSet 100 X-59 model (blade strut), Mach 1.4, *h/L* = 1.2, α = 2.1°, ϕ_{m2r} = 0°

An evaluation of the last third of the SigSet 100 sweep is made in Figure 6-17(a) against four other SigSets which were taken at the same model and tunnel conditions, though three of those SigSets (23, 48, and 54) did not cover the full sweep range, but just from 4” to 12”. SigSet 10 covered the full sweep range as did #100, but it had a larger sweep increment (*SweepInc* in the legend)—0.96” vs. 0.32”.

The plot shows that SigSets 10.3 and 100.3 agree well with each other, but not with the other three SigSets having the reduced sweep range. Recomputing the averages for these two SigSets over the 4”-to-12” sweep range (now denoted as 10.9 and 100.9; the .9 just being an index for record-keeping purposes) of the others brings all the curves into agreement as shown in Figure 6-17(b). This, as well as the comparison shown in Figure 6-16, indicates the sensitivity of the signatures to the sweep range, and the need for making repeat SigSet comparisons at the same sweep range.

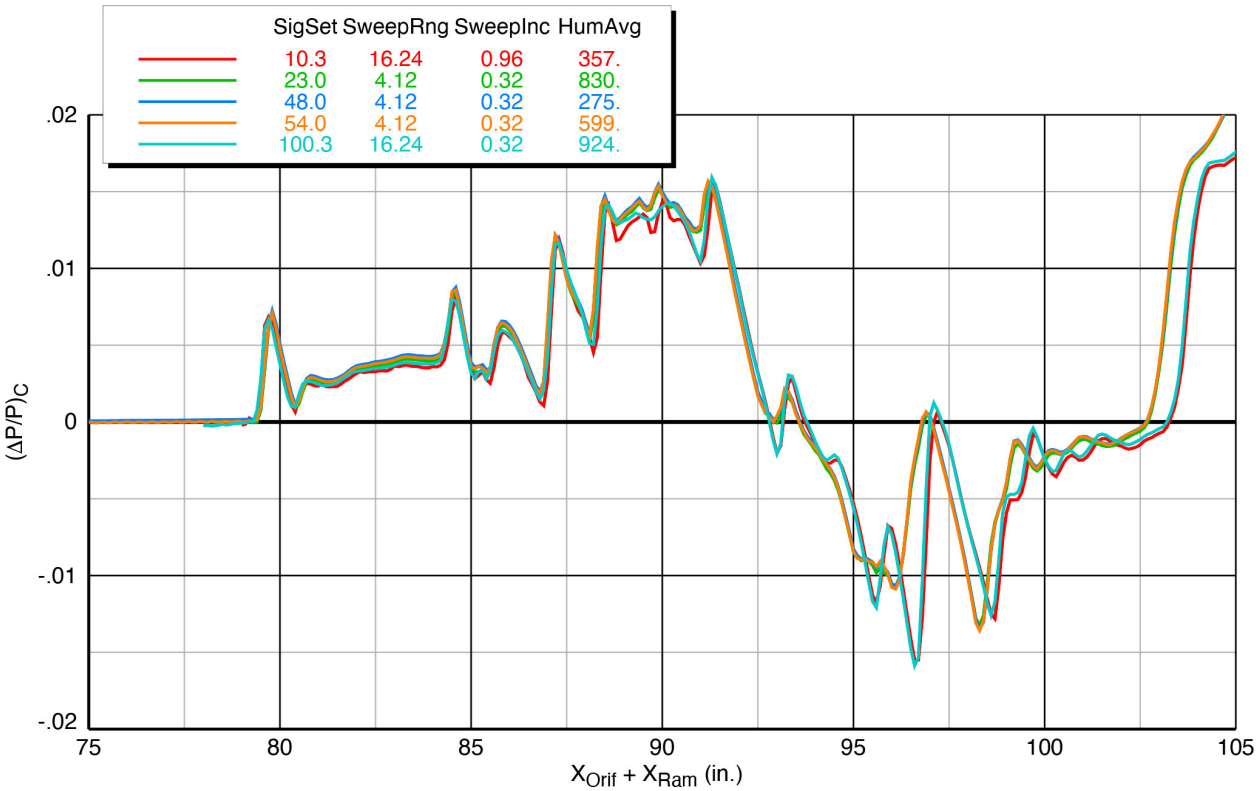

(a) Last-third sweep ranges (16” to 24”) for SigSets 10 and 100

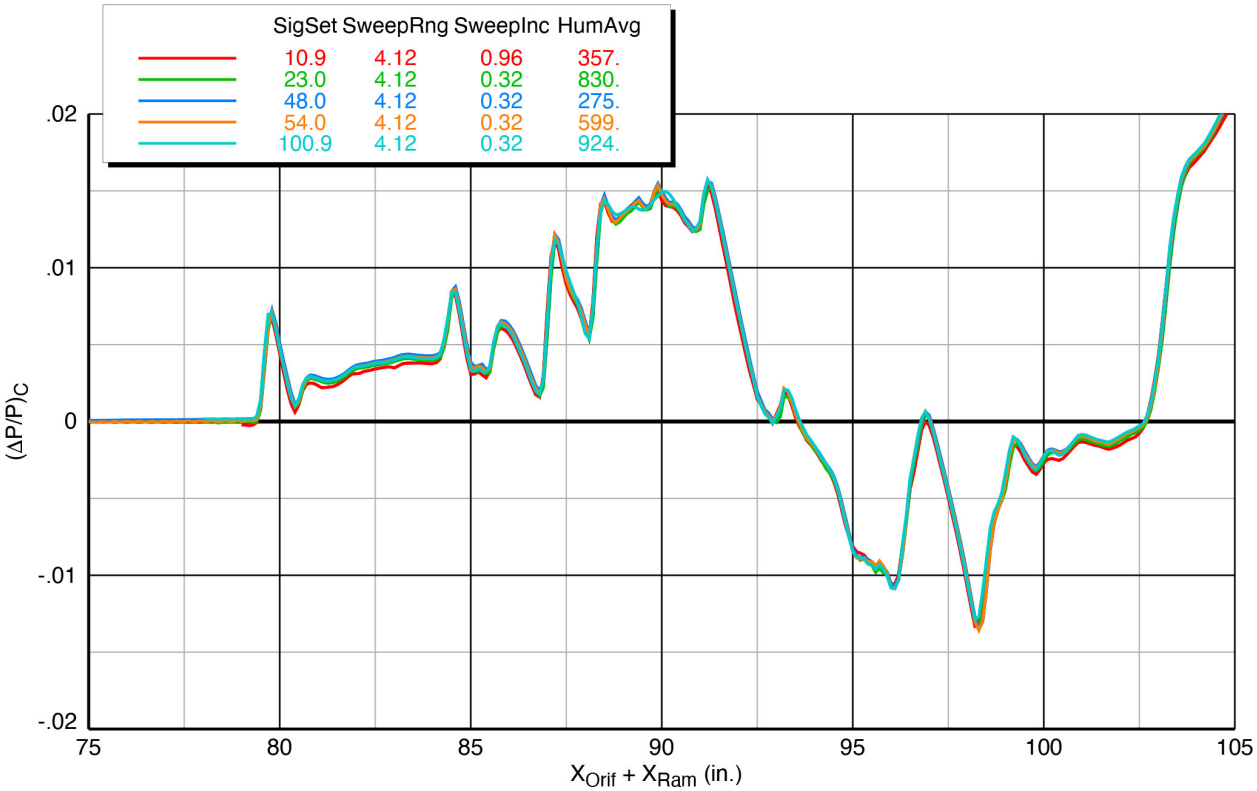

(b) Sweep ranges (4” to 12”) for SigSets 10 and 100 matching the others

Figure 6-17 Comparison of SigSet 100.3 with four repeat runs, X-59 model (blade strut) Mach 1.4, *h/L* = 1.2, α = 2.1°, ϕ_{m2r} = 0°

A similar set of plots is presented next for SigSet 99, which has the same conditions as SigSet 100 except that the model nose is 2 body lengths from the rail instead of 1.2 lengths. The layout diagram for the model in this position is provided in Figure 6-18. Note that even at the ram-retracted position, the rear of the model is forward of the rail shocks, so this should help minimize the interference from them, though the model shocks do still have to pass through the rail shocks to get to the orifices.

The aligned overlay and waterfall plots of Figure 6-19 show that for this model height (*h/L* = 2), the model pressures at the rail are weaker than those from the closer distance (*h/L* = 1.2, Figure 6-12), as expected—the highest average corrected pressure ratio is just over 0.010 at the 2-body-length distance, whereas it is close to 0.015 at the 1.2-body-length distance.

The plots of Figure 6-19 show that the signatures in the early runs in the sweep are shifted forward relative to the later runs, and the amount of the shifting is not uniform over the length of the signatures. The nose shock positions from the first to last runs are spread over an approximate distance of 0.5”, but the middle and aft portions of the signatures are spread by more than 1”. The reasons for this non-uniform shifting and elongation of the signatures as measured at the various ram positions over a 24” range are not well understood, but the mutual interference among the model and rail shocks can have unanticipated effects on the data.

The overlay plots for each third of SigSet 99 are shown in Figures 6-20 through 6-22. As indicated for SigSet 100, the scatter in the first third of the sweep is fairly large, and then reduced significantly in the middle third, but increased again in the last third—in contrast to the similar plot (Figure 6-15) for SigSet 100.

The averaged signatures by themselves for each third of the sweep are compared in Figure 6-23. As observed in Figure 6-19, there is a rearward shift with sweep range among the three average curves, but this shift is not consistent over the lengths of the signatures.

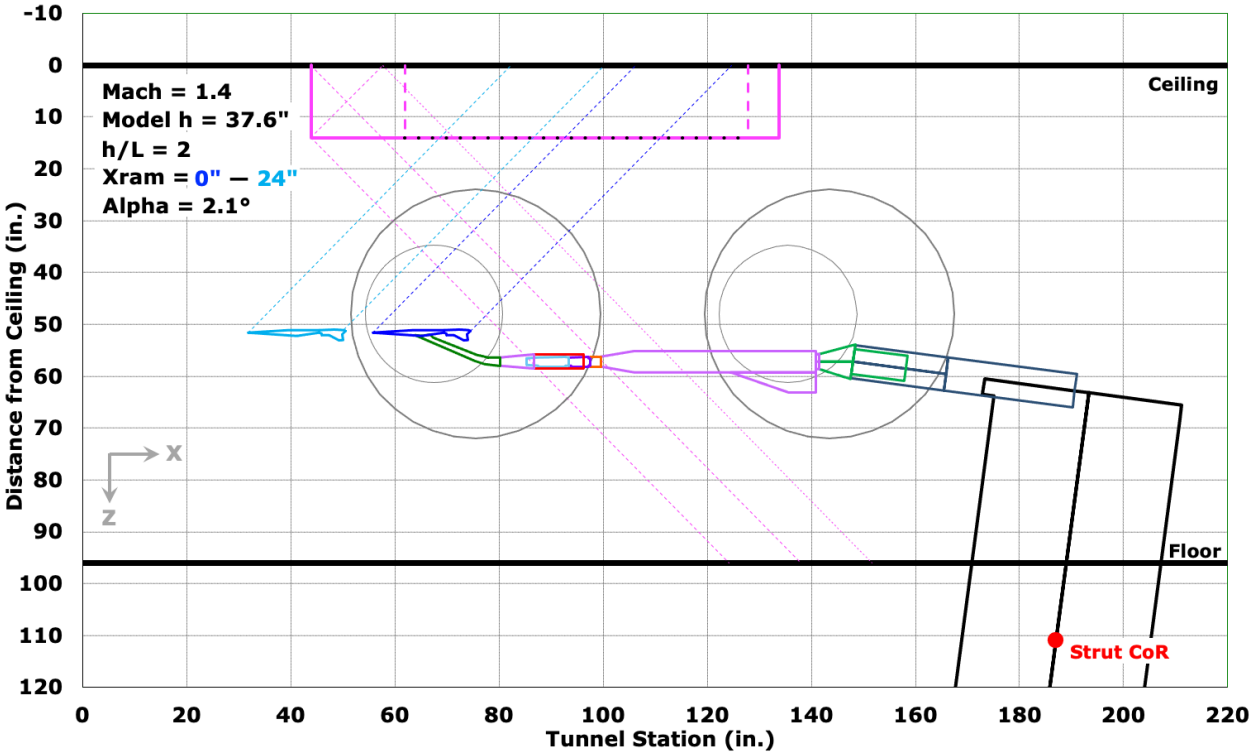

Figure 6-18 Layout diagram of X-59 model at *h/L* = 2 showing full 24” ram range in SigSet 99

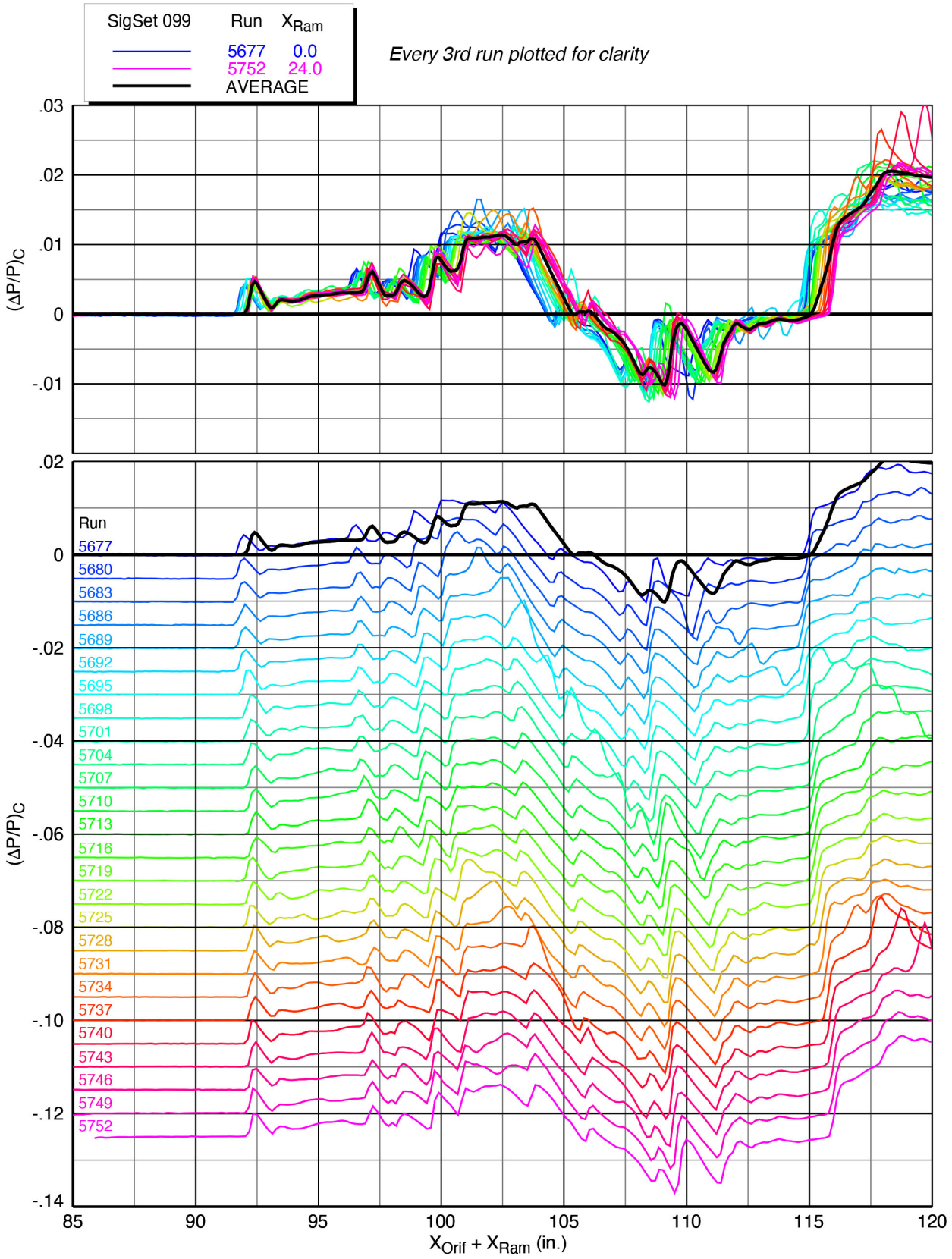

Figure 6-19 Aligned pressure signatures for SigSet 99 in overlay and waterfall plots X-59 model (blade strut), Mach 1.4, h/L = 2, α = 2.1°, ϕ_{m2r} = 0°

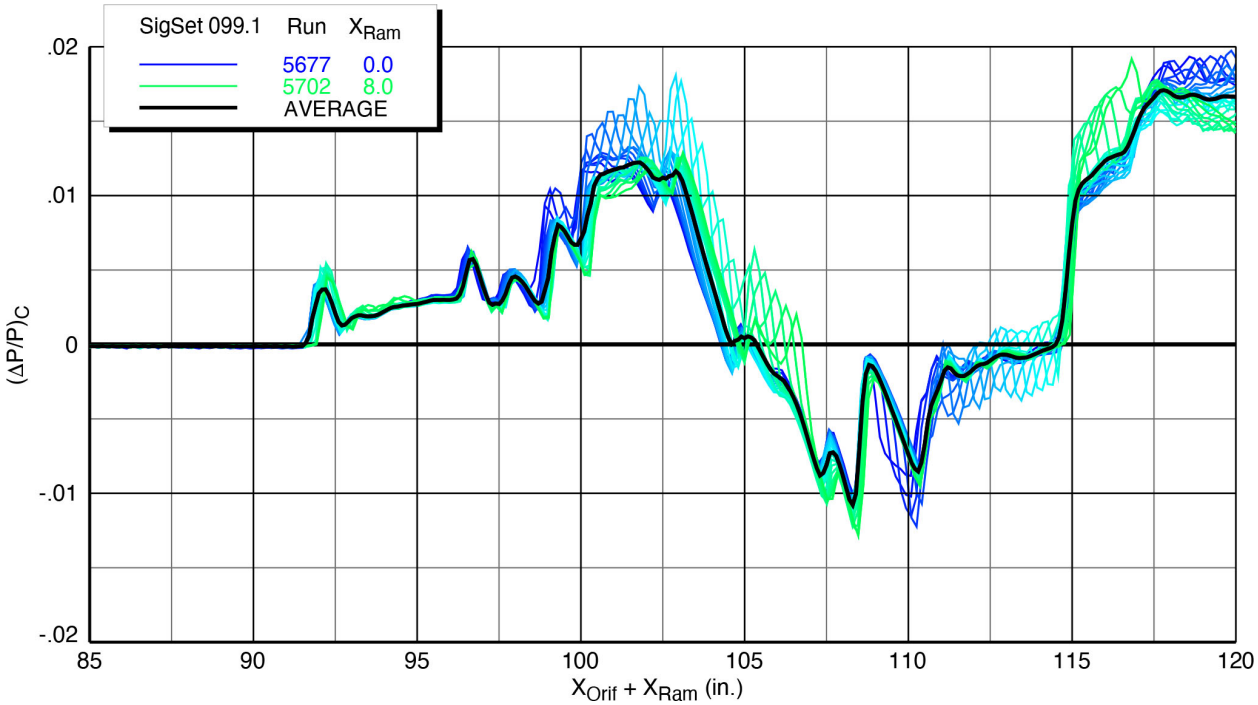

Figure 6-20 Aligned pressure signatures for first third of SigSet 99 in overlay plot X-59 model (blade strut), Mach 1.4, h/L = 2, α = 2.1°, ϕ_{m2r} = 0°

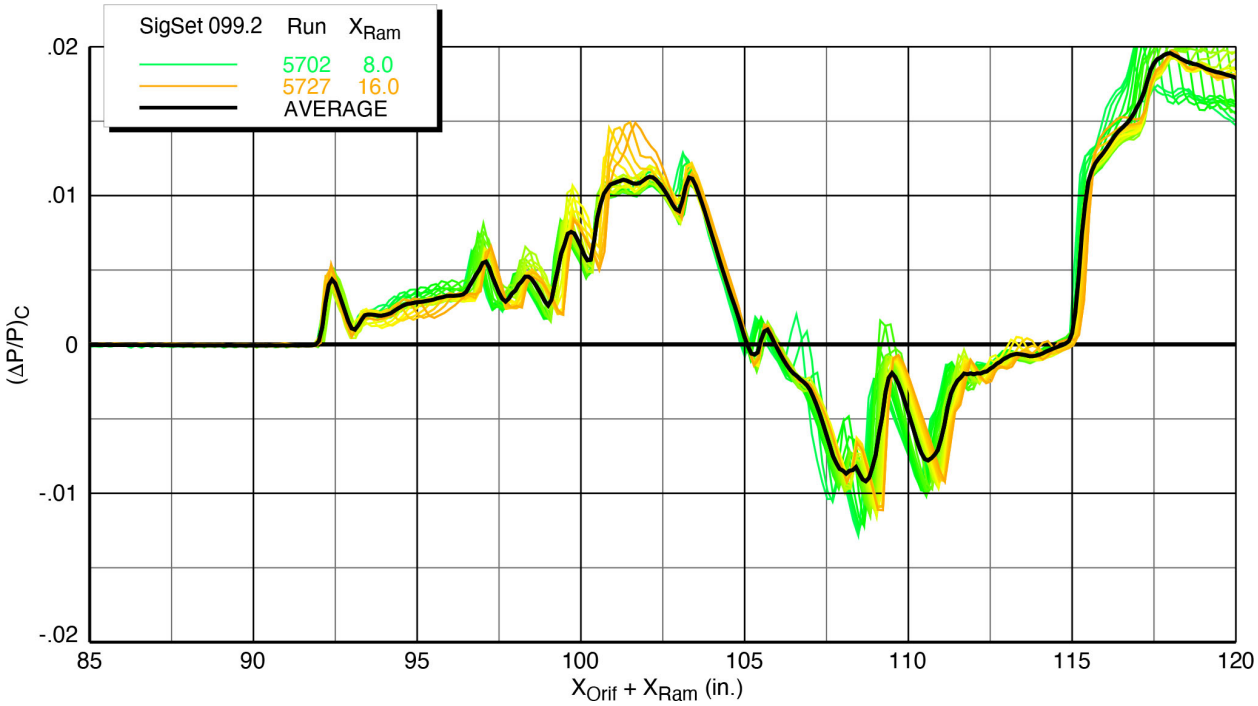

Figure 6-21 Aligned pressure signatures for second third of SigSet 99 in overlay plot X-59 model (blade strut), Mach 1.4, h/L = 2, α = 2.1°, ϕ_{m2r} = 0°

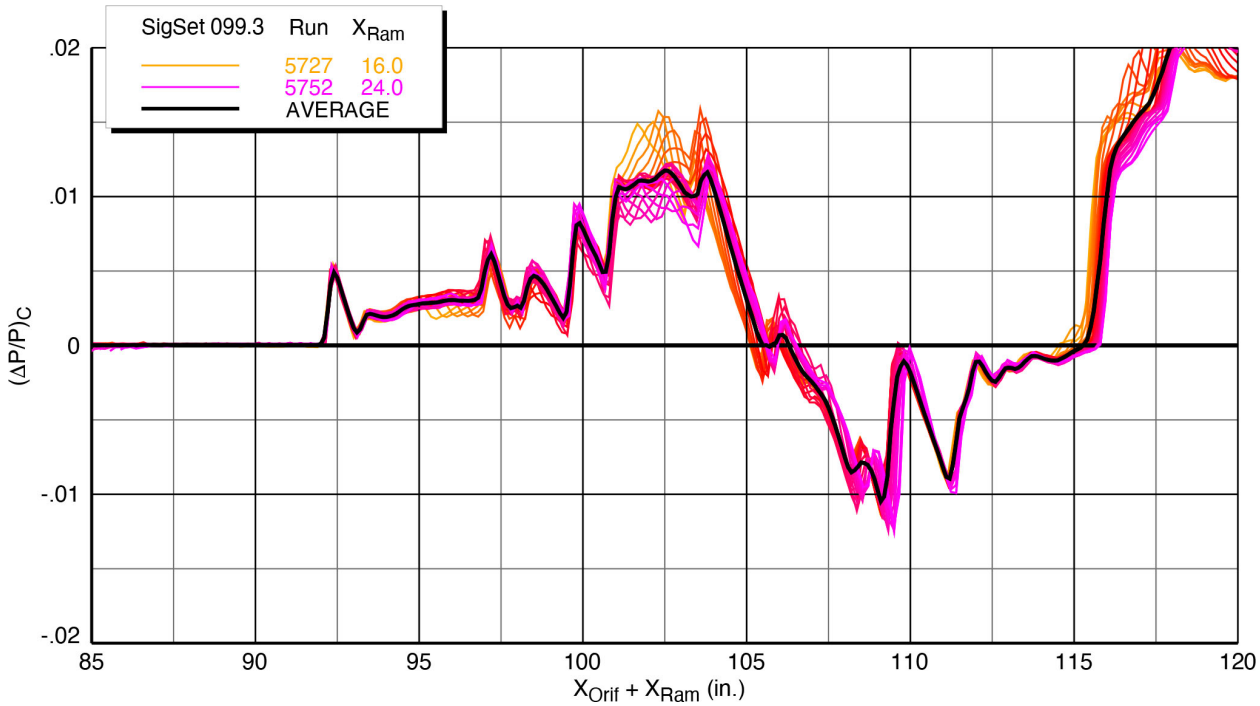

Figure 6-22 Aligned pressure signatures for last third of SigSet 99 in overlay plot X-59 model (blade strut), Mach 1.4, *h/L* = 2, α = 2.1°, ϕ_{m2r} = 0°

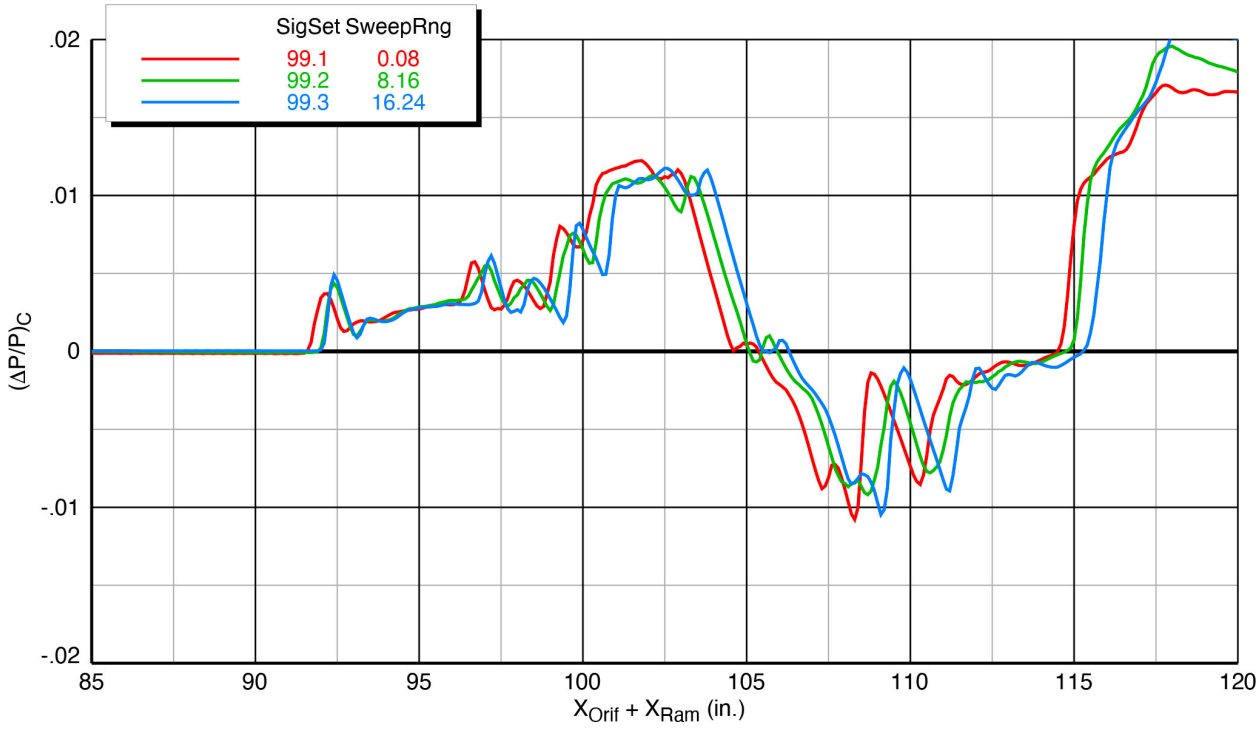

Figure 6-23 Average pressure signatures for each third of SigSet 99 X-59 model (blade strut), Mach 1.4, *h/L* = 2, α = 2.1°, ϕ_{m2r} = 0°

One more example of the rearward signature shift at the further-aft sweep ranges is shown in Figure 6-24, where the two signatures at the same X_{Ram} sweep range (8” to 16”) repeat very well, but the one from 16” to 24” is shifted aft starting at the location of the second shock wave. It is surmised that the sweeps that position the shocks further forward on the rail are generally better because of possible less interference of the rail shocks on the model.

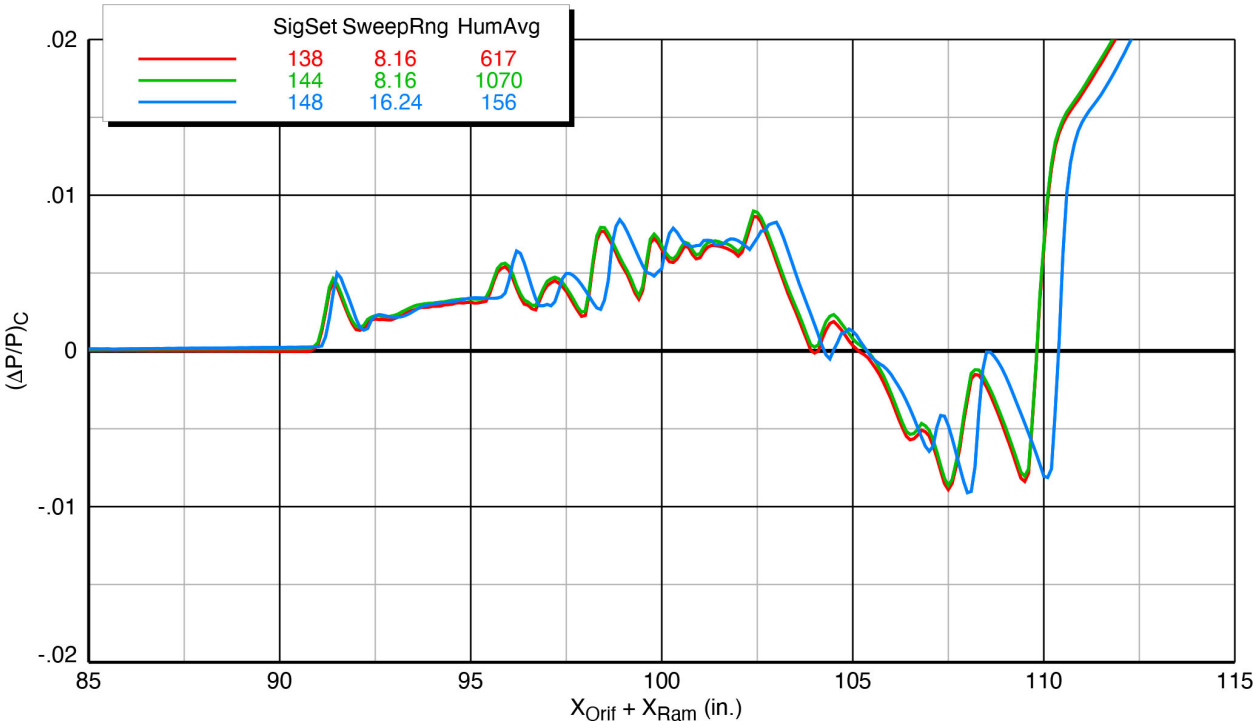

Figure 6-24 Rearward shift of X-59 model (sting) signatures with aft X_{Ram} sweep range Mach 1.36, h/L = 2, α = 2.1°, ϕ_{m2r} = 0°

Plots in the next two sections, Effects of Humidity and Repeatability, will have some overlap with this current section on Signature Quality with Ram Position in that differences among signatures having different X_{Ram} sweep ranges will be apparent as the effects of humidity and repeatability are attempted to be shown.

6.5. Effects of Humidity

In many recent NASA sonic boom wind tunnel tests, it was believed that humidity had to be kept to very low levels (< 300 ppm by weight, in some cases) to not have a detrimental effect on the pressure data. This belief arose from seeing gaps among pressure signatures acquired at different humidity levels, but the gaps could also have been caused by subtle changes in the tunnel flow, or ESP reference pressures or calibrations which were not investigated at the time.

The Glenn 8x6-ft supersonic wind tunnel has the means to limit the rate of humidity increase during a running shift, but it does not have the capability to control it and keep it at a low level. As discussed previously in Section 3.1, the tunnel uses large dryer beds in the tunnel circuit to remove some of the moisture from the air, but with the tunnel not being fully sealed from the outside air, the ambient humidity gets drawn into the tunnel and the desiccant beads in the dryer beds can only absorb so much moisture throughout a shift before they get saturated. If the humidity in the local area is high, then the tunnel humidity can sometimes exceed a prescribed maximum level before the end of a running shift, necessitating that operations be stopped prematurely. Thus, it was important for this test to understand whether humidity would have a significant impact on the data, and if so, what maximum level of humidity would be allowed for taking data. The purpose of this section is therefore to present data showing the effects of humidity on the pressure signature measurements, as to whether there is any measurable effect or not.

Selected plots of averaged signatures for the X-59 model with the blade strut and sting mounts at various humidity levels are presented in the following figures:

• Figure 6-25	Blade strut	Mach 1.36	h/L = 1.2	α = 2.1°	
• Figure 6-26	Blade strut	Mach 1.4	h/L = 3	α = 2.1°	
• Figure 6-27	Blade strut	Mach 1.4	h/L = 1.2	α = 2.1°	ϕ_{m2r} varying
• Figure 6-28	Blade strut	Mach 1.4	h/L = 2	α = 2.1°	*stab* = 3.92°
• Figure 6-29	Blade strut	Mach 1.47	h/L = 2	α = 1.8°	
• Figure 6-30	Sting	Mach 1.36	h/L = 2	α = 2.1°	
• Figure 6-31	Sting	Mach 1.4	h/L = 3	α = 2.1°	

Starting with this section, the X locations on the data plots will be normalized by the model length (18.80”) and denoted as $(X_{Orif} + X_{Ram})/L$, so that the signature length relative to that of the model can be easily observed. The rear of the model in the signatures is just prior to the large increases in pressure caused by the shocks from the transition sections on the blade strut and sting.

The plots in Figures 6-25 and 6-26 include *SweepInc* in the legends because they include the early signature sets in the test during which X sweeps were conducted with greater X_{Ram} spacing—0.48” and 0.96”, corresponding roughly to 3- and 6-orifice spacing on the rail, respectively. It was decided after SigSet 13 to run the rest of the sweeps in the test with 0.32” X_{Ram} spacing, equivalent to approximately 2 orifices.

Figure 6-25(a) shows that the signature for SigSet 13 differs significantly in the middle and aft portions from the other two signatures, and that it has a humidity level of 1120 ppm, while the others have humidity on the order of 600 or less. One might think that excessive humidity might be a contributor to the different pressure levels, but the plot legend indicates that the average curve for SigSet 13 was computed over an X_{Ram} range from 0” to 12” (which was the total range acquired for the runs in this SigSet). The average was recomputed to match the X_{Ram} range the other two curves (4” to 12”), and the plot in Figure 6-25(b) shows that SigSet 13.9 now falls on

top of the other two curves. This indicates that there are no effects of humidity in this case wherein the range of humidity in the plot is more than 1,000 ppm.

Figure 6-26 contains four signatures with two of them (SigSets 12.1 and 25) at high humidity (~900 ppm) and two (SigSets 26 and 113.1) at low humidity (~100 ppm). In subfigure (a), SigSet 12.1 with high humidity is very close to SigSet 113.1 with low humidity, and the same is true for the other pair of signatures. Note that 12.1 and 113.1 are averaged over a sweep range from 0” to 8” while the others are averaged over 16” to 24”, and the two pairs of signatures (12.1 and 113.1, 25 and 26) do not match. As the sweep ranges for SigSets 12 and 113 are moved forward on the rail in subfigures (b) and (c), SigSet 113.3 comes very close to matching 25 and 26 in (c), but 12.3 is the one that is most different. The reason for this difference is unknown, but it is apparent that there don’t seem to be any trends of humidity influence on the signatures.

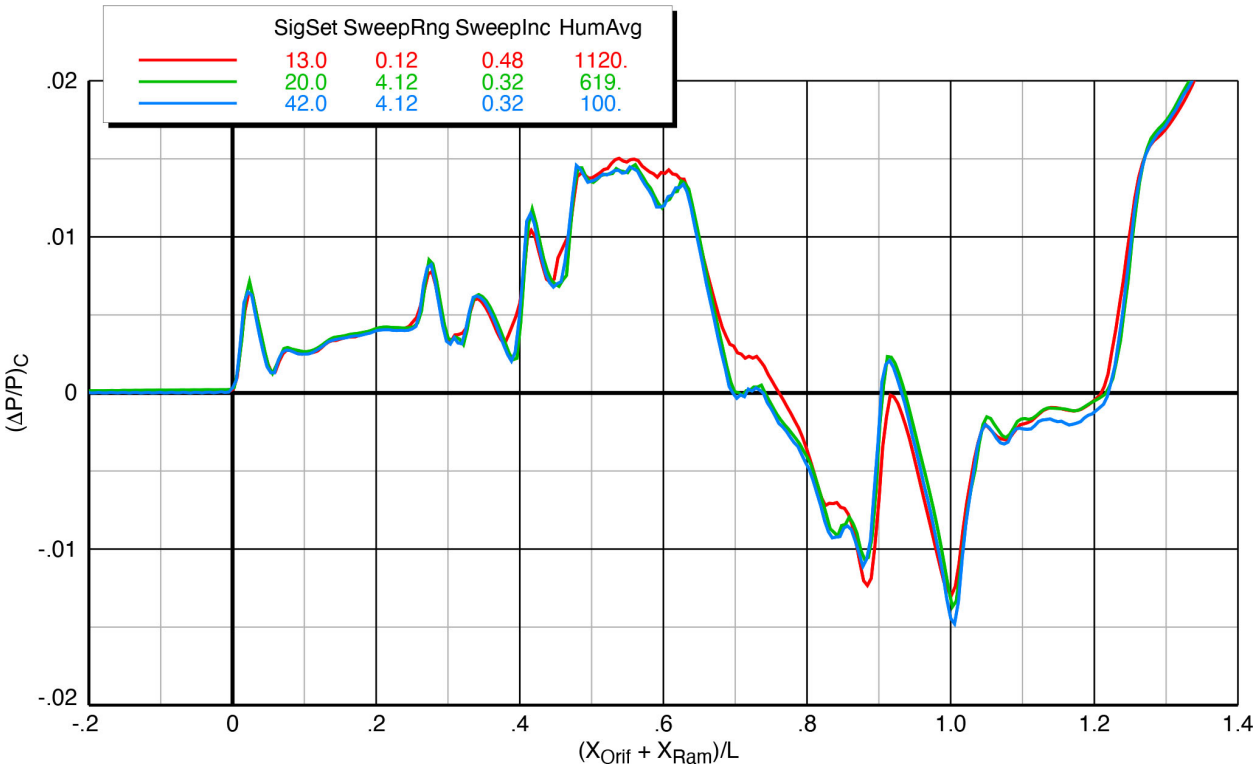

(a) SigSet 13 averaged over X_{Ram} = 0" to 12", others over 4" to 12"

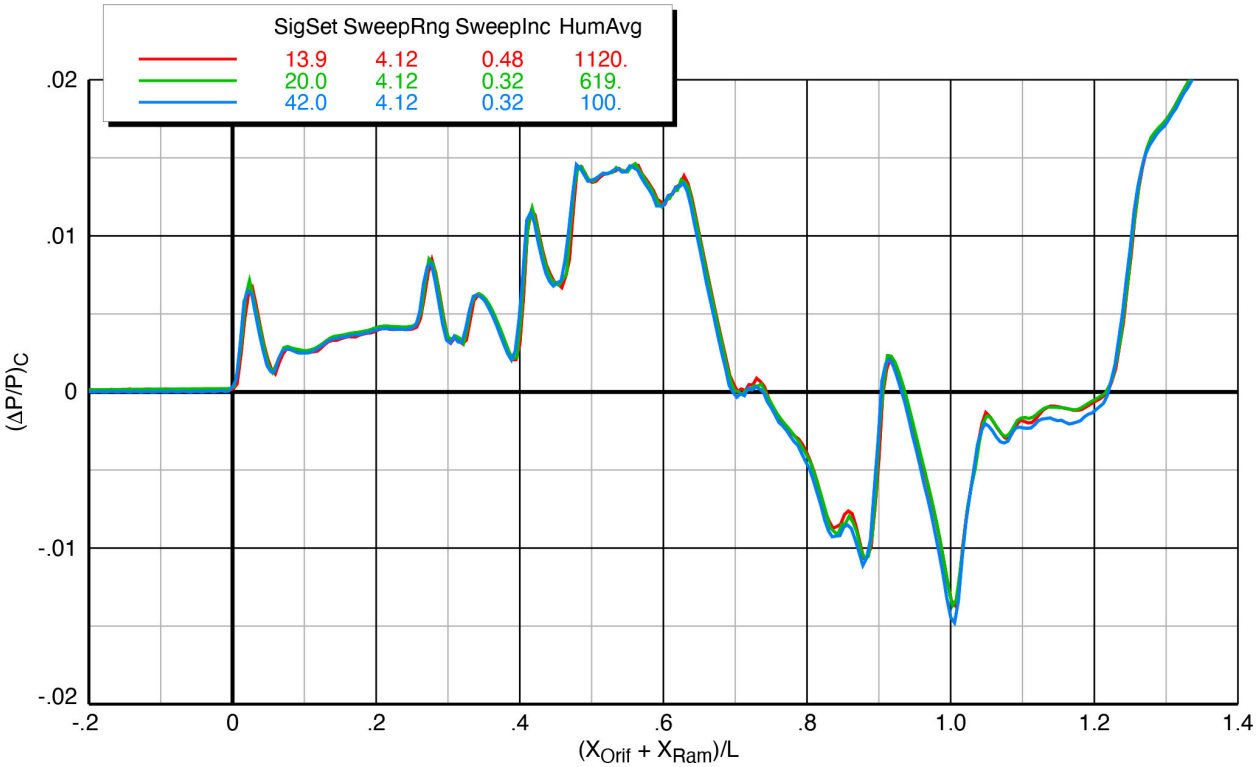

(b) All SigSets averaged over 4" to 12"

Figure 6-25 Effects of humidity and sweep range on X-59 model (blade strut) spatially-averaged pressure signatures, Mach 1.36, h/L = 1.2, α = 2.1°, ϕ_{m2r} = 0°

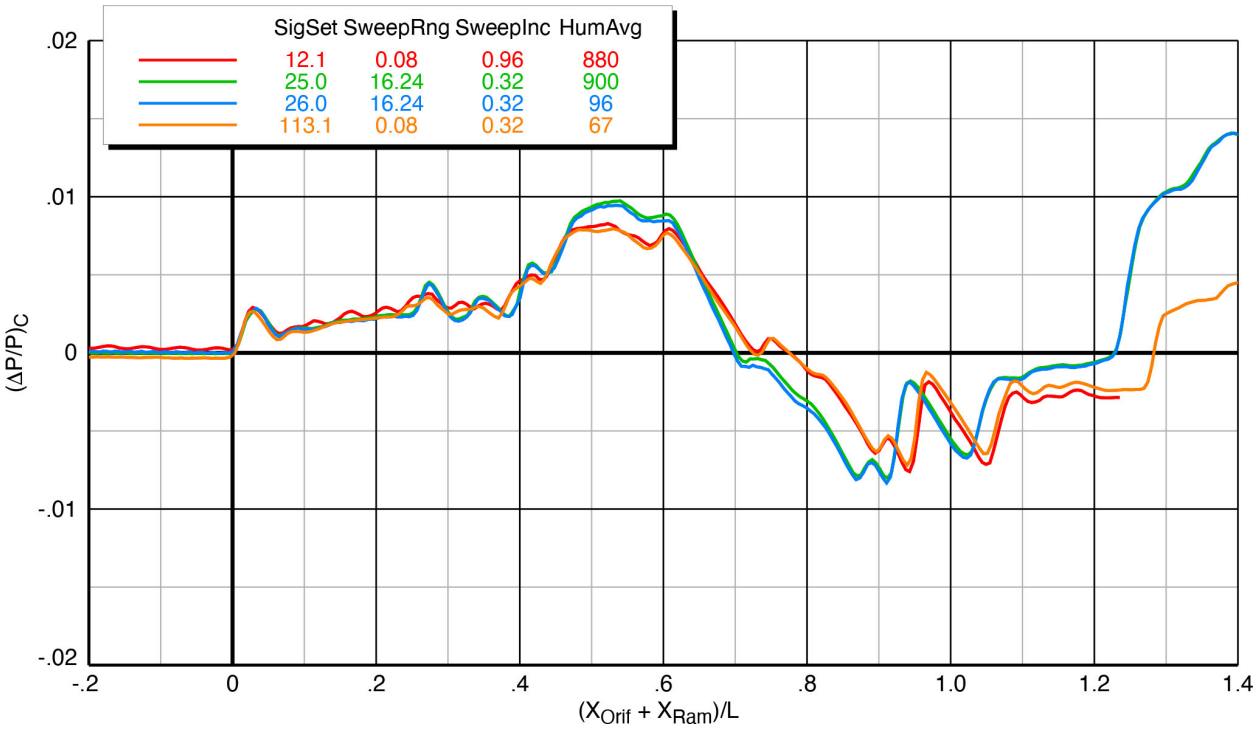

(a) SigSets 12 and 113 averaged over X_{Ram} = 0” to 8”, others over 16” to 24”

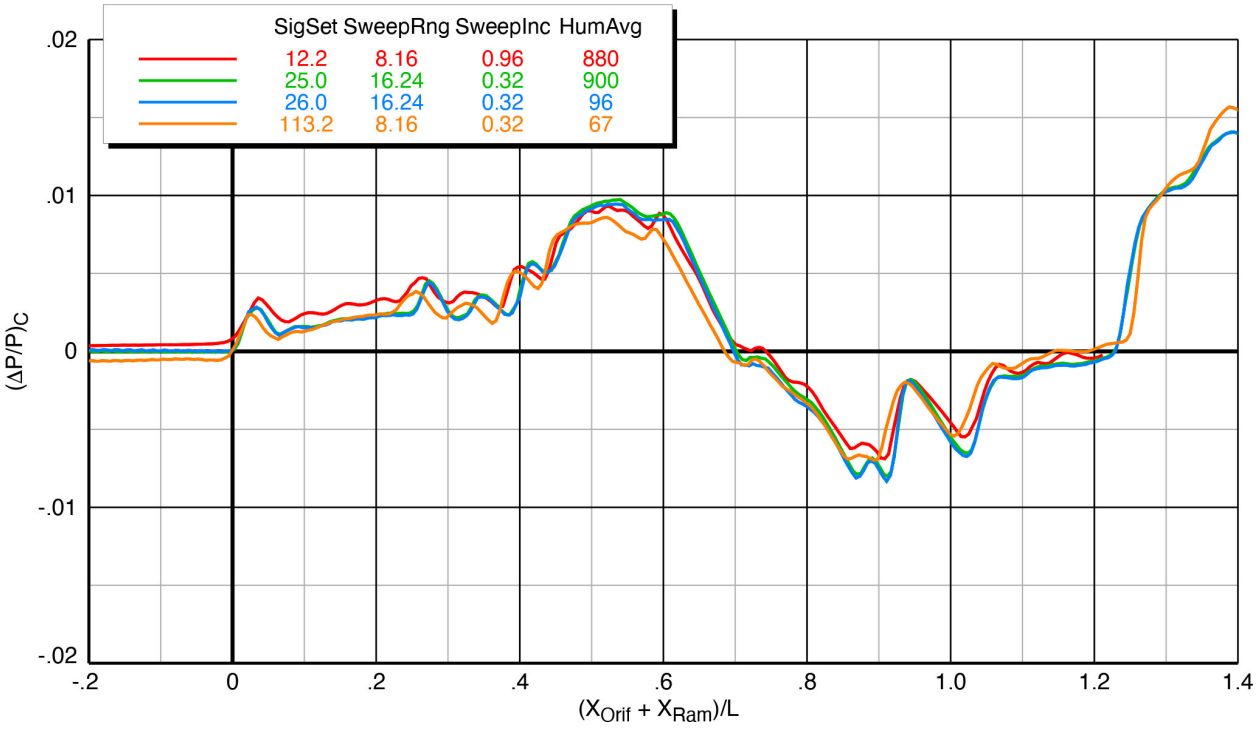

(b) SigSet 13 average computed over X_{Ram} = 8” to 16”, others over 16” to 24”

Figure 6-25 Effects of humidity and sweep range on X-59 (blade strut) spatially-averaged pressure signatures, Mach 1.4, h/L = 3, α = 2.1°, ϕ_{m2r} = 0° (continued)

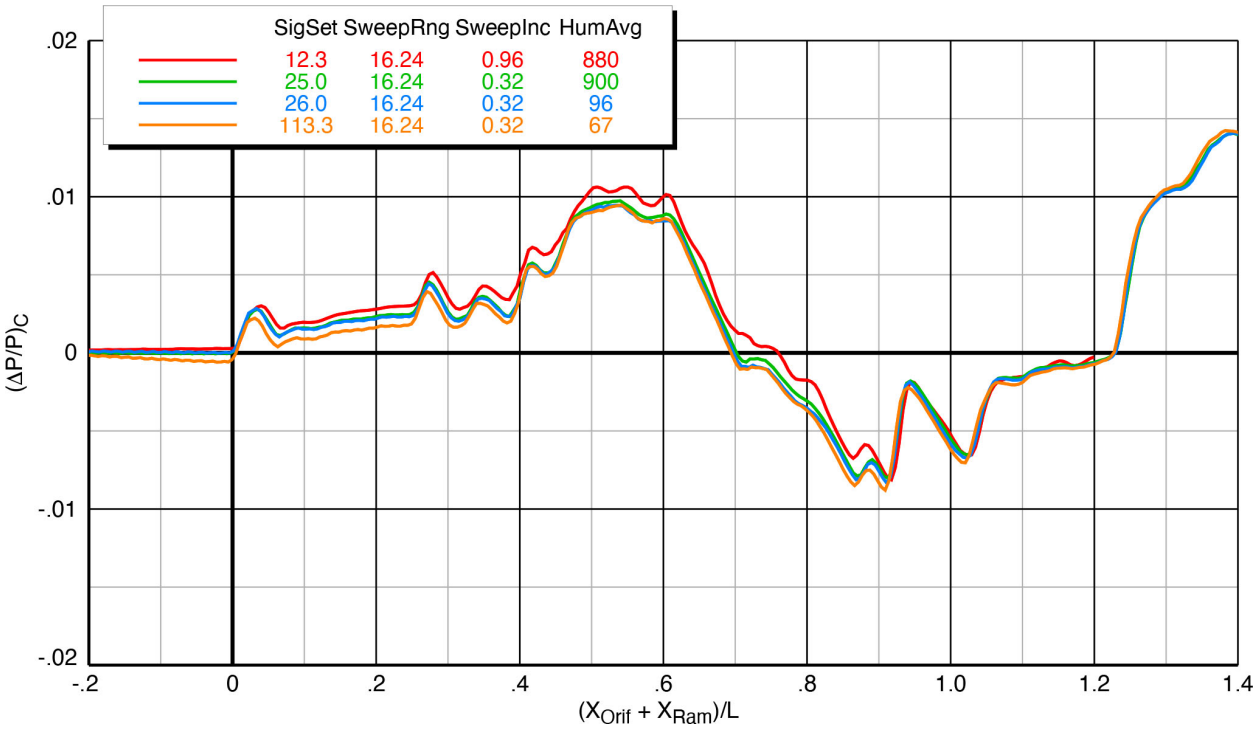

(c) All SigSets averaged over X_{Ram} = 16" to 24"

Figure 6-26 Effects of humidity and sweep range on X-59 (blade strut) spatially-averaged pressure signatures, Mach 1.4, *h/L* = 3, α = 2.1°, ϕ_{m2r} = 0° (concluded)

Two signatures (101 and 102) with humidity levels greater than 1,100 ppm are plotted in Figure 6-27(a) with the immediately prior and following signatures (100 and 103) which have lower humidity levels. (The very low humidity level of 174 ppm for SigSet 103 was a result of it being run at the start of the next shift when the tunnel air was very dry. And note that the model-to-rail roll angle is not the same for the four signatures on this plot, but the following discussion about the possible effects of humidity should still be valid.) It could be surmised regarding subfigure (a) that the gap between the with high- and low-humidity signatures could be caused by the humidity differences, but it turned out that the choice of reference run for SigSets 101 and 102 accounted for the gap, as shown by the gap having closed up in subfigure (b). When these two signatures were corrected with reference run 5881 (taken immediately after SigSet 102), the forward parts of them lowered to the pressure levels of SigSets 100 and 103, indicating that humidity differences were not the cause of the gap in the upper plot. Also note that SigSet 103 has a different sweep range that the others—it is surprising that it matches the others so well in light of the discussion above about sweep range having a significant effect on the data.

Regarding the roll angle differences among these four signatures, there are some differences among the curves in the rear halves of the signatures which are caused by the differences in roll angle. The fact that all four curves match very well in the front can probably be attributed to the long nose on the model which would not create many pressure differences when rolled.

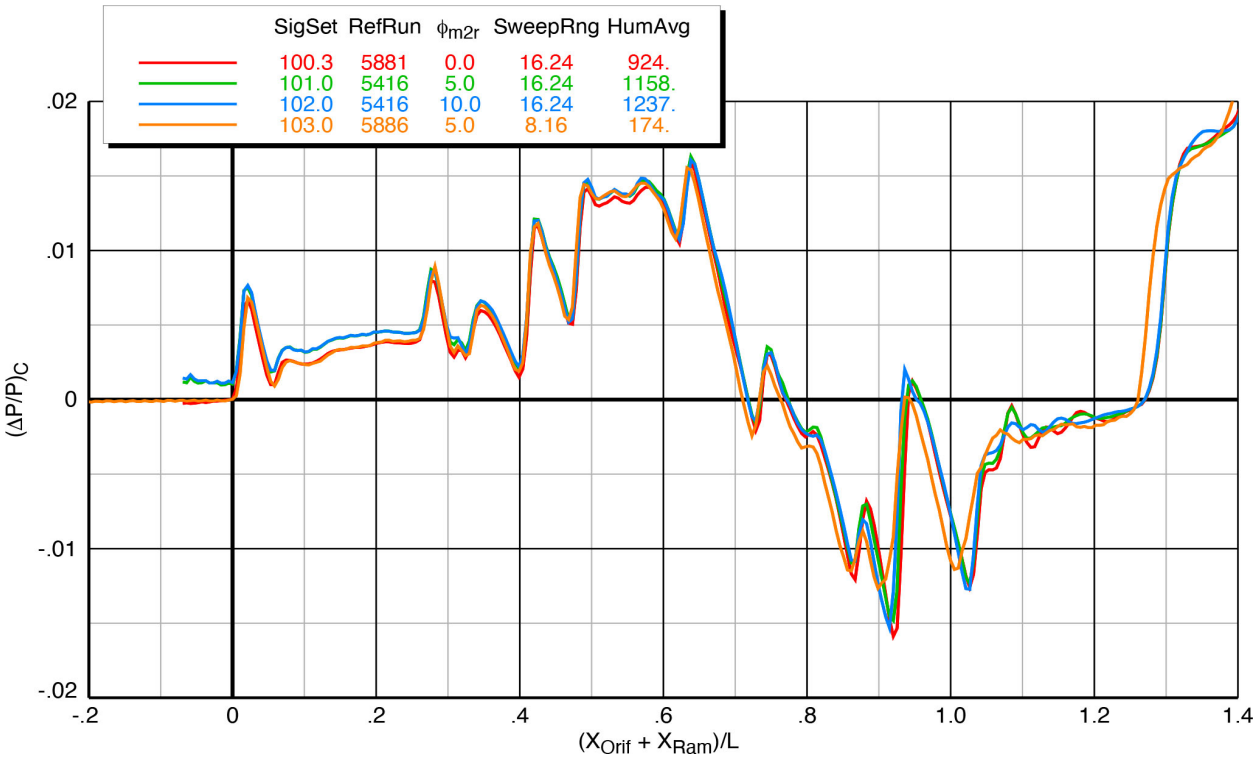

(a) Prior reference run 5416 used for correction of SigSets 101 and 102

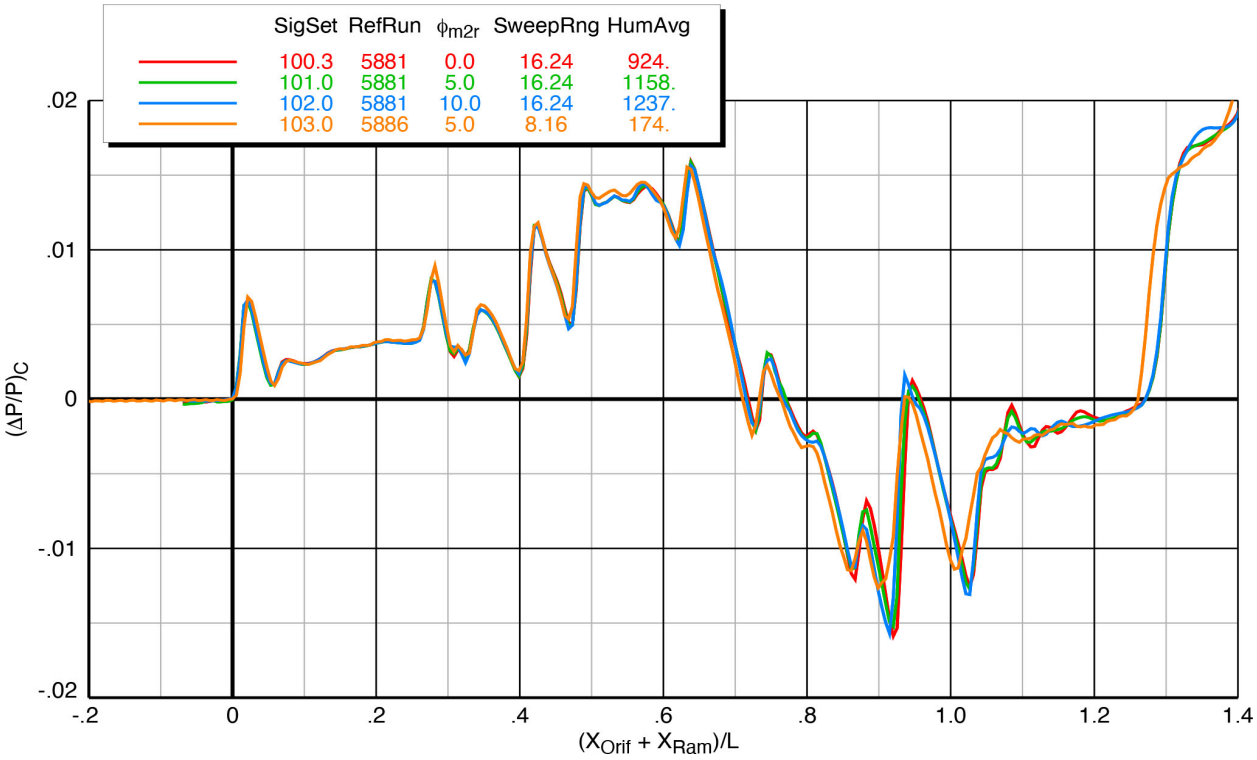

(b) Following reference run 5881 used for correction of SigSets 101 and 102

Figure 6-27 Effects of humidity and reference run on X-59 (blade strut) spatially-averaged pressure signatures, Mach 1.4, *h/L* = 1.2, α = 2.1°, ϕ_{m2r} varying

Additional plots in Figures 6-28 through 6-31 provide comparisons of repeat signatures at widely-varying humidity levels, in which the lowest humidity level is 185 ppm and the highest is 1525 ppm, but the greatest difference between any two of the curves on one plot is 579 ppm. If there is a significant effect of humidity on the pressure data, then it seems that this difference should be sufficient to show the effects. However, the pairs of signatures in all four of these figures exhibit excellent repeatability, and aside from a few minor differences between curves on a plot, there is no discernable trend of humidity affecting the pressures. On this basis of this result, therefore, the test crew did not see a need to curtail test operations due to rising humidity levels as long as they were below approximately 1500 ppm. Above this level, moisture in the tunnel air became visible in the form of fog, creating a safety issue with not being able to clearly see the model in the camera views. In this case, the tunnel had to be shut down for the day and the dryer beds had to be reactivated during a following shift before the test could resume.

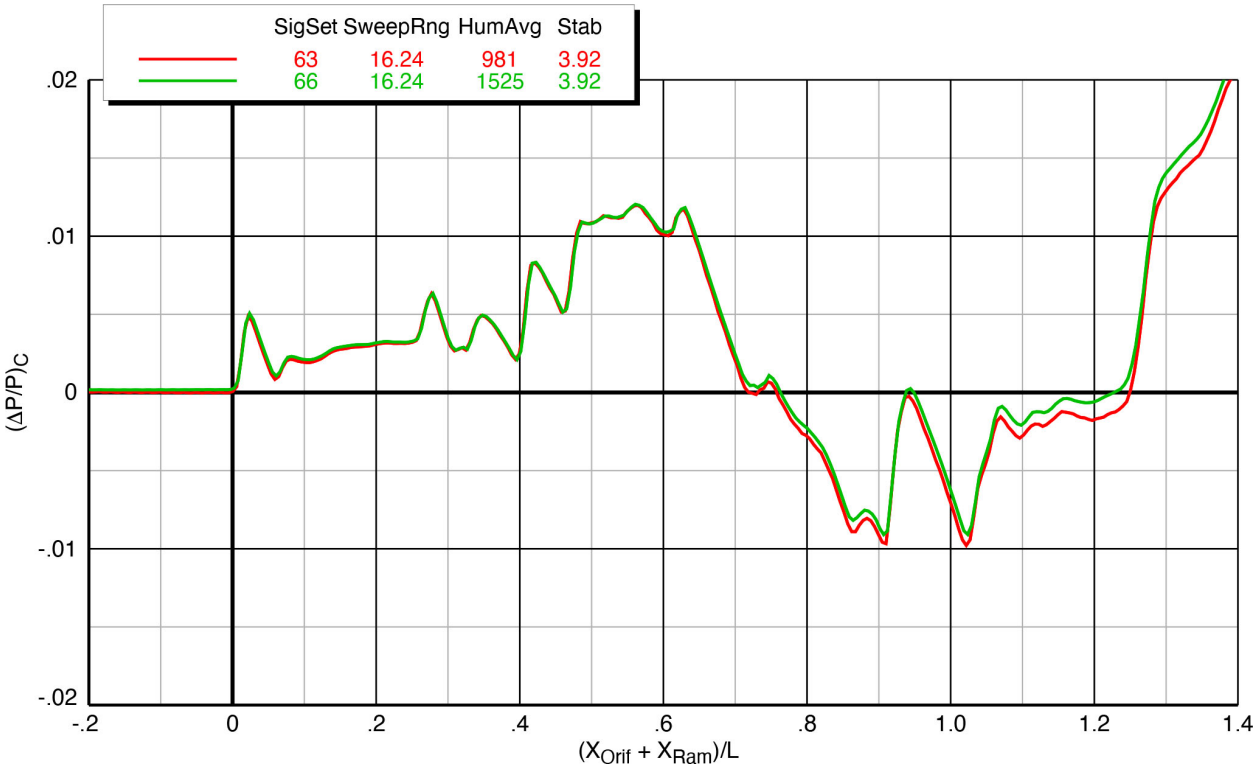

Figure 6-28 Effect of humidity on X-59 model (blade strut) spatially-averaged pressure signatures, Mach 1.4, *h/L* = 2, α = 2.1°, ϕ_{m2r} = 0°, stabilators 3.92°

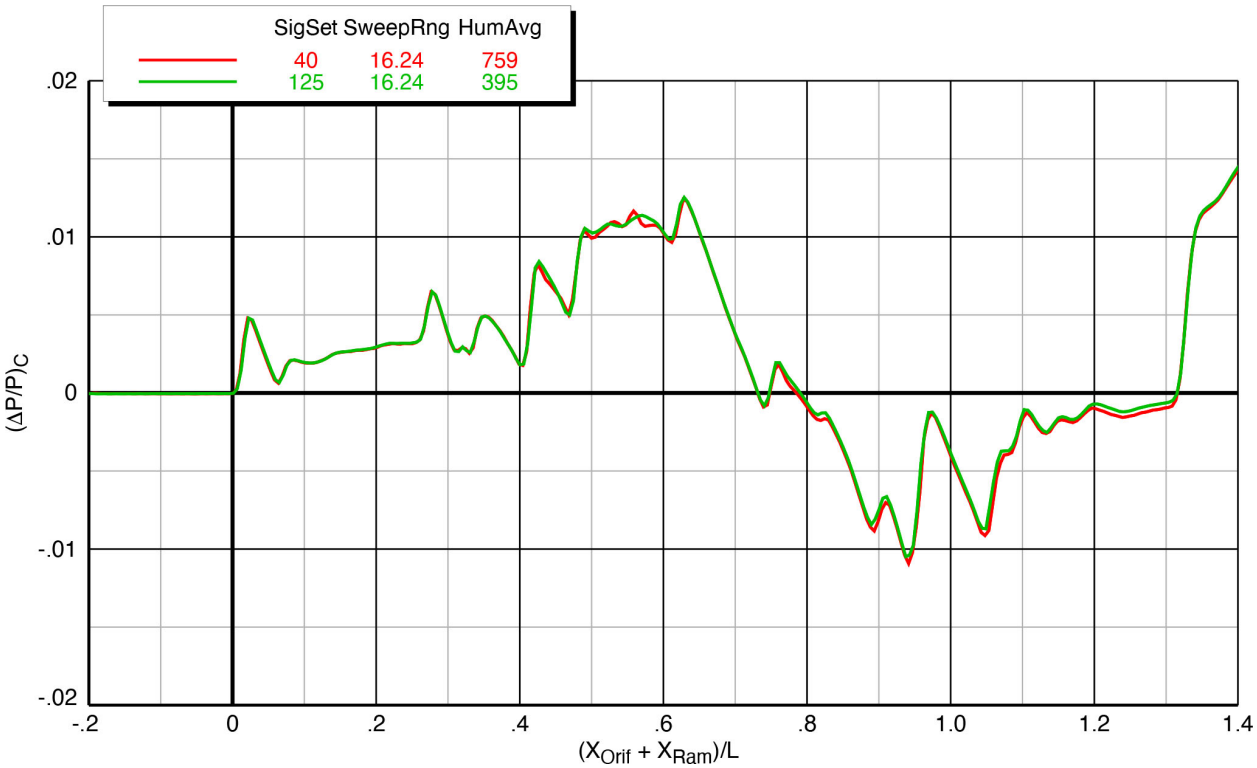

Figure 6-29 Effect of humidity on X-59 model (blade strut) spatially-averaged pressure signatures, Mach 1.47, *h/L* = 2, α = 1.8°, ϕ = 0°

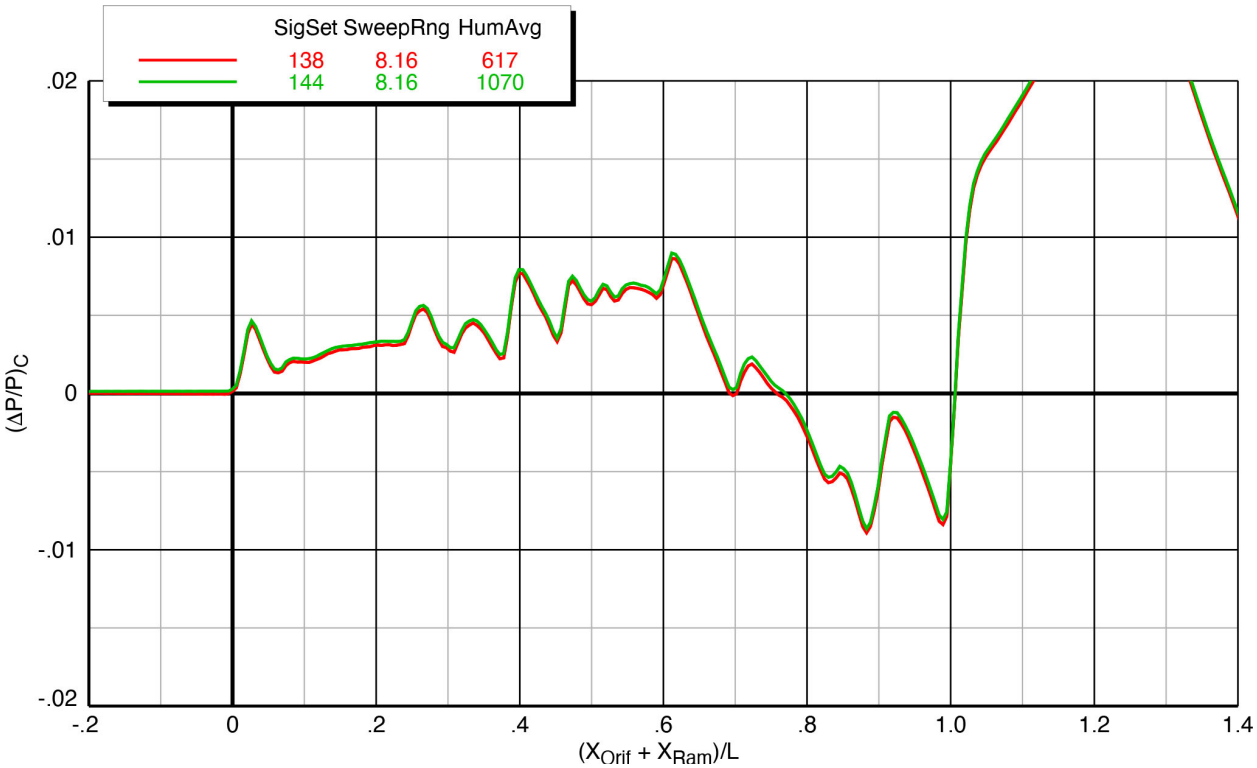

Figure 6-30 Effect of humidity on X-59 model (sting) spatially-averaged pressure signatures, Mach 1.36, *h/L* = 2, α = 2.1°, ϕ = 0°

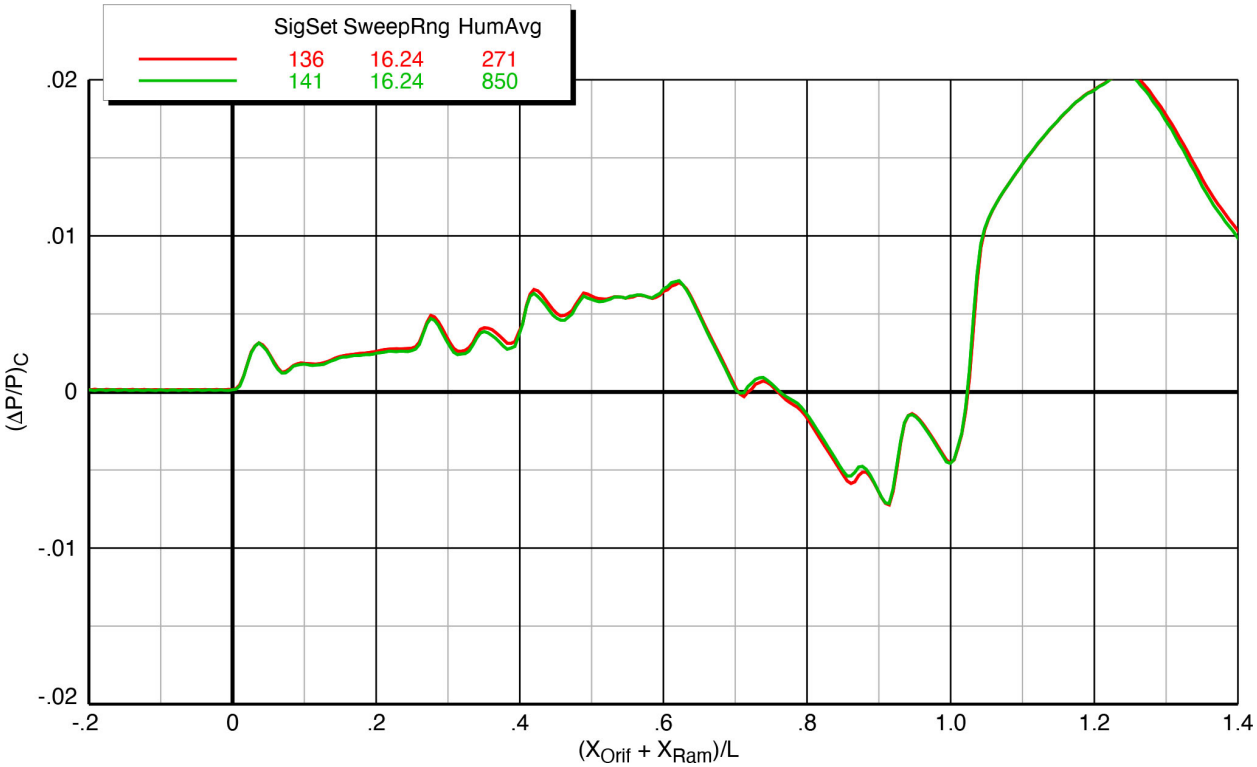

Figure 6-31 Effect of humidity on X-59 model (sting) spatially-averaged pressure signatures, Mach 1.4, *h/L* = 3, α = 2.1°, ϕ = 0°

The average humidity levels (*HumAvg*) for the SigSets plotted in the remainder of this report will continue to be included in the legends to give the reader further information about the humidity effects. The X_{Ram} sweep ranges (*SweepRng*) will be left in the legends as well so that one can see whether the measurements for the curves on a plot were taken on the same portion of the rail.

Data from the moisture monitors in the 8x6 tunnel reported the moisture levels in both dew point and humidity in parts per million by weight. The variation of these two parameters for each of the three test Mach numbers is plotted in Figure 6-32.

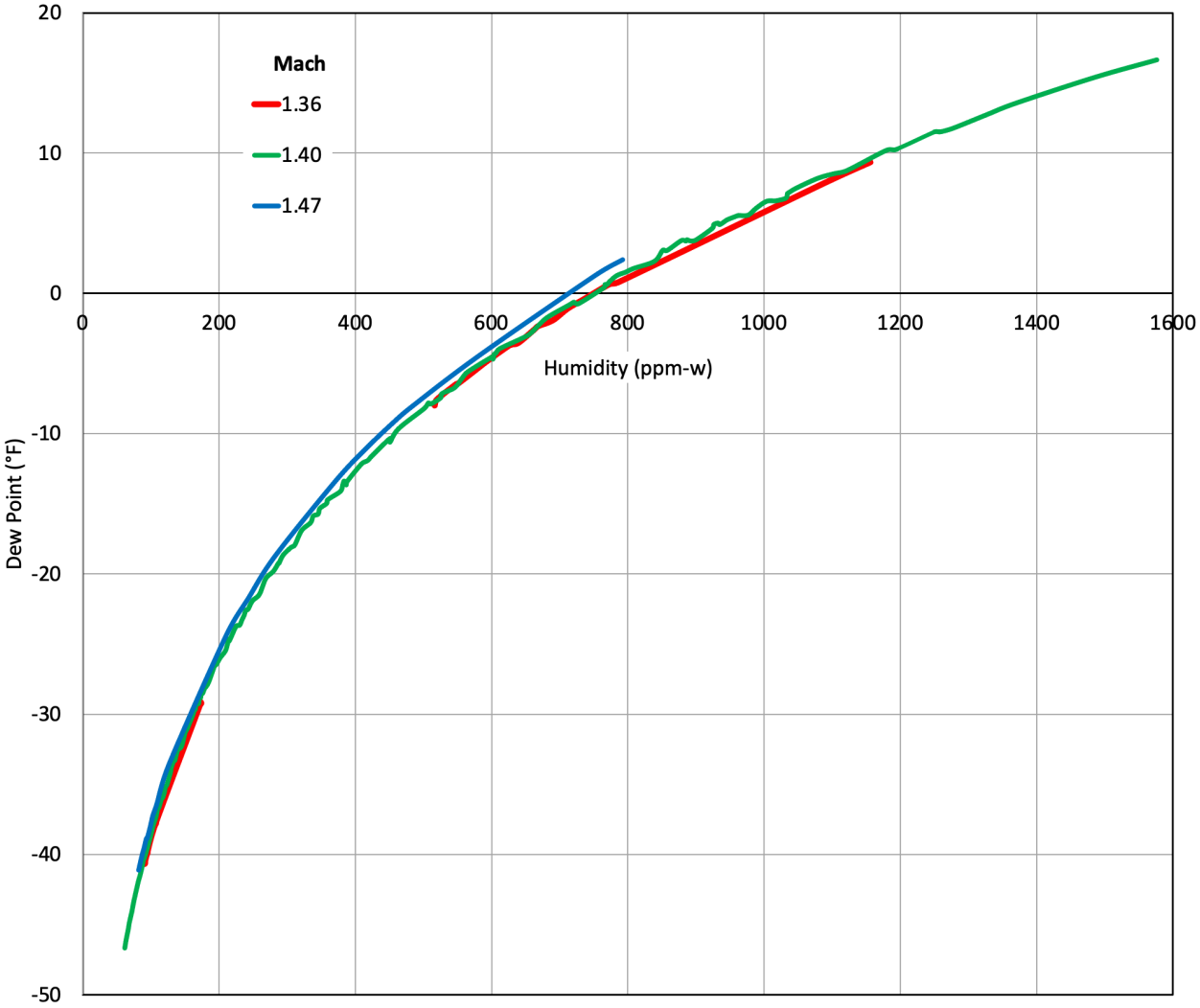

Figure 6-32 Dew point variation with humidity in 8x6 wind tunnel at the three test Mach numbers

6.6. Repeatability

Data quality is addressed in this section as observed in the repeatability of reference runs and model signatures.

6.6.1. Reference Run Repeatability

Selected groups of reference runs at each of the three Mach numbers run in this test are presented below in Figures 6-33 through 6-36. In all cases here, the model was the X-59 model with the blade strut mount, and it was positioned in the tunnel at h = 73” below the rail, α = 1°, and ϕ = 180° as depicted in the layout diagram of Figure 4-16(b).

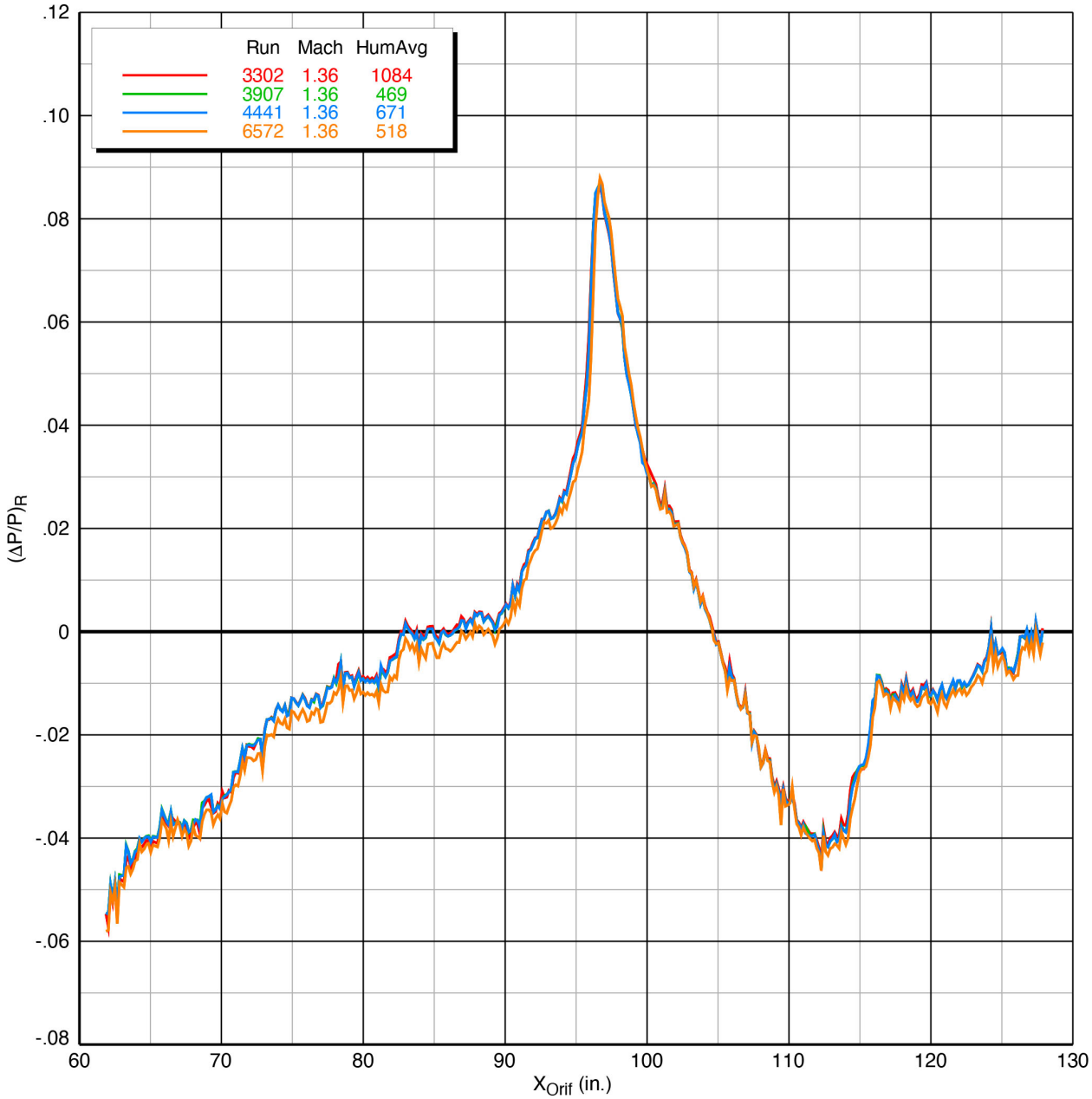

Figure 6-33 Short- and long-term repeatability of selected reference runs at Mach 1.36

The first three reference runs in Figure 6-33 at Mach 1.36 repeat very well with almost no discernable gaps among them, but the fourth run, 6572, has lower pressures over most of the front half of the signature and toward the end of the signature. The reasons for these differences are not known, since the wind tunnel operating crew consistently strived to make sure there were no inadvertent changes to the tunnel, model, and test conditions throughout the test. It was generally found that short-term repeatability was very good, while long-term repeatability tended to be not as good. The range of runs in this figure, from 3302 to 6572, represents a sizable fraction of the total number of runs obtained in the test (run numbers from 2709 to 9134), so the span of more than 3,000 runs on this plot can be classified as long-term repeat runs (over an almost 3-week period).

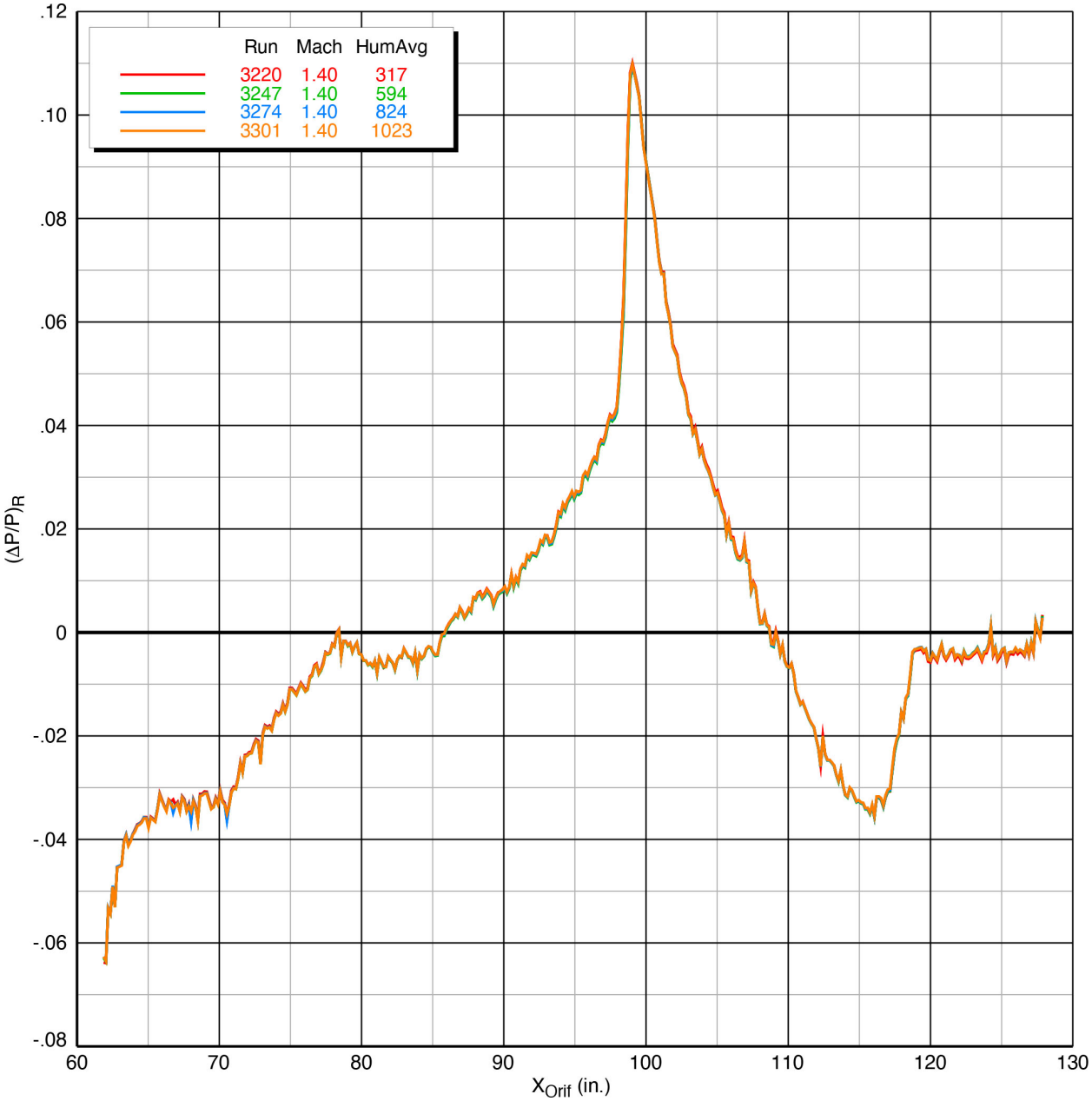

Figure 6-34 Short-term repeatability of selected reference runs at Mach 1.4

The four reference runs in Figure 6-34 at Mach 1.4 show excellent repeatability—not surprisingly in that these are short-term repeat runs (from 3220 to 3301). A second plot at the same Mach number in Figure 6-35 consists of runs over a greater range, and there is a sizable gap between the first pair of runs and the second pair. Note that the first pair spans a long range of run numbers, from 3301 to 6147, but these runs repeat very well. Then the very next reference run after 6147, which is 6155, has significantly lower pressure values than the runs before it. The only runs in between these two were some test conditions recorded for schlieren imaging. The two latter runs in the plot span a range of almost 500 run numbers, yet they repeat very well. An inadvertent change in reference pressure applied to the ESP modules plumbed to the rail orifices could easily account for such changes in the rail pressures, but this may not have been checked at the time of these runs.

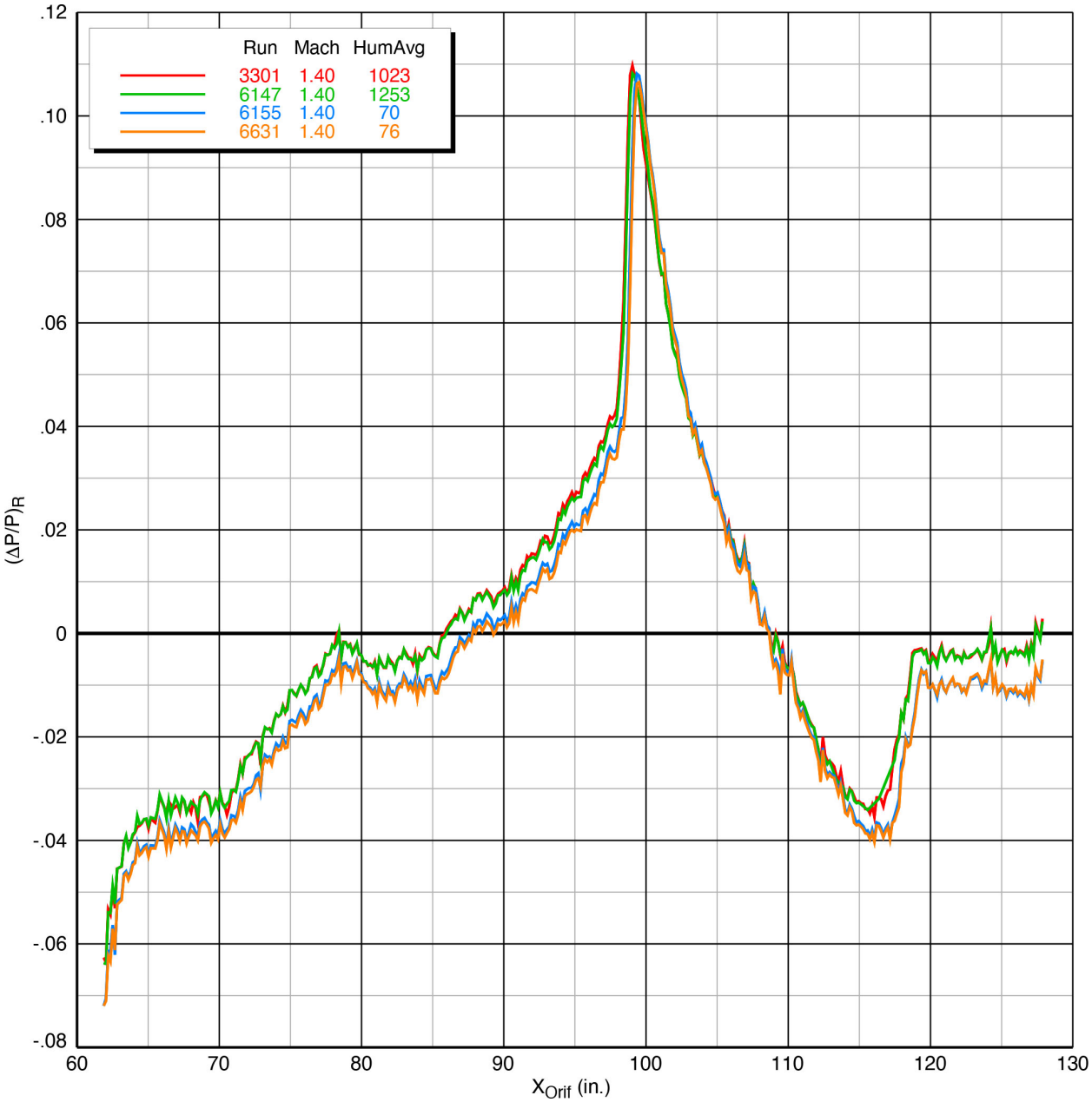

Figure 6-35 Short- and long-term repeatability of selected reference runs at Mach 1.4

Finally, a set of reference runs at Mach 1.47 are presented in Figure 6-36. Having run numbers that span across those in the previous plot that showed a gap in measured pressures, it is not surprising that the last run in this plot, 6519, has mostly lower pressures than the other runs in the plot up to number 4230.

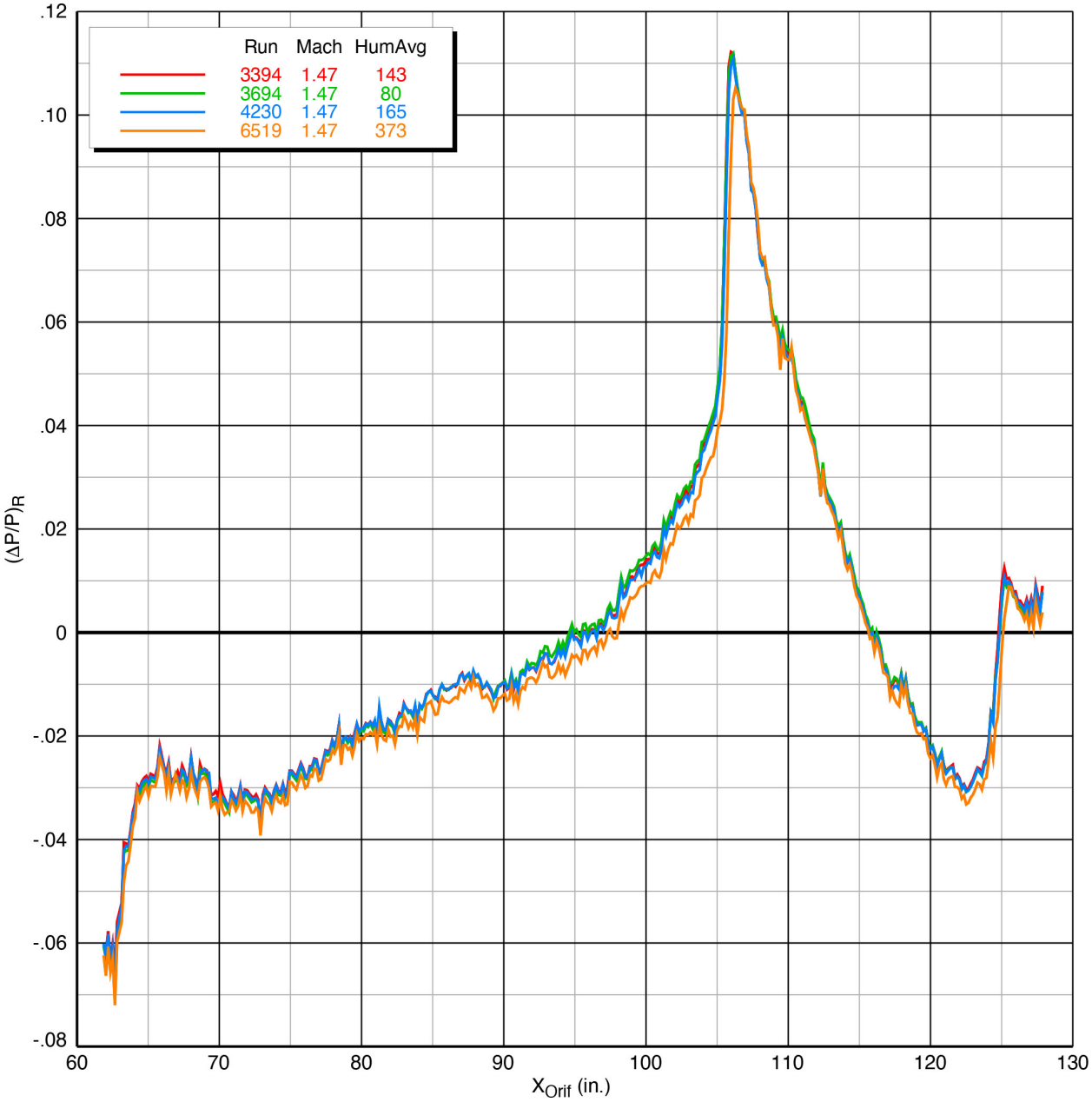

Figure 6-36 Short- and long-term repeatability of selected reference runs at Mach 1.47

6.6.2. X-59 Model Signature Repeatability

Plots of repeatability of various X-59 model signatures are presented in the following figures:

- Figure 6-37 Blade strut Mach 1.36 h/L = 2 α = 1.8° ϕ_{m2r} = 0°
- Figure 6-38 Blade strut Mach 1.4 h/L = 2 α = 2.1° ϕ_{m2r} = 15°
- Figure 6-39 Sting Mach 1.4 h/L = 1.2 α = 2.1° ϕ_{m2r} = 30°
- Figure 6-38 Sting Mach 1.4 h/L = 2 α = 2.1° ϕ_{m2r} = 0°
- Figure 6-41 Blade strut Mach 1.36 h/L = 3 α = 2.1° ϕ_{m2r} = 0°
- Figure 6-42 Blade strut Mach 1.4 h/L = 2 α = 2.1° ϕ_{m2r} = 0°
- Figure 6-43 Blade strut Mach 1.47 h/L = 1.2 α = 2.1° ϕ_{m2r} = 0°
- Figure 6-44 Sting Mach 1.4 h/L = 3 α = 2.1° ϕ_{m2r} = 0°
- Figure 6-45 Sting Mach 1.47 h/L = 2 α = 2.1° ϕ_{m2r} = 0°

Various sets of repeated signatures are presented in Figures 6-37 through 6-45 to show examples of SigSet combinations that repeated very well and others that had small differences among them. The signatures chosen for comparison in each plot were intentionally selected to have the same sweep ranges so that measurements on different portions of the rail would not be a factor.

The first three plots (through Figure 6-39) repeated well over most of the signature lengths but had some small deviations, mostly near the middle of the signatures. The five plots in Figures 6-40 through 6-44 show excellent repeatability with only very minor deviations among the curves. Note that in some cases, there are large humidity differences (up to more than 700 ppm) among the curves, but these differences do not appear to cause any variations among them.

In Figure 6-45(a), the front half of the signature for SigSet 146 is shifted upward slightly relative to SigSet 149, and the rear half is shifted downward. As discussed in the previous section, at times there were unexplained shifts among the reference runs. The discrepancy between these two SigSets prompted a recompute of SigSet 146 to be corrected by the following reference run (7292), instead of the prior one (7163), which was the default. The recomputed SigSet 146 is plotted in Figure 6-45(b), where it now overlaps SigSet 149.

Figure 6-46 shows a comparison of the reference runs before and after SigSet 146, and minor differences between them can be seen which can account for the changes in the data for this SigSet.

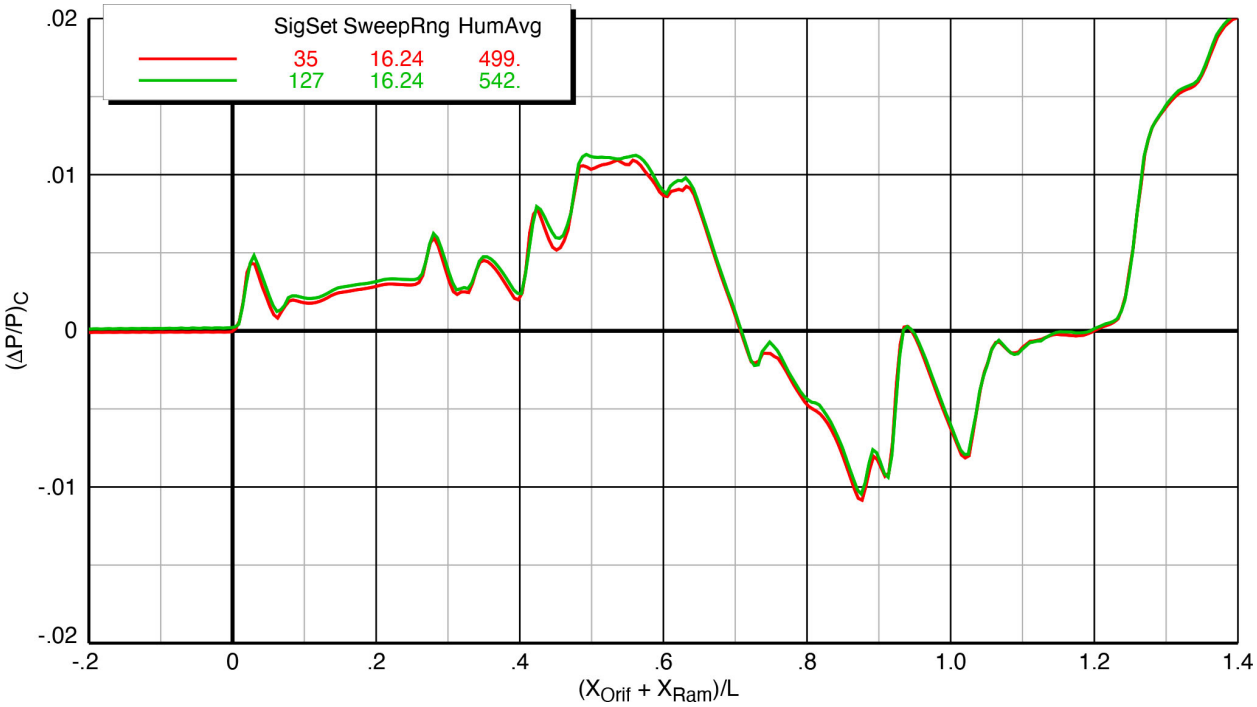

Figure 6-37 Repeatability of X-59 model (blade strut) signatures Mach 1.36, *h/L* = 2, α = 1.8°, ϕ_{m2r} = 0°

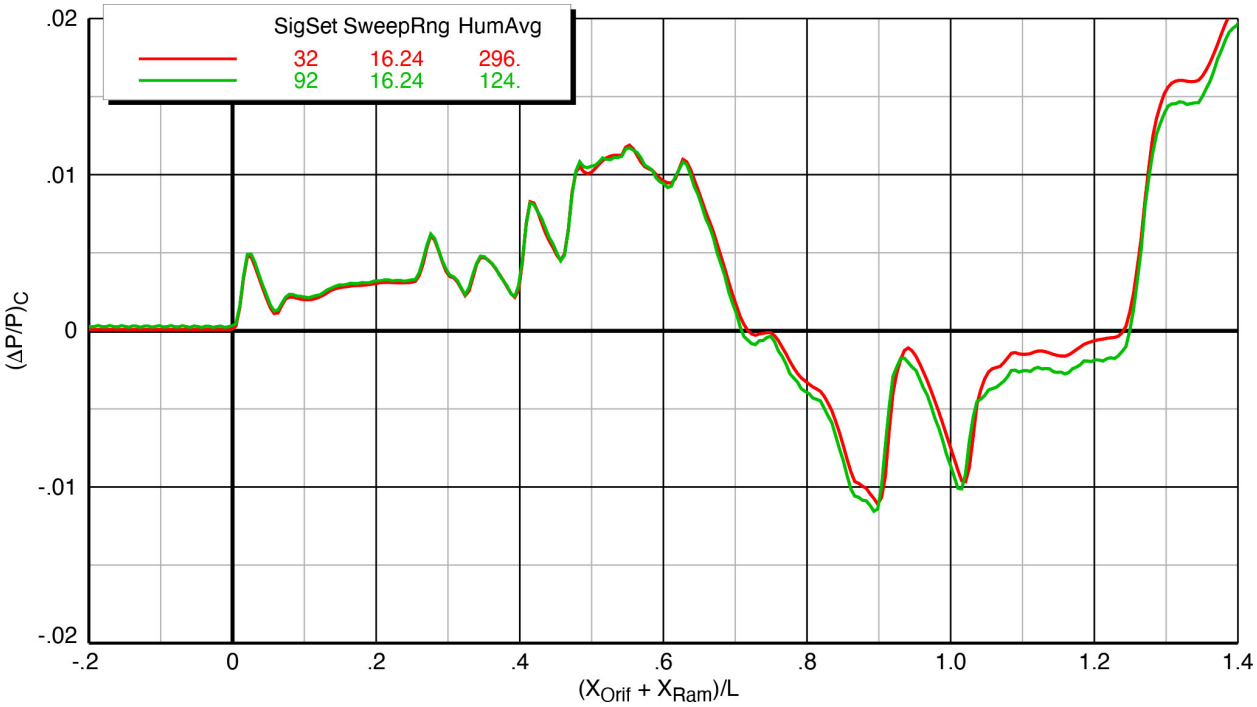

Figure 6-38 Repeatability of X-59 model (blade strut) signatures Mach 1.4, *h/L* = 2, α = 2.1°, ϕ_{m2r} = 15°

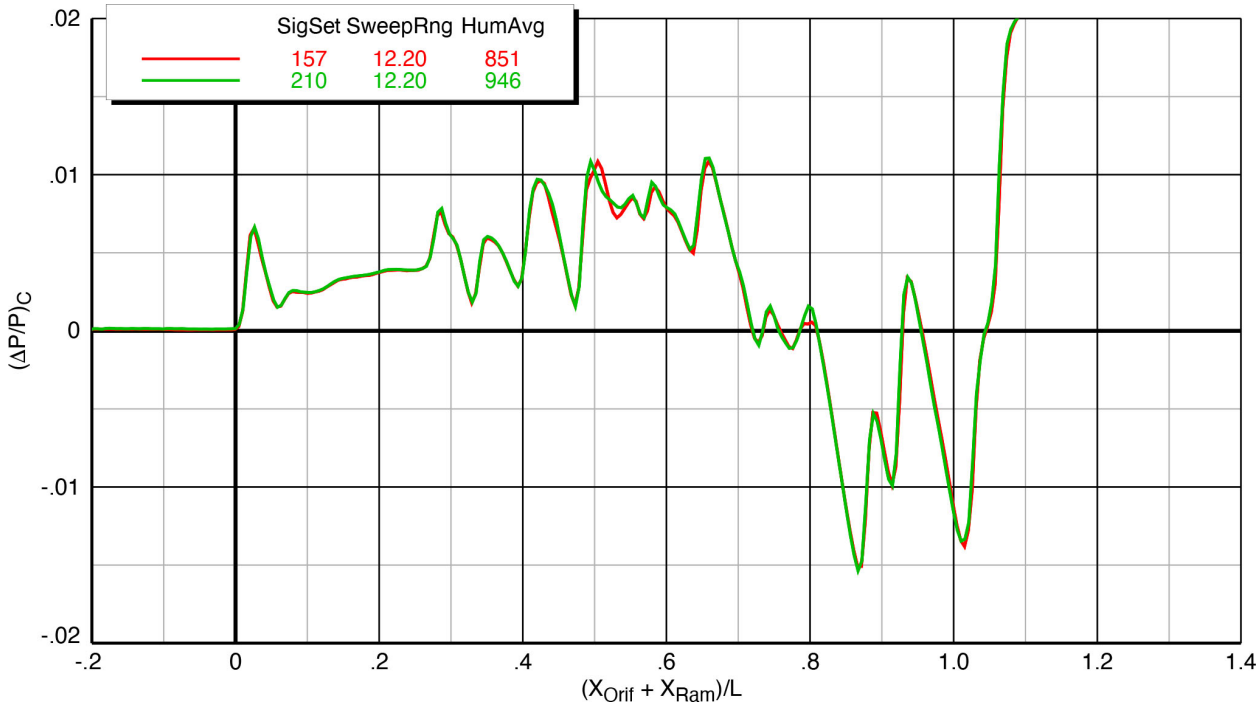

Figure 6-39 Repeatability of X-59 model (sting) signatures Mach 1.4, *h/L* = 1.2, α = 2.1°, ϕ_{m2r} = 30°

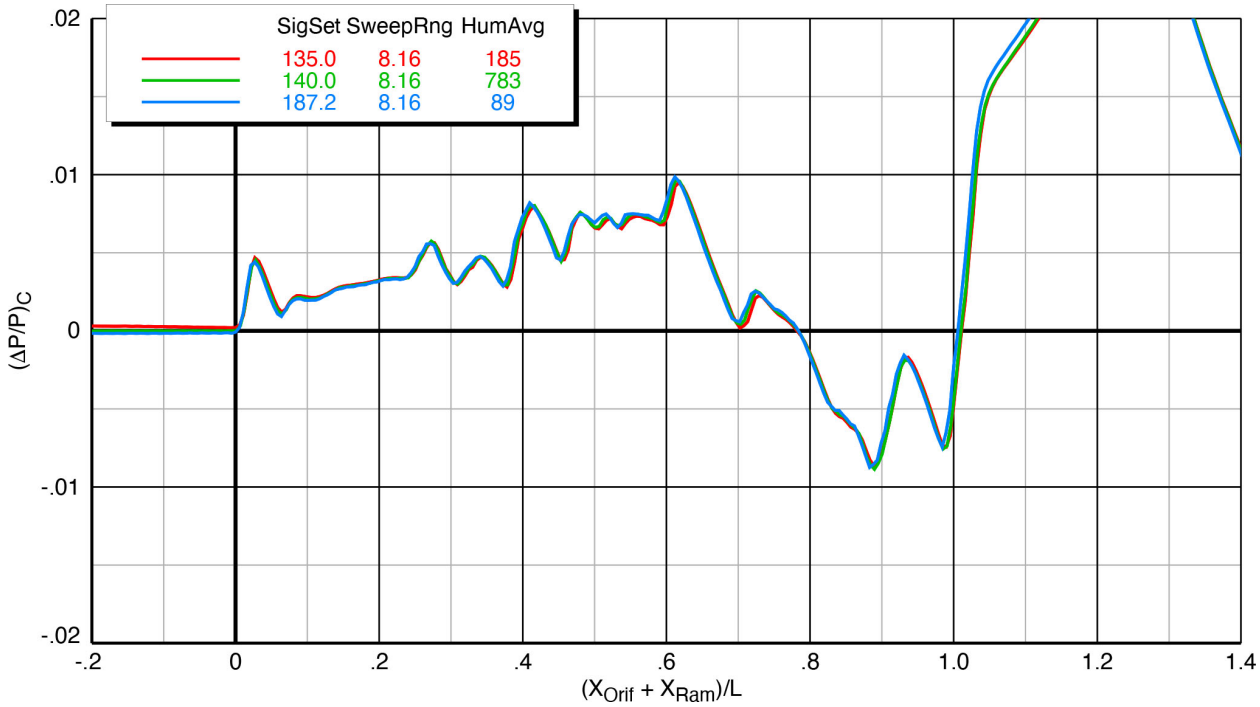

Figure 6-40 Repeatability of X-59 model (sting) signatures Mach 1.4, *h/L* = 2, α = 2.1°, ϕ_{m2r} = 0°

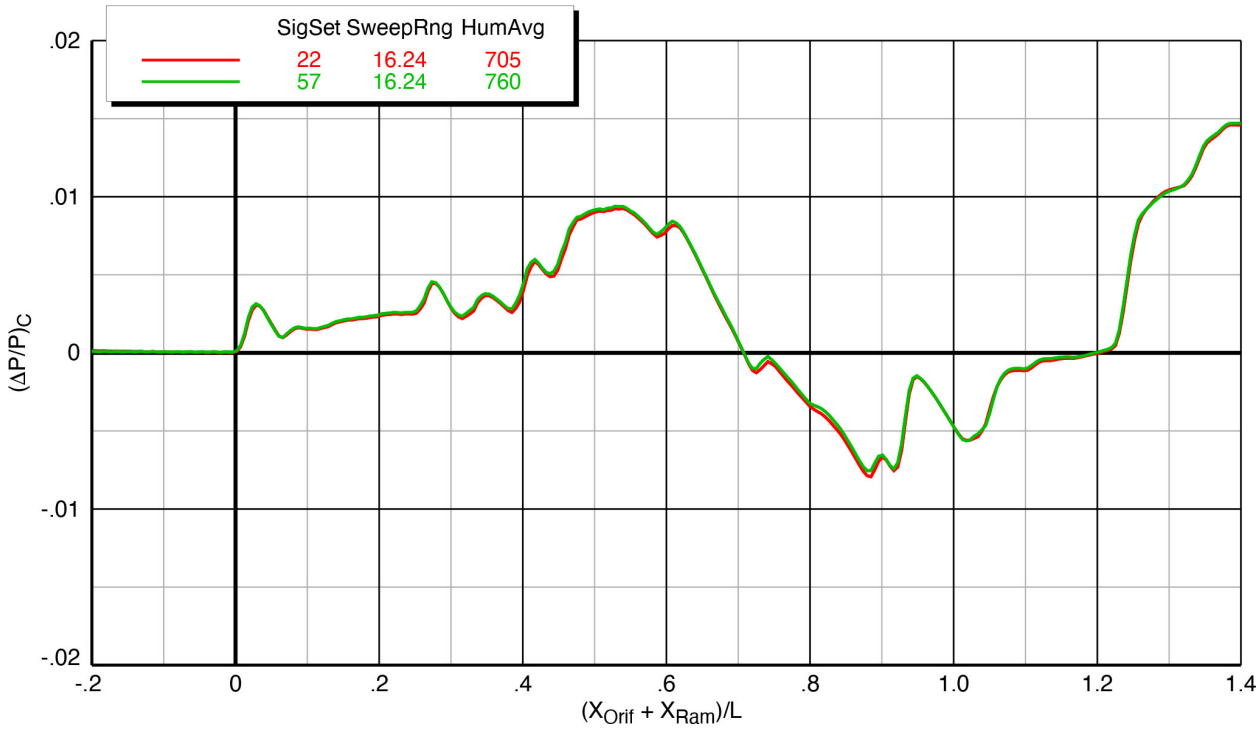

Figure 6-41 Repeatability of X-59 model (blade strut) signatures Mach 1.36, *h/L* = 3, α = 2.1°, ϕ_{m2r} = 0°

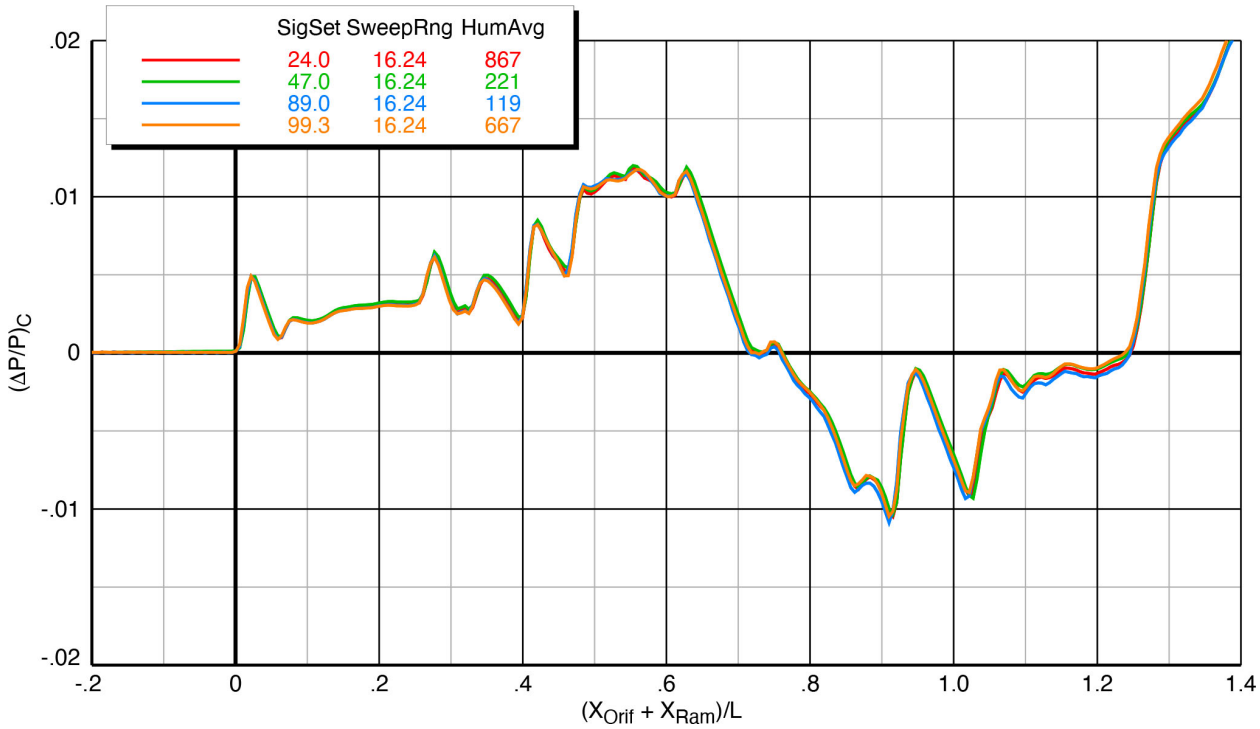

Figure 6-42 Repeatability of X-59 model (blade strut) signatures Mach 1.4, *h/L* = 2, α = 2.1°, ϕ_{m2r} = 0°

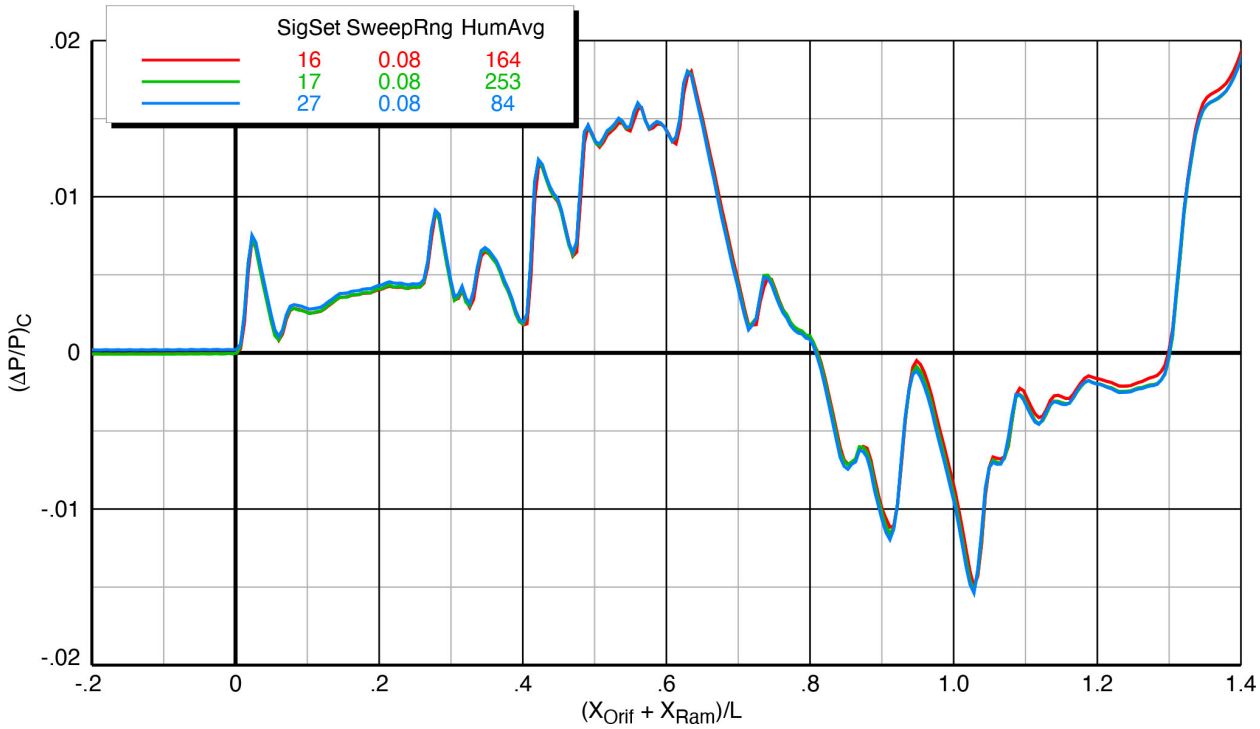

Figure 6-43 Repeatability of X-59 model (blade strut) signatures Mach 1.47, *h/L* = 1.2, α = 2.1°, ϕ_{m2r} = 0°

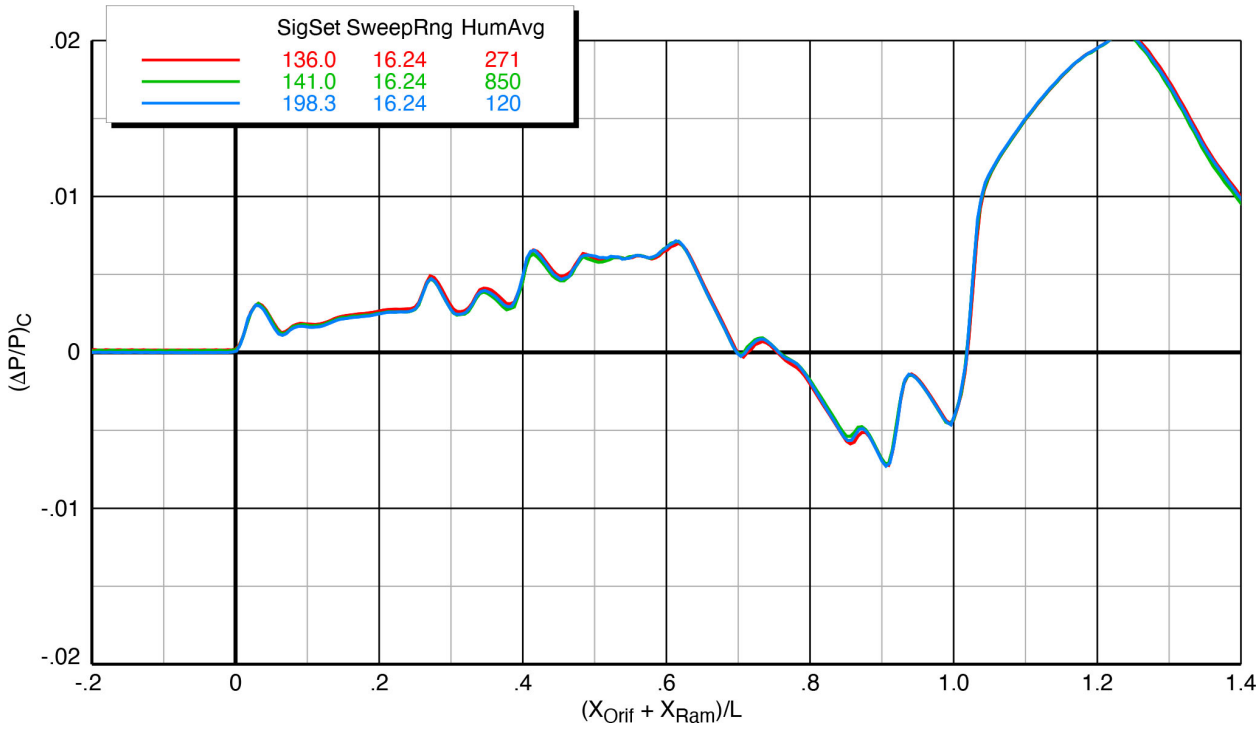

Figure 6-44 Repeatability of X-59 model (sting) signatures Mach 1.4, *h/L* = 3, α = 2.1°, ϕ_{m2r} = 0°

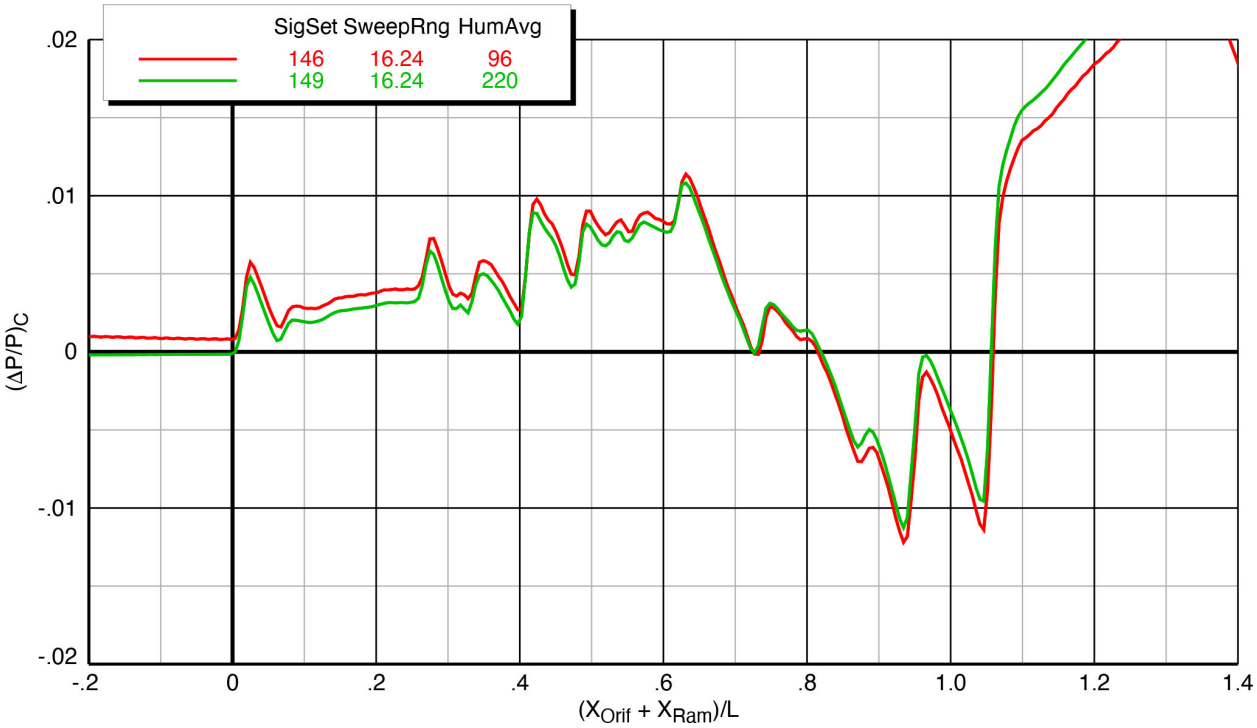

(a) Prior reference run 7163 used for correction

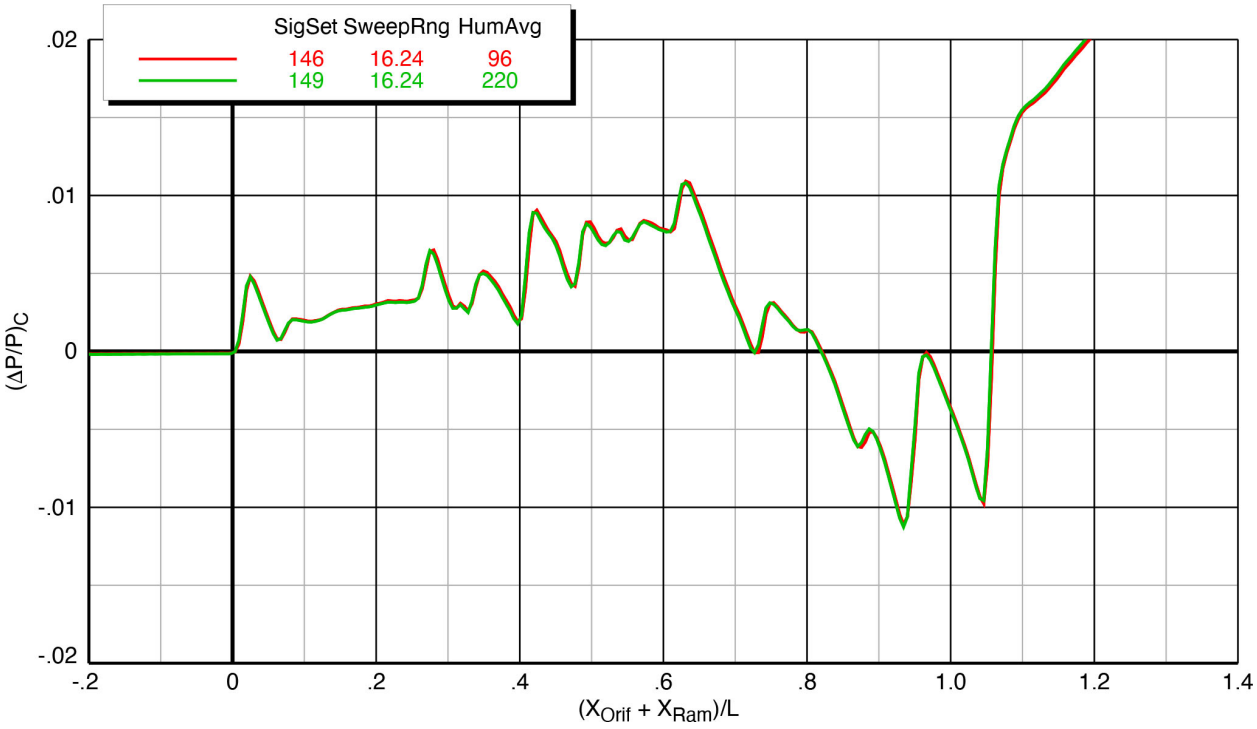

(b) Following reference run 7292 used for correction

Figure 6-45 Repeatability of X-59 model (sting) signatures using different reference runs for SigSet 146, Mach 1.47, *h/L* = 2, α = 2.1°, ϕ_{m2r} = 0°

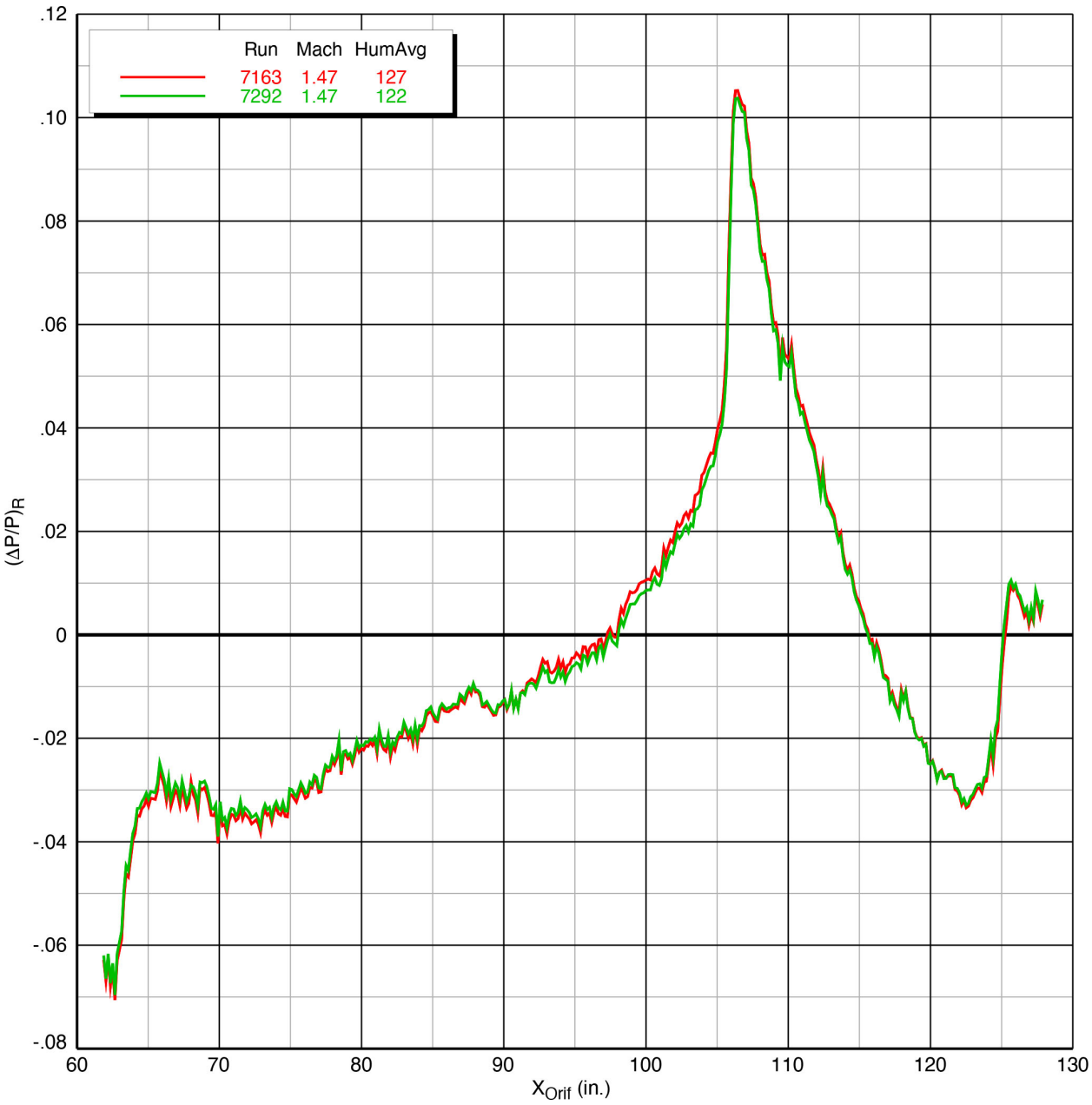

Figure 6-46 Reference runs before and after SigSet 146

6.7. Uncertainty Quantification

6.7.1. Spatial Averaging

For the purpose of this uncertainty analysis, the uncorrected and corrected pressure ratios from the rail data in Equations 1 through 3 above are given additional names:

$$DPR(X_{Orif}) = (\Delta P/P)_R = \left(\frac{P_{Rail}-P_\infty}{P_\infty}\right)_{Reference\ Run} \quad (4)$$

$$DPU_i(X_{Orif}) = (\Delta P/P)_U = \left(\frac{P_{Rail}-P_\infty}{P_\infty}\right)_{Data\ Run} \quad (5)$$

$$DPRC_i(X_{Orif}) = (\Delta P/P)_C = DPU_i(X_{Orif}) - DPR(X_{Orif}) \quad (6)$$

As stated above regarding Equation 3, $DPRC_i$ is the normalized model pressure signature with the reference run removed. The subscript i indicates a specific linear actuator ram position among the typically 26 positions at which data were acquired for use in the spatial average. Prior to computing this average, the 26 individual pressure signatures are adjusted in this uncertainty analysis to a common model height relative to the rail to account for small height variations during the ram translation.

$$\overline{h_{Nose}} = \frac{1}{N}\sum_{i=1}^{N} h_{i,Nose} \quad (7)$$

Where N = number of ram positions, individual signatures

$$DPC_i(X_{Orif}) = DPRC_i\sqrt{\frac{h_{i,Nose}}{\overline{h_{Nose}}}} \quad (8)$$

Once the individual signatures have the reference signature removed and are adjusted to the average model height during the sweep, the pressure signatures are aligned spatially to account for the linear ram extension. This alignment is done by adding the ram extension distance, $X_{i,Ram}$, to the rail orifice locations as shown in Equation 9, resulting in the parameter $X_{i,1}$. Figure 6-3 shows the 26 individual pressure signatures with the reference run removed, but not aligned. Figure 6-4 shows the aligned waterfall plot for the same signatures.

$$X_{i,1} = X_{Orif} + X_{i,Ram} \quad (9)$$

A Mach angle correction is made to account for changes in Mach number, M_i, and model height relative to the rail, h_{Nose}, as seen in Equation 10. Although applied to each data run to improve signature alignment for averaging, this correction also aligns signatures to a common reference frame to simplify comparisons between data acquired at different Mach numbers and heights relative to the rail. For example, if the model is positioned at a fixed location in the tunnel for runs at Mach 1.36 and 1.47, the signatures will be measured at different locations on the rail due to the Mach angle difference between the two runs. Applying Equation 10 will shift the signatures such that the nose shock from the model is aligned between the two runs when DPC is plotted as a function of $X_{i,2}$, allowing for direct comparisons to be made between the two cases.

$$X_{i,2} = X_{i,1} - h_{i,Nose}\sqrt{M_i^2 - 1} \quad (10)$$

An additional correction is made to account for variations in the model attitude. Equation 11 is used to compute the combined pitch and yaw angle, ξ, in the plane of the rail (tunnel *X*-*Z* plane). This angle is used to compute a relative amplitude correction to the *X* coordinate as

seen in Equation 12, where the initial model setpoint, ξ_1, is subtracted from the subsequent model setpoints, ξ_i, to compute the relative difference. Note that, if ξ were to remain constant during a series of data runs, Equation 12 would reduce to $X_2 = X_3$. In practice, this correction is usually small because test facilities can maintain model setpoints to tight tolerances during testing.

$$\xi_i = \alpha_i \cos(\phi_{i,Rail}) + \beta_i sin(\phi_{i,Rail}) \tag{11}$$

$$X_{i,3} = X_{i,2} + (X_{i,Nose} - X_{i,2}) tan(\xi_i - \xi_1) \sqrt{M_i^2 - 1} \tag{12}$$

Theoretically, the mean signature is obtained at each port where the shifted signatures align perfectly. In practice, interpolation is required between the port measurements on the rail to properly align the signatures with minimal set point error. X_4 is defined as a uniformly-spaced vector capturing the full range of X_3 values and typically spaced using half the pressure rail orifice spacing ($\Delta X_{Orif} = 0.1575$"). The fully aligned and adjusted pressure signatures (DPC as a function of X_3) are interpolated onto the X_4vector using a shape-preserving piecewise-cubic interpolation (*pchip* 1-dimensional interpolation in Matlab) without extrapolation.

$$X_4 = [X_{3,min} : (\Delta X_{Orf})/2 : X_{3,max}] \tag{13}$$

Once the pressure signatures are aligned and interpolated onto the common reference frame (X_4), the grand mean signature is obtained by summing the individual signatures at each interpolation location (DPC as a function of X_4) and dividing by the number of signatures aligned at each position as shown in Equation 14. In Figure 6-4, the individual signatures in SigSet 89 are plotted vs. $X_{Orif} + X_{Ram}$, which aligns the signatures and is similar to X_4 in that it is a measure of distance along the signature. Note that the number of signatures that make up the grand mean will vary with $X_{Orif} + X_{Ram}$, or X_4. For example, at $X_{Orif} + X_{Ram} = 80$ in Figure 6-4, there are approximately 8 signatures that have a measured value at the front of the signature that can be included in the average as a result of the alignment process, where all 26 signatures can be included in the average at $X_{Orif} + X_{Ram} = 100$.

$$\overline{DPC}(X_4) = \frac{1}{N} \sum_{i=1}^{N} DPC_i \tag{14}$$

Figure 6-47 shows the final grand mean boom signature overlaid with the individual signatures that were averaged to compute the grand mean boom signature (note that the X_4 scale does not line up with the abscissa scale in Figure 6-4 because of the adjustments in X made in the computation of X_4 above).

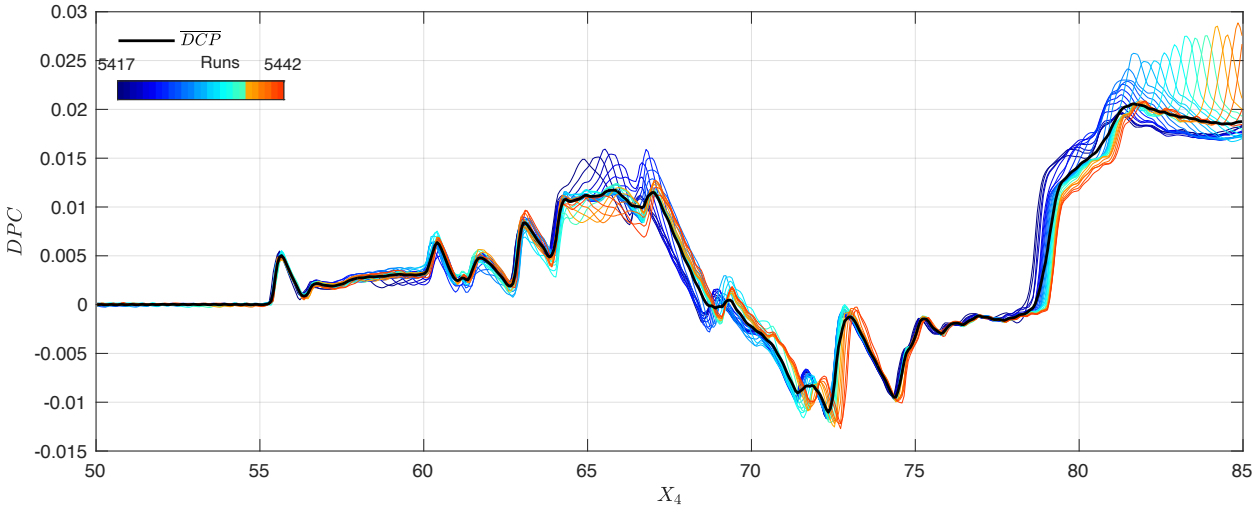

Figure 6-47 Grand mean signature and individual signatures for SigSet 89

6.7.2. Uncertainty Quantification

There are numerous sources of uncertainty that could be analyzed and quantified for the pressure signature calculations including, but not limited to, uncertainties in the tunnel calibration, model setpoint uncertainty, measurement sensor accuracy and resolution, and measurement repeatability. Only a subset of these uncertainties is addressed in the current analysis. The uncertainty quantification of the pressure signatures has been developed to capture three sources of uncertainty:

- Uncertainty of the time-averaged reference runs (Section 6.7.2.1)
- Uncertainty of the time-averaged data runs (Section 6.7.2.2)
- Uncertainty of the spatially-averaged data runs acquired at different linear ram positions (Section 6.7.2.3)

Each of these uncertainties are quantified as independent terms and are combined using a root-sum-square to set the total uncertainty for each signature set (Section 6.7.2.4).

Since the primary application of the uncertainty band is to compare signature sets from the same test, no fossilized uncertainties (from tunnel or instrument calibration errors) are included in the uncertainty buildup. Some of the fossilized uncertainties, due primarily to calibration of the pressure measurement devices, may be mitigated by subtraction of the reference signatures. An additional uncertainty could be developed from analyzing repeated signature sets acquired throughout the test, but the within-test-repeatability uncertainty has not been included here. At best, the uncertainty intervals provided represent a minimum level of uncertainty.

6.7.2.1. Reference Run Temporal Uncertainty

The temporal uncertainty of a reference run is computed using two-second block averages acquired over a 60-second window. The variance of the reference run samples is used as defined in Equation 15 where N_t is the number of two-second blocks acquired and j is the index of the two-second blocks.

$$\sigma^2_{DPR}(X_{Orif}) = \frac{1}{N_t-1}\sum_{j=1}^{N_i}\left(DPC_j - \overline{DPR}\right)^2 \quad (15)$$

σ^2_{DPR} is computed as a function of X_{Orif} as acquired, but to combine with the spatial uncertainty of the pressure signatures, it must be interpolated onto the X_4 reference frame. This

is done by using the X_3values for each of the data runs which results in N representations of σ_{DPR}^2 as a function of X_4. σ_{DPR}^2 is then averaged to compute the final form of the reference run temporal uncertainty as seen in Equation 16.

$$\overline{\sigma_{DPR}^2}(X_4) = \frac{1}{N}\sum_{i=1}^{N}\sigma_{t,DPR}^2 \tag{16}$$

A scalar value for the temporal uncertainty is computed by averaging over the temporal uncertainty vector as seen in Equation 17 where TA is the time average, N_p is the number of points in the X_4 vector, and k is the index for points in the X_4 vector.

$$\sigma_{TA}^2 = \frac{1}{N_p}\sum_{k=1}^{N_p}\overline{\sigma_{k,DPR}^2} \tag{17}$$

6.7.2.2. Data Run Temporal Uncertainty

The temporal uncertainty of a data run is computed using two-second block averages acquired over a 15-second window. The variance of the data run samples is used as defined in Equation 18 where N_t is the number of two second blocks acquired, j is the index of the two-second blocks, N is the number of ram positions used to compute the grand mean, and i is the index of the ram positions.

$$\sigma_{DPU}^2(X_{Orif}) = \frac{1}{N_t - N}\sum_{i=1}^{N}\sum_{j=1}^{N_t}\left(DPU_{ij} - \overline{DPU}_i\right)^2 \tag{18}$$

σ_{DPU}^2 is computed as a function of X_{Orif}, but it must be interpolated onto the X_4 reference frame to combine with the spatial uncertainty of the pressure signatures. This is done by using the X_3 values for each of the data runs which results in N representations of σ_{DPU}^2 as a function of X_4. σ_{DPU}^2 is then averaged to compute the final form of the reference run temporal uncertainty as seen in Equation 19.

$$\overline{\sigma_{DPU}^2}(X_4) = \frac{1}{N}\sum_{i=1}^{N}\sigma_{t,DPU}^2 \tag{19}$$

6.7.2.3. Spatial Uncertainty

The spatial uncertainty is developed by computing the variance of the individual data runs used to generate the final grand mean signature as seen in Equation 20.

$$\sigma_{AR}^2(X_4) = \frac{1}{N-1}\sum_{j=1}^{N}\left(DPC_j - \overline{DPC}\right)^2 \tag{20}$$

Because the reference run was used to compute DPC, the temporal uncertainty component is removed from the spatial variance as seen in Equation 21 so as not to double count the temporal uncertainty.

$$\sigma_{SP}^2(X_4) = \left|\sigma_{AR}^2 - \sigma_{TA}^2\right| \tag{21}$$

6.7.2.4. Combined Uncertainty

The final combined uncertainty is computed by taking the root-sum-square of the two temporal uncertainties and the spatial uncertainty as seen in Equation 22.

$$\sigma_{DPC}(X_4) = \sqrt{\overline{\sigma_{DPR}^2} + \overline{\sigma_{DPU}^2} + \sigma_{SP}^2} \tag{22}$$

This uncertainty can be used to represent the 95% confidence bounds that an additional data run, DPC, will fall in the range of $DPC \pm 2\sigma_{DPC}$. However, because the averaged signatures are the data that are reported, the standard deviation of the mean is of greater

interest as the spatial averaging was performed to reduce the uncertainty. The standard deviation of the mean is computed as seen in Equation 23.

$$\sigma_{\overline{DPC}}(X_4) = \frac{\sigma_{DPC}}{\sqrt{N}} \tag{23}$$

This uncertainty can be used to represent the 95% confidence bounds that a repeated averaged dataset, $\overline{DPC}$, will fall in the range of $\overline{DPC} \pm 2\sigma_{\overline{DPC}}$. It should be noted that using 2σ to define the 95% coverage implies a normal distribution; however, it is best to not assume a distribution given the low sample sizes for the experimental data. The grand mean signature computed from the data in Figure 6-47 is plotted with the uncertainty bounds in Figure 6-48.

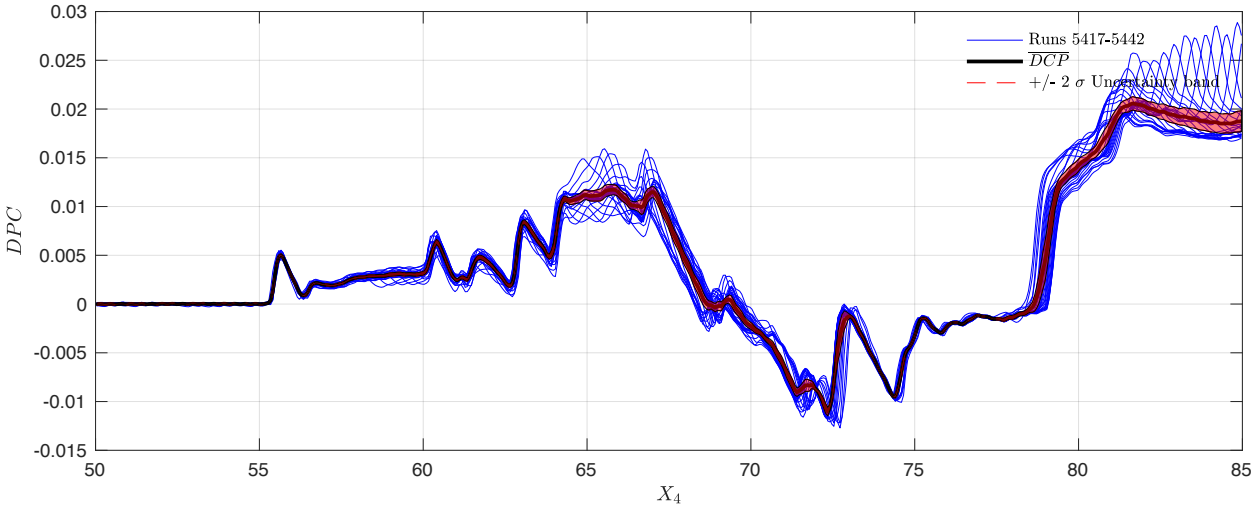

(a) Uncertainty bounds with individual signatures for SigSet 89

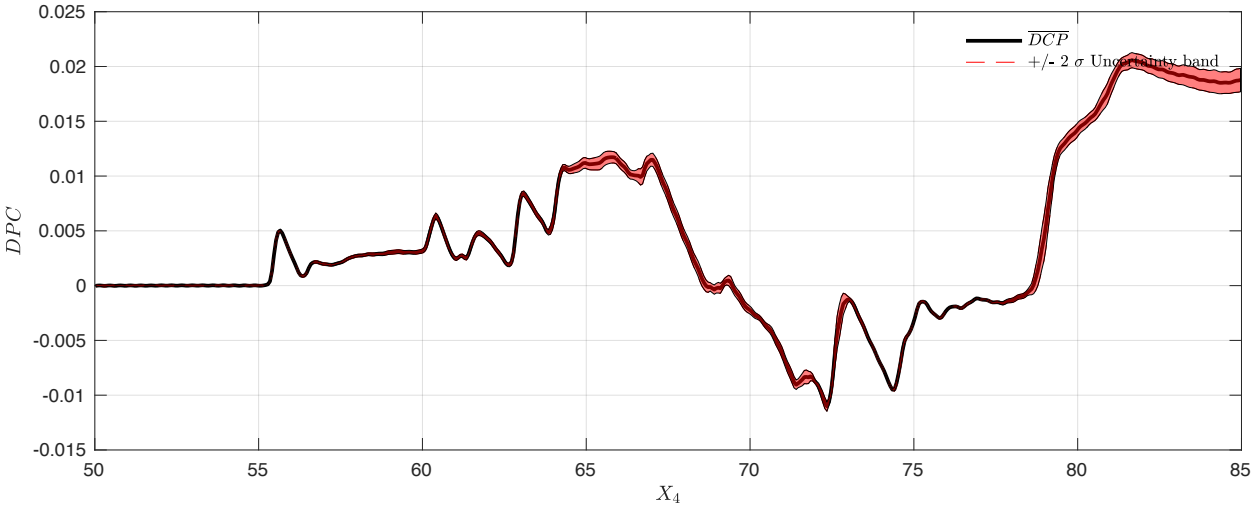

(b) Uncertainty bounds without individual signatures for SigSet 89

Figure 6-48 Grand mean signature with uncertainty quantification

6.8. Effect of Control Surface Deflections

Plots showing the effects of deflecting the stabilator, T-tail, flaps, and ailerons on the X-59 pressure signatures are provided in this section.

6.8.1. Effect of Stabilator Deflections

The effects of deflecting the stabilator on the model signatures are presented in the following figures:

- Figure 6-49 Blade strut Mach 1.4 h/L = 1.2 α = 2.1°
- Figure 6-50 Blade strut Mach 1.4 h/L = 2 α = 2.1°
- Figure 6-51 Blade strut Mach 1.4 h/L = 3 α = 2.1°
- Figure 6-52 Blade strut Mach 1.4 h/L = 2 α = 1.8°
- Figure 6-53 Blade strut Mach 1.4 h/L = 2 α = 2.4°

With the stabilator being at the rear of the vehicle, the changes in the pressure signatures are expected to be seen near the end of the signatures. In the plots below, the changes are observed in the region of X/L (short for $(X_{Orif} + X_{Ram})/L$) = 0.9 to 1.1, and the portion of the signature ahead of this is not impacted. As the stabilator is deflected and producing more or less lift than at the nominal angle of 3.42°, the change in shock strength for that portion of the signature is evident in all of the plots. It is odd though, that in Figure 6-51, the signature for SigSet 65 with the highest stabilator deflection is above the other two signatures over most of their length, as opposed to just at the rear. This appears to be just an anomaly in the repeatability and not a result of the high humidity since SigSet 76 has humidity that is nearly as high.

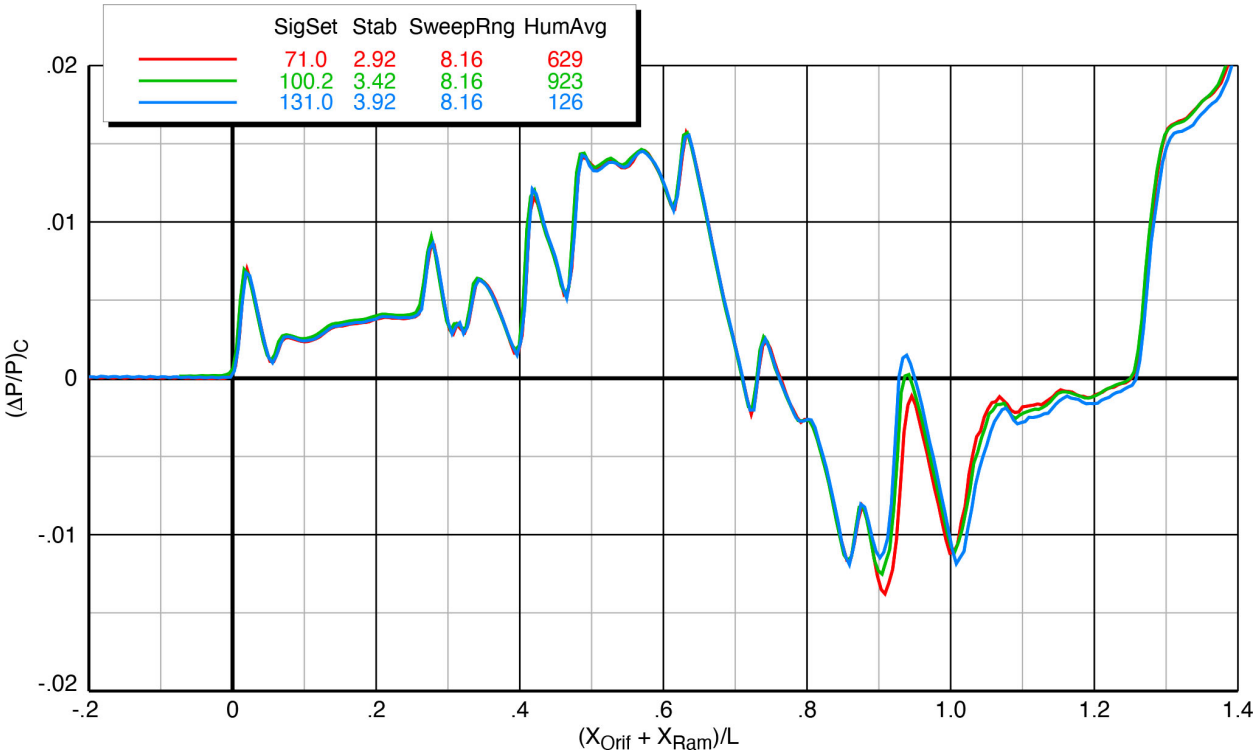

Figure 6-49 Effect of stabilator deflections on X-59 model (blade strut) spatially-averaged pressure signatures, Mach 1.4, h/L = 1.2, α = 2.1°, ϕ_{m2r} = 0°

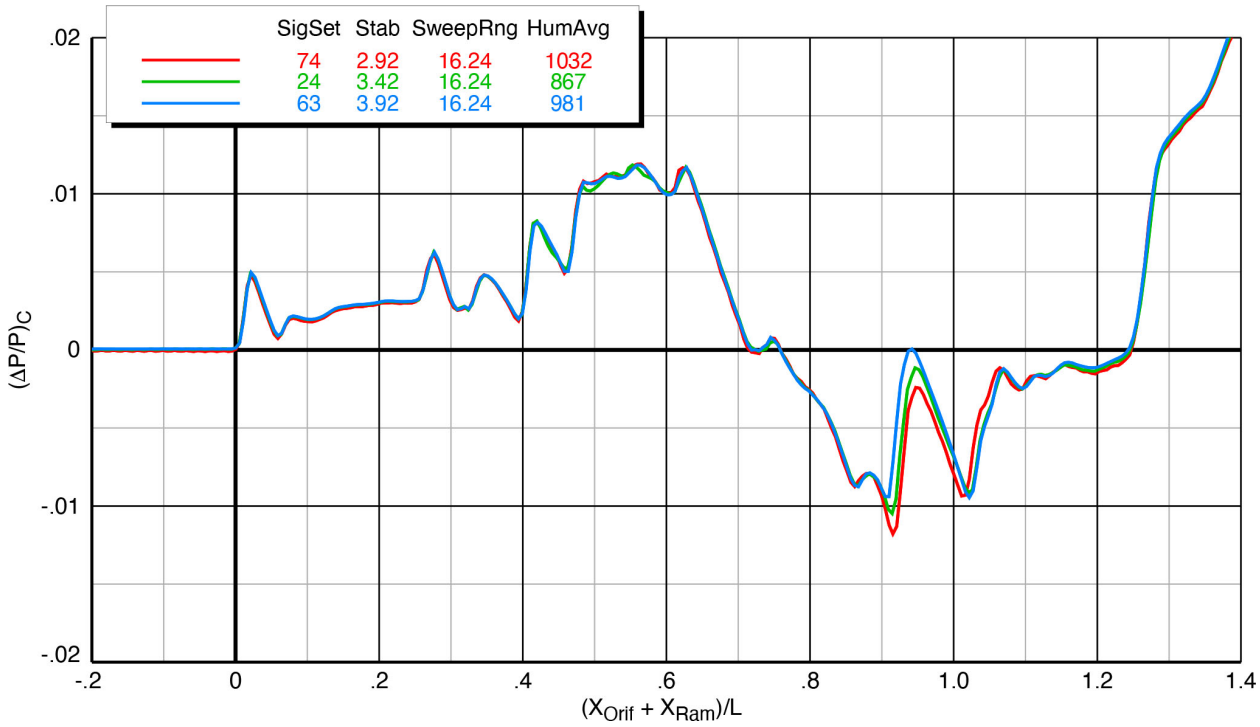

Figure 6-50 Effect of stabilator deflections on X-59 model (blade strut) spatially-averaged pressure signatures, Mach 1.4, *h/L* = 2, α = 2.1°, ϕ_{m2r} = 0°

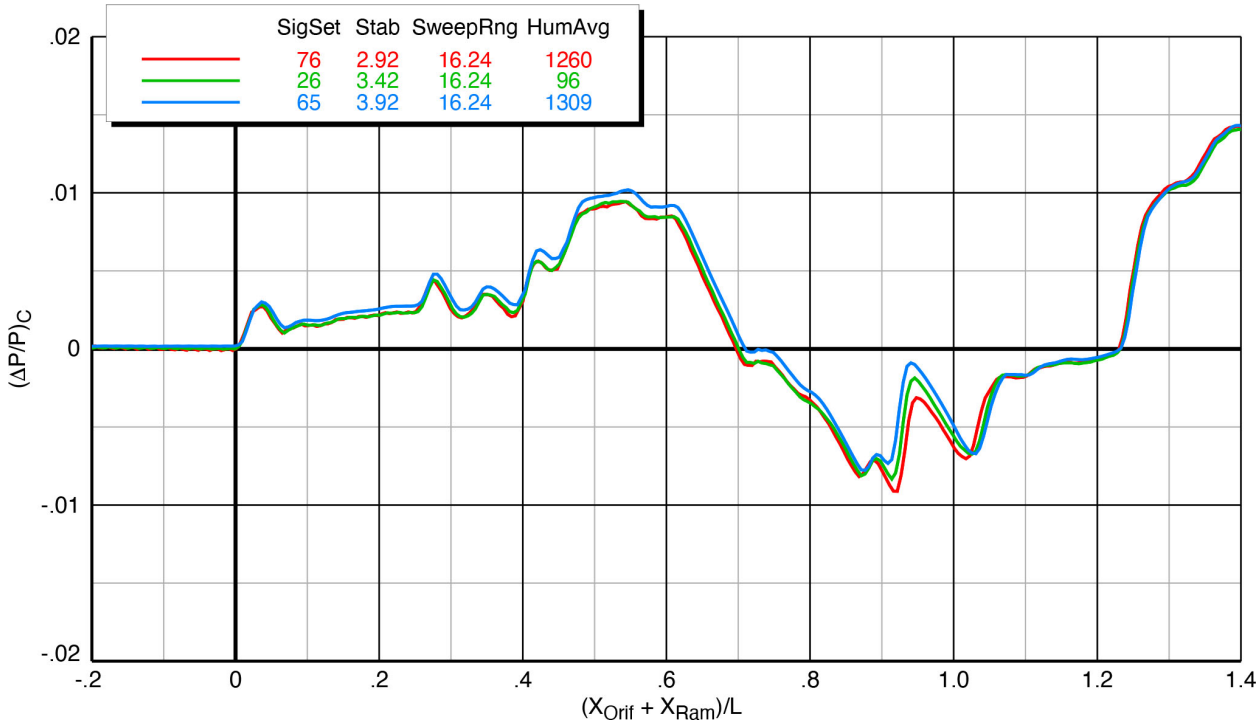

Figure 6-51 Effect of stabilator deflections on X-59 model (blade strut) spatially-averaged pressure signatures, Mach 1.4, *h/L* = 3, α = 2.1°, ϕ_{m2r} = 0°

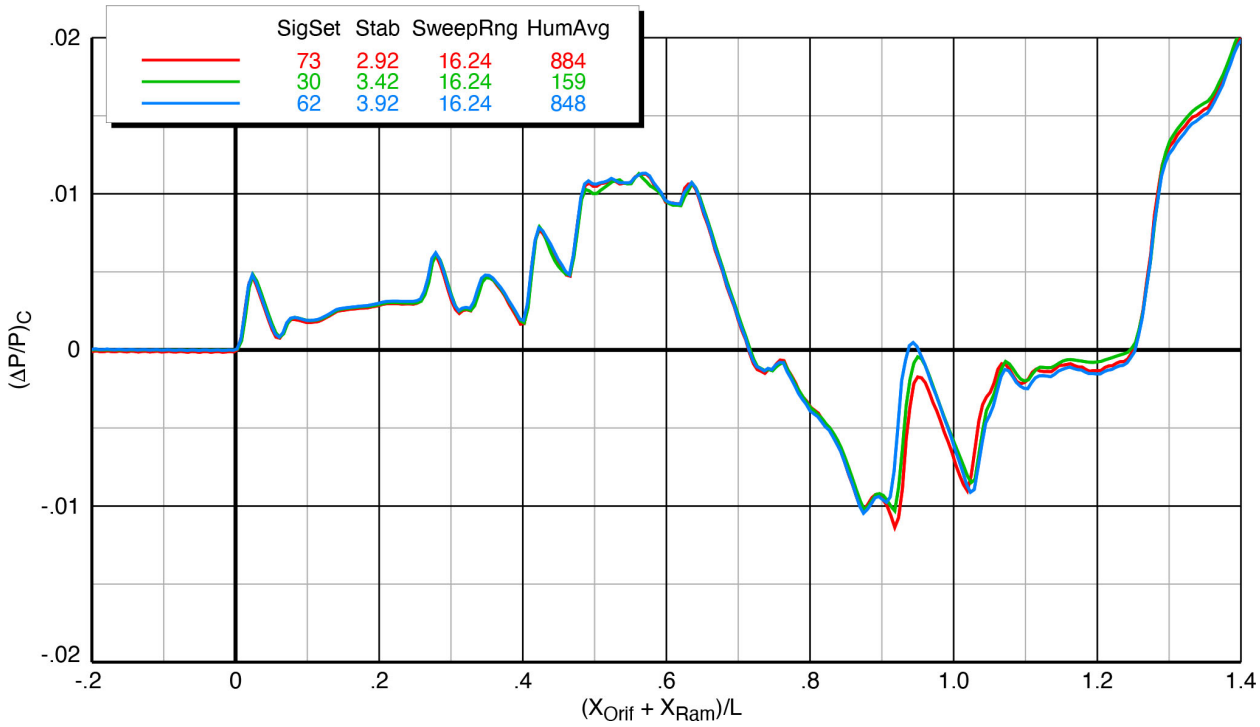

Figure 6-52 Effect of stabilator deflections on X-59 model (blade strut) spatially-averaged pressure signatures, Mach 1.4, *h/L* = 2, α = 1.8°, ϕ_{m2r} = 0°

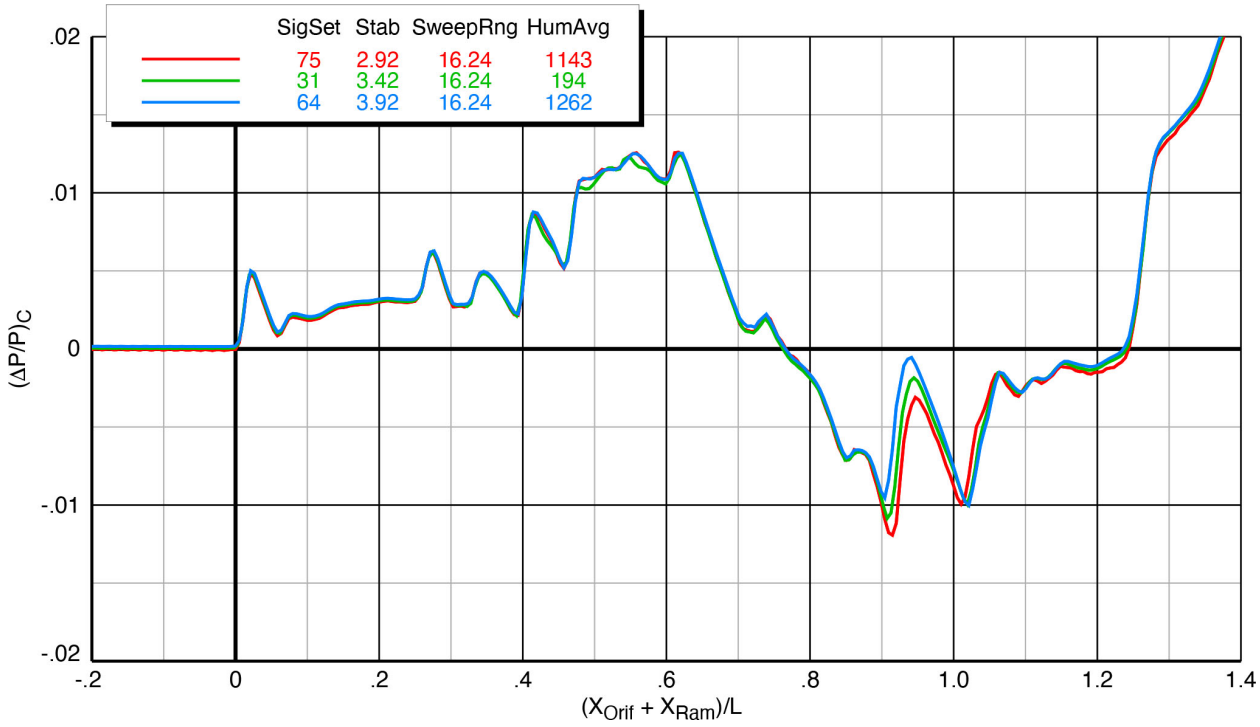

Figure 6-53 Effect of stabilator deflections on X-59 model (blade strut) spatially-averaged pressure signatures, Mach 1.4, *h/L* = 2, α = 2.4°, ϕ_{m2r} = 0°

6.8.2. Effect of T-tail Deflections

The effects of deflecting the T-tail on the model signatures are presented in the following figures:

- Figure 6-54 Blade strut Mach 1.4 h/L = 1.2 α = 2.1°
- Figure 6-55 Blade strut Mach 1.4 h/L = 2 α = 2.1°
- Figure 6-56 Blade strut Mach 1.4 h/L = 3 α = 2.1°

The T-tail is directly above the stabilator on the X-59, but its influence on the pressure signatures is aft of that of the stabilator because the shocks propagate downward from the vehicle roughly along the Mach line angle (~44° for Mach 1.4). Thus, the increments in the shock locations from the T-tail should be near or just aft of the stabilator shocks, and they do appear in the three plots below in the region of X/L = 1.02 to 1.05.

In Figure 6-54, the portions of the signatures in this region show the normal progression of the shocks moving forward with increasing T-tail deflection, but in the other two plots, that progression is not as clear. In Figure 6-55, the curve for the nominal, 3.7°, T-tail deflection, is elevated above the other two over a wide range ahead of and behind where the T-tail influence should be. In Figure 6-56, the nominal curve overlaps the curve for the 2.7° T-tail deflection in that region but is lower than both other curves ahead of that. These appear to be cases where the repeatability is not quite as good as desired.

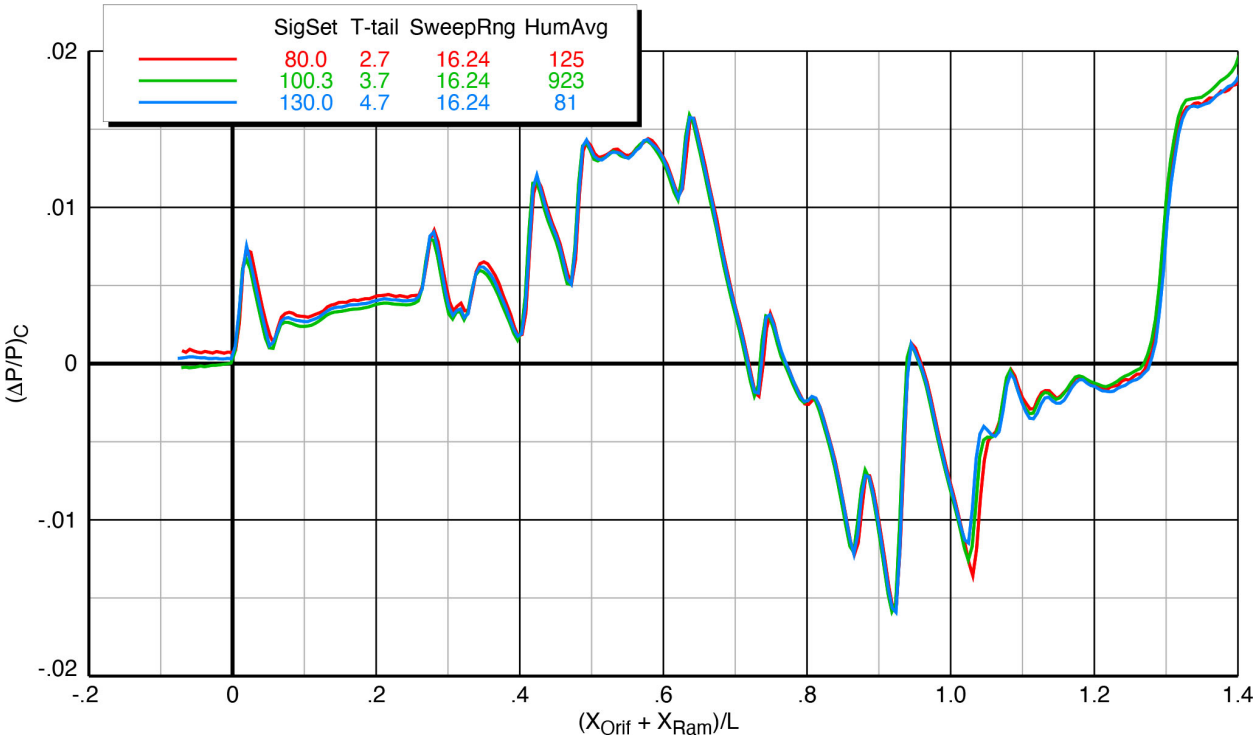

Figure 6-54 Effect of T-tail deflections on X-59 model (blade strut) spatially-averaged pressure signatures, Mach 1.4, h/L = 1.2, α = 2.1°, ϕ_{m2r} = 0°

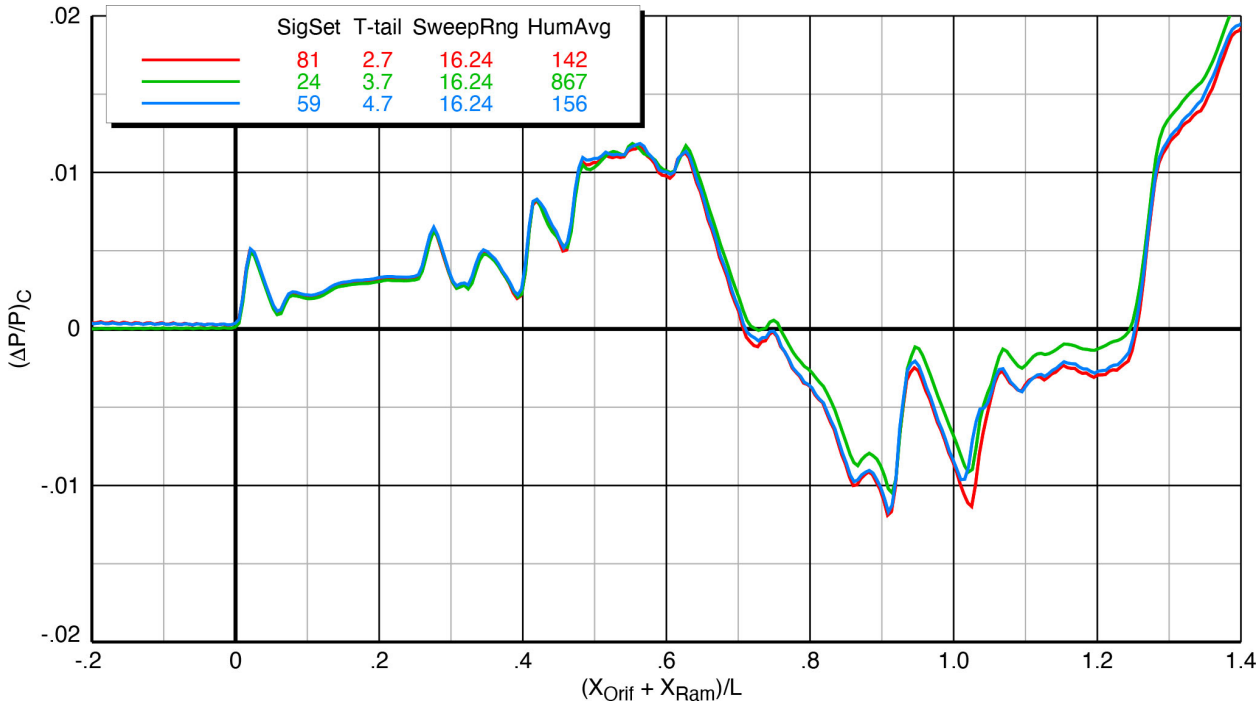

Figure 6-55 Effect of T-tail deflections on X-59 model (blade strut) spatially-averaged pressure signatures, Mach 1.4, *h/L* = 2, α = 2.1°, ϕ_{m2r} = 0°

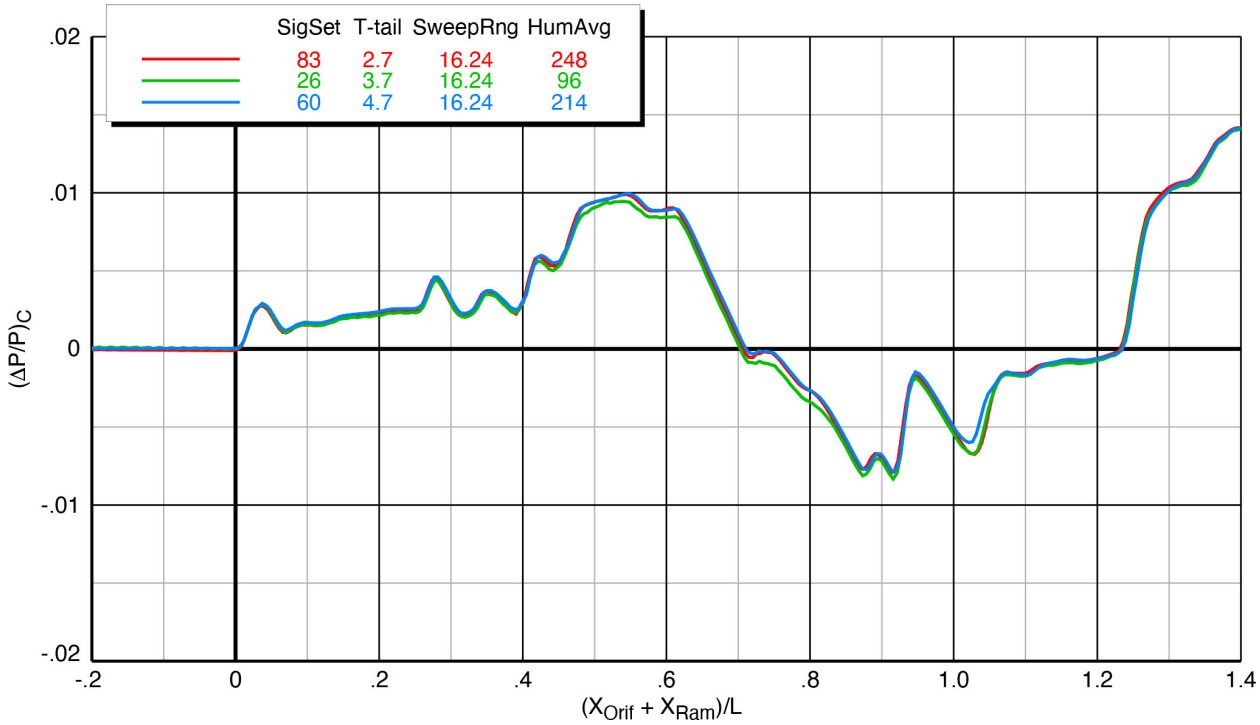

Figure 6-56 Effect of T-tail deflections on X-59 model (blade strut) spatially-averaged pressure signatures, Mach 1.4, *h/L* = 3, α = 2.1°, ϕ_{m2r} = 0°

6.8.3. Effect of Flap Deflections

The effects of deflecting the flaps on the model signatures are presented in the following figures:

- Figure 6-57 Blade strut Mach 1.4 *h/L* = 1.2 α = 2.1°
- Figure 6-58 Blade strut Mach 1.4 *h/L* = 2 α = 2.1°
- Figure 6-59 Blade strut Mach 1.4 *h/L* = 3 α = 2.1°
- Figure 6-60 Sting Mach 1.4 *h/L* = 1.2 α = 2.1°
- Figure 6-61 Sting Mach 1.4 *h/L* = 2 α = 2.1°
- Figure 6-62 Sting Mach 1.4 *h/L* = 3 α = 2.1°

Flap angles of -2.9° and -2.4° were run on the blade strut configuration, and these angles plus the -1.9°-deflection were run on the sting configuration. The reason for not running the -1.9° angle on the blade strut configuration is that it was felt that shocks from the blade strut could have contaminated the data from the wing control surfaces and that the flaps were separated enough from the sting to have better-quality data on the sting configuration. Thus, it was decided to not spend the extra test time getting the third set of flap-deflection data on the blade strut configuration.

Increments in the signatures from the flap deflections are apparent in the plots below in the *X/L* range of approximately 0.7 to 1.0. The increments between the -2.9° and -2.4° deflections are very small for both model-mounting configurations, but the increment to the -1.9° deflection (for the sting configuration) is quite a bit larger in the 0.82 to 0.89 *X/L* range. The increments observed for both configurations become significantly smaller at model height from the rail is increased.

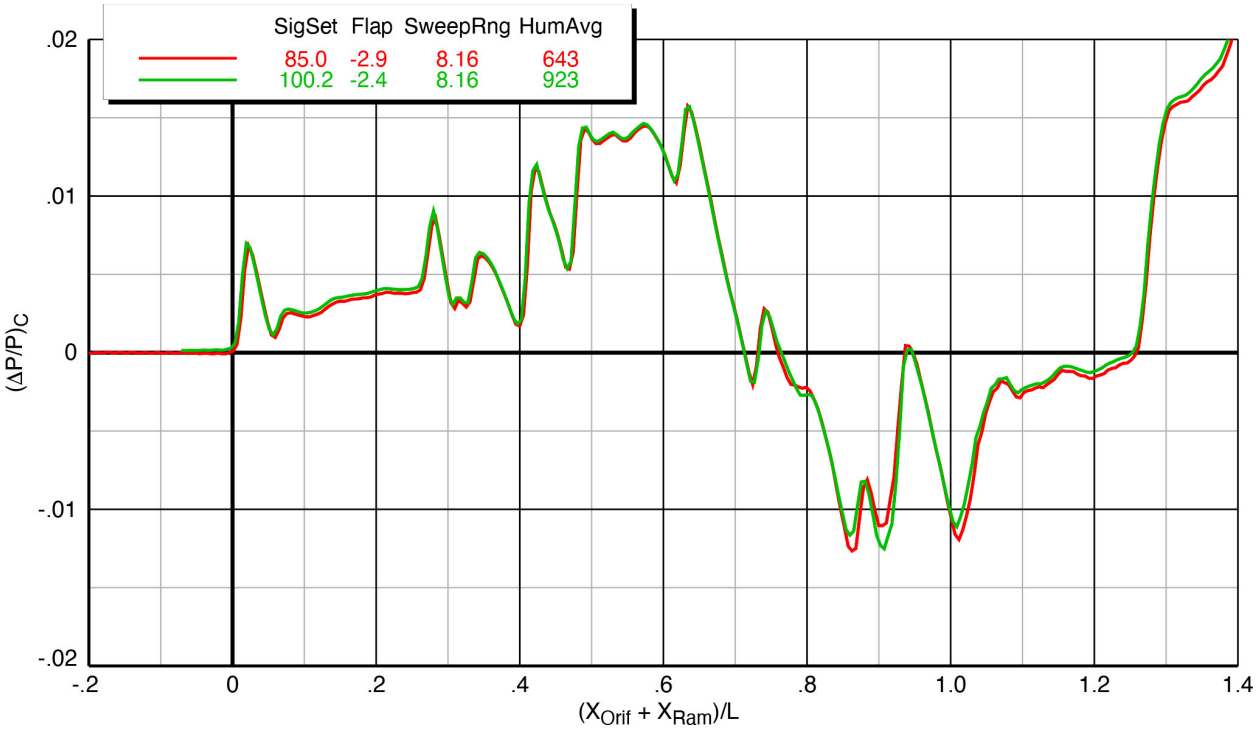

Figure 6-57 Effect of flap deflections on X-59 model (blade strut) spatially-averaged pressure signatures, Mach 1.4, *h/L* = 1.2, α = 2.1°, ϕ_{m2r} = 0°

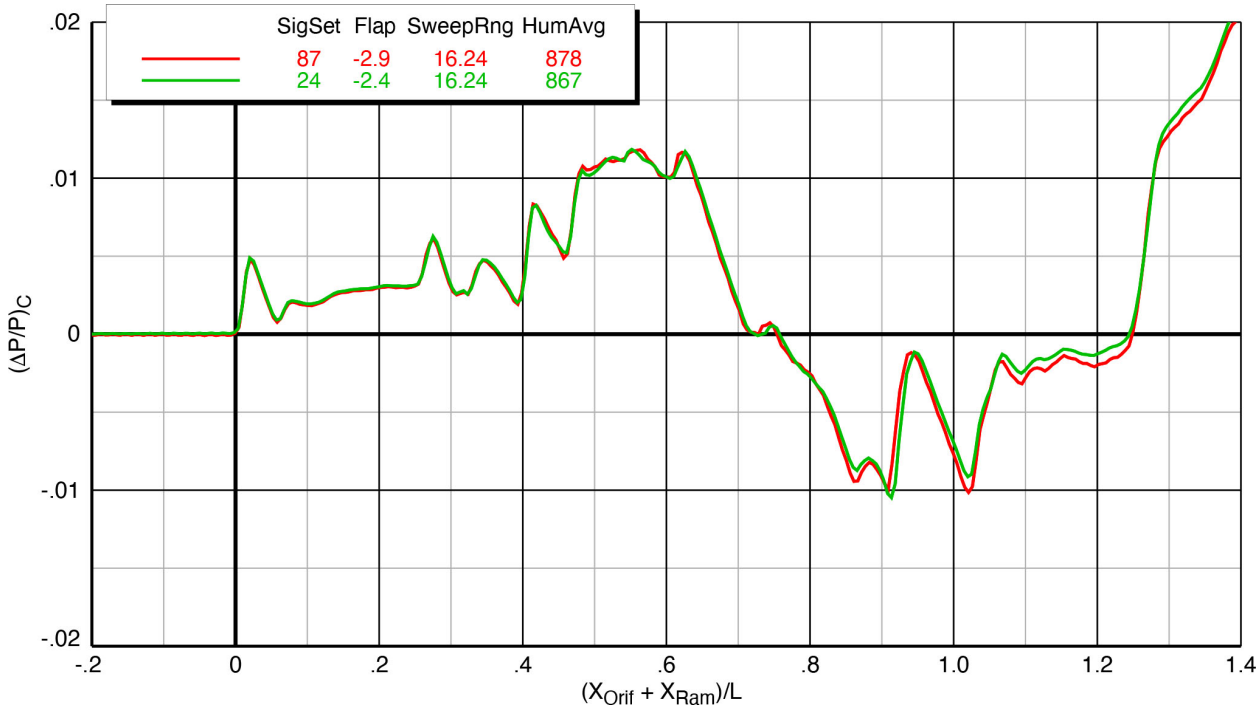

Figure 6-58 Effect of flap deflections on X-59 model (blade strut) spatially-averaged pressure signatures, Mach 1.4, *h/L* = 2, α = 2.1°, ϕ_{m2r} = 0°

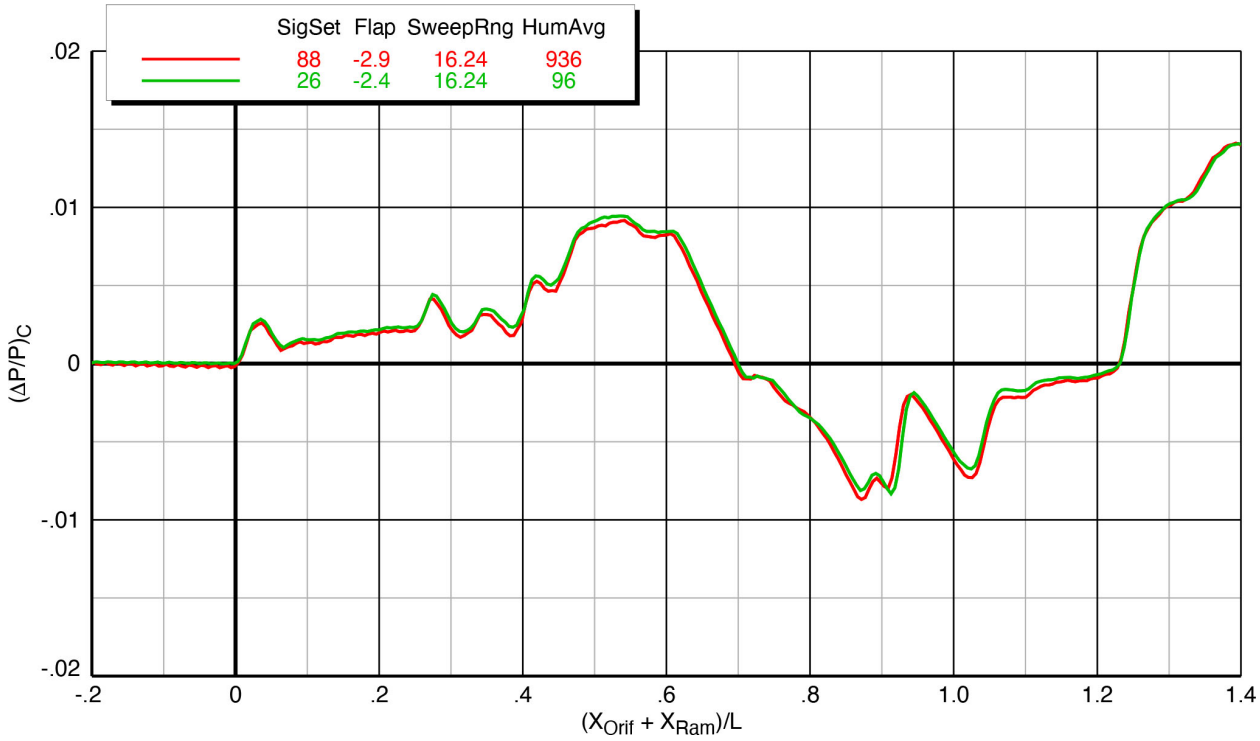

Figure 6-59 Effect of flap deflections on X-59 model (blade strut) spatially-averaged pressure signatures, Mach 1.4, *h/L* = 3, α = 2.1°, ϕ_{m2r} = 0°

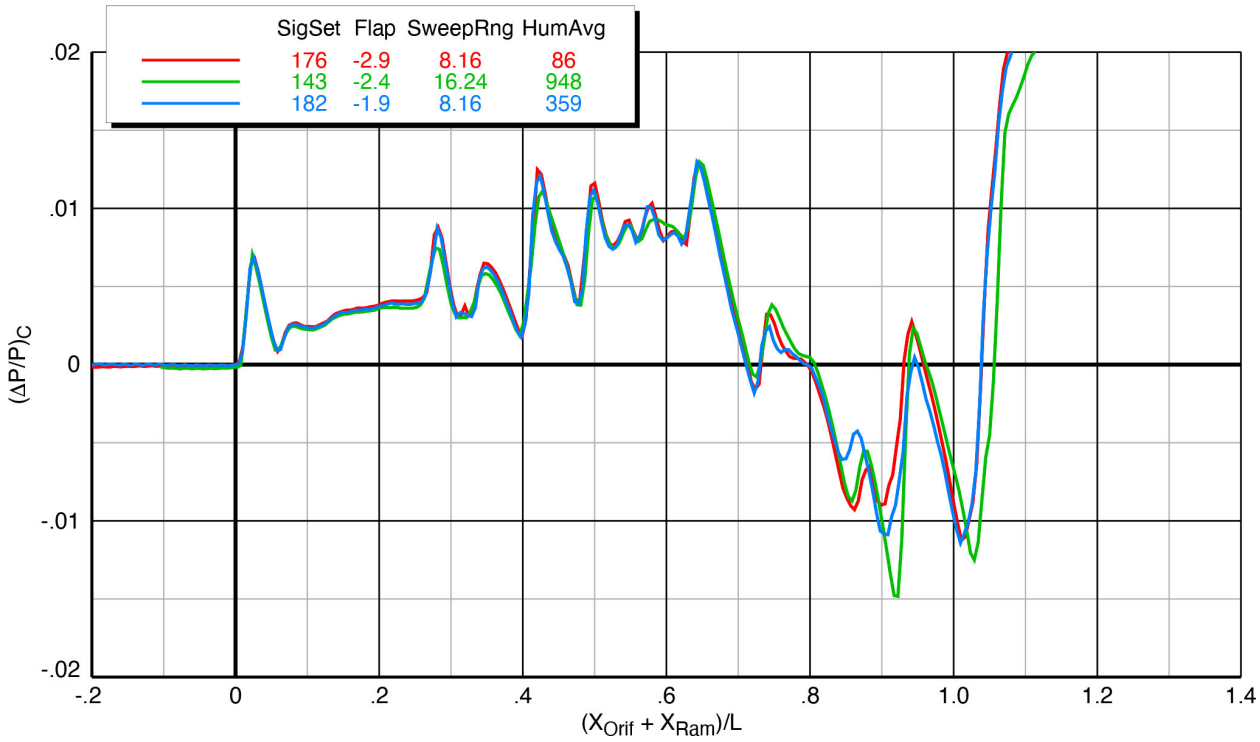

Figure 6-60 Effect of flap deflections on X-59 model (sting) spatially-averaged pressure signatures, Mach 1.4, *h/L* = 1.2, α = 2.1°, ϕ_{m2r} = 0°

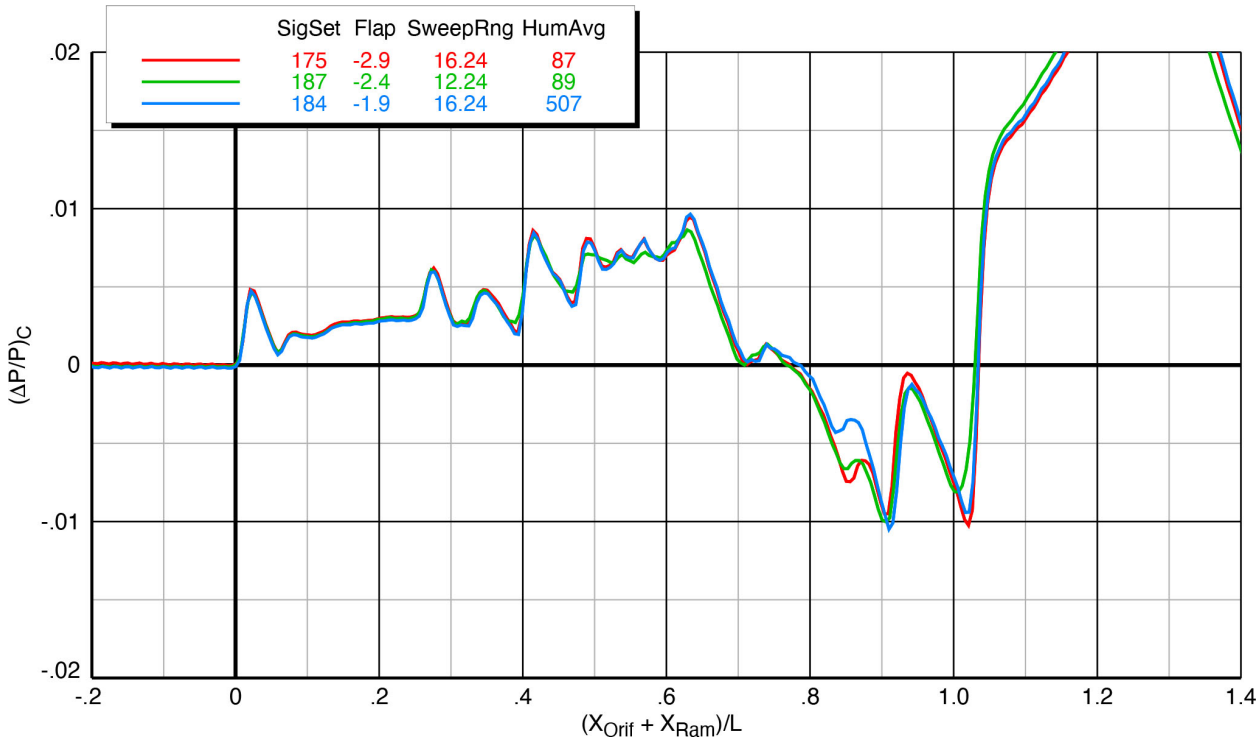

Figure 6-61 Effect of flap deflections on X-59 model (sting) spatially-averaged pressure signatures, Mach 1.4, *h/L* = 2, α = 2.1°, ϕ_{m2r} = 0°

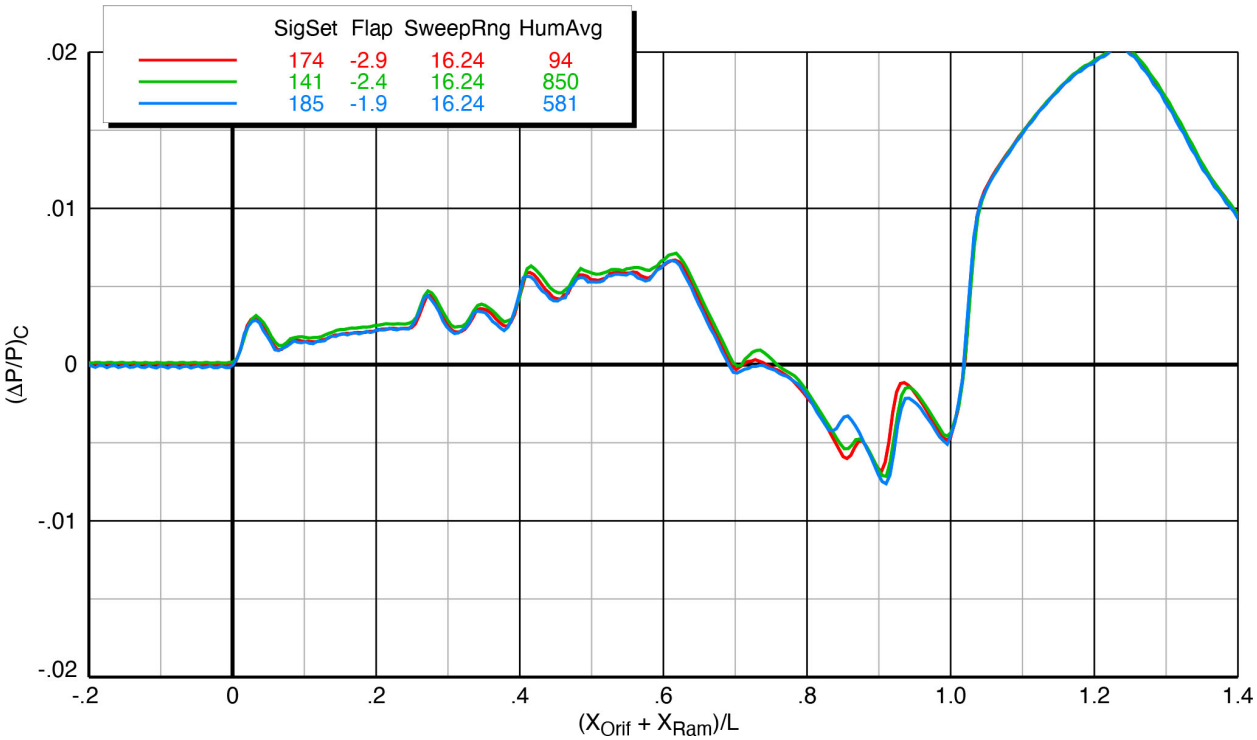

Figure 6-62 Effect of flap deflections on X-59 model (sting) spatially-averaged pressure signatures, Mach 1.4, *h/L* = 3, α = 2.1°, ϕ_{m2r} = 0°

6.8.4. Effect of Aileron Deflections

The effects of deflecting the ailerons on the model signatures are presented in the following figures:

- Figure 6-63 Blade strut Mach 1.4 *h/L* = 1.2 α = 2.1°
- Figure 6-64 Blade strut Mach 1.4 *h/L* = 2 α = 2.1°
- Figure 6-65 Blade strut Mach 1.4 *h/L* = 3 α = 2.1°
- Figure 6-66 Sting Mach 1.4 *h/L* = 1.2 α = 2.1°
- Figure 6-67 Sting Mach 1.4 *h/L* = 2 α = 2.1°
- Figure 6-68 Sting Mach 1.4 *h/L* = 3 α = 2.1°

The same priorities of the model-mounting configuration for the flap-effects data apply to the aileron-effects data as well for the same reasons. The increments in the signatures from the aileron deflections are in the same approximate *X/L* range identified for the flap deflections.

Recall that the aileron deflections are symmetric on both sides of the wing, as opposed to one up and one down for roll control.

The effects of deflecting the ailerons on both model configurations are observed in the same region of the plots as for the flap deflections: from approximately *X/L* = 0.7 to 1.0. On the blade strut configuration, the deflection effects from 1.1° to 1.6° are small and not consistent over the three different heights as to which deflection angle yields the lowest overall pressures. On the sting configuration, the deflection effects include the 0.6° aileron angle and are larger, though still not consistent in the pressure trends over the three different heights.

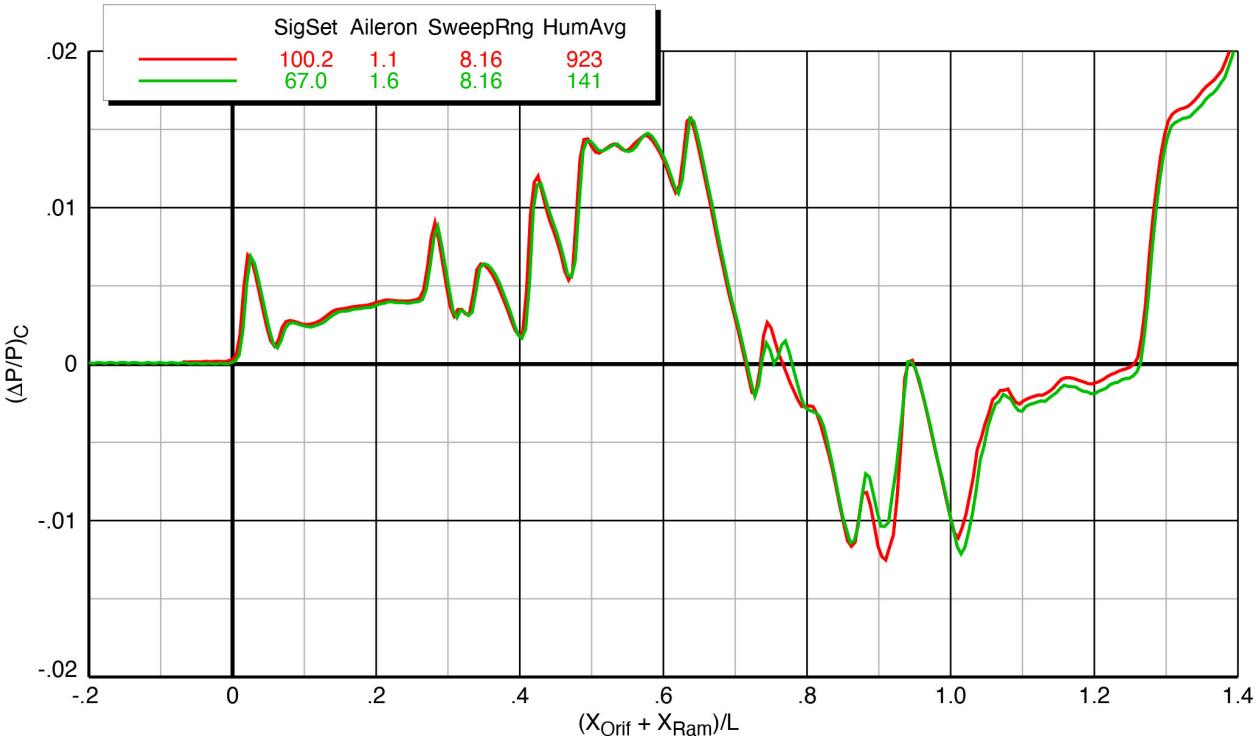

Figure 6-63 Effect of aileron deflections on X-59 model (blade strut) spatially-averaged pressure signatures, Mach 1.4, *h/L* = 1.2, α = 2.1°, ϕ_{m2r} = 0°

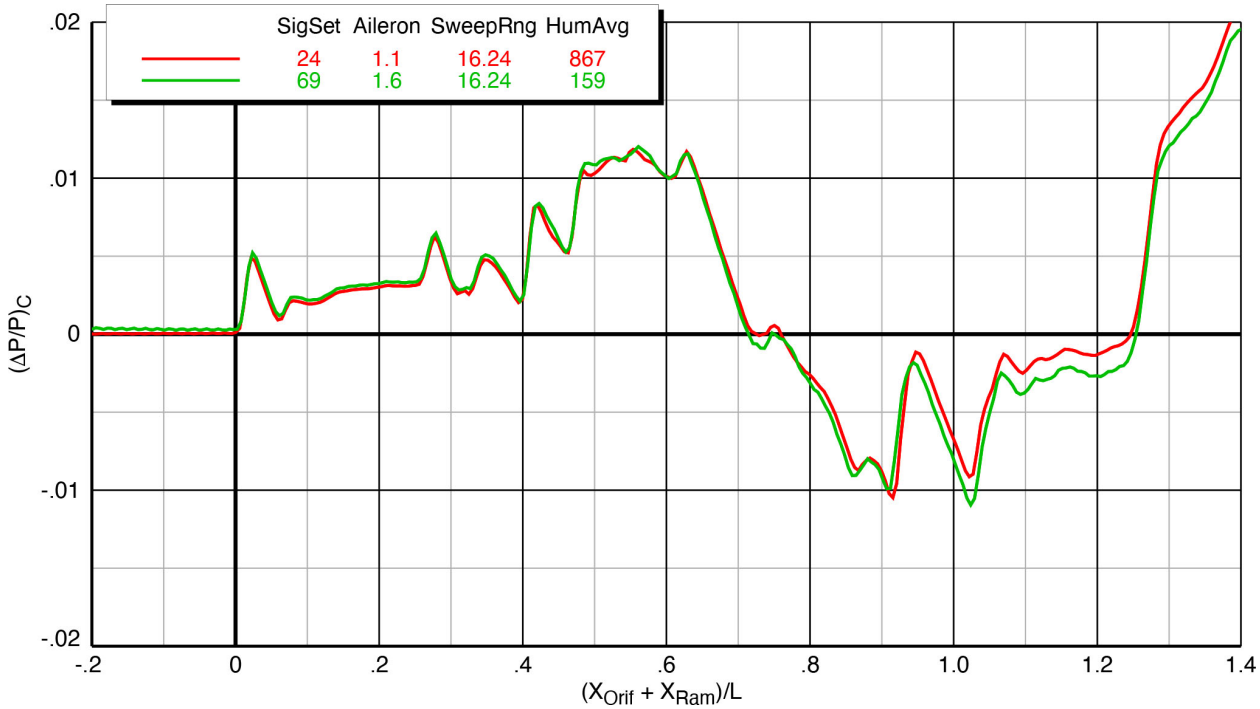

Figure 6-64 Effect of aileron deflections on X-59 model (blade strut) spatially-averaged pressure signatures, Mach 1.4, *h/L* = 2, α = 2.1°, ϕ_{m2r} = 0°

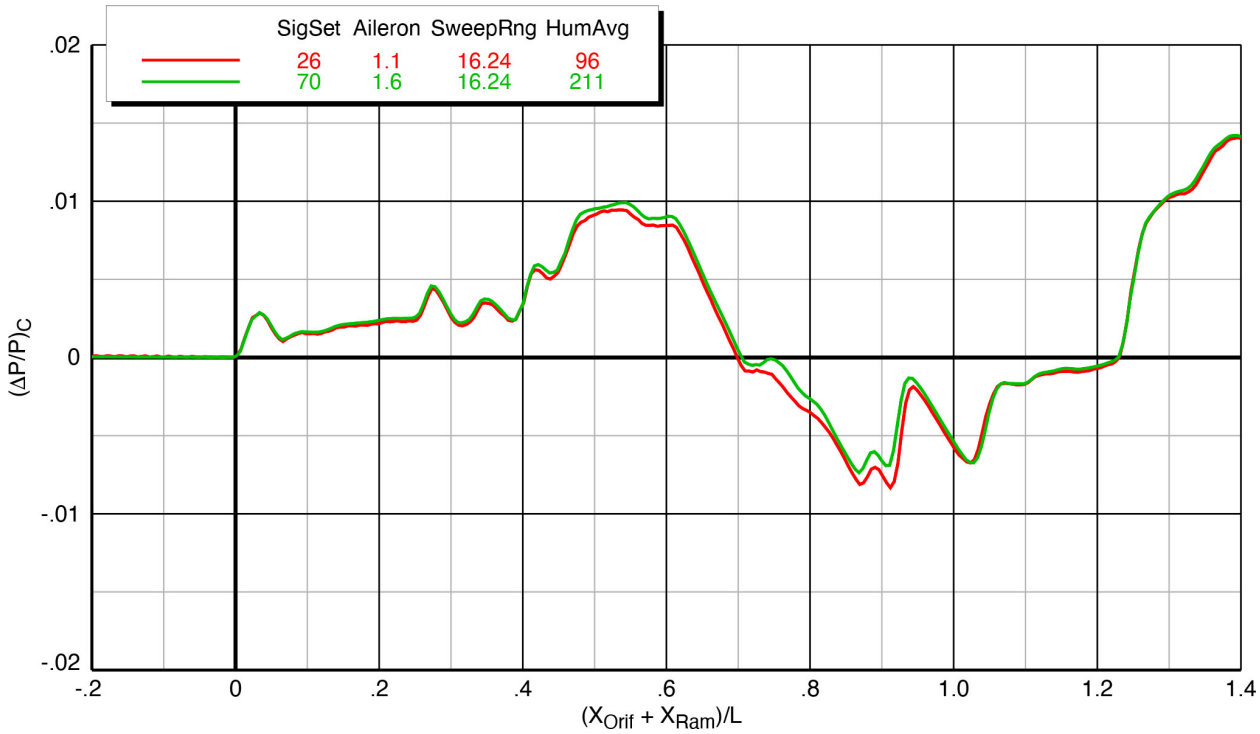

Figure 6-65 Effect of aileron deflections on X-59 model (blade strut) spatially-averaged pressure signatures, Mach 1.4, *h/L* = 3, α = 2.1°, ϕ_{m2r} = 0°

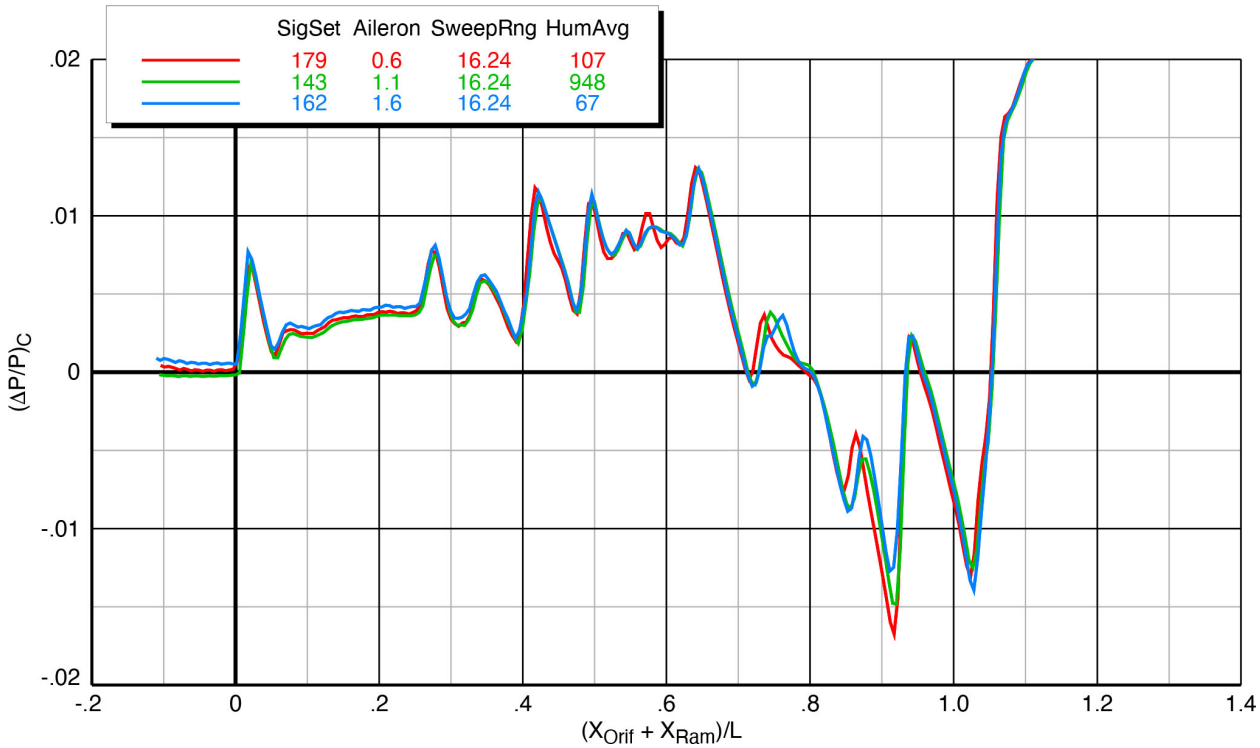

Figure 6-66 Effect of aileron deflections on X-59 model (sting) spatially-averaged pressure signatures, Mach 1.4, *h/L* = 1.2, α = 2.1°, ϕ_{m2r} = 0°

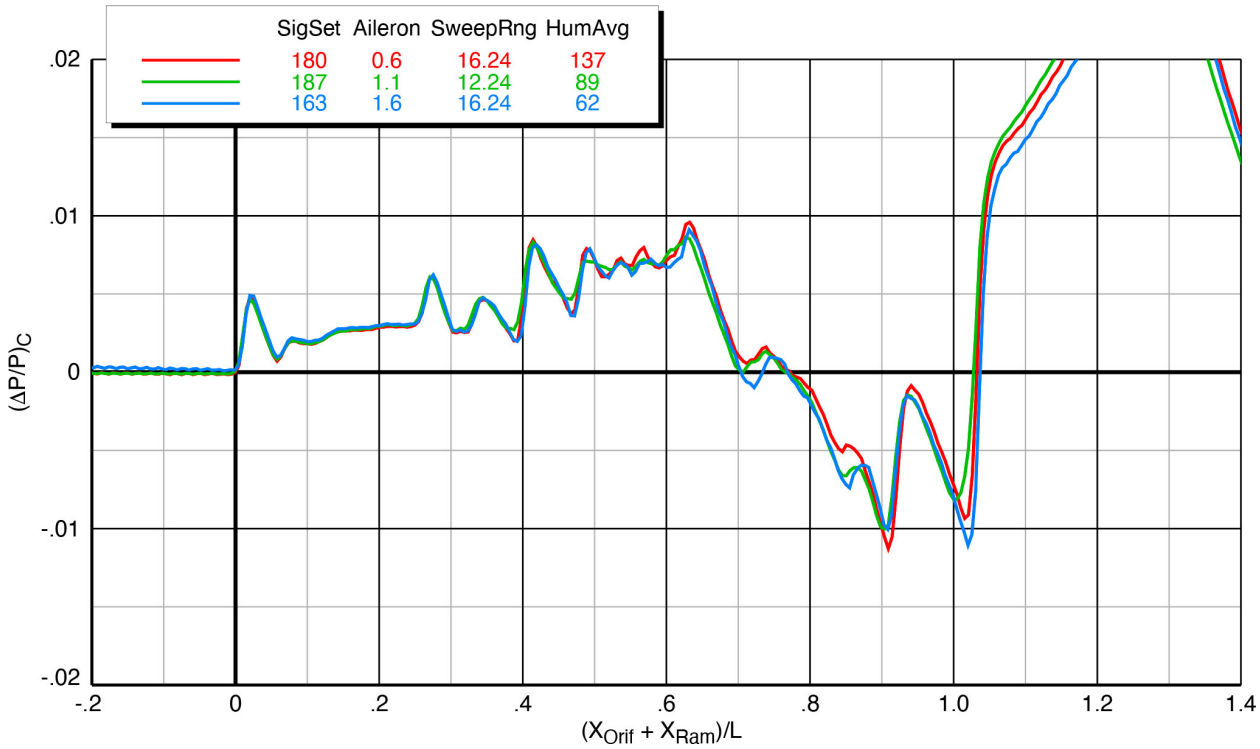

Figure 6-67 Effect of aileron deflections on X-59 model (sting) spatially-averaged pressure signatures, Mach 1.4, *h/L* = 2, α = 2.1°, ϕ_{m2r} = 0°

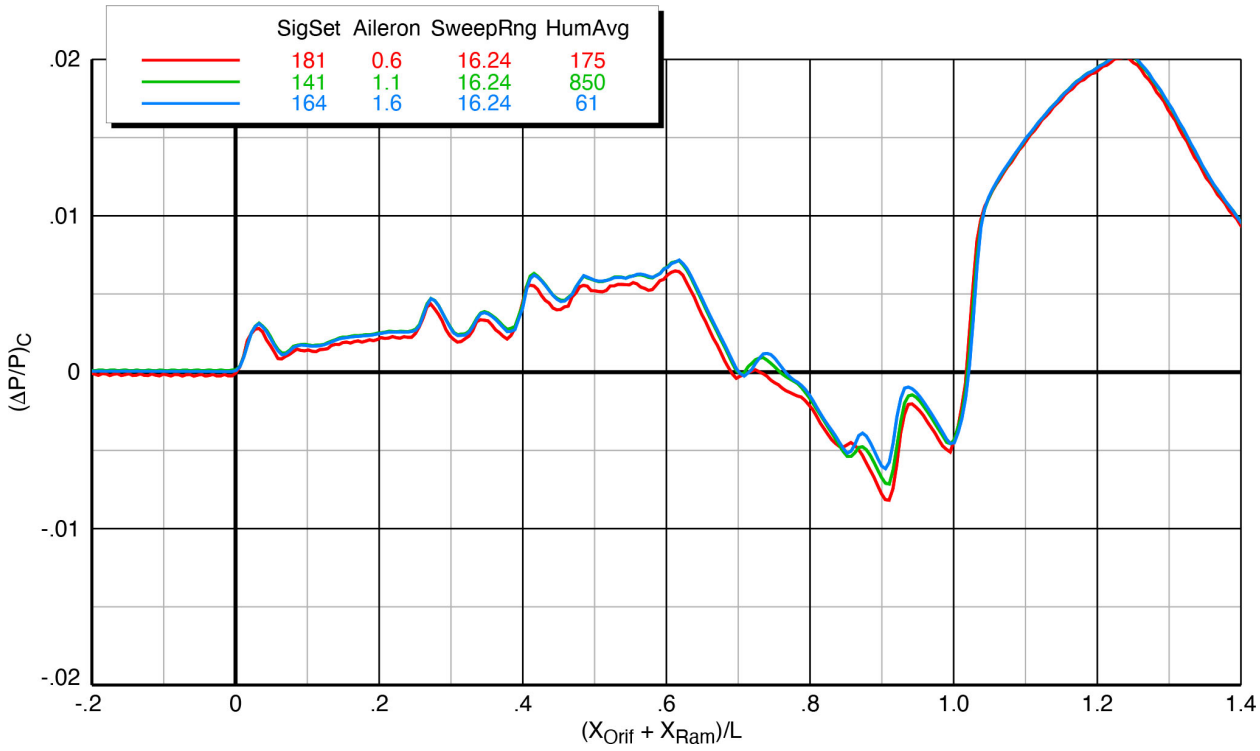

Figure 6-68 Effect of aileron deflections on X-59 model (sting) spatially-averaged pressure signatures, Mach 1.4, h/L = 3, α = 2.1°, ϕ_{m2r} = 0°

6.9. Effect of Angle of Attack

The effects of angle of attack on the model signatures are presented in the following figures:

- Figure 6-69 Blade strut Mach 1.36 *h/L* = 2
- Figure 6-70 Blade strut Mach 1.4 *h/L* = 1.2
- Figure 6-71 Blade strut Mach 1.4 *h/L* = 2
- Figure 6-72 Blade strut Mach 1.4 *h/L* = 3
- Figure 6-73 Blade strut Mach 1.47 *h/L* = 2
- Figure 6-74 Sting Mach 1.4 *h/L* = 1.2

The plots below show that changes in the model angle of attack from 1.8° to 2.4° raise the overall pressure levels in the middle and aft portions of the signatures, but not in the forward part of the signatures up to about 0.3 *X/L*. The X-59's long nose has a mostly-rounded shape and is not intended to be a lifting surface, so it is not surprising that this portion of the signature does not show much sensitivity to angle of attack. The shock from the canard is at about 0.35 *X/L*, and it shows a very slight amount of increase with angle of attack. The lifting surfaces aft of this point show fairly consistent trends of higher pressure levels with angle of attack, but the individual shocks do not show significant strength increases, though they do move forward somewhat with increasing model angle.

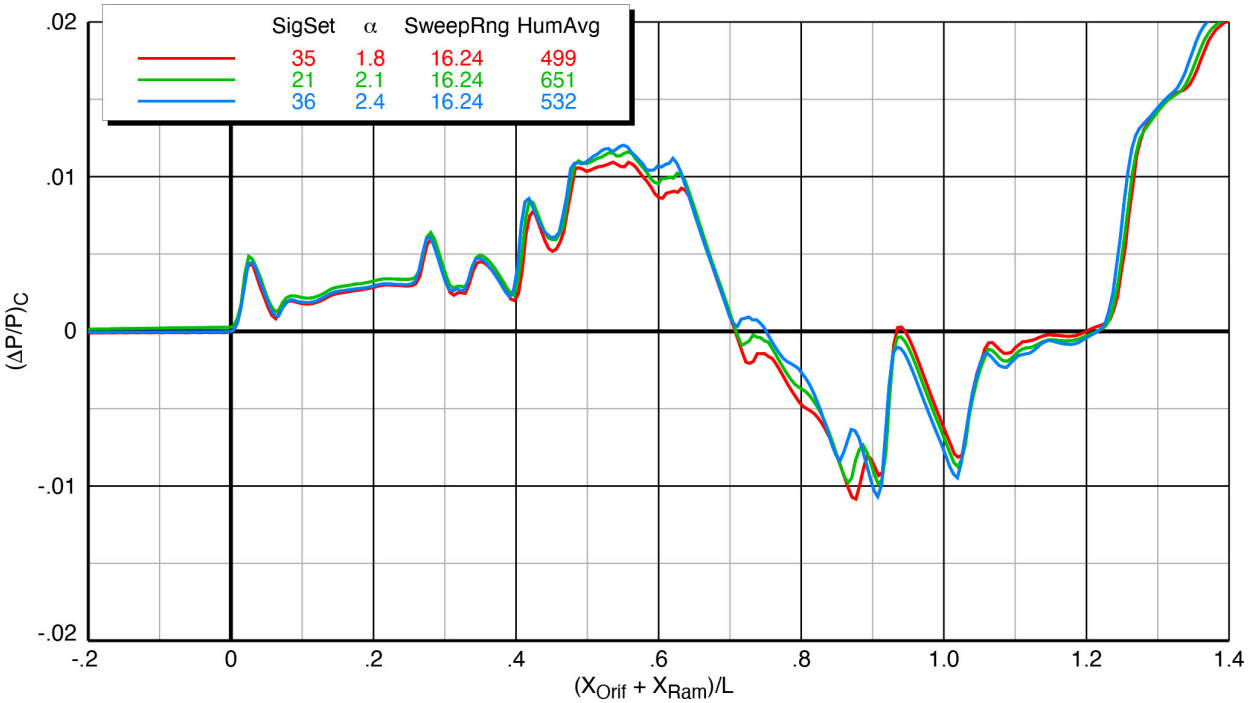

Figure 6-69 Effect of angle of attack on X-59 model (blade strut) spatially-averaged pressure signatures, Mach 1.36, *h/L* = 2, ϕ_{m2r} = 0°

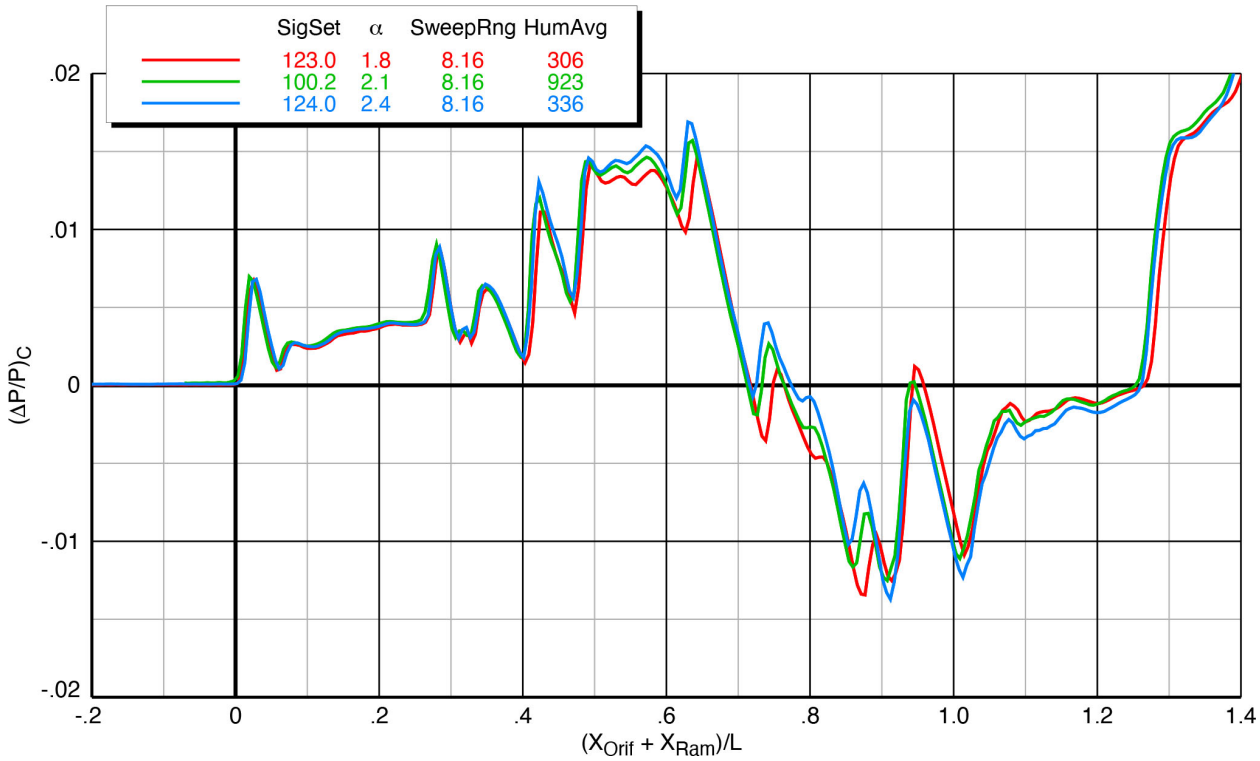

Figure 6-70 Effect of angle of attack on X-59 model (blade strut) spatially-averaged pressure signatures, Mach 1.4, *h/L* = 1.2, ϕ_{m2r} = 0°

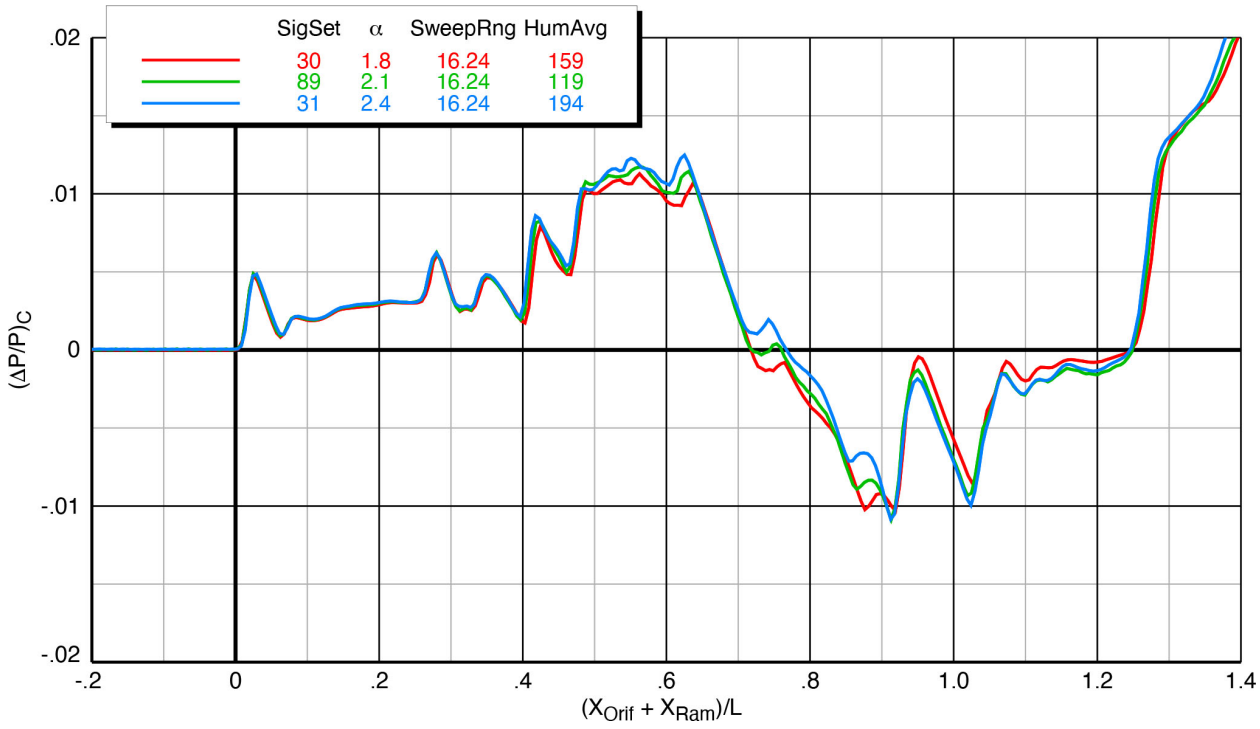

Figure 6-71 Effect of angle of attack on X-59 model (blade strut) spatially-averaged pressure signatures, Mach 1.4, *h/L* = 2, ϕ_{m2r} = 0°

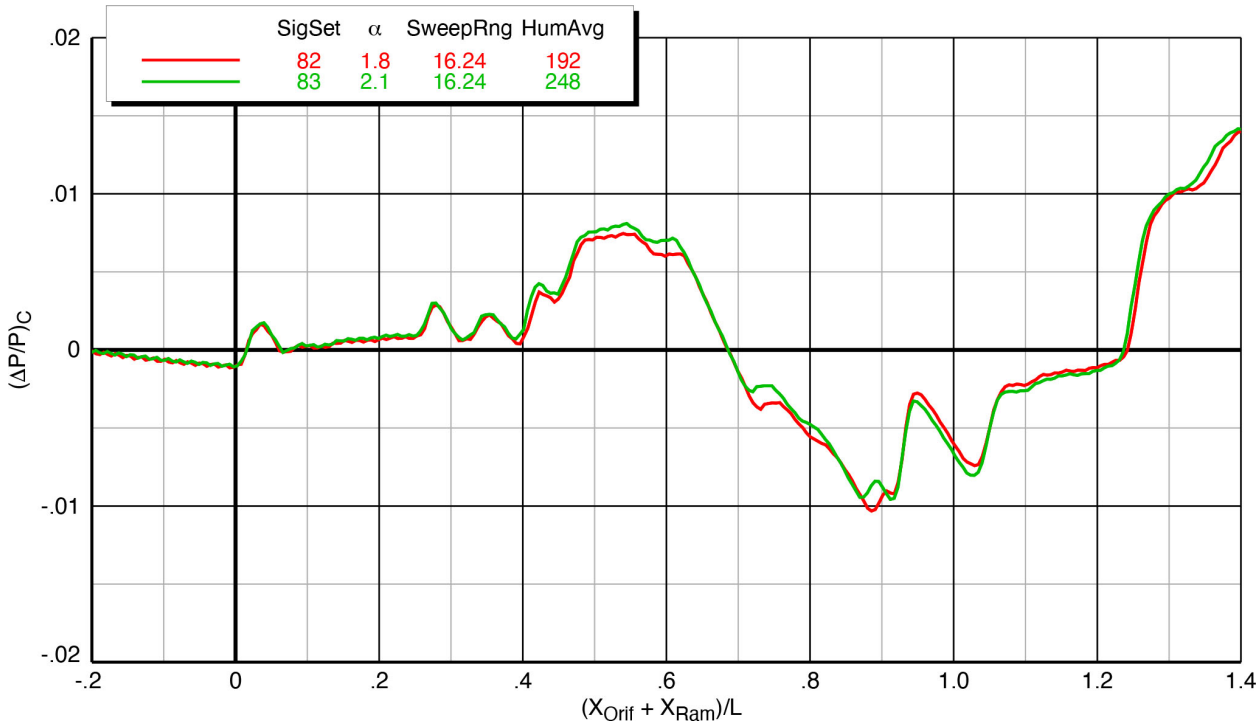

Figure 6-72 Effect of angle of attack on X-59 model (blade strut) spatially-averaged pressure signatures, Mach 1.4, *h/L* = 3, ϕ_{m2r} = 0°, T-tail = 2.7°

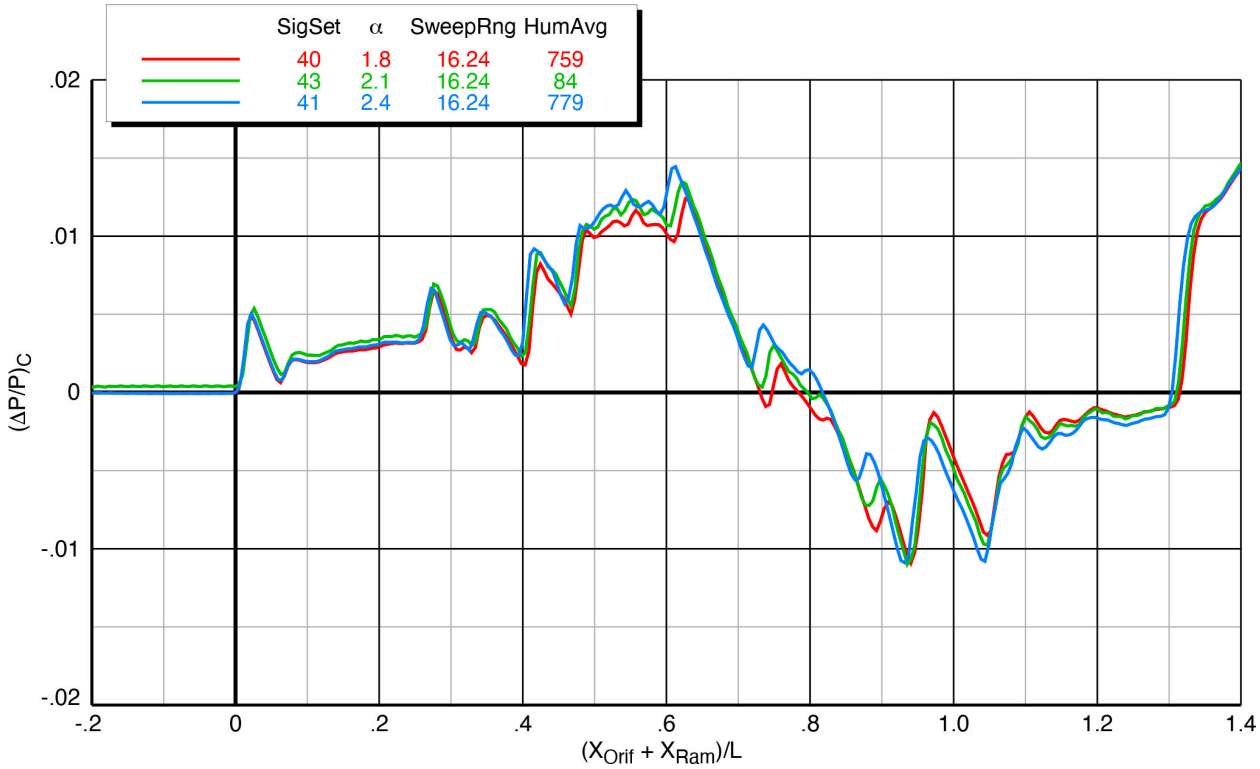

Figure 6-73 Effect of angle of attack on X-59 model (blade strut) spatially-averaged pressure signatures, Mach 1.47, *h/L* = 2, ϕ_{m2r} = 0°

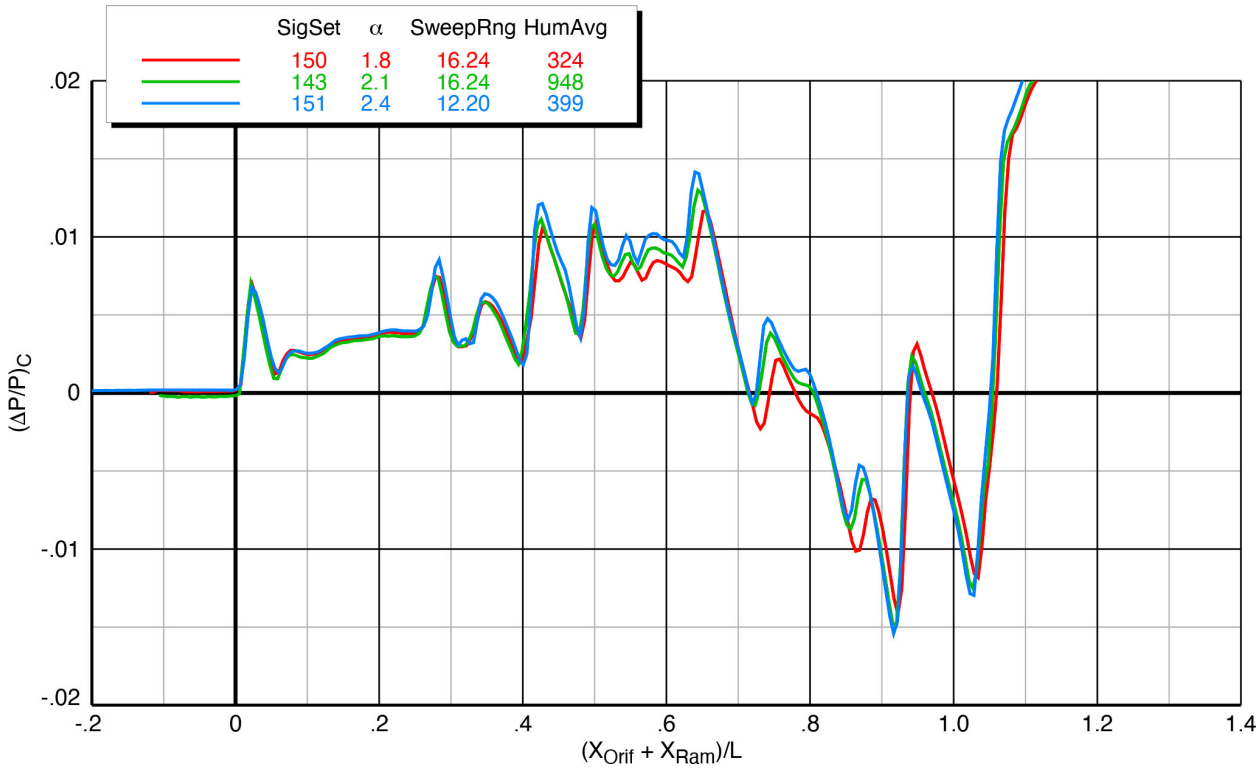

Figure 6-74 Effect of angle of attack on X-59 model (sting) spatially-averaged pressure signatures, Mach 1.4, *h/L* = 1.2, ϕ_{m2r} = 0°

6.10. Effect of Height

The effects of height on the model signatures are presented in the following figures:

- Figure 6-75 Blade strut Mach 1.36 α = 2.1°
- Figure 6-76 Blade strut Mach 1.4 α = 2.1°
- Figure 6-77 Blade strut Mach 1.47 α = 2.1°
- Figure 6-78 Sting Mach 1.36 α = 2.1°
- Figure 6-79 Sting Mach 1.4 α = 2.1°
- Figure 6-80 Sting Mach 1.47 α = 2.1°

Changing the model height relative to the pressure rail has a very large effect on the signatures as evidenced in the six plots below. Increasing the height shows the aging of the signatures in terms of decreasing overall pressure levels and shock strengths. The locations of the shock waves stay about the same at the different heights in the plots at all three Mach numbers and both model-mounting configurations.

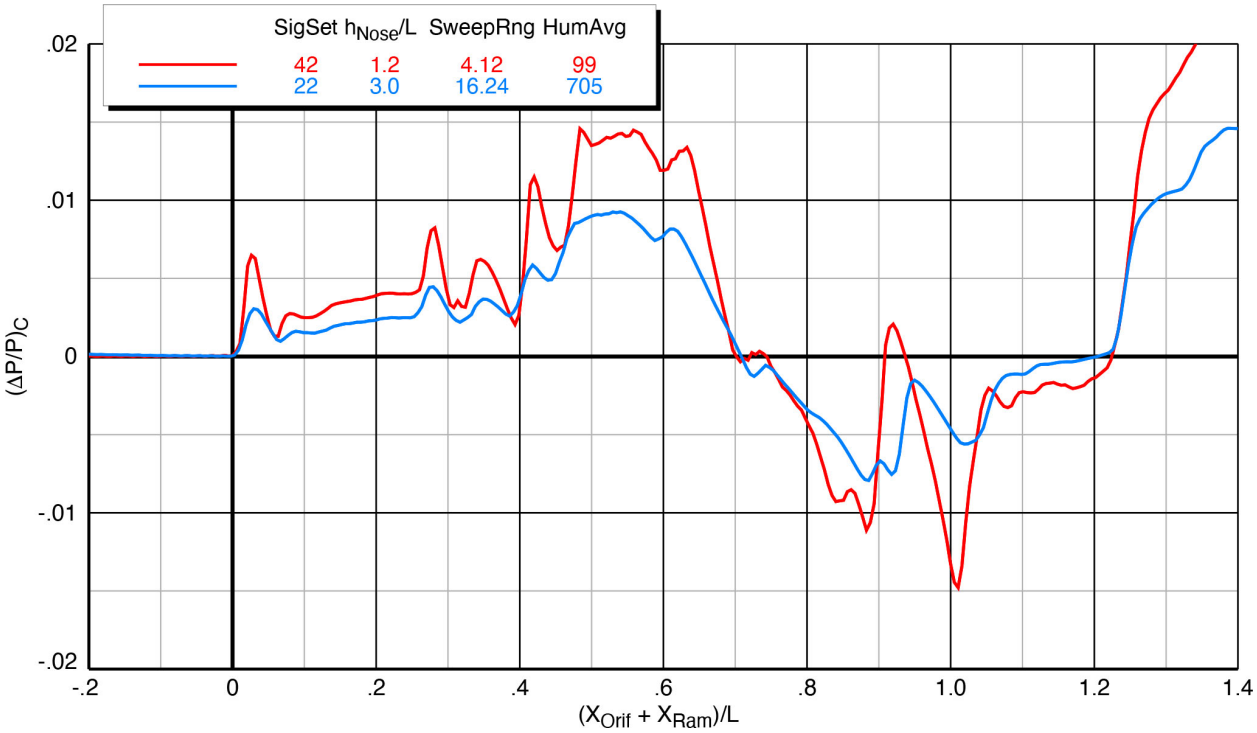

Figure 6-75 Effect of height on X-59 model (blade strut) spatially-averaged pressure signatures, Mach 1.36, α = 2.1°, ϕ_{m2r} = 0°

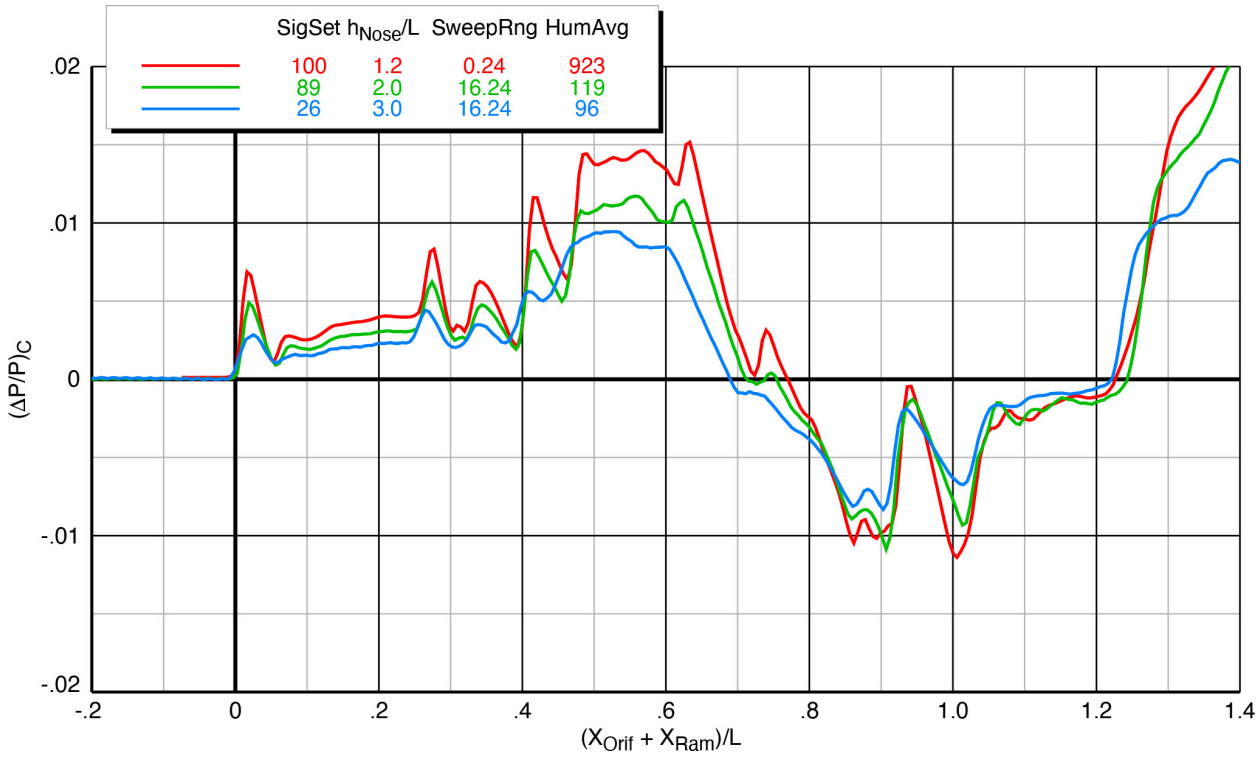

Figure 6-76 Effect of height on X-59 model (blade strut) spatially-averaged pressure signatures, Mach 1.4, α = 2.1°, ϕ_{m2r} = 0°

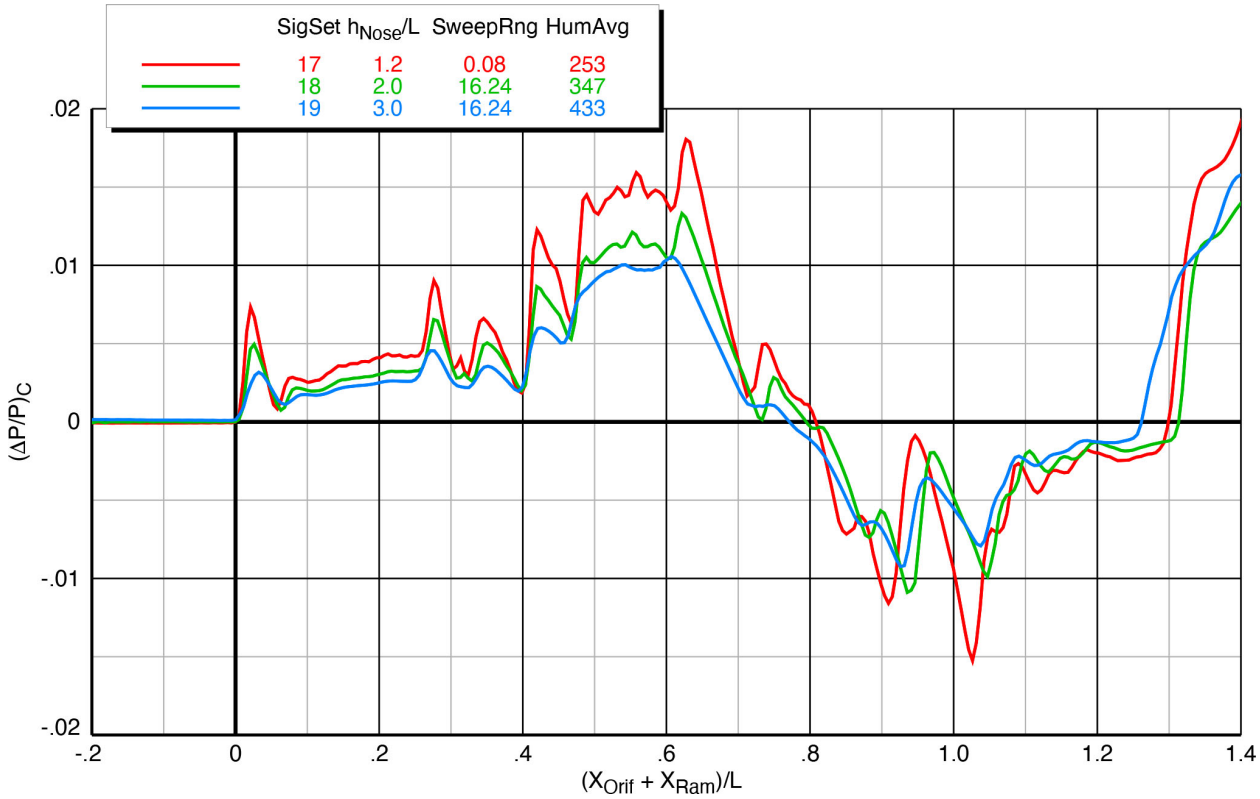

Figure 6-77 Effect of height on X-59 model (blade strut) spatially-averaged pressure signatures, Mach 1.47, α = 2.1°, ϕ_{m2r} = 0°

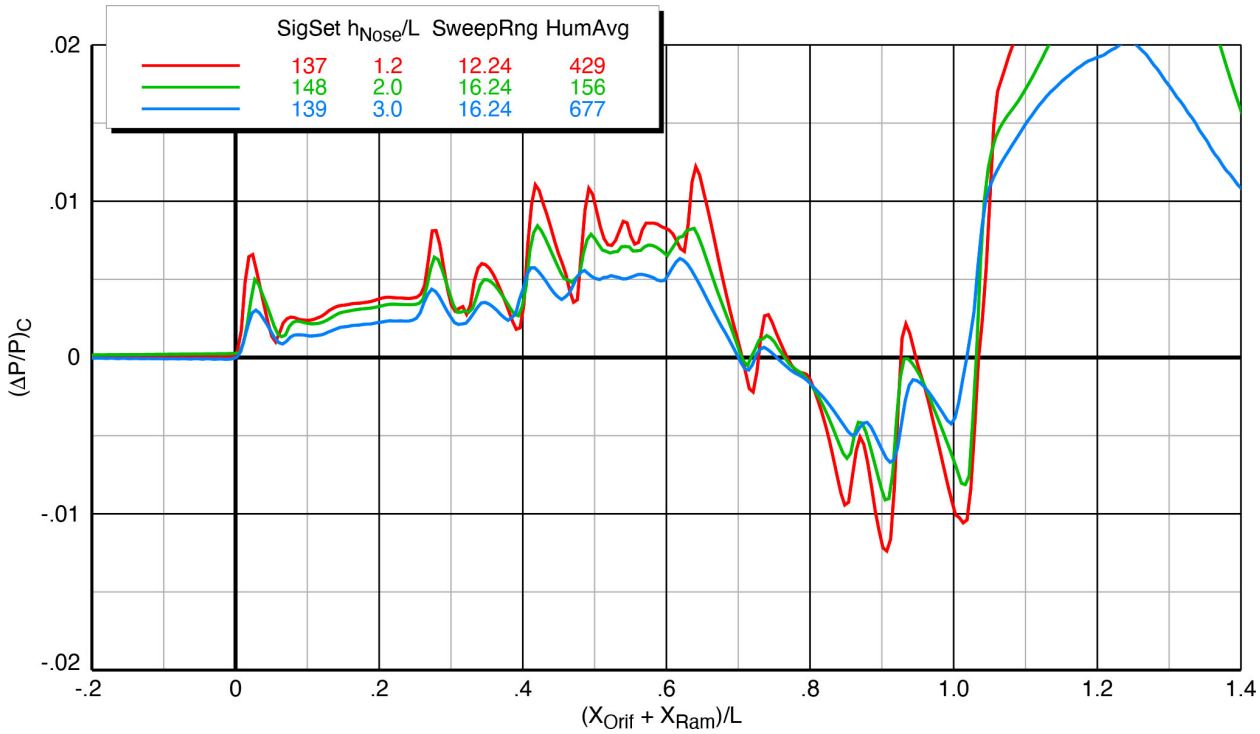

Figure 6-78 Effect of height on X-59 model (sting) spatially-averaged pressure signatures, Mach 1.36, α = 2.1°, ϕ_{m2r} = 0°

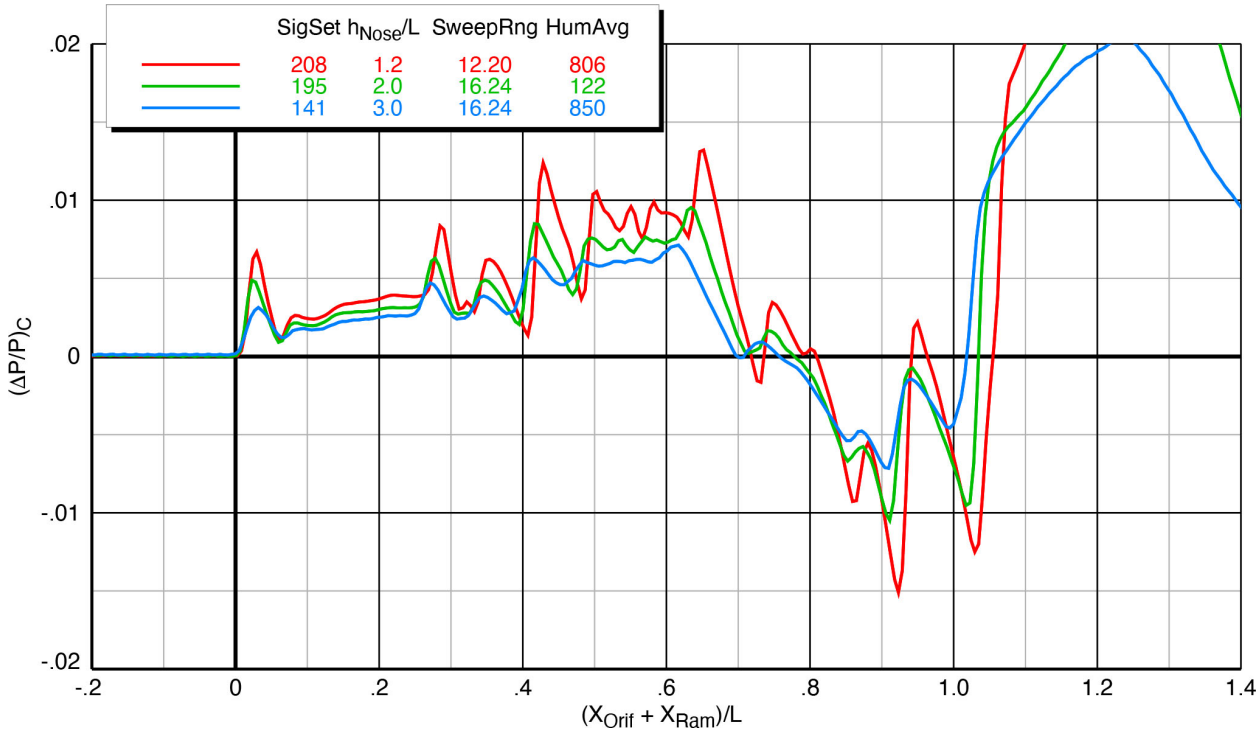

Figure 6-79 Effect of height on X-59 model (sting) spatially-averaged pressure signatures, Mach 1.4, α = 2.1°, ϕ_{m2r} = 0°

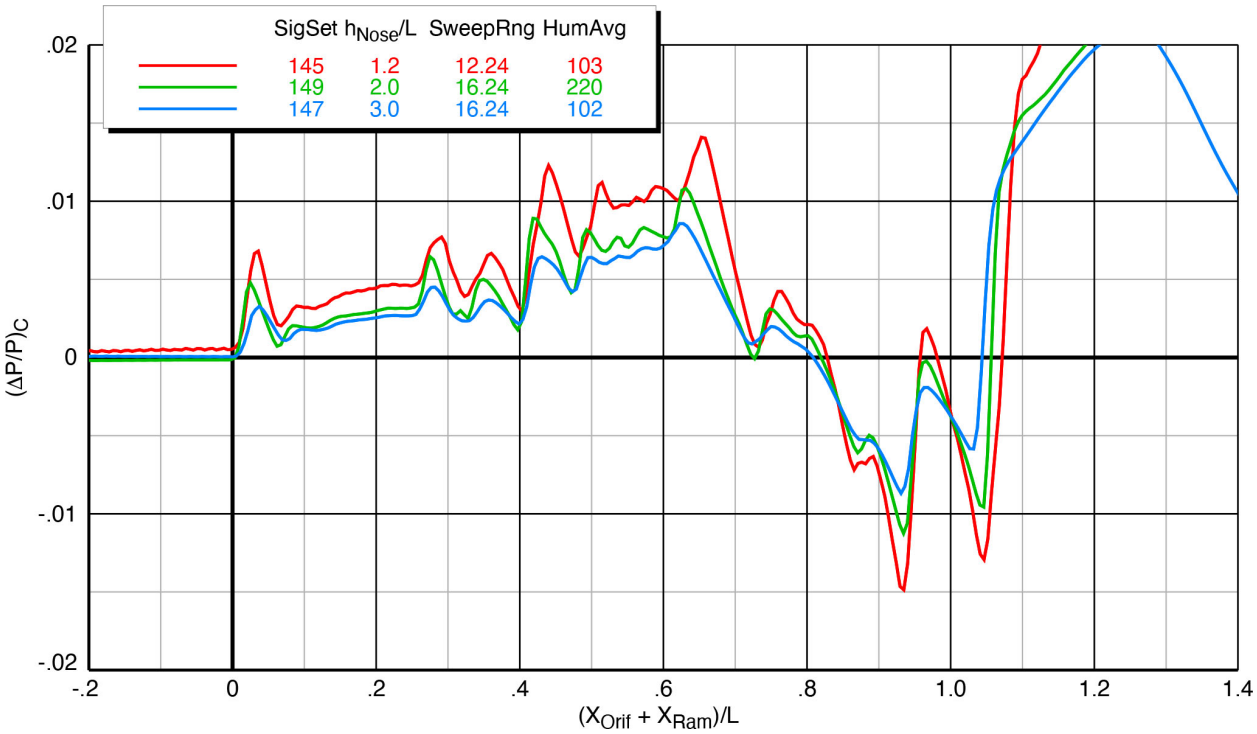

Figure 6-80 Effect of height on X-59 model (sting) spatially-averaged pressure signatures, Mach 1.47, α = 2.1°, ϕ_{m2r} = 0°

6.11. Effect of Roll Angle

Signature measurements were taken at various roll angles for the following tunnel and model conditions listed below, and plotted in the identified by figure numbers:

- Figure 6-81 Blade strut Mach 1.36 h/L = 2 α = 2.1° 15° roll increments
- Figure 6-82 Blade strut Mach 1.4 h/L = 1.2 α = 2.1° 15° & 5° roll increments
- Figure 6-83 Blade strut Mach 1.4 h/L = 2 α = 2.1° 15° & 5° roll increments
- Figure 6-84 Blade strut Mach 1.4 h/L = 3 α = 2.1° 15° & 5° roll increments
- Figure 6-85 Blade strut Mach 1.47 h/L = 2 α = 2.1° 15° roll increments
- Figure 6-86 Sting Mach 1.4 h/L = 1.2 α = 2.1° 15° & 5° roll increments
- Figure 6-87 Sting Mach 1.4 h/L = 1.2 α = 2.1° 15° & 5° roll increments
- Figure 6-88 Sting Mach 1.4 h/L = 1.2 α = 2.1° 15° & 5° roll increments

The model was set at roll angles from 5° to 45° relative to the pressure rail to assess the changes in the signatures at equivalent off-track angles away from the centerline boom propagation. At Mach 1.36 and 1.47, only the data at 15° roll increments were acquired, but the full roll-angle sweeps at every 5° were acquired at Mach 1.4 for both the blade strut and sting configurations. There is a general reduction in pressure levels in the middle part of the signatures at all heights and Mach numbers as the roll angle is increased, but in the aft part, the signature changes are more complicated with all the interactions of the shock waves from the multiple surfaces at the rear of the vehicle.

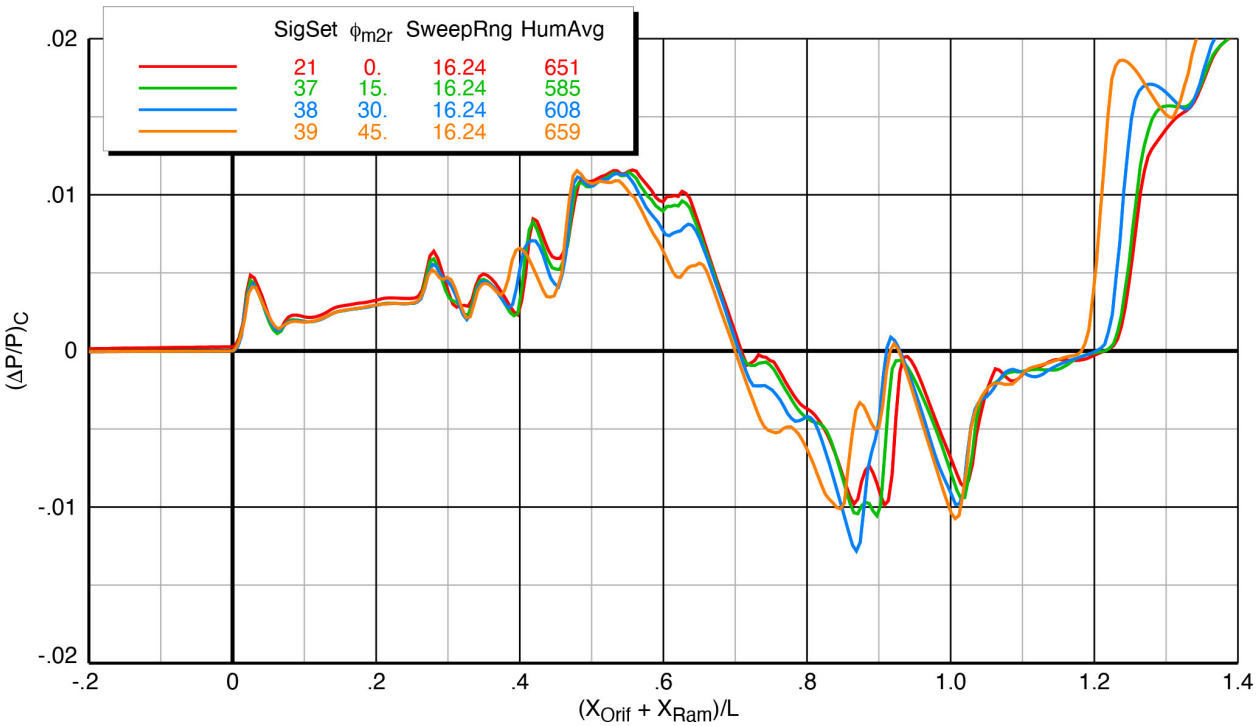

Figure 6-81 Effect of roll angle (15° increments) on X-59 model (blade strut) spatially-averaged pressure signatures, Mach 1.36, h/L = 2, α = 2.1°

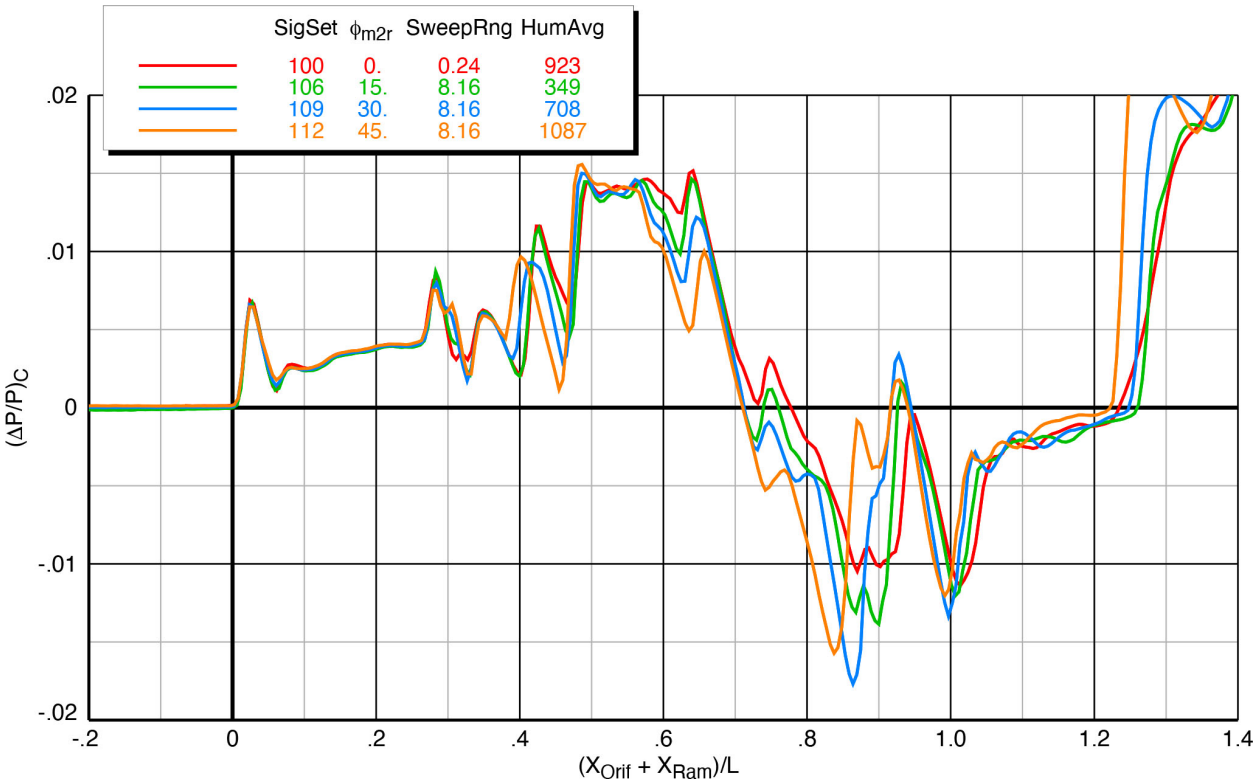

(a) 15° roll angle increments

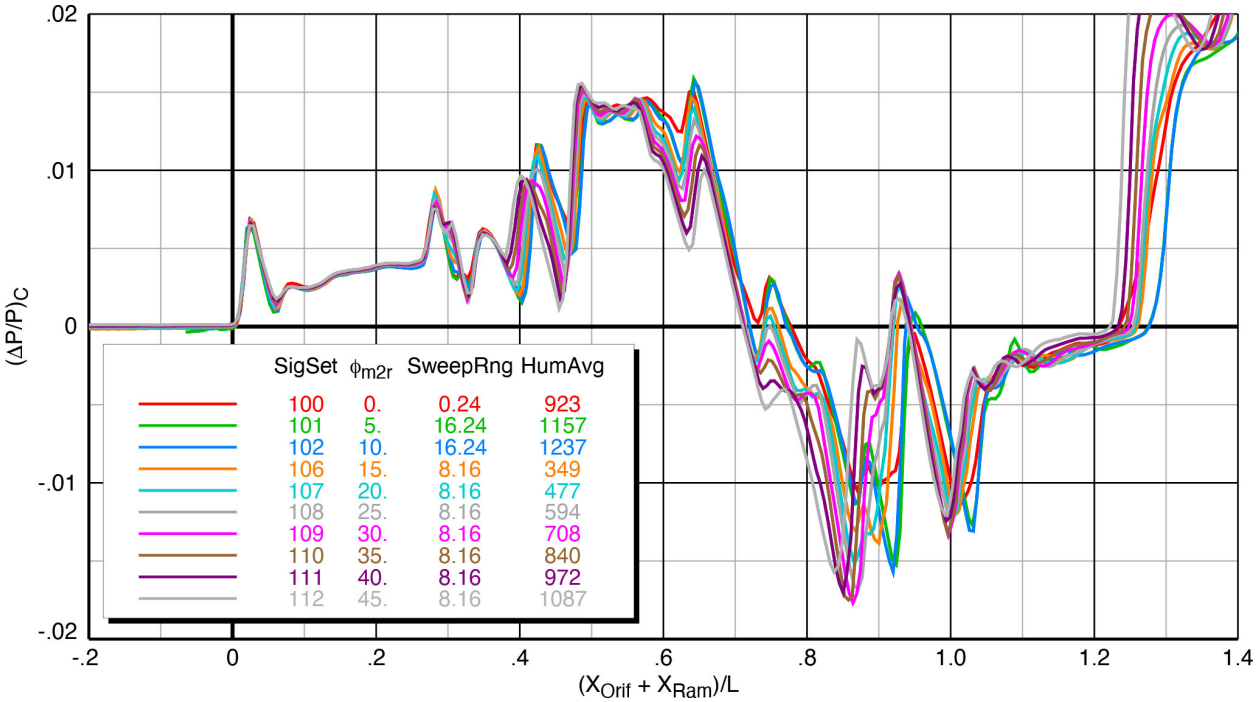

(b) 5° roll angle increments

Figure 6-82 Effect of roll angle on X-59 model (blade strut) spatially-averaged pressure signatures, Mach 1.4, *h/L* = 1.2, α = 2.1°

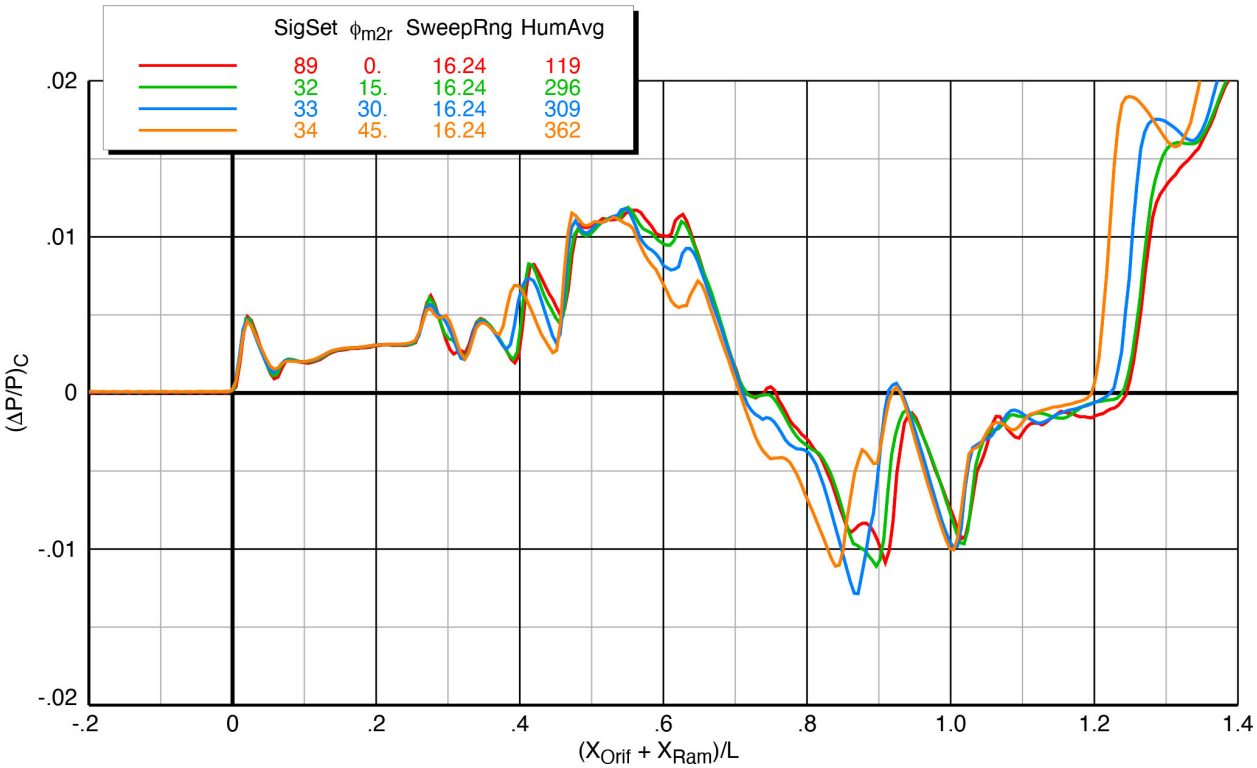

(a) 15° roll angle increments

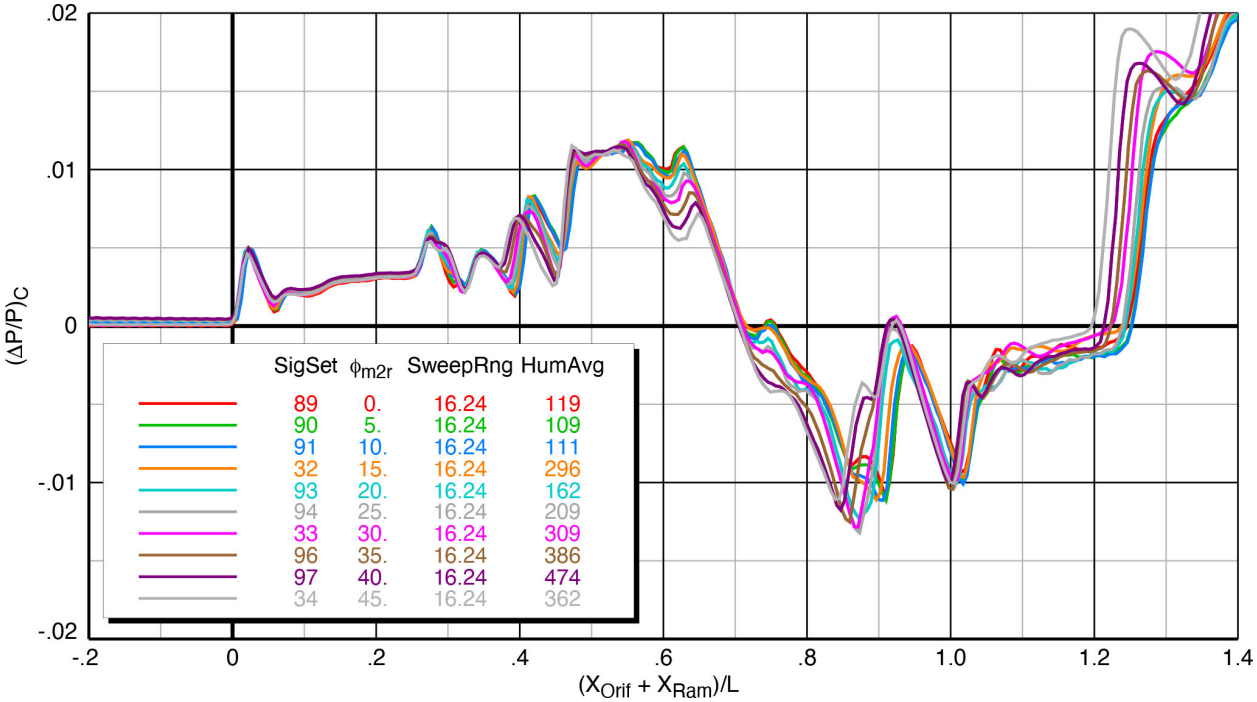

(b) 5° roll angle increments

Figure 6-83 Effect of roll angle (5° increments) on X-59 model (blade strut) spatially-averaged pressure signatures, Mach 1.4, *h/L* = 2, α = 2.1°

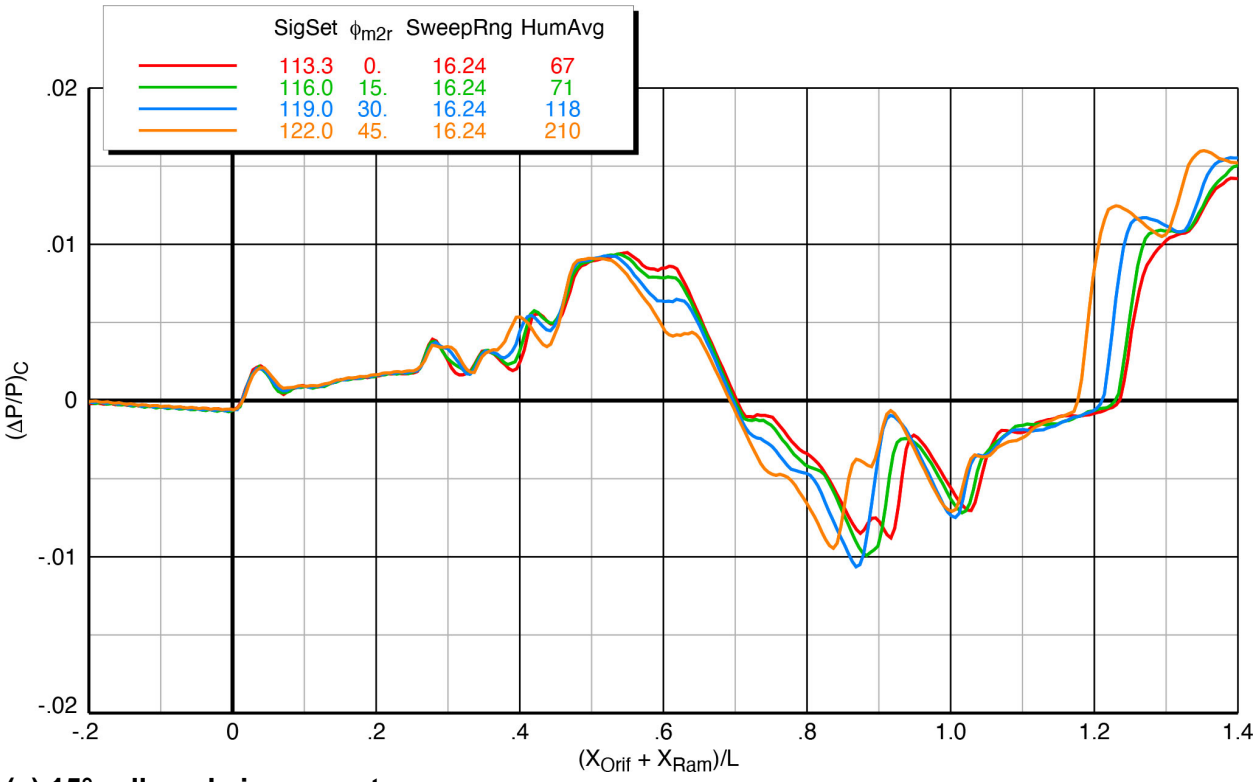

(a) 15° roll angle increments

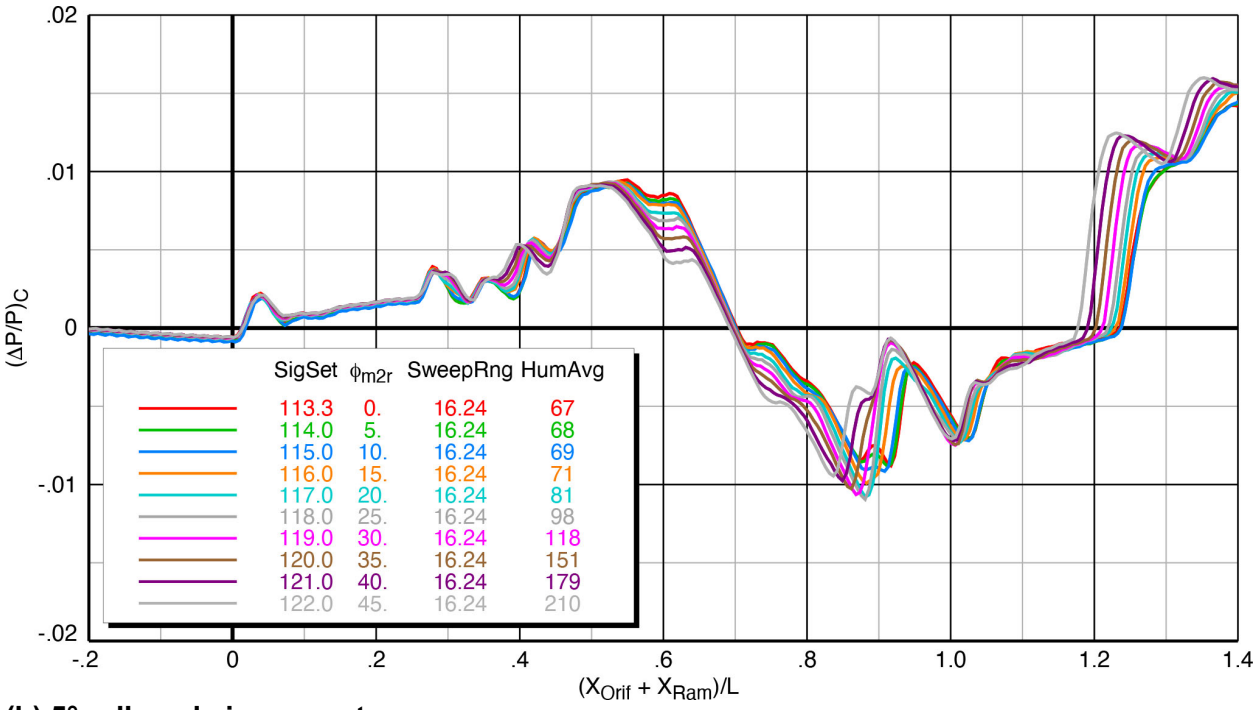

(b) 5° roll angle increments

Figure 6-84 Effect of roll angle (5° increments) on X-59 model (blade strut) spatially-averaged pressure signatures, Mach 1.4, *h/L* = 3, α = 2.1°

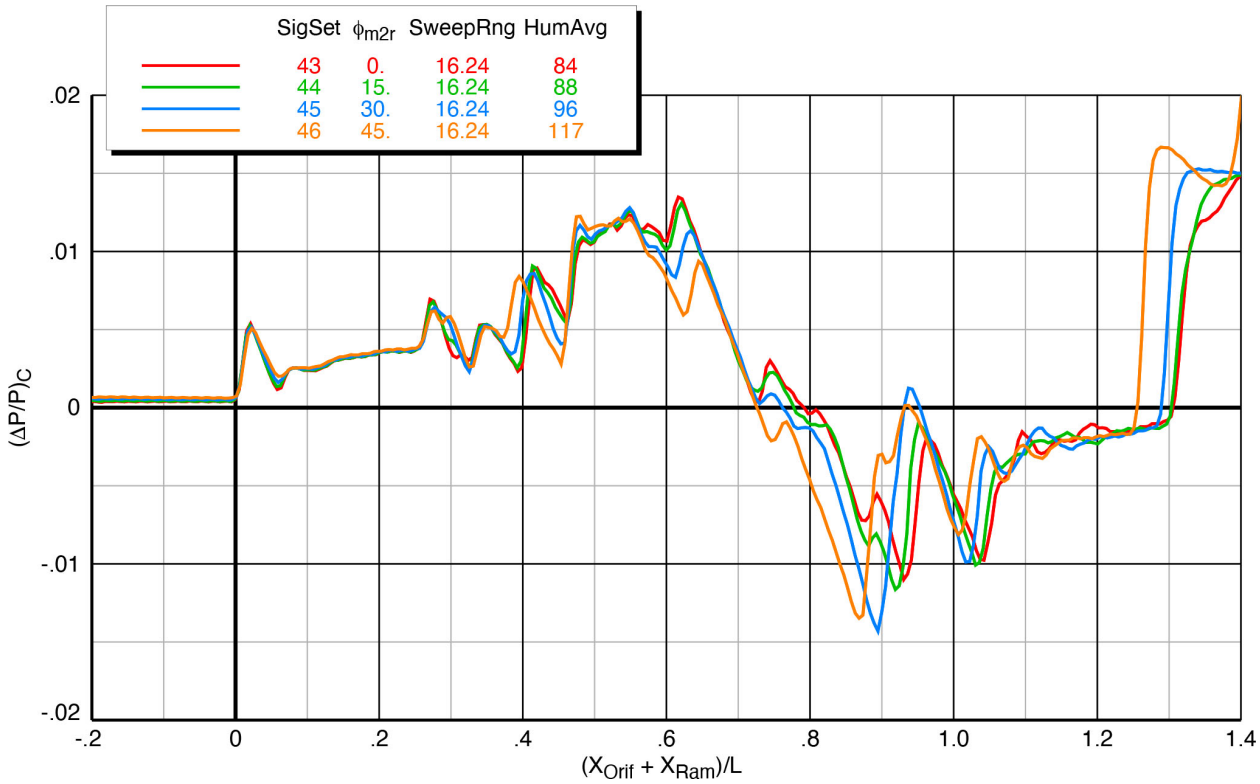

Figure 6-85 Effect of roll angle (15° increments) on X-59 model (blade strut) spatially-averaged pressure signatures, Mach 1.47, *h/L* = 2, α = 2.1°

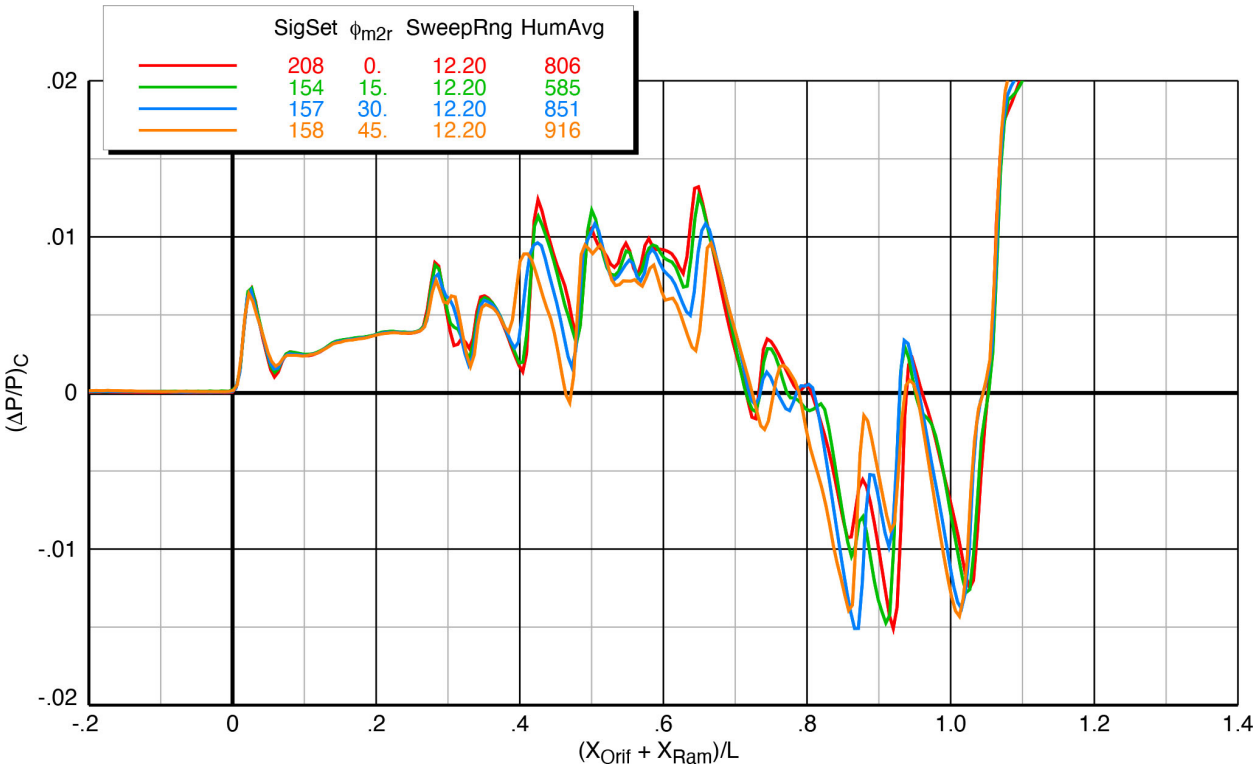

(a) 15° roll angle increments

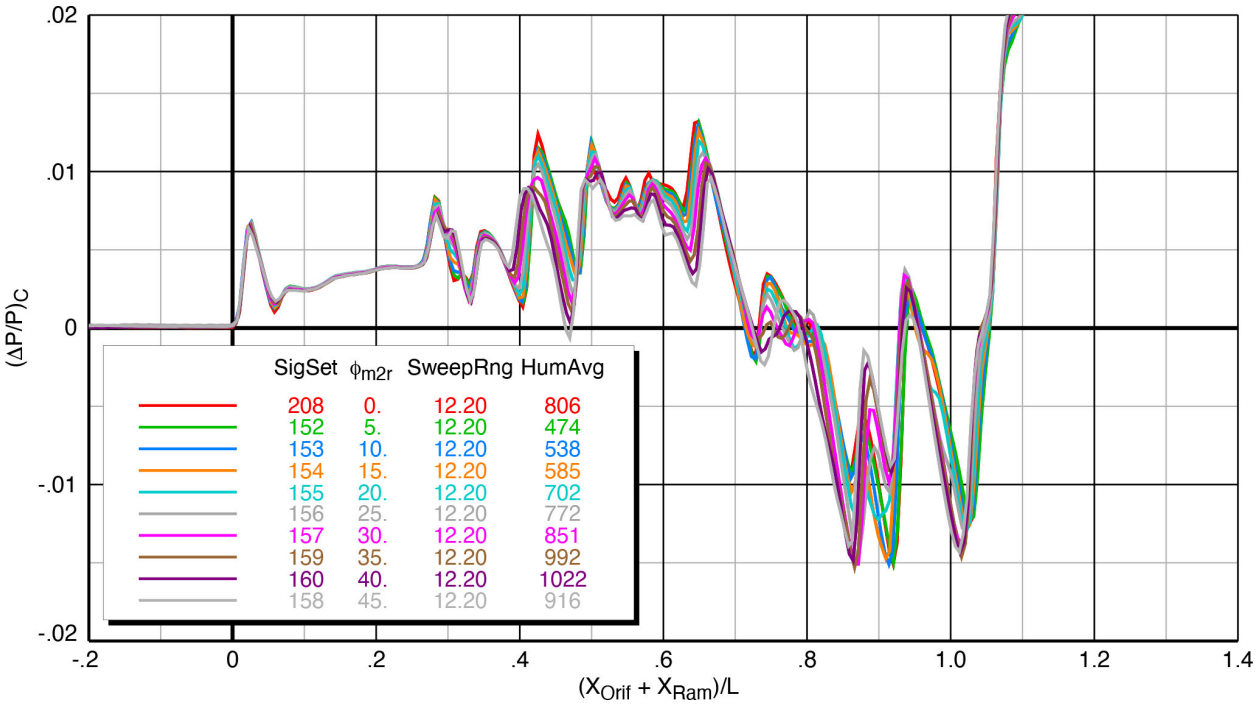

(b) 5° roll angle increments

Figure 6-86 Effect of roll angle (5° increments) on X-59 model (sting) spatially-averaged pressure signatures, Mach 1.4, *h/L* = 1.2, α = 2.1°

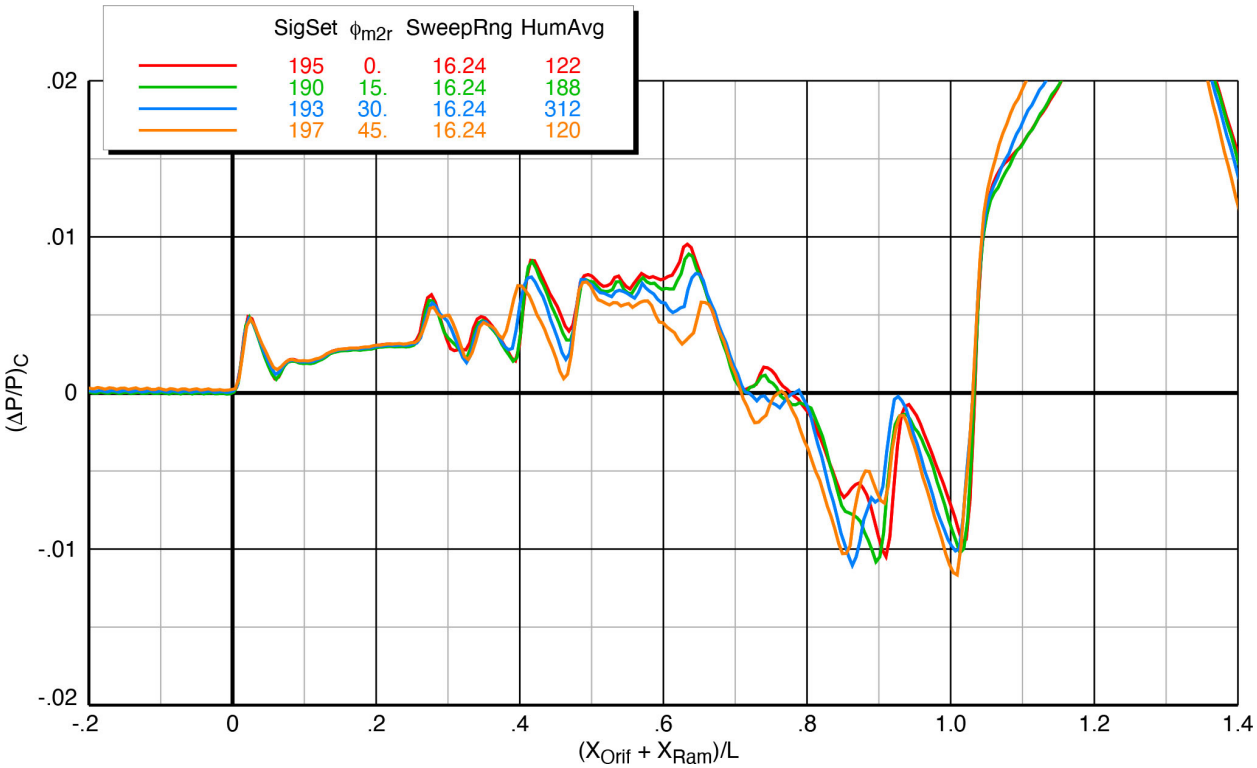

(a) 15° roll angle increments

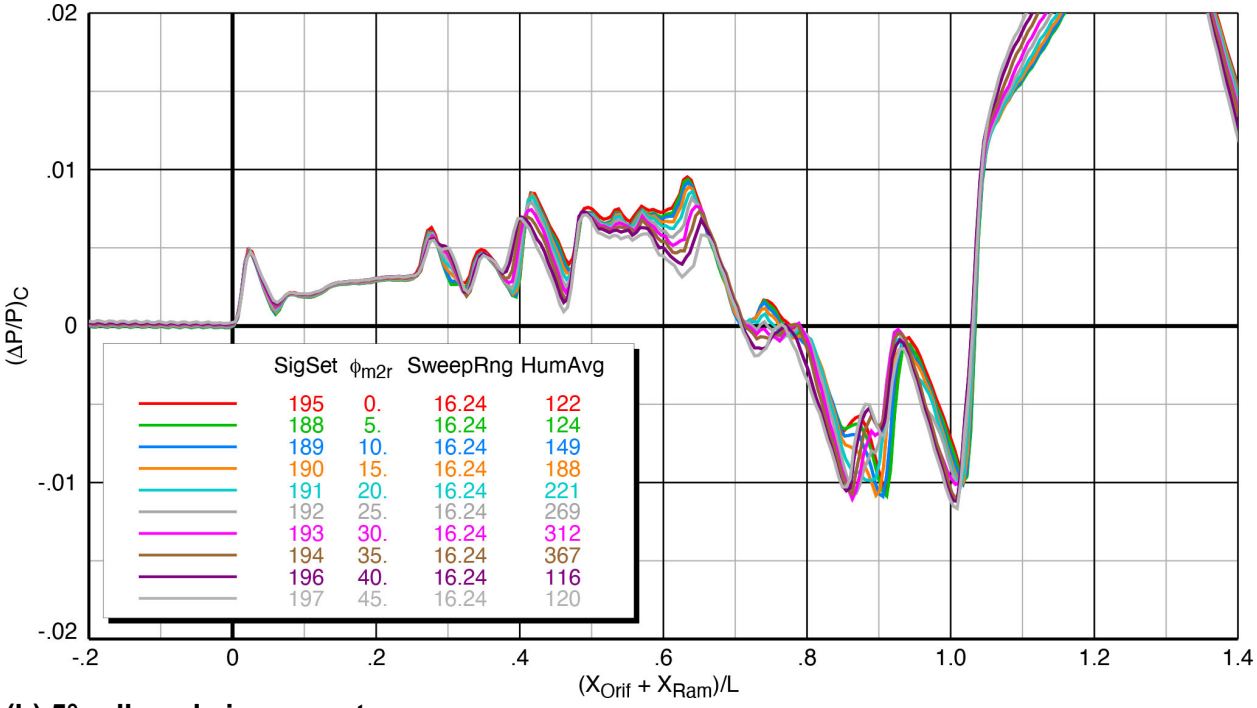

(b) 5° roll angle increments

Figure 6-87 Effect of roll angle (5° increments) on X-59 model (sting) spatially-averaged pressure signatures, Mach 1.4, *h/L* = 2, α = 2.1°

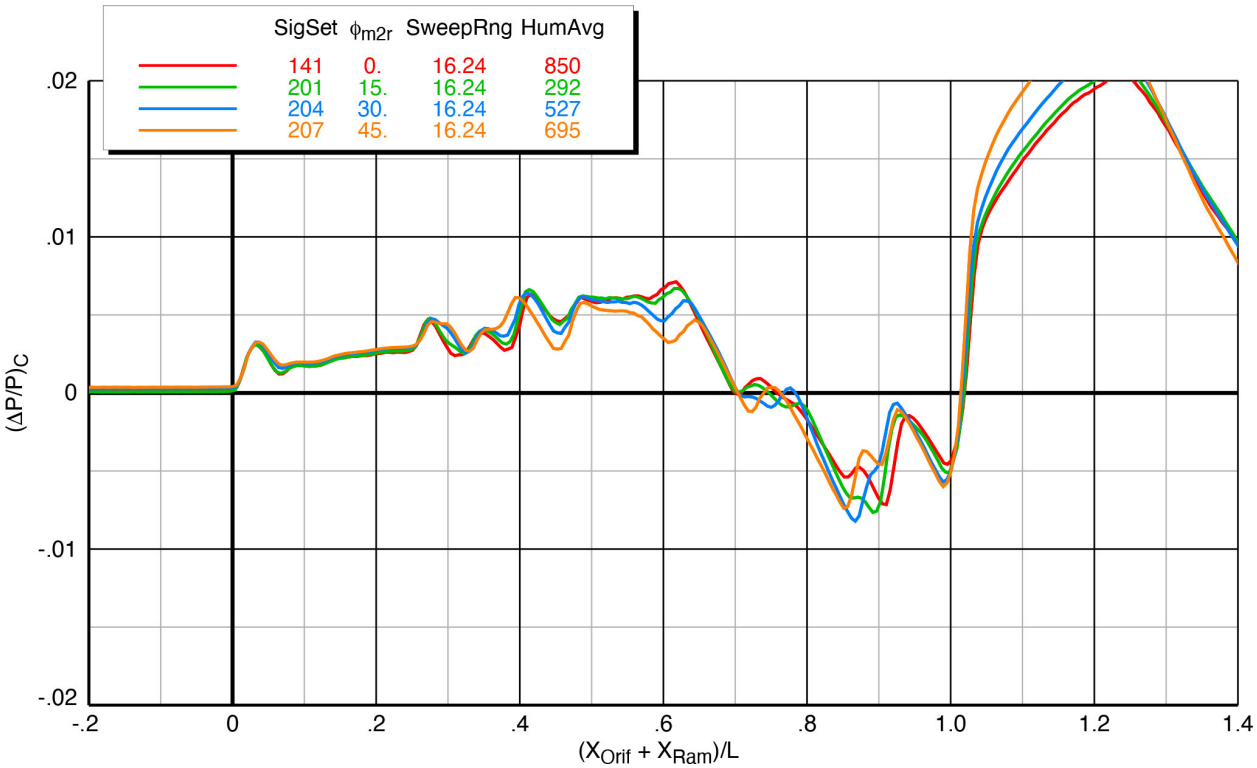

(a) 15° roll angle increments

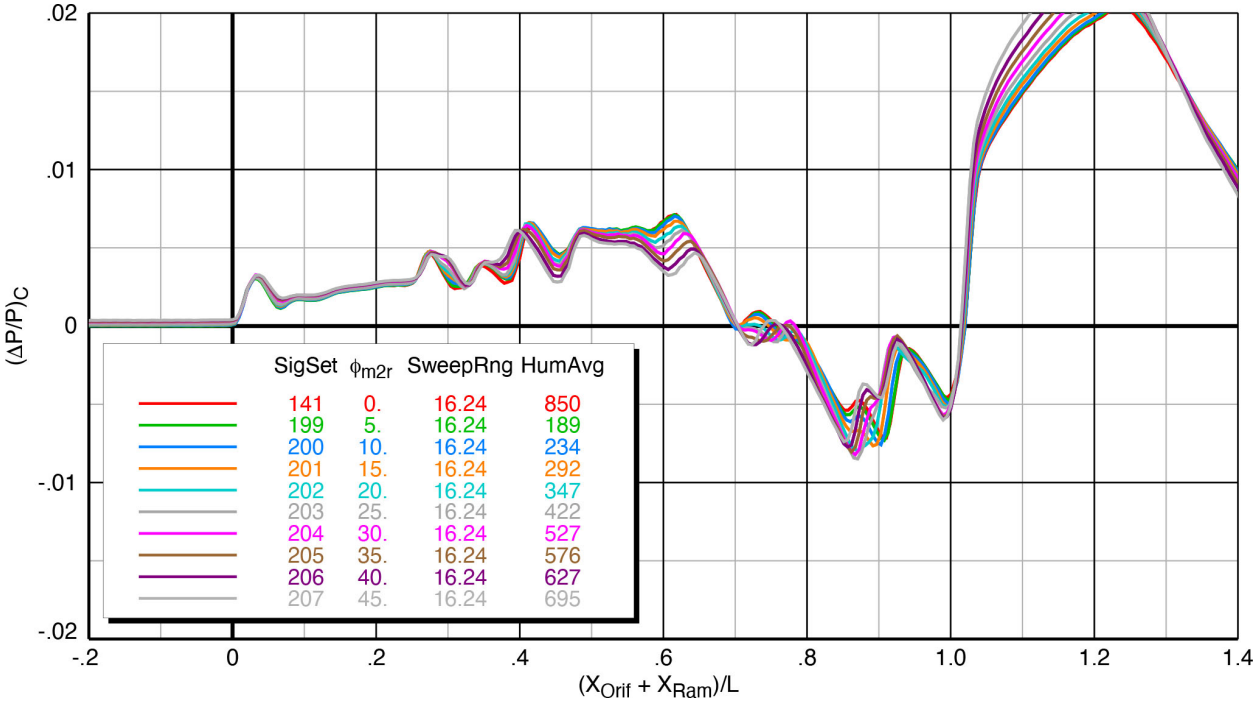

(b) 5° roll angle increments

Figure 6-88 Effect of roll angle (5° increments) on X-59 model (sting) spatially-averaged pressure signatures, Mach 1.4, *h/L* = 3, α = 2.1°

6.12. Effect of Mach Number

The effects of Mach number on the reference runs and model signatures are presented in the following figures:

- Figure 6-90 Reference runs
- Figure 6-90 AS-2 $h/L = 1.2$ $\alpha = 0°$
- Figure 6-91 Blade strut $h/L = 1.2$ $\alpha = 2.1°$
- Figure 6-92 Blade strut $h/L = 2$ $\alpha = 2.1°$
- Figure 6-93 Blade strut $h/L = 3$ $\alpha = 2.1°$
- Figure 6-94 Sting $h/L = 1.2$ $\alpha = 2.1°$
- Figure 6-95 Sting $h/L = 2$ $\alpha = 2.1°$
- Figure 6-96 Sting $h/L = 3$ $\alpha = 2.1°$

A comparison of the reference run pressures for the three test Mach numbers is presented in Figure 6-90. The trend of the reflected rail shock peak moving aft with Mach number is as expected because of the increasing Mach line angle (42.7° at Mach 1.36, 44.4° at Mach 1.40, 47.1° at Mach 1.47), but it is not known why there is a difference in the magnitudes of the shock peaks between Mach 1.36 and the other two Mach numbers. One might expect that the shock peaks would get higher with Mach number, and yet the peaks at the two highest Mach numbers are nearly identical. Similar plots of other reference run comparisons not included herein also show similar shock peak magnitudes between the two highest Mach numbers, though with some slight variations among them (but still significantly higher than the peaks at Mach 1.36).

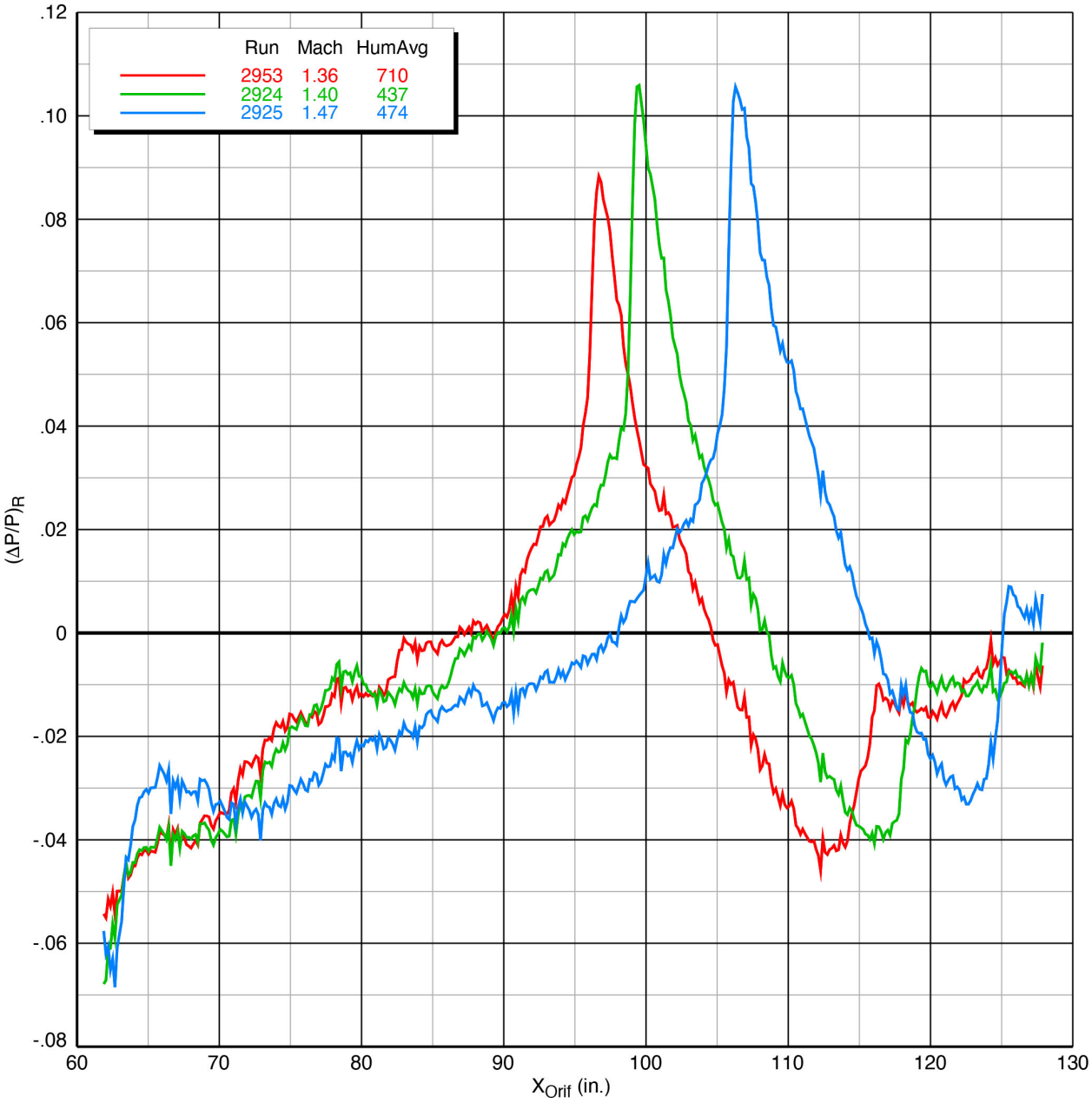

Figure 6-89 Effect of Mach number on reference runs

Plots of Mach number effects on AS-2 and X-59 signatures are presented in Figures 6-90 through 6-96. The primary effect of increasing Mach number on a pressure field around an aircraft is to increase the angle of the shock waves away from the vertical. Thus, for a given model position in the wind tunnel, as Mach number is increased, the model shocks fall further aft on the rail. This effect is taken out in the data plots below because the signatures are all aligned with the start of the nose shock being at *X/L* = 0. However, there is also some stretching of the signatures with Mach number, as evidenced in all of the X-59 model signatures below.

The one plot of the AS-2 model signatures shows only a slight amount of stretching between the Mach 1.4 and 1.47 curves in the expansion region between *X/L* = 0.25 and 0.35. The curve at Mach 1.36 does not look right with the reduced slope of the initial shock relative to the other curves, but the reason for this was not investigated during the test.

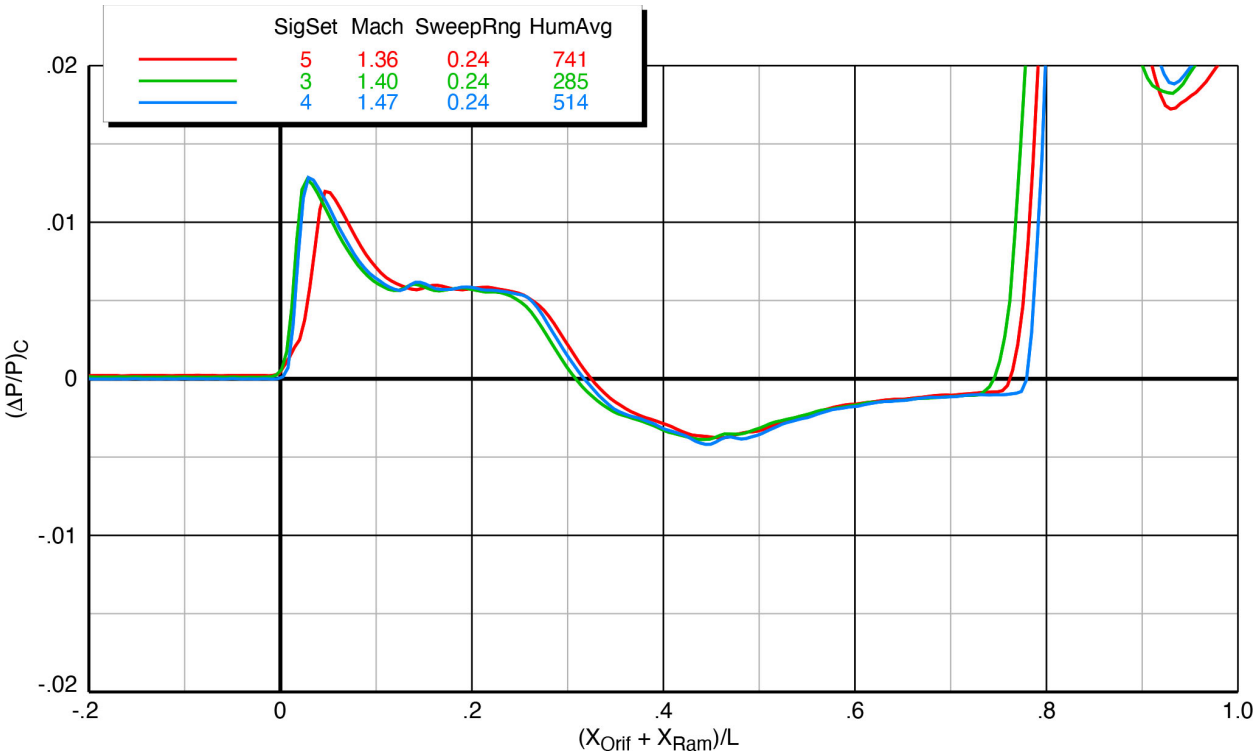

Figure 6-90 Effect of Mach number on AS-2 model spatially-averaged pressure signatures, *h/L* = 1.2, α = 0°, ϕ = 0°

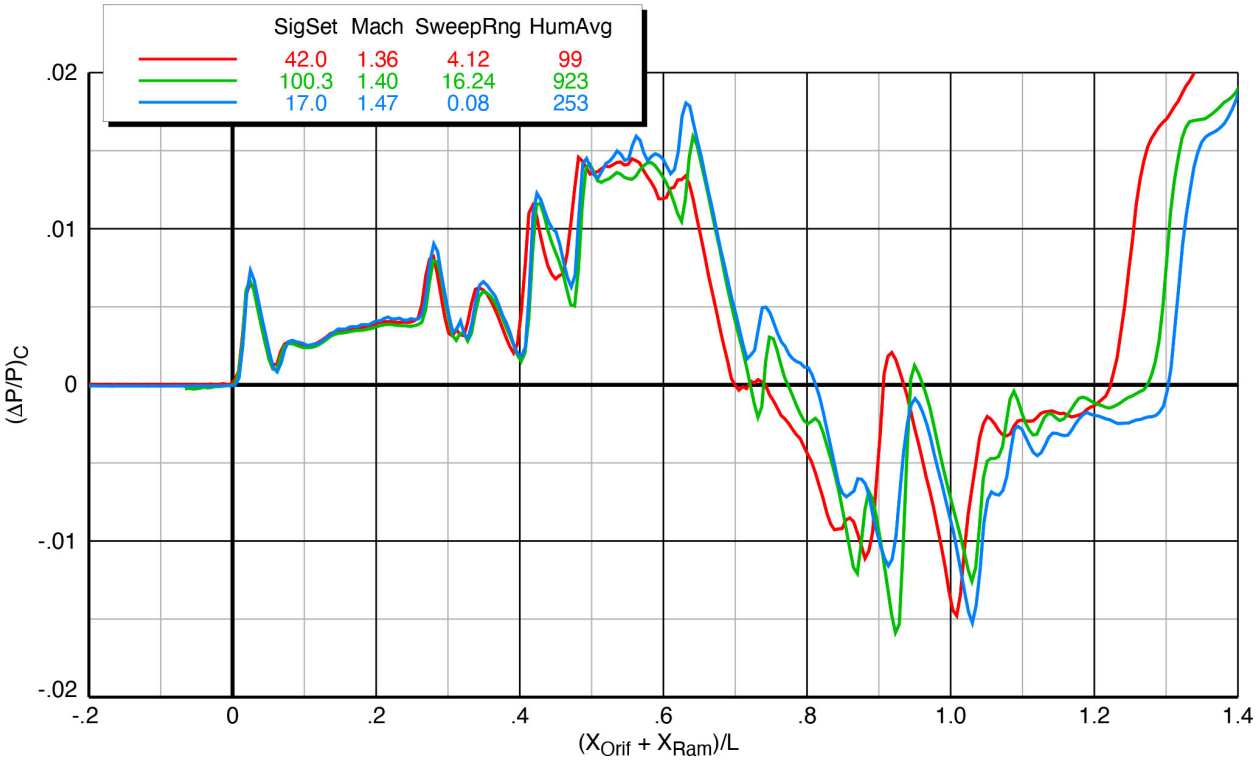

Figure 6-91 Effect of Mach number on X-59 model (blade strut) spatially-averaged pressure signatures, *h/L* = 1.2, α = 2.1°, ϕ = 0°

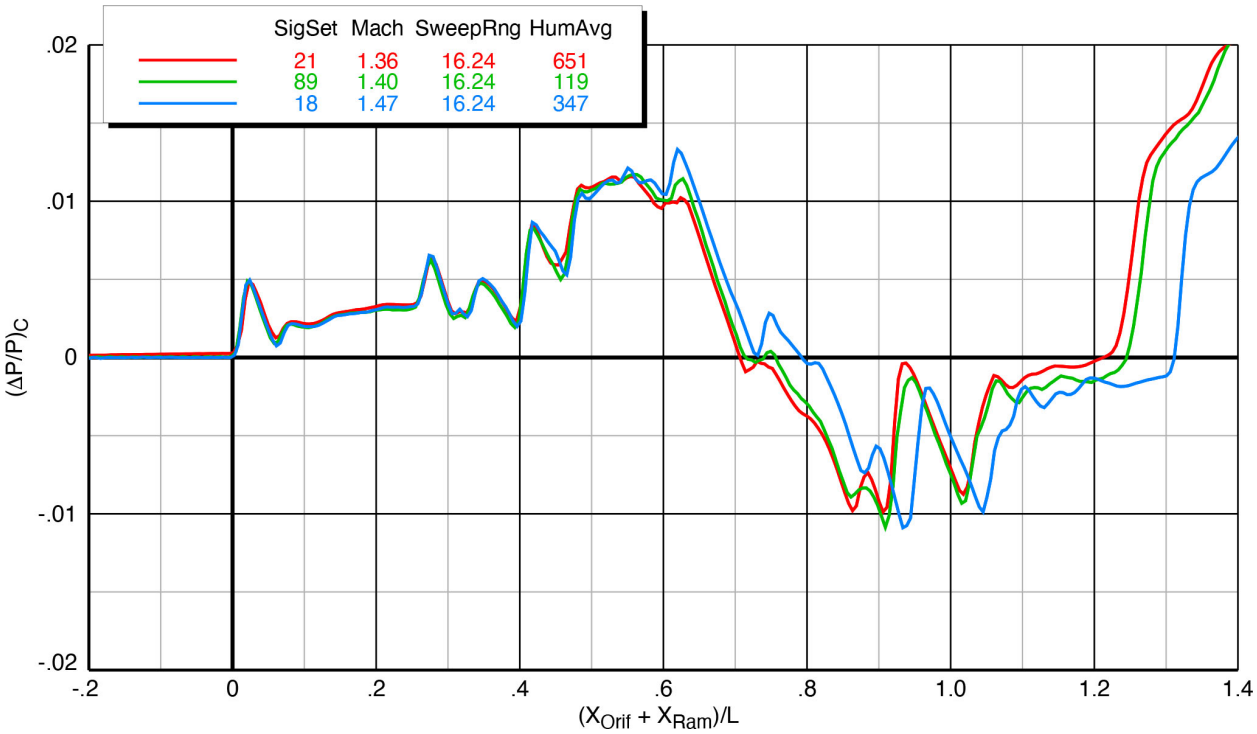

Figure 6-92 Effect of Mach number on X-59 model (blade strut) spatially-averaged pressure signatures, *h/L* = 2, α = 2.1°, ϕ = 0°

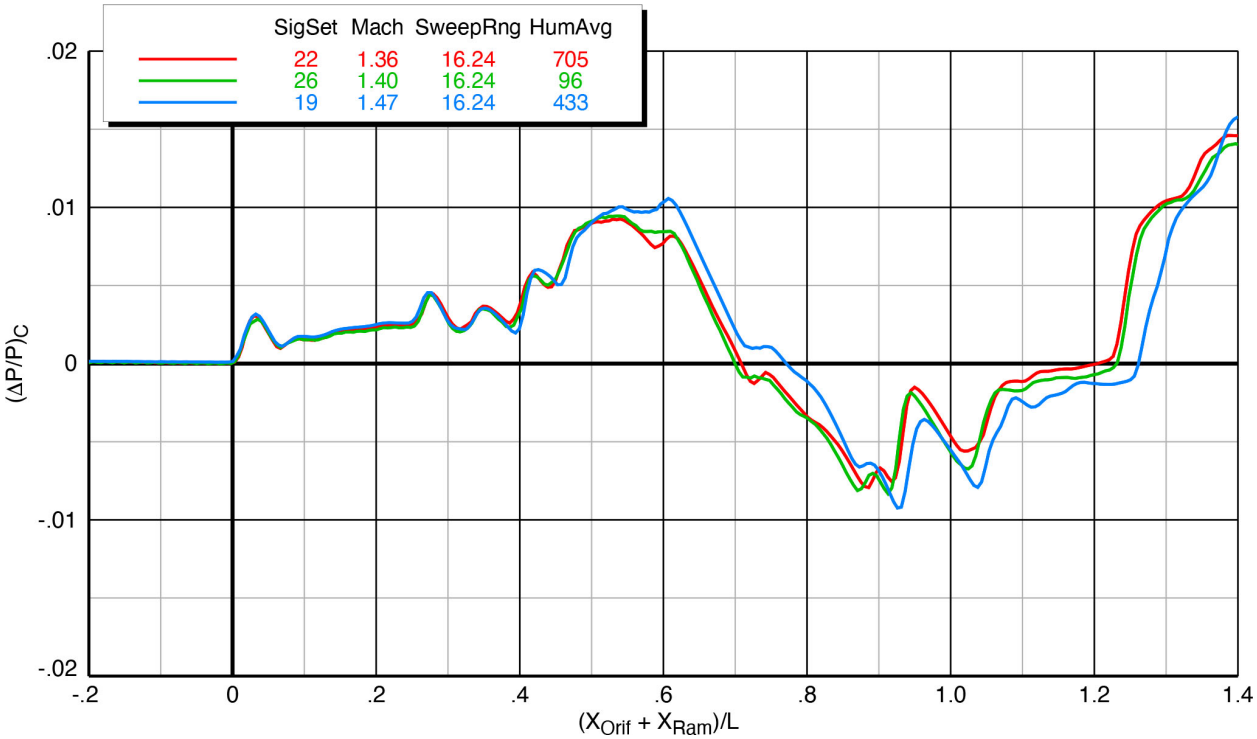

Figure 6-93 Effect of Mach number on X-59 model (blade strut) spatially-averaged pressure signatures, *h/L* = 3, α = 2.1°, ϕ = 0°

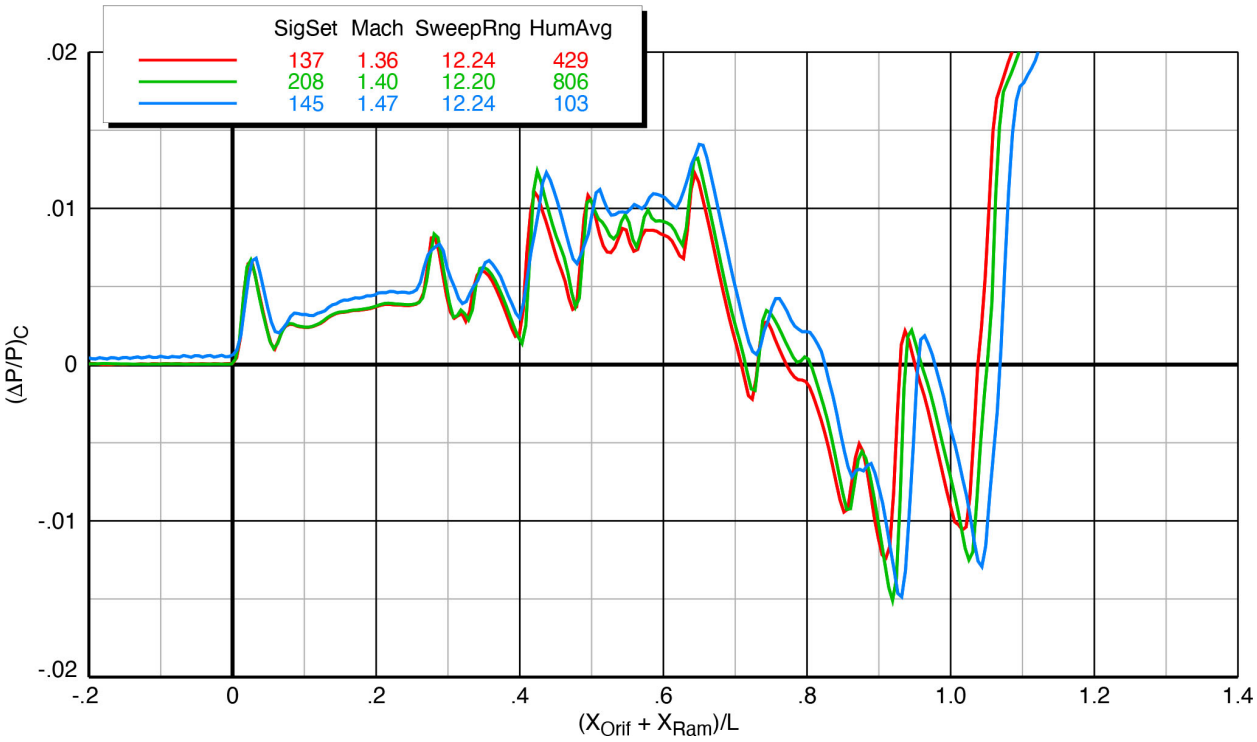

Figure 6-94 Effect of Mach number on X-59 model (sting) spatially-averaged pressure signatures, *h/L* = 1.2, α = 2.1°, ϕ = 0°

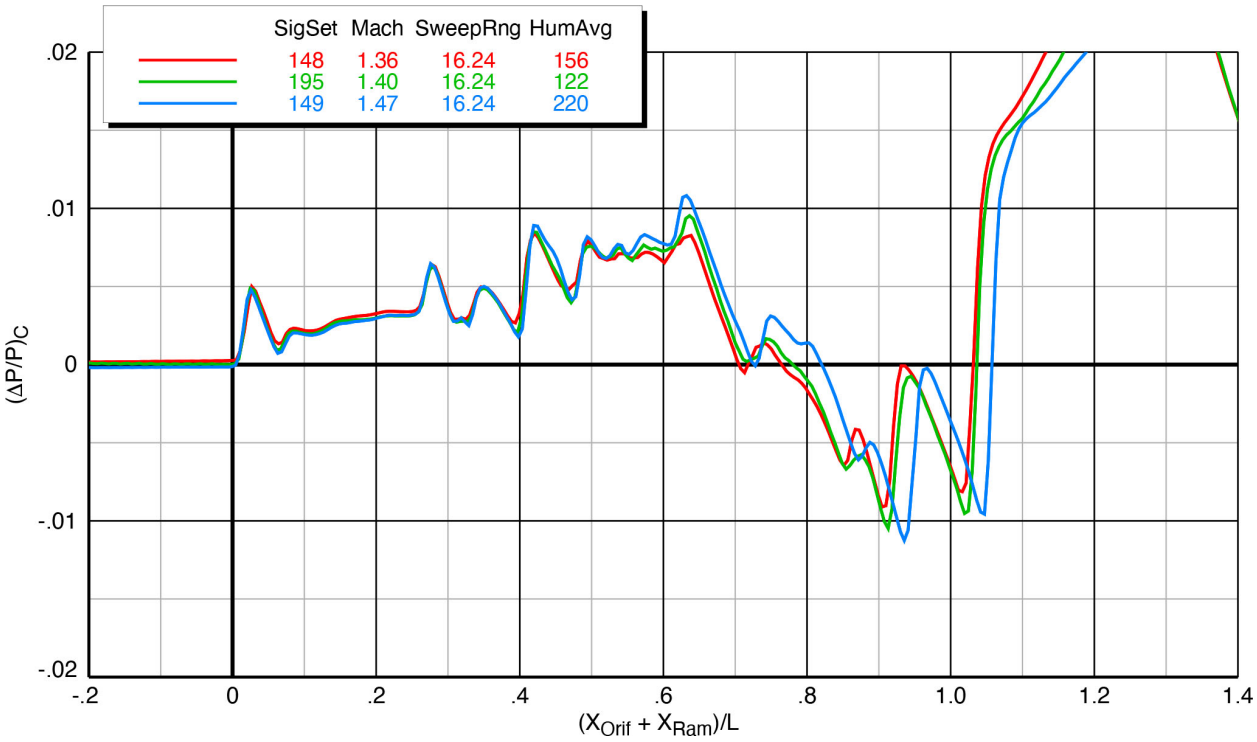

Figure 6-95 Effect of Mach number on X-59 model (sting) spatially-averaged pressure signatures, *h/L* = 2, α = 2.1°, ϕ = 0°

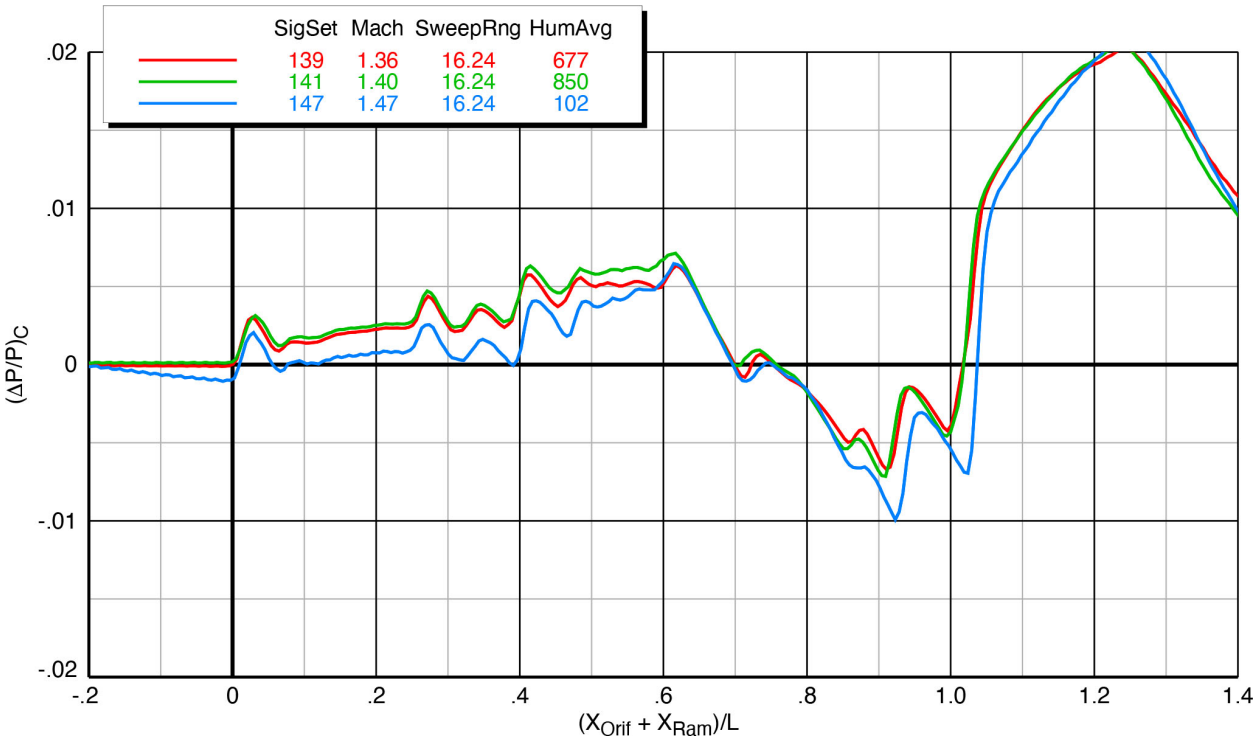

Figure 6-96 Effect of Mach number on X-59 model (sting) spatially-averaged pressure signatures, *h/L* = 3, α = 2.1°, ϕ = 0°

6.13. Blade Strut vs. Sting Mount

Comparisons of the signatures for the model mounted on the blade strut vs. the sting are presented in the following figures:

- Figure 6-97 Mach 1.36 *h/L* = 1.2 α = 2.1°
- Figure 6-98 Mach 1.36 *h/L* = 2 α = 2.1°
- Figure 6-99 Mach 1.36 *h/L* = 3 α = 2.1°
- Figure 6-100 Mach 1.4 *h/L* = 1.2 α = 2.1°
- Figure 6-101 Mach 1.4 *h/L* = 2 α = 2.1°
- Figure 6-102 Mach 1.4 *h/L* = 3 α = 2.1°
- Figure 6-103 Mach 1.47 *h/L* = 1.2 α = 2.1°
- Figure 6-104 Mach 1.47 *h/L* = 2 α = 2.1°
- Figure 6-105 Mach 1.47 *h/L* = 3 α = 2.1°

Any hardware that is used to support a model in a wind tunnel necessitates a compromise in the outer model line (OML) of the model which adversely affects the aerodynamics of the model and the pressure field surrounding it. A common way to provide data to correct for, or at least partially mitigate these effects, is to test the model with two or more different mounting configurations. For the X-59 sonic boom model, it was decided to design a mount that would attach at the top center of the model so that the aft end would have a clean OML that matches the airplane, as well as a sting mount that attaches through (or in this case, in place of) the engine nacelle so that the upper part of the model is not compromised. Neither configuration provides a complete pressure signature that matches what an airplane would produce in free

air, but the combination of the signatures from the two mounting configurations can offer insights into what a composite signature would look like.

In the plot legends, the model-mounting configuration is specified as either Blade or Sting. In most of the plots, the sweep ranges match, but there are a few cases in which they don't, and the comparison of the signatures is therefore not as valid as if it would be if they did. However, this set of plots at all three Mach numbers and all three heights offers a very useful picture of the effects of each mounting type on the pressure data.

In all the plots below, the signatures are nearly identical up to the shock from the leading edge of the blade strut which falls at or near *X/L* = 0.45. The pressures fluctuate a bit aft of this point, which are from the flow passing around the strut and interacting with the wing as they pass around to the bottom of the model. At an *X/L* around 0.75, the sting configuration has a small pressure rise which is either greater than, or in some cases nearly equal to, a similar pressure rise for the blade configuration. This is likely from the fairing in front of the inlet on the sting configuration, or from the inlet opening on the blade configuration. The large shock in the *X/L* range of 0.90 to 0.95 is from the stabilator leading edge, and this appears to be fairly equal between the two configurations. The most notable difference at the aft end of the signatures is that for the blade configuration, the pressures ramp up slowly towards the ambient level ($\Delta P/P$ = 0) before encountering the strong shock from the transition area near the top of the blade, whereas the sudden growth in the sting area at 2" behind the nozzle exit creates a strong shock that overtakes the rear of the signature at *X/L* approximately equal to 1.0.

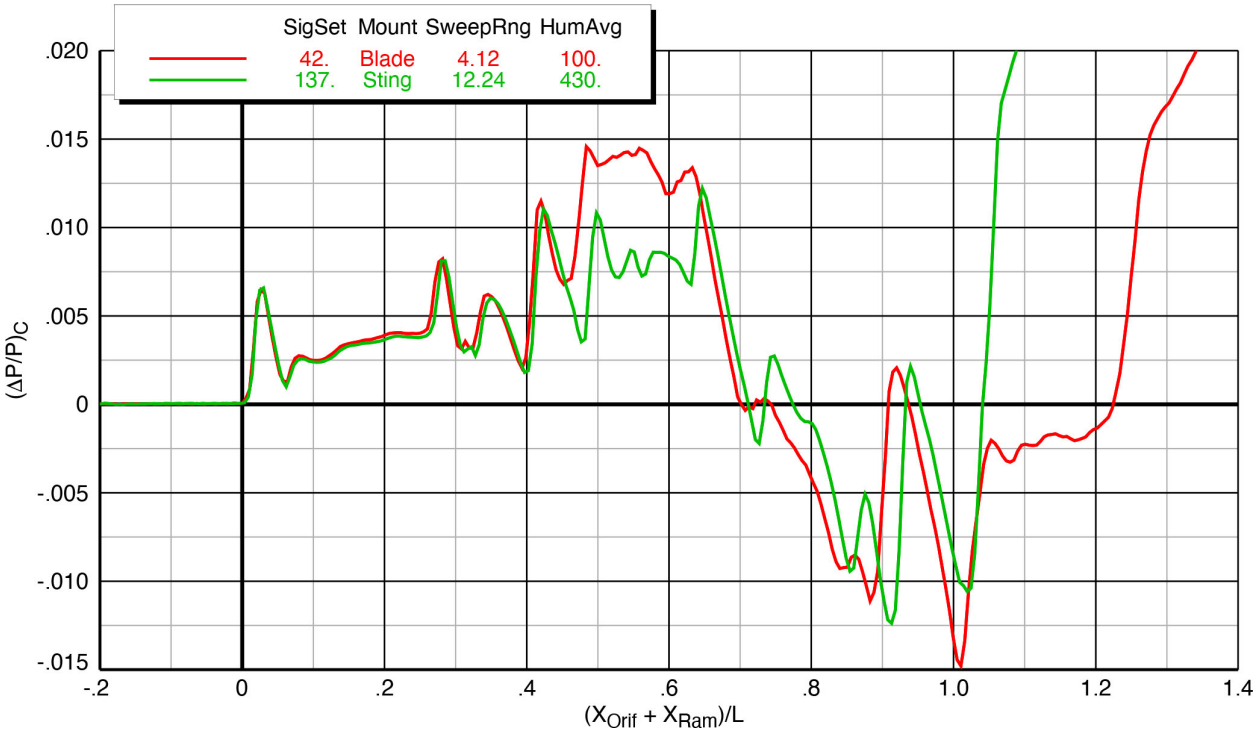

Figure 6-97 Comparison of blade strut vs. sting mounts on X-59 model averaged signatures, Mach 1.36, *h/L* = 1.2, α = 2.1°, ϕ = 0°

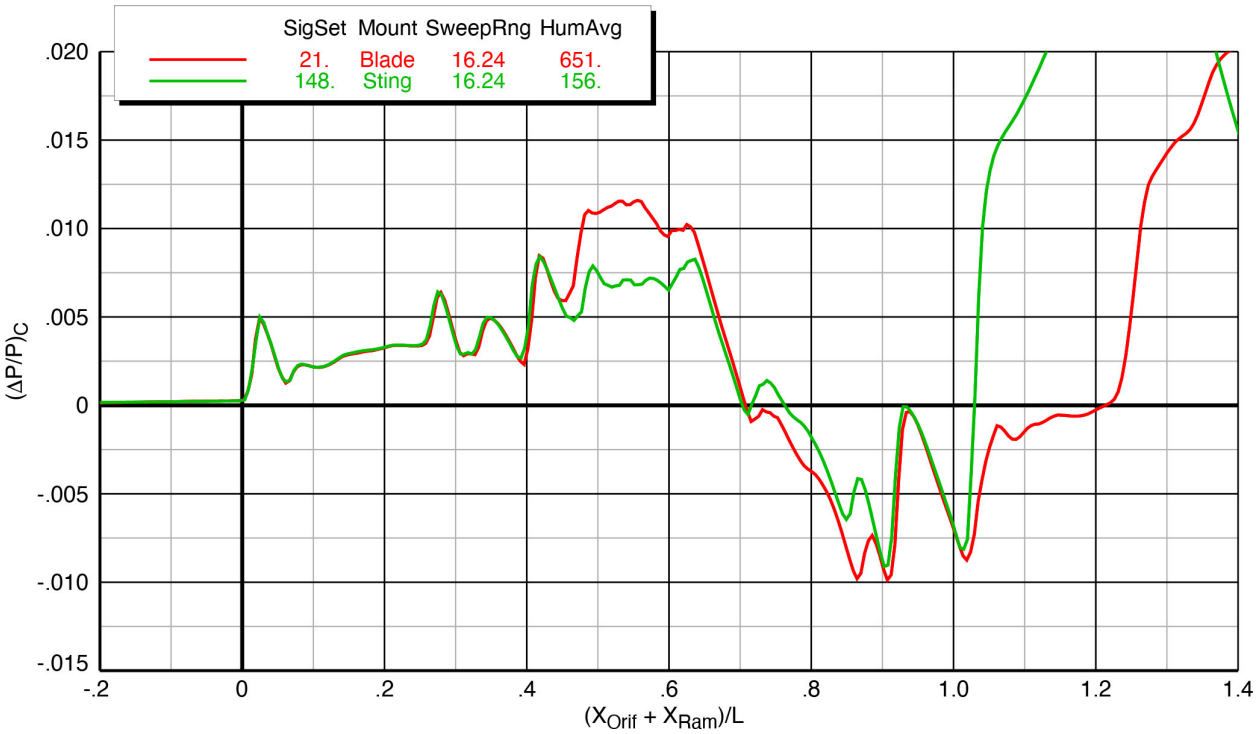

Figure 6-98 Comparison of blade strut vs. sting mounts on X-59 model averaged signatures, Mach 1.36, *h/L* = 2, α = 2.1°, ϕ = 0°

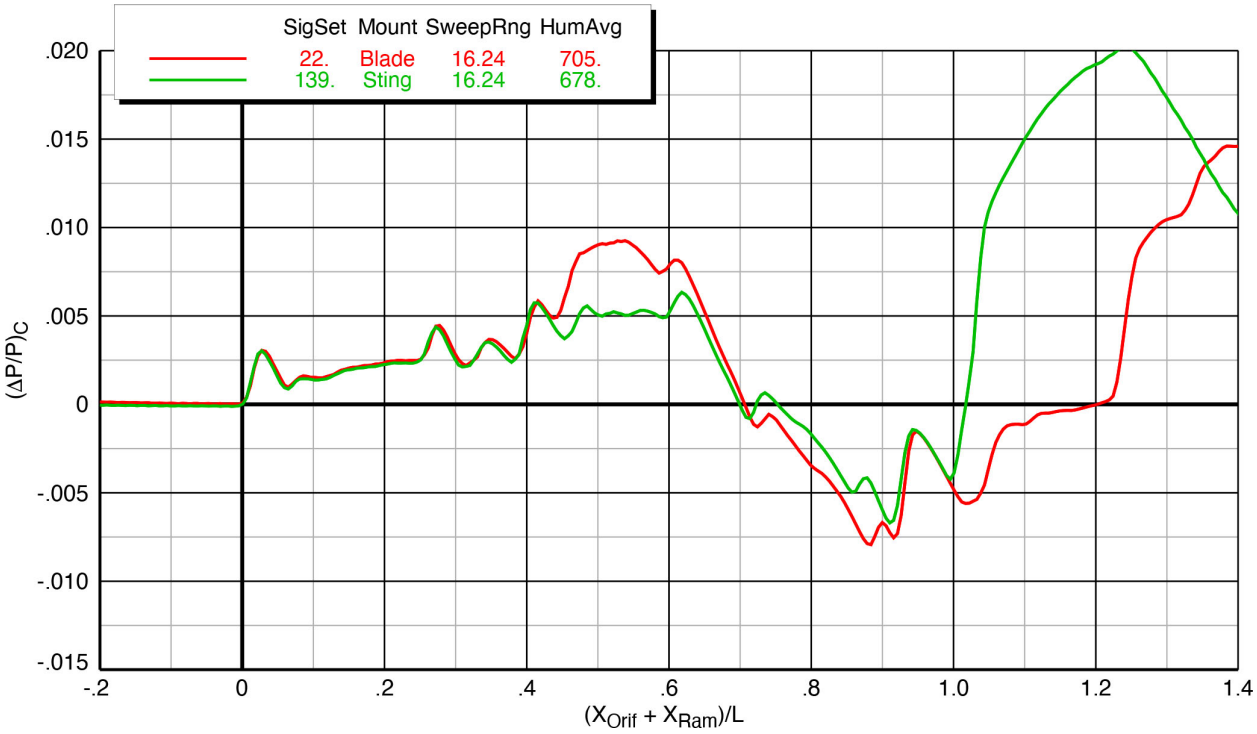

Figure 6-99 Comparison of blade strut vs. sting mounts on X-59 model averaged signatures, Mach 1.36, *h/L* = 3, α = 2.1°, ϕ = 0°

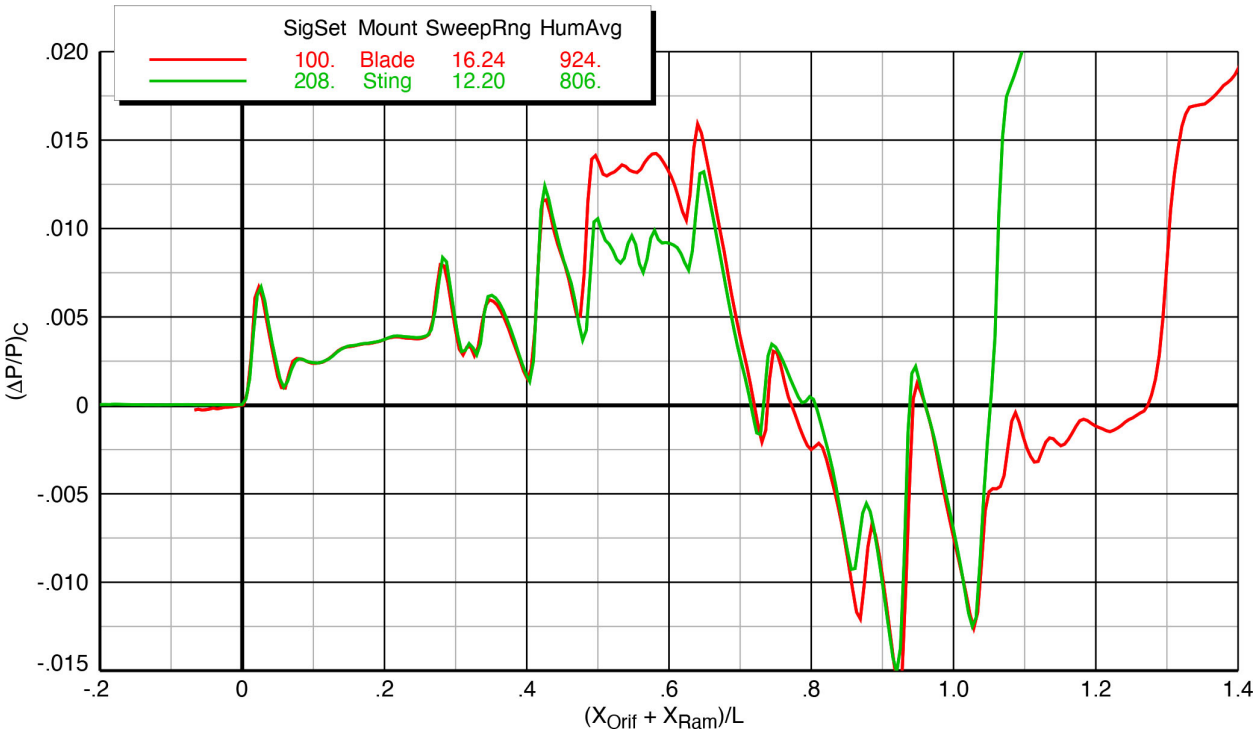

Figure 6-100 Comparison of blade strut vs. sting mounts on X-59 model averaged signatures, Mach 1.4, *h/L* = 1.2, α = 2.1°, ϕ = 0°

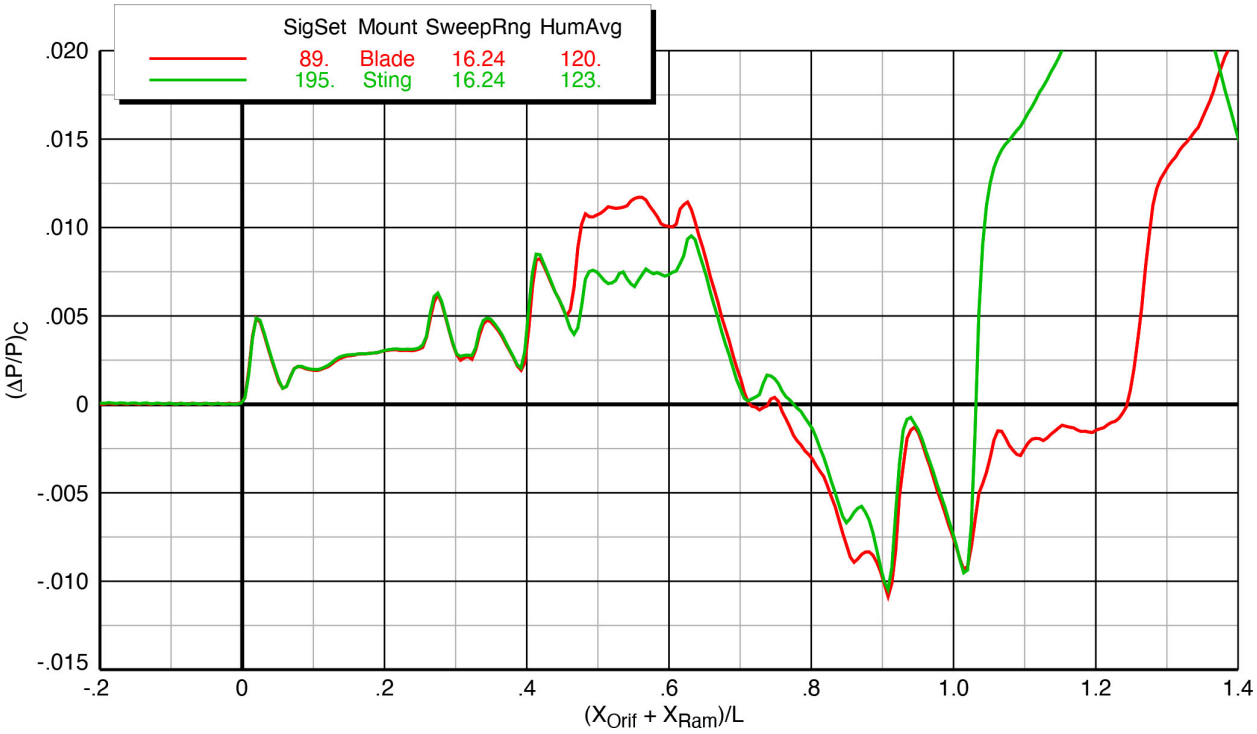

Figure 6-101 Comparison of blade strut vs. sting mounts on X-59 model averaged signatures, Mach 1.4, *h/L* = 2, α = 2.1°, ϕ = 0°

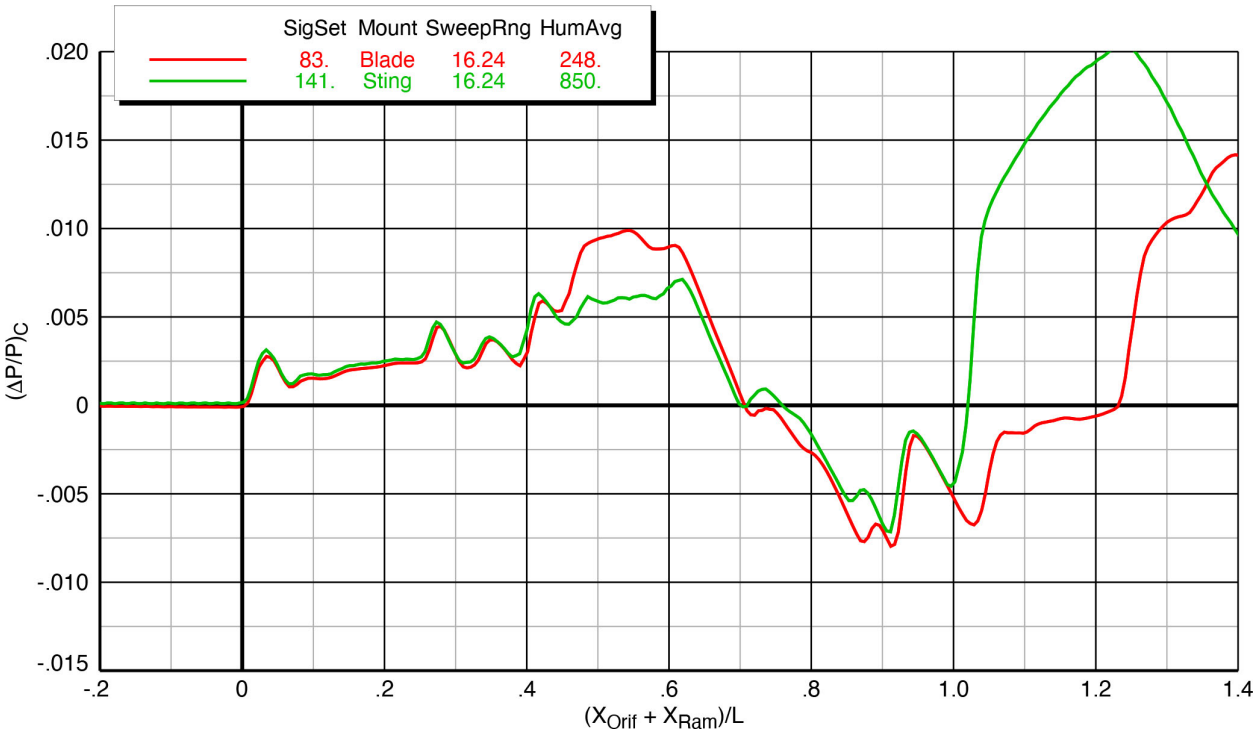

Figure 6-102 Comparison of blade strut vs. sting mounts on X-59 model averaged signatures, Mach 1.4, *h/L* = 3, α = 2.1°, ϕ = 0°

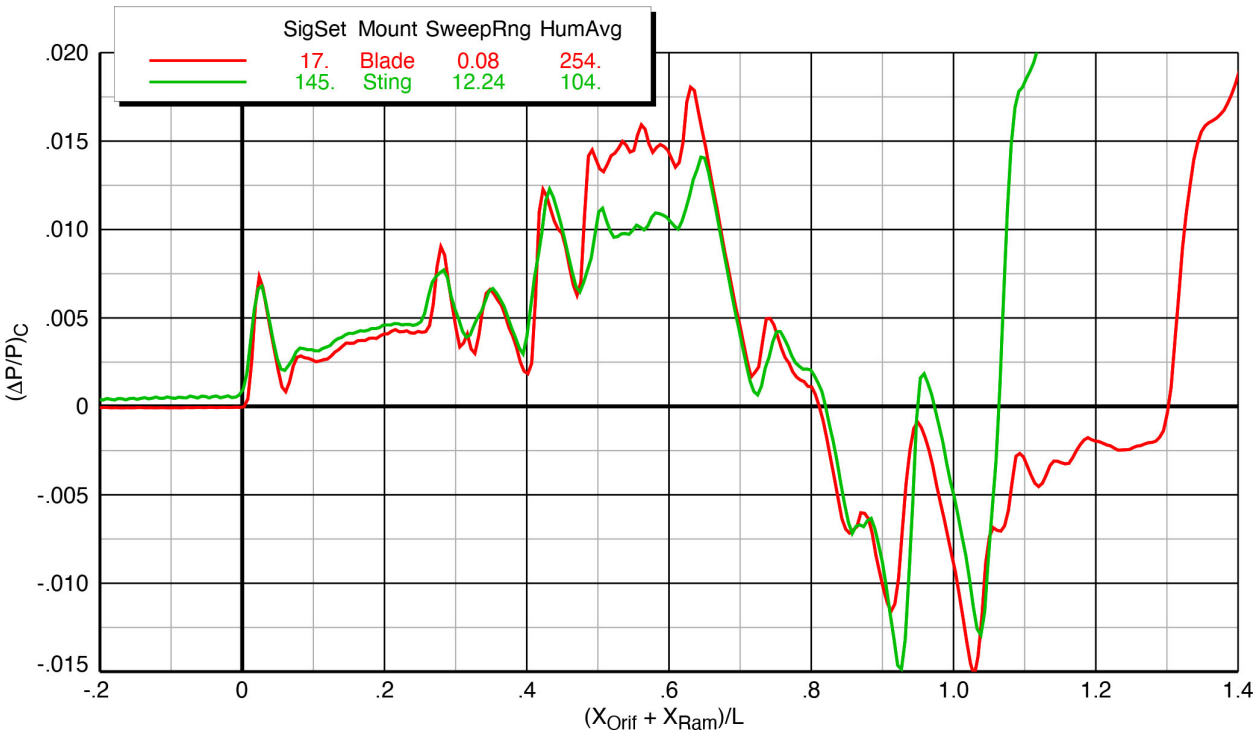

Figure 6-103 Comparison of blade strut vs. sting mounts on X-59 model averaged signatures, Mach 1.47, *h/L* = 1.2, α = 2.1°, ϕ = 0°

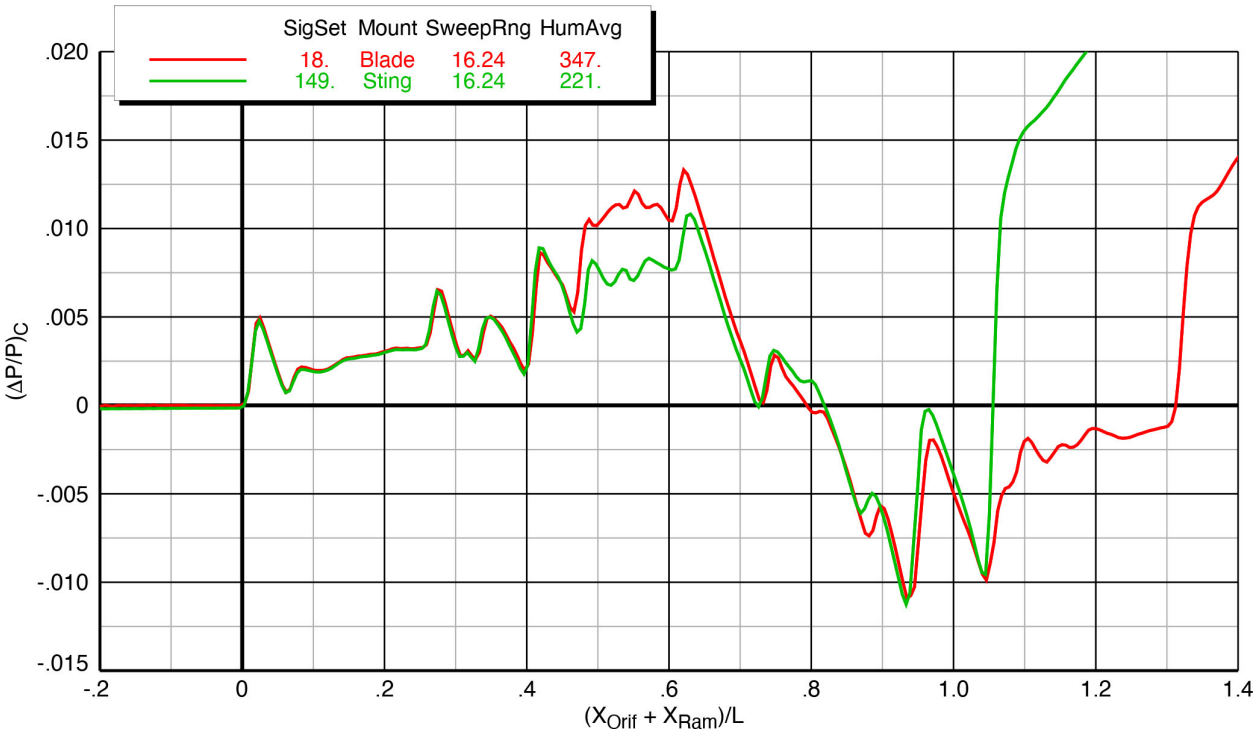

Figure 6-104 Comparison of blade strut vs. sting mounts on X-59 model averaged signatures, Mach 1.47, *h/L* = 2, α = 2.1°, ϕ = 0°

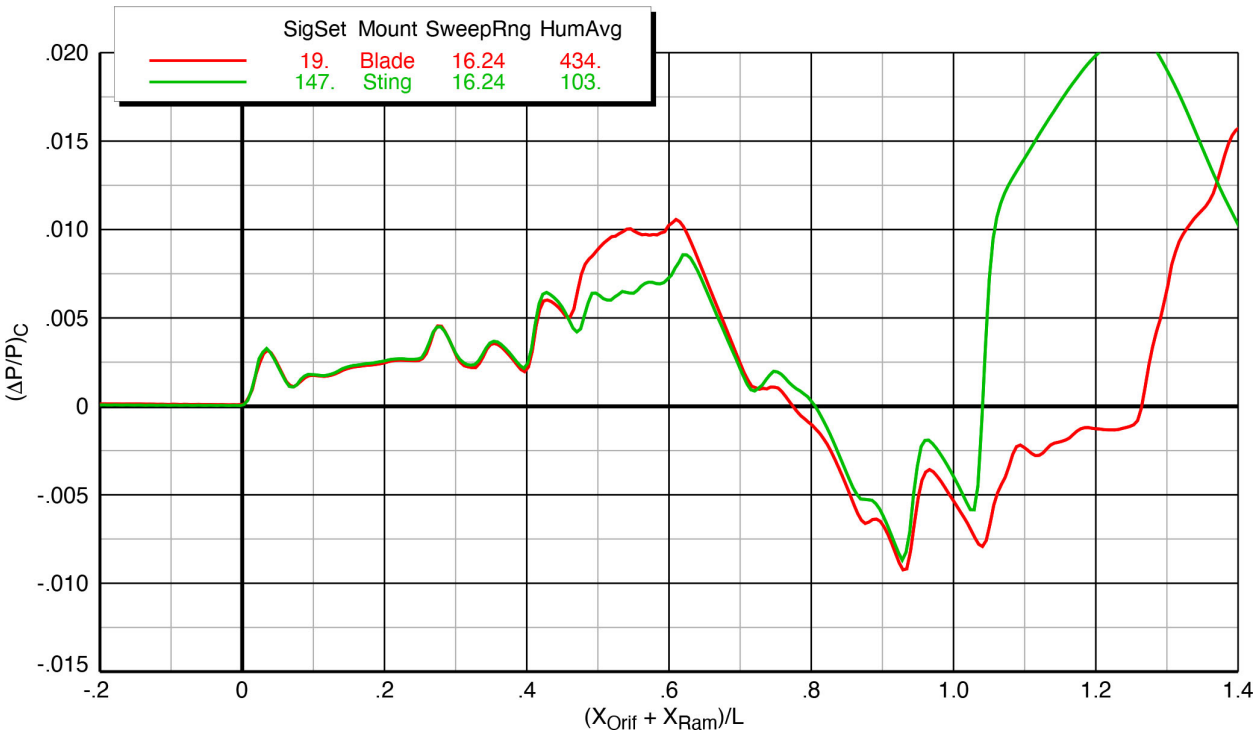

Figure 6-105 Comparison of blade strut vs. sting mounts on X-59 model averaged signatures, Mach 1.47, *h/L* = 3, α = 2.1°, ϕ = 0°

7. Conclusions

A sonic boom test of a 1.62%-scale model of the X-59 airplane was successfully completed in the Glenn 8- by 6-Foot Supersonic Wind Tunnel in September and October 2021. A total of 196 spatially-averaged pressure signatures were obtained during the 5-1/2 weeks of test time. The signatures provided insight into the near-field sonic boom characteristics of the X-59 at various angles of attack and roll, Mach numbers, and control deflections. Many repeat runs were conducted to assess the quality of the data, and the repeatability was generally very good, though there were at times some unknown influences on the pressure data that compromised some of the signatures. The range of the *X* sweeps selected within the 24” of available ram extension typically had a very significant influence on the quality of the signatures and the scatter among the runs within a sweep. There was generally less scatter among runs in which the pressures were measured at further-forward locations on the rail, allowing for better repeatability of the averaged signatures.

The data showed clear trends of signature aging over distances of 1.2 to 3 body lengths from the rail. Increments in the shock wave strengths and locations from various control deflections are easily apparent in the rear part of the signature data. Varying the angles of attack and roll, and varying the Mach number, had the expected effect on the signatures.

Humidity varied substantially throughout the test, starting out low (usually less than 100 ppm) at the start of a running shift and often exceeding 1,000 ppm by the end of the shift. However, the data plots consistently showed that even large differences in humidity between averaged signatures did not affect the pressure measurements.

The data from this test will be used in validating CFD codes that are used for sonic boom predictions, and in preparing the data sets that will be used to compare to the signatures measured in flight and on the ground from the X-59 flight tests. A companion report[16] has been prepared which compares the experimental data from this test to the CFD predictions.

8. References

1. https://www.nasa.gov/aeroresearch/programs/aavp/cst
2. https://www.nasa.gov/aeroresearch/programs/aavp
3. Morgenstern, John, Norstrud, Nicole, Sokhey Jack, Martens, S., and Alonso, Juan: *"Advanced Concept Studies for Supersonic Commercial Transports Entering Service in the 2018 to 2020 Period", Phase I Final Report*, NASA/CR-2013-217820, February 2013.
4. Morgenstern, John, et al: *"Advanced Concept Studies for Supersonic Commercial Transports Entering Service in the 2018 to 2020 Period", Phase II Final Report*, NASA/CR-2015-218719, July 2015
5. Magee, Todd E., Wilcox, Peter A., Fugal, Spencer R., Acheson, Kurt E., Adamson, Eric E., Bidwell, Alicia L., and Shaw, Stephen G.: *System-Level Experimental Validations for Supersonic Commercial Transport Aircraft Entering Service in the 2018–2020 Time Period, Phase I Final Report*, NASA CR-2013-217797, February 2013
6. Magee, Todd E., Fugal, Spencer R., Fink, Lawrence E., Adamson, Eric E., and Shaw, Stephen G.: *System-Level Experimental Validations for Supersonic Commercial Transport Aircraft Entering Service in the 2018–2020 Time Period, Phase II Final Report,* NASA CR-2015-218983, November 2015
7. Durston, Donald A., Elmiligui, Alaa A., Cliff, Susan E., Winski, Courtney S., Carter, Melissa B., and Walker, Eric L.: *Experimental and Computational Sonic Boom Assessment of Boeing N+2 Low Boom Models,* NASA TP-2015-218482, January 2015
8. Cliff, Susan E., Durston, Donald A., Elmiligui, Alaa A., Walker, Eric L., and Carter, Melissa B.: *Experimental and Computational Sonic Boom Assessment of Lockheed Martin N+2 Low Boom Models,* NASA TP-2015-218483, January 2015
9. https://www.nasa.gov/X59
10. https://www.nasa.gov/image-feature/x-59-wind-tunnel-testing-at-nasa-glenn
11. Soeder, Ronald H.: *NASA Lewis 8- by 6-Foot Supersonic Wind Tunnel User Manual,* NASA TM 105771, February 1993
12. Magee, Todd E., Shaw, Stephen G., and Fugal, Spencer R.: *Experimental Validations of a Low-Boom Aircraft Design,* AIAA Paper 2013-0646, 51st AIAA Aerospace Sciences Meeting, Grapevine TX, January 2013
13. Castner, Raymond S. and Simerly, Stephanie R.: *Assessment of the NASA Glenn 8- by 6-Foot Supersonic Wind Tunnel Supersonic Test Section for Sonic Boom and Supersonic Testing,* NASA/TM-20220000420, September 2022
14. https://www.nasa.gov/aero/x-59-research-aircraft-overview
15. Crawford, Bradley L.: *Angle Measurement System (AMS) for Establishing Model Pitch and Roll Zero, and Performing Single Axis Angle Comparisons,* AIAA Paper 2007-1162, 45th AIAA Aerospace Sciences Meeting, Reno, NV, January 2007
16. Carter, Melissa B., Elmiligui, Alaa A., Park, Michael A., Shea, Patrick R., Winski, Courtney S., Durston, Donald A., Jensen, James C., Wagner, Jacob M., Neuhoff, Scott M., and Wolter, John D.: Experimental and Computational Study of the X-59 Wind Tunnel Model at Glenn Research Center 8- by 6-foot Supersonic Wind Tunnel. NASA/TM-20220011496, September 2022

9. Appendix

A listing of all the SigSets obtained in this test is provided below. The SigSets are grouped by model configuration, with subgroups for baseline configuration, alpha and roll variations, and various control surface deflections. Repeat SigSets are shown in the rows with gray numbers immediately below the corresponding primary SigSet numbers in black. The primary SigSets were judged to have the best-quality data among a group of repeats.

- Mach numbers are in **bold** to make column easily identifiable
- SigSet and X_{ram} numbers in **bold** are sweeps originally from 0" to 24" ram extension
- Run numbers in cyan identify alternate ranges of runs used in averaging for best-quality data
- SigSets with numbers greater than 1000 were made after the test to combine two successive SigSets to contain an X_{ram} range from 12.2" to 24"
- Height variations are listed in magenta, red, and orange for easier visual comparison
- Alternate alpha angles (1.8° and 2.4°) are listed in green
- Alternate roll angles (greater than 0°) are listed in blue

SigSet #	Start Run	End Run	Preferred Ref Run	Model	Flaps (deg)	Ailerons (deg)	Stab (deg)	T-Tail (deg)	Mach	Height /L	Alpha (deg)	Roll m2r (deg)	Start Xram (in.)	End Xram (in.)	Sweep Inc (in.)
AS-2 model															
5	2954	2979	2954	AS2	—	—	—	—	**1.36**	1.2	0°	0°	**0**	**24**	0.96
3	2898	2923	2898	AS2	—	—	—	—	**1.4**	1.2	0°	0°	**0**	**24**	0.96
2	2839	2844	2839										0	5	0.96
6	2982	3007	2982										12	20	0.32
7	3008	3033	3008	AS2	—	—	—	—	**1.4**	2.0	0°	0°	8	16	0.32
8	3034	3059	3034	AS2	—	—	—	—	**1.4**	3.0	0°	0°	16	24	0.32
4	2926	2951	2926	AS2	—	—	—	—	**1.47**	1.2	0°	0°	**0**	**24**	0.96
X-59 blade, baseline runs															
42	4099	4124	4099	X-59 Blade	-2.4°	1.1°	3.42°	3.7°	**1.36**	1.2	2.1°	0°	4	12	0.32
13	3304	3329	3302	"	"	"	"	"	"	"	"	"	0	12	0.48
20	3502	3527	3501	"	"	"	"	"	"	"	"	"	4	12	0.32
21	3528	3553	3528	X-59 Blade	-2.4°	1.1°	3.42°	3.7°	**1.36**	2.0	2.1°	0°	16	24	0.32
14	3341	3366	3393	"	"	"	"	"	"	"	"	"	12	20	0.32
55	4442	4467	4441	"	"	"	"	"	"	"	"	"	12	24	0.48
22	3554	3579	3554	X-59 Blade	-2.4°	1.1°	3.42°	3.7°	**1.36**	3.0	2.1°	0°	16	24	0.32
15	3367	3392	3393	"	"	"	"	"	"	"	"	"	16	24	0.32
57	4470	4495	4441	"	"	"	"	"	"	"	"	"	16	24	0.32
100	5791	5828	5753	X-59 Blade	-2.4°	1.1°	3.42°	3.7°	**1.4**	1.2	2.1°	0°	12.2	24	0.32
10	3221	3246	3220	"	"	"	"	"	"	"	"	"	0	24	0.96
23	3582	3607	3581	"	"	"	"	"	"	"	"	"	4	12	0.32
48	4258	4283	4231	"	"	"	"	"	"	"	"	"	4	12	0.32
54	4414	4439	4231	"	"	"	"	"	"	"	"	"	4	12	0.32
89	5417	5442	5417	X-59 Blade	-2.4°	1.1°	3.42°	3.7°	**1.4**	2.0	2.1°	0°	16	24	0.32
11	3248	3273	3247	"	"	"	"	"	"	"	"	"	0	24	0.96
24	3608	3633	3581	"	"	"	"	"	"	"	"	"	16	24	0.32
47	4232	4257	4231	"	"	"	"	"	"	"	"	"	16	24	0.32
99	5677	5752	5881	"	"	"	"	"	"	"	"	"	0	24	0.32
26	3668	3693	3668	X-59 Blade	-2.4°	1.1°	3.42°	3.7°	**1.4**	3.0	2.1°	0°	16	24	0.32
12	3275	3300	3274	"	"	"	"	"	"	"	"	"	0	24	0.96
25	3634	3659	3581	"	"	"	"	"	"	"	"	"	16	24	0.32
113	6156	6231	6155	"	"	"	"	"	"	"	"	"	0	24	0.32
17	3422	3447	3422	X-59 Blade	-2.4°	1.1°	3.42°	3.7°	**1.47**	1.2	2.1°	0°	0	8	0.32
16	3395	3420	3394	"	"	"	"	"	"	"	"	"	0	8	0.32
27	3695	3720	3694	"	"	"	"	"	"	"	"	"	0	8	0.32
18	3448	3473	3448	X-59 Blade	-2.4°	1.1°	3.42°	3.7°	**1.47**	2.0	2.1°	0°	16	24	0.32
28	3721	3746	3694	"	"	"	"	"	"	"	"	"	16	24	0.32
43	4126	4151	4125	"	"	"	"	"	"	"	"	"	16	24	0.32
19	3474	3499	3474	X-59 Blade	-2.4°	1.1°	3.42°	3.7°	**1.47**	3.0	2.1°	0°	16	24	0.32
29	3747	3772	3773	"	"	"	"	"	"	"	"	"	16	24	0.32

SigSet #	Start Run	End Run	Preferred Ref Run	Model	Flaps (deg)	Ailerons (deg)	Stab (deg)	T-Tail (deg)	Mach	Height /L	Alpha (deg)	Roll m2r (deg)	Start Xram (in.)	End Xram (in.)	Sweep Inc (in.)
X-59 blade, alpha variations															
35	3908	3933	3908	X-59 Blade	-2.4°	1.1°	3.42°	3.7°	**1.36**	2.0	1.8°	0°	16	24	0.32
127	6573	6594	6572	"	"	"	"	"	"	"	"	"	16	24	0.32
36	3934	3959	3934	X-59 Blade	-2.4°	1.1°	3.42°	3.7°	**1.36**	2.0	2.4°	0°	16	24	0.32
128	6596	6621	6572	"	"	"	"	"	"	"	"	"	16	24	0.32
123	6467	6492	6467	X-59 Blade	-2.4°	1.1°	3.42°	3.7°	**1.4**	1.2	1.8°	0°	8	16	0.32
49	4284	4309	4231	"	"	"	"	"	"	"	"	"	4	24	0.32
124	6493	6518	6493	X-59 Blade	-2.4°	1.1°	3.42°	3.7°	**1.4**	1.2	2.4°	0°	8	16	0.32
50	4310	4335	4231	"	"	"	"	"	"	"	"	"	4	24	0.32
30	3775	3800	3775	X-59 Blade	-2.4°	1.1°	3.42°	3.7°	**1.4**	2.0	1.8°	0°	16	24	0.32
31	3801	3826	3801	X-59 Blade	-2.4°	1.1°	3.42°	3.7°	**1.4**	2.0	2.4°	0°	16	24	0.32
40	4041	4066	4041	X-59 Blade	-2.4°	1.1°	3.42°	3.7°	**1.47**	2.0	1.8°	0°	0	8	0.32
125	6520	6545	6519	"	"	"	"	"	"	"	"	"	16	24	0.32
41	4067	4092	4067	X-59 Blade	-2.4°	1.1°	3.42°	3.7°	**1.47**	2.0	2.4°	0°	8	16	0.32
126	6546	6571	6519	"	"	"	"	"	"	"	"	"	16	24	0.32
X-59 blade, roll variations															
37	3960	3985	3960	X-59 Blade	-2.4°	1.1°	3.42°	3.7°	**1.36**	2.0	2.1°	15°	16	24	0.32
38	3986	4011	3986	X-59 Blade	-2.4°	1.1°	3.42°	3.7°	**1.36**	2.0	2.1°	30°	16	24	0.32
39	4012	4037	4012	X-59 Blade	-2.4°	1.1°	3.42°	3.7°	**1.36**	2.0	2.1°	45°	16	24	0.32
101	5829	5854	5829	X-59 Blade	-2.4°	1.1°	3.42°	3.7°	**1.4**	1.2	2.1°	5°	16	24	0.32
103	5887	5912	5886	"	"	"	"	"	"	"	"	"	8	24	0.32
102	5855	5880	5855	X-59 Blade	-2.4°	1.1°	3.42°	3.7°	**1.4**	1.2	2.1°	10°	16	24	0.32
104	5913	5938	6147	"	"	"	"	"	"	"	"	"	8	24	0.32
105	5939	5964	6147	"	"	"	"	"	"	"	"	"	16	24	0.32
106	5965	5990	5965	X-59 Blade	-2.4°	1.1°	3.42°	3.7°	**1.4**	1.2	2.1°	15°	8	16	0.32
51	4336	4361	4231	"	"	"	"	"	"	"	"	"	4	24	0.32
107	5991	6016	5991	X-59 Blade	-2.4°	1.1°	3.42°	3.7°	**1.4**	1.2	2.1°	20°	8	16	0.32
108	6017	6042	6017	X-59 Blade	-2.4°	1.1°	3.42°	3.7°	**1.4**	1.2	2.1°	25°	8	16	0.32
109	6043	6068	6043	X-59 Blade	-2.4°	1.1°	3.42°	3.7°	**1.4**	1.2	2.1°	30°	8	16	0.32
52	4362	4387	4231	"	"	"	"	"	"	"	"	"	4	24	0.32
110	6069	6094	6069	X-59 Blade	-2.4°	1.1°	3.42°	3.7°	**1.4**	1.2	2.1°	35°	8	16	0.32
111	6095	6120	6095	X-59 Blade	-2.4°	1.1°	3.42°	3.7°	**1.4**	1.2	2.1°	40°	8	16	0.32
112	6121	6146	6121	X-59 Blade	-2.4°	1.1°	3.42°	3.7°	**1.4**	1.2	2.1°	45°	8	16	0.32
53	4388	4413	4231	"	"	"	"	"	"	"	"	"	4	24	0.32
90	5443	5468	5443	X-59 Blade	-2.4°	1.1°	3.42°	3.7°	**1.4**	2.0	2.1°	5°	16	24	0.32
91	5469	5494	5469	X-59 Blade	-2.4°	1.1°	3.42°	3.7°	**1.4**	2.0	2.1°	10°	16	24	0.32
32	3828	3853	3827	X-59 Blade	-2.4°	1.1°	3.42°	3.7°	**1.4**	2.0	2.1°	15°	16	24	0.32
92	5495	5520	5881	"	"	"	"	"	"	"	"	"	16	24	0.32
93	5521	5546	5521	X-59 Blade	-2.4°	1.1°	3.42°	3.7°	**1.4**	2.0	2.1°	20°	16	24	0.32
94	5547	5572	5547	X-59 Blade	-2.4°	1.1°	3.42°	3.7°	**1.4**	2.0	2.1°	25°	16	24	0.32
33	3854	3879	3854	X-59 Blade	-2.4°	1.1°	3.42°	3.7°	**1.4**	2.0	2.1°	30°	16	24	0.32
95	5573	5598	5881	"	"	"	"	"	"	"	"	"	16	24	0.32
96	5599	5624	5599	X-59 Blade	-2.4°	1.1°	3.42°	3.7°	**1.4**	2.0	2.1°	35°	16	24	0.32
97	5625	5650	5625	X-59 Blade	-2.4°	1.1°	3.42°	3.7°	**1.4**	2.0	2.1°	40°	16	24	0.32
34	3880	3905	3880	X-59 Blade	-2.4°	1.1°	3.42°	3.7°	**1.4**	2.0	2.1°	45°	16	24	0.32
98	5651	5676	5881	"	"	"	"	"	"	"	"	"	16	24	0.32
114	6232	6257	6232	X-59 Blade	-2.4°	1.1°	3.42°	3.7°	**1.4**	3.0	2.1°	5°	16	24	0.32
115	6258	6283	6258	X-59 Blade	-2.4°	1.1°	3.42°	3.7°	**1.4**	3.0	2.1°	10°	16	24	0.32
116	6284	6309	6284	X-59 Blade	-2.4°	1.1°	3.42°	3.7°	**1.4**	3.0	2.1°	15°	16	24	0.32
117	6310	6335	6310	X-59 Blade	-2.4°	1.1°	3.42°	3.7°	**1.4**	3.0	2.1°	20°	16	24	0.32
118	6336	6361	6336	X-59 Blade	-2.4°	1.1°	3.42°	3.7°	**1.4**	3.0	2.1°	25°	16	24	0.32
119	6362	6387	6362	X-59 Blade	-2.4°	1.1°	3.42°	3.7°	**1.4**	3.0	2.1°	30°	16	24	0.32
120	6388	6413	6388	X-59 Blade	-2.4°	1.1°	3.42°	3.7°	**1.4**	3.0	2.1°	35°	16	24	0.32
121	6414	6439	6414	X-59 Blade	-2.4°	1.1°	3.42°	3.7°	**1.4**	3.0	2.1°	40°	16	24	0.32
122	6440	6465	6440	X-59 Blade	-2.4°	1.1°	3.42°	3.7°	**1.4**	3.0	2.1°	45°	16	24	0.32
44	4152	4177	4152	X-59 Blade	-2.4°	1.1°	3.42°	3.7°	**1.47**	2.0	2.1°	15°	16	24	0.32
45	4178	4203	4178	X-59 Blade	-2.4°	1.1°	3.42°	3.7°	**1.47**	2.0	2.1°	30°	16	24	0.32
46	4204	4229	4204	X-59 Blade	-2.4°	1.1°	3.42°	3.7°	**1.47**	2.0	2.1°	45°	16	24	0.32

SigSet #	Start Run	End Run	Preferred Ref Run	Model	Flaps (deg)	Ailerons (deg)	Stab (deg)	T-Tail (deg)	Mach	Height /L	Alpha (deg)	Roll m2r (deg)	Start Xram (in.)	End Xram (in.)	Sweep Inc (in.)
X-59 blade, control surface deflections															
86	5332	5357	5332	X-59 Blade	-2.9°	1.1°	3.42°	3.7°	**1.4**	1.2	2.1°	0°	16	24	0.32
85	5306	5331	5301	"	"	"	"	"	"	"	"	"	8	24	0.32
87	5358	5383	5358	X-59 Blade	-2.9°	1.1°	3.42°	3.7°	**1.4**	2.0	2.1°	0°	16	24	0.32
88	5384	5409	5384	X-59 Blade	-2.9°	1.1°	3.42°	3.7°	**1.4**	3.0	2.1°	0°	16	24	0.32
68	4869	4894	4869	X-59 Blade	-2.4°	1.6°	3.42°	3.7°	**1.4**	1.2	2.1°	0°	16	24	0.32
67	4843	4868	4842	"	"	"	"	"	"	"	"	"	8	24	0.32
69	4895	4920	4895	X-59 Blade	-2.4°	1.6°	3.42°	3.7°	**1.4**	2.0	2.1°	0°	16	24	0.32
70	4921	4946	4921	X-59 Blade	-2.4°	1.6°	3.42°	3.7°	**1.4**	3.0	2.1°	0°	16	24	0.32
72	4977	5002	4977	X-59 Blade	-2.4°	1.1°	2.92°	3.7°	**1.4**	1.2	2.1°	0°	16	24	0.32
71	4951	4976	4950	"	"	"	"	"	"	"	"	"	8	24	0.32
132	6714	6739	6714	X-59 Blade	-2.4°	1.1°	3.92°	3.7°	**1.4**	1.2	2.1°	0°	16	24	0.32
61	4584	4609	4583	"	"	"	"	"	"	"	"	"	8	24	0.32
131	6688	6713	6687	"	"	"	"	"	"	"	"	"	8	24	0.32
74	5029	5054	5029	X-59 Blade	-2.4°	1.1°	2.92°	3.7°	**1.4**	2.0	2.1°	0°	16	24	0.32
63	4636	4661	4636	X-59 Blade	-2.4°	1.1°	3.92°	3.7°	**1.4**	2.0	2.1°	0°	16	24	0.32
66	4716	4741	4715	"	"	"	"	"	"	"	"	"	16	24	0.32
76	5081	5106	5081	X-59 Blade	-2.4°	1.1°	2.92°	3.7°	**1.4**	3.0	2.1°	0°	16	24	0.32
65	4689	4714	4689	X-59 Blade	-2.4°	1.1°	3.92°	3.7°	**1.4**	3.0	2.1°	0°	16	24	0.32
79 & 80 1079	5180	5192	5166	X-59 Blade	-2.4°	1.1°	3.42°	2.7°	**1.4**	1.2	2.1°	0°	12.2	24	0.32
130	6658	6683	6658	X-59 Blade	-2.4°	1.1°	3.42°	4.7°	**1.4**	1.2	2.1°	0°	16	24	0.32
58	4502	4527	4501	"	"	"	"	"	"	"	"	"	6	24	0.32
129	6632	6657	6631	"	"	"	"	"	"	"	"	"	6	24	0.32
81	5219	5244	5219	X-59 Blade	-2.4°	1.1°	3.42°	2.7°	**1.4**	2.0	2.1°	0°	16	24	0.32
59	4528	4553	4528	X-59 Blade	-2.4°	1.1°	3.42°	4.7°	**1.4**	2.0	2.1°	0°	16	24	0.32
83	5271	5296	5271	X-59 Blade	-2.4°	1.1°	3.42°	2.7°	**1.4**	3.0	2.1°	0°	16	24	0.32
60	4554	4579	4554	X-59 Blade	-2.4°	1.1°	3.42°	4.7°	**1.4**	3.0	2.1°	0°	16	24	0.32
77	5107	5132	5107	X-59 Blade	-2.4°	1.1°	2.92°	3.7°	**1.4**	1.2	1.8°	0°	8	16	0.32
78	5133	5158	5133	X-59 Blade	-2.4°	1.1°	2.92°	3.7°	**1.4**	1.2	2.4°	0°	8	16	0.32
73	5003	5028	5003	X-59 Blade	-2.4°	1.1°	2.92°	3.7°	**1.4**	2.0	1.8°	0°	16	24	0.32
62	4610	4635	4610	X-59 Blade	-2.4°	1.1°	3.92°	3.7°	**1.4**	2.0	1.8°	0°	16	24	0.32
75	5055	5080	5055	X-59 Blade	-2.4°	1.1°	2.92°	3.7°	**1.4**	2.0	2.4°	0°	16	24	0.32
64	4663	4688	4663	X-59 Blade	-2.4°	1.1°	3.92°	3.7°	**1.4**	2.0	2.4°	0°	16	24	0.32
82	5245	5270	5245	X-59 Blade	-2.4°	1.1°	3.42°	2.7°	**1.4**	3.0	1.8°	0°	16	24	0.32
X-59 sting, baseline runs															
137	6935	6972	6897	X-59 Sting	-2.4°	1.1°	3.42°	3.7°	**1.36**	1.2	2.1°	0°	**0**	**24**	0.32
148	7294	7319	7294	X-59 Sting	-2.4°	1.1°	3.42°	3.7°	**1.36**	2.0	2.1°	0°	16	24	0.32
138	6973	6998	6896	"	"	"	"	"	"	"	"	"	8	24	0.32
144	7133	7158	7132	"	"	"	"	"	"	"	"	"	8	24	0.32
139	6999	7024	6999	X-59 Sting	-2.4°	1.1°	3.42°	3.7°	**1.36**	3.0	2.1°	0°	16	24	0.32
208	9030	9055	9030	X-59 Sting	-2.4°	1.1°	3.42°	3.7°	**1.4**	1.2	2.1°	0°	12	20	0.32
134	6767	6842	6763	"	"	"	"	"	"	"	"	"	0	24	0.32
142	7079	7104	7026	"	"	"	"	"	"	"	"	"	0	24	0.32
143	7105	7130	7131	"	"	"	"	"	"	"	"	"	16	24	0.32
195	8640	8665	8640	X-59 Sting	-2.4°	1.1°	3.42°	3.7°	**1.4**	2.0	2.1°	0°	16	24	0.32
135	6843	6868	6895	"	"	"	"	"	"	"	"	"	8	24	0.32
140	7027	7052	7026	"	"	"	"	"	"	"	"	"	8	24	0.32
187	8376	8451	8372	"	"	"	"	"	"	"	"	"	0	24	0.32
141	7053	7078	7053	X-59 Sting	-2.4°	1.1°	3.42°	3.7°	**1.4**	3.0	2.1°	0°	16	24	0.32
136	6869	6894	6895	"	"	"	"	"	"	"	"	"	16	24	0.32
198	8719	8794	8718	"	"	"	"	"	"	"	"	"	0	24	0.32
145	7164	7239	7164	X-59 Sting	-2.4°	1.1°	3.42°	3.7°	**1.47**	1.2	2.1°	0°	**0**	**24**	0.32
149	7321	7346	7321	X-59 Sting	-2.4°	1.1°	3.42°	3.7°	**1.47**	2.0	2.1°	0°	16	24	0.32
146	7240	7265	7292	"	"	"	"	"	"	"	"	"	16	24	0.32
147	7266	7291	7266	X-59 Sting	-2.4°	1.1°	3.42°	3.7°	**1.47**	3.0	2.1°	0°	16	24	0.32
X-59 sting, alpha variations															
150	7348	7373	7348	X-59 Sting	-2.4°	1.1°	3.42°	3.7°	**1.4**	1.2	1.8°	0°	16	24	0.32
151	7374	7399	7374	X-59 Sting	-2.4°	1.1°	3.42°	3.7°	**1.4**	1.2	2.4°	0°	12	20	0.32

SigSet #	Start Run	End Run	Preferred Ref Run	Model	Flaps (deg)	Ailerons (deg)	Stab (deg)	T-Tail (deg)	Mach	Height /L	Alpha (deg)	Roll m2r (deg)	Start Xram (in.)	End Xram (in.)	Sweep Inc (in.)
X-59 sting, roll variations															
152	7400	7425	7400	X-59 Sting	-2.4°	1.1°	3.42°	3.7°	**1.4**	1.2	2.1°	5°	12	20	0.32
153	7426	7451	7426	X-59 Sting	-2.4°	1.1°	3.42°	3.7°	**1.4**	1.2	2.1°	10°	12	20	0.32
154	7452	7477	7452	X-59 Sting	-2.4°	1.1°	3.42°	3.7°	**1.4**	1.2	2.1°	15°	12	20	0.32
209	9056	9081	9029	"	"	"	"	"	"	"	"	"	12	24	0.32
155	7478	7504	7478	X-59 Sting	-2.4°	1.1°	3.42°	3.7°	**1.4**	1.2	2.1°	20°	12	20	0.32
156	7505	7530	7505	X-59 Sting	-2.4°	1.1°	3.42°	3.7°	**1.4**	1.2	2.1°	25°	12	20	0.32
157	7532	7557	7532	X-59 Sting	-2.4°	1.1°	3.42°	3.7°	**1.4**	1.2	2.1°	30°	12	20	0.32
210	9082	9107	9029	"	"	"	"	"	"	"	"	"	12	24	0.32
159	7584	7609	7584	X-59 Sting	-2.4°	1.1°	3.42°	3.7°	**1.4**	1.2	2.1°	35°	12	20	0.32
160	7610	7635	7610	X-59 Sting	-2.4°	1.1°	3.42°	3.7°	**1.4**	1.2	2.1°	40°	12	20	0.32
158	7558	7583	7558	X-59 Sting	-2.4°	1.1°	3.42°	3.7°	**1.4**	1.2	2.1°	45°	12	20	0.32
211	9108	9133	9029	"	"	"	"	"	"	"	"	"	12	24	0.32
188	8452	8477	8452	X-59 Sting	-2.4°	1.1°	3.42°	3.7°	**1.4**	2.0	2.1°	5°	16	24	0.32
189	8478	8503	8478	X-59 Sting	-2.4°	1.1°	3.42°	3.7°	**1.4**	2.0	2.1°	10°	16	24	0.32
190	8504	8529	8504	X-59 Sting	-2.4°	1.1°	3.42°	3.7°	**1.4**	2.0	2.1°	15°	16	24	0.32
191	8530	8555	8530	X-59 Sting	-2.4°	1.1°	3.42°	3.7°	**1.4**	2.0	2.1°	20°	16	24	0.32
192	8556	8581	8556	X-59 Sting	-2.4°	1.1°	3.42°	3.7°	**1.4**	2.0	2.1°	25°	16	24	0.32
193	8582	8607	8582	X-59 Sting	-2.4°	1.1°	3.42°	3.7°	**1.4**	2.0	2.1°	30°	16	24	0.32
194	8608	8633	8608	X-59 Sting	-2.4°	1.1°	3.42°	3.7°	**1.4**	2.0	2.1°	35°	16	24	0.32
196	8666	8691	8666	X-59 Sting	-2.4°	1.1°	3.42°	3.7°	**1.4**	2.0	2.1°	40°	16	24	0.32
197	8692	8717	8692	X-59 Sting	-2.4°	1.1°	3.42°	3.7°	**1.4**	2.0	2.1°	45°	16	24	0.32
199	8795	8820	8795	X-59 Sting	-2.4°	1.1°	3.42°	3.7°	**1.4**	3.0	2.1°	5°	16	24	0.32
200	8821	8846	8821	X-59 Sting	-2.4°	1.1°	3.42°	3.7°	**1.4**	3.0	2.1°	10°	16	24	0.32
201	8847	8872	8847	X-59 Sting	-2.4°	1.1°	3.42°	3.7°	**1.4**	3.0	2.1°	15°	16	24	0.32
202	8873	8898	8873	X-59 Sting	-2.4°	1.1°	3.42°	3.7°	**1.4**	3.0	2.1°	20°	16	24	0.32
203	8899	8924	8899	X-59 Sting	-2.4°	1.1°	3.42°	3.7°	**1.4**	3.0	2.1°	25°	16	24	0.32
204	8925	8950	8925	X-59 Sting	-2.4°	1.1°	3.42°	3.7°	**1.4**	3.0	2.1°	30°	16	24	0.32
205	8951	8976	8951	X-59 Sting	-2.4°	1.1°	3.42°	3.7°	**1.4**	3.0	2.1°	35°	16	24	0.32
206	8977	9002	8977	X-59 Sting	-2.4°	1.1°	3.42°	3.7°	**1.4**	3.0	2.1°	40°	16	24	0.32
207	9003	9028	9003	X-59 Sting	-2.4°	1.1°	3.42°	3.7°	**1.4**	3.0	2.1°	45°	16	24	0.32
X-59 sting, control surface deflections															
177	8096	8121	8096	X-59 Sting	-2.9°	1.1°	3.42°	3.7°	**1.4**	1.2	2.1°	0°	16	24	0.32
176	8070	8095	8122	"	"	"	"	"	"	"	"	"	8	24	0.32
182 & 183 1182	8247	8285	8233	X-59 Sting	-1.9°	1.1°	3.42°	3.7°	**1.4**	1.2	2.1°	0°	12.2	24	0.32
175	8044	8069	8044	X-59 Sting	-2.9°	1.1°	3.42°	3.7°	**1.4**	2.0	2.1°	0°	16	24	0.32
184	8286	8311	8286	X-59 Sting	-1.9°	1.1°	3.42°	3.7°	**1.4**	2.0	2.1°	0°	16	24	0.32
174	8018	8043	8018	X-59 Sting	-2.9°	1.1°	3.42°	3.7°	**1.4**	3.0	2.1°	0°	16	24	0.32
185	8312	8337	8312	X-59 Sting	-1.9°	1.1°	3.42°	3.7°	**1.4**	3.0	2.1°	0°	16	24	0.32
178 & 179 1178	8139	8177	8125	X-59 Sting	-2.4°	0.6°	3.42°	3.7°	**1.4**	1.2	2.1°	0°	12.2	24	0.32
161 & 162 1161	7655	7693	7641	X-59 Sting	-2.4°	1.6°	3.42°	3.7°	**1.4**	1.2	2.1°	0°	12.2	24	0.32
180	8178	8203	8178	X-59 Sting	-2.4°	0.6°	3.42°	3.7°	**1.4**	2.0	2.1°	0°	16	24	0.32
163	7694	7719	7694	X-59 Sting	-2.4°	1.6°	3.42°	3.7°	**1.4**	2.0	2.1°	0°	16	24	0.32
181	8204	8229	8204	X-59 Sting	-2.4°	0.6°	3.42°	3.7°	**1.4**	3.0	2.1°	0°	16	24	0.32
164	7720	7745	7720	X-59 Sting	-2.4°	1.6°	3.42°	3.7°	**1.4**	3.0	2.1°	0°	16	24	0.32